Response prediction of acoustically-excited composite honeycomb sandwich structures with double curvature

by

Paul Robert Cunningham

of the

School of Engineering Sciences
Aeronautics and Astronautics
Faculty of Engineering and Applied Science
University of Southampton
England

Doctor of Philosophy

June 2001

UNIVERSITY OF SOUTHAMPTON

ABSTRACT

FACULTY OF ENGINEERING AND APPLIED SCIENCE

SCHOOL OF ENGINEERING SCIENCES
AERONAUTICS AND ASTRONAUTICS

Doctor of Philosophy

RESPONSE PREDICTION OF ACOUSTICALLY-EXCITED COMPOSITE HONEYCOMB SANDWICH STRUCTURES WITH DOUBLE CURVATURE

by Paul Robert Cunningham

Composite honeycomb sandwich structures have been favoured in the aircraft industry for many years due to their low-weight, high stiffness, and improved fatigue resistance. The response of doubly curved, composite honeycomb sandwich panels to high intensity, random pressure loads has received little attention, and there is a need to update current design guides to include this type of structure.

A set of four doubly curved honeycomb sandwich panels were manufactured at the University of Southampton. The panels were tested to determine some of the resonance frequencies of vibration, and the results were used to validate the Finite Element models of the four panels. These FE models were used to study the effects of various design parameters on the free vibration response, and the work resulted in various sensitivity parameters which could potentially be used as a guide for designers.

The major part of the work involved testing the panels in a Progressive Wave Tube (PWT) facility with random acoustic excitation at grazing incidence to the concave panel surface. The measured strain response of the panels was predominately in the fundamental bending mode, with face plate strain levels which differed between the inner and outer face plates, highlighting the significant effect that double curvature can have on the relative strain levels in the face plates.

A new method was developed for estimating the shear strain in the core of the sandwich panels using a finite difference approximation. The technique was validated using a cantilevered sandwich beam, giving excellent agreement between experiment and theory for both static and dynamic response. The work resulted in a new viable technique which has potential for use in generating S/N data for the core during random fatigue testing of sandwich coupon structures.

Three methods were used to predict the response of the panels to random acoustic excitation. A combination of the single-degree-of-freedom approach and the FE method with an estimate of the joint acceptance gave excellent agreement with the measured RMS strains. Blevin's method resulted in an overestimate, and the classical Mile's approach resulted in a gross under-estimation. Finally, a novel travelling wave approach was used in the FE analysis, giving good agreement with the measured RMS strains and power spectral density, particularly for the fundamental mode.

Acknowledgements

There are many people, without whose advice, support, encouragement, and patience, I would have never seen this work through to completion. I would like to take this time to gratefully acknowledge these few and offer my sincere thanks:

To Professor Bob White, who gave me the opportunity to carry out this work, and for whose support, encouragement and advice I am extremely grateful.

To my good friends Professor Robin Langley, Dr Guglielmo Aglietti and Mr David Millar; for many years of encouragement and advice, and for countless hours of amusing banter. You helped keep me sane...almost!

I am indebted to Hamble Group (Aerostructures) Ltd., and in particular Robin Phillips and Jacky Ridewood, who very kindly provided me with an abundance of advice, help and materials used to manufacture the test panels. I would also like to thank Ying Xiao for kindly allowing me to use the Progressive Wave Tube spatial data that she acquired.

To my Mum and Dad; your patience and support have been legendary over the years. Thank-you for bearing my ups and downs, and never losing confidence in me.

To my fiancée Tara, who stood by me during the final stages of the work, and kept pushing me back towards the computer. Thank-you for everything.

Finally, to all my family, friends, and collegues. Thank-you for your encouragement.

This work is dedicated to the memory
of my grandfathers,

Maurice James Perkins

and

Wilfred George Cunningham.

Contents

List of Figures

List of Tables

Nomenclature

a	a constant
	length (m)
A	semi-empirical constant
	area (m^2)
b	a constant
	breadth (m)
B	a constant
	bandwidth (Hz)
c	core thickness (m)
	wavespeed (m/s^2)
c_v	viscous damping coefficient
C	arbitrary constant
d	depth, thickness (m)
dB	decibels
D	flexural rigidity of a beam (Nm^2)
e	exponent
E	estimated value
	Young's Modulus of Elasticity (N/m^2)
f	frequency (Hz)
	face plate thickness (m)
F_n	generalised force
G_{xx}	single-sided spectral density
	shear modulus (N/m^2)
$\mathbf{H}$	frequency response function
i	complex number $\sqrt{-1}$
	index value
j	index value
J_n	joint acceptance

k_a	acoustic wavenumber $(1/m)$
k_1	structural wavenumber in x-direction $(1/m)$
k_2	structural wavenumber in y-direction $(1/m)$
K	strain gauge factor
$\mathbf{K}$	stiffness matrix
L	total length (m)
m	a constant
	mass per unit area
M	bending moment (Nm)
$\mathbf{M}$	mass matrix
N	normal force (N)
p	pressure (N/m^2)
$p(x)$	probability
P	load (N)
Q	shear force (N)
R	resistance (Ω)
R_x	radius of curvature in x-direction (m)
R_y	radius of curvature in y-direction (m)
S_{xx}	double-sided spectral density $(Units^2/Hz)$
t	time (s)
u	response amplitude (m)
V	a constant
	voltage
w	out-of-plane displacement (m)
x, y, z	cartesian coordinates

ϵ	direct strain (m/m)
ω	radian frequency (rad/s)
ρ	density (kg/m^3)
ϕ	mode shape
	eigenvector
π	constant (3.141592654)
λ	wavelength (m)
μ	mean value
	micro $(\times 10^{-3})$

σ	direct stress (N/m^2)
	standard deviation
γ	shear strain
γ_1	skewness
γ_2	kurtosis
ν	Poisson's ratio
τ	shear stress (N/m^2)
ψ	spatial distribution of pressure
ζ	viscous damping ratio
$\Re$	real part of complex number
$\Im$	imaginary part of complex number

AFD	Acoustic Flaw Detection
CFRP	Carbon-Fibre Reinforced Plastic
ESDU	Engineering Sciences Data Unit
FE	Finite Element
FFT	Fast Fourier Transform
NDT	Non-Destructive Testing
OASPL	Overall Sound Pressure Level
ppr	power plant radial
PWT	Progressive Wave Tube
RMS	Root Mean Square
SNR	Signal-to-Noise Ratio
SPL	Sound Pressure Level
SWG	Standard Wire Gauge

Chapter 1

Introduction

1.1 The general problem

The dynamic response of aircraft structures to random pressure loading from aerodynamic and engine acoustic sources can lead to acoustic fatigue failures [1, 2, 3, 4, 5, 6, 7] and it is the understanding of these acoustic sources, coupled with the development of structural response prediction models, which will enable the engineer to design against acoustic fatigue. Since the introduction of the gas turbine engine, and its development from the early turbojet to the modern high bypass turbofans of today, the acoustic fatigue of aircraft structures has remained an important design issue. Much work has been carried out over the years in an attempt to predict the stresses that could be encountered in service due to the random acoustic loading produced by the gas turbine engine [8, 9, 10, 11]. However, with the introduction of advanced composite materials, a new set of issues have had to be addressed which concern the very different fatigue characteristics of this new type of structure [4]. One particular type of composite structure, the honeycomb sandwich panel, has a very high stiffness to weight ratio, and has found favour in the aircraft industry over the years. Panels employing a mixture of carbon fibre reinforced plastics and resin impregnated paper honeycomb can be found in applications such as fairings and floor panels, ailerons, helicopter rotor blades, and engine intake barrel panels. The latter type of structure, shown in figure 1.1, has a complicated geometry due to the shape of the engine intake, and as such can be considered to be doubly curved. The dynamic response of sandwich structures to acoustic excitation has previously been investigated [13, 14, 15, 16], but only for flat and singly curved geometries. In addition, the engine intake barrel panel represents a different type of problem to those previously investigated due to the particular nature of the acoustic excitation [16]. The fan of a high bypass engine

Figure 1.1: A nose cowl showing the intake barrel segments [12].

can produce noise levels at fan related frequencies which exceed those produced by the efflux of the engine by as much as 30 dB/Hz [16]. In addition, the maximum noise levels produced by the efflux occur during take-off and are also directly related to the engine power, whereas the noise produced by the fan is a function of the fan rpm and can be just as severe during cruise as for take-off. Therefore, fatigue of engine intake barrels can occur both during take off and cruise. The engine intake barrel represents one typical application of the composite sandwich structure having a doubly curved geometry. With the increase in use of composite materials for aircraft manufacture, it is inevitable that this type of structure will be used in a wider range of applications due to its favourable characteristics in terms of high stiffness, low weight, low cost, ease of manufacture, and perhaps, improved fatigue resistance [15]. However, there has been very little work on the dynamic response of carbon fibre honeycomb panels with double curvature to random acoustic excitation.

1.2 Historical review of acoustic fatigue

1.2.1 Early investigations

With the introduction of the gas turbine engine in the early nineteen fifties and the resulting rapid development of more powerful engines, there followed an increase in the

number of reported fatigue failures of the skin structures close to the jet exhaust [1]. This led to a range of investigations by both the UK and the USA aircraft industries and research establishments in an attempt to both understand and alleviate this problem. The majority of these early investigations involved experimental studies using both simple test panels [5, 17, 18, 19] and actual aircraft structures [20, 21], and excitation was provided by sirens, random noise generators and aircraft engines [22, 23, 6]. This early work led to the development of the first design nomographs for acoustically excited aircraft structures [24].

A response prediction method for acoustically excited metallic structures was first developed by Miles [25]. In that study, Miles considered an elastic structure subjected to random loading and simplified the analysis by assuming the structure to have only a single degree of freedom. He also used the concept of cumulative damage [26] to analyse the fatigue behaviour of such structures. Miles derived an expression for the equivalent root mean square stress for a single degree of freedom system under random loading. Miner's hypothesis of cumulative damage was then used to estimate the fatigue life of the structure [26].

Powell [27] took this work one stage further by considering the normal mode approach. The modes of vibration of the structure were assumed to be uncoupled, hence the response of the structure to random pressure loads could be given as a series of N independent equations (one for each mode). Powell developed an expression for the power spectrum of the total stress fluctuation, and in addition he introduced the concept of "joint acceptance", which is a measure of the effectiveness of the complex pressure field in exciting a particular mode. The cumulative damage law was again used in the estimation of fatigue life.

Following on from Powell's work, Clarkson [8] simplified the theory for panel-type structures by assuming that the major part of the response results from the contribution of one predominant mode. He also assumed that the excitation pressures were exactly in phase over the whole structure and derived an expression for the mean square stress in terms of the viscous damping ratio and resonant frequency,

$$\overline{\sigma^2(t)} = \frac{\pi}{4\zeta} f_n G_p(f_n) \sigma_0^2 \tag{1.1}$$

where σ_0 is the static stress at the point of interest due to a uniform pressure of unit magnitude, ζ is the viscous damping ratio, and $G_p(f_n)$ is the excitation pressure spectral density at the resonant frequency f_n [4]. This expression was first derived by Miles [25] and is still used today as a design tool for structures subjected to

random pressure loading. In order to justify his approach, Clarkson [8] examined the application of the theory to a range of structures, which included flat plates, aircraft control surfaces, and integrally stiffened skins, and compared the results with several experiments. Clarkson [8] concluded that considering the severe simplifications in this theory, the agreement with experimental measurements was satisfactory, and in order to obtain greater accuracy a multi-modal analysis of the structural response would be necessary.

The work continued in an attempt to improve the estimation procedure with developments of Powell's method by Bozich [28], and Barnoski and Maurer [29], and improvements to the design nomographs by Ballentine [13], Bayerdorfer [30], Arcas [10], and Rudder and Plumblee [31]. With the improvements in computing power in the late nineteen sixties, developments were also made in the use of the finite element method to estimate the response of flat and curved skin stringer panels to random acoustic loads [32, 33, 34, 9].

In relation to the engine nacelle structure, simplified shell theory was used by Soovere [35] to investigate the failure of large fan engine intake ducts. Although this early research was concerned with intake ducts constructed from stiffened aluminium alloy panels, it still provides some insight into the possible explanations for the failures experienced in such structures which are subject to this particular type of acoustic loading. Soovere found that the duct shell stress spectrum exhibited a similar spectral content to that of the fan noise. This initially led to the conclusion that the duct shell response was forced, however, after further examination the buzz-saw[1] stress components were found to be amplified over a small region of the circumferential mode number which occurred in the vicinity of the shell resonances [35]. It was pointed out, however, that engine hunting would considerably reduce the dwell time on resonance [35].

1.2.2 Developments with respect to composite structures

By the mid to late nineteen seventies there were considerable advances in the design and manufacture of composite structures. Work began to ascertain the effects that random acoustic loading would have on the fatigue life of these new materials which included boron and glass fibres, Kevlar, and the most promising for aircraft applications; carbon fibre reinforced plastic (CFRP). One of the earliest studies of the response of CFRP plates to random acoustic loading was made by White [38].

[1]Otherwise known as multiple-pure tones or combination tones which are multiples of the basic fan rotation frequency and are produced when the tip speed of the fan becomes supersonic [36, 37].

In this paper, comparisons were made between CFRP and aluminium plates and the author showed the nonlinear characteristics of the CFRP plates at high excitation levels (above 130 dB re $2 \times 10^{-5} Pa$). This nonlinear behaviour was also found during the investigations of Wolfe and Jacobson [39] for tests carried out on a series of multi-bay boron-epoxy and graphite-epoxy panels. Although developed for metallic structures, equation 1.1 was used by White and Mousley [40] to compare experimental measurement of overall plate response with theoretical predictions for CFRP plates. The single mode predictions using the ESDU data sheets [41], which are based on equation 1.1, were found to be in very good agreement with the measured values for excitation levels up to 145 dB. Some nonlinear effects were observed during this investigation, and the authors went on to study the combination of random acoustic loading and in-plane compression, where the "snap through" effect was observed. The conclusions drawn indicated that at response levels below those that produce marked non-linearities, the single mode method can be used to estimate the RMS response of simple composite plate structures.

In terms of fatigue, the methods developed for metallic structures are not strictly applicable to composite structures. This is because the methods rely on surface strain estimates, whereas for composite materials it is the combination of internal stresses/strains at a critical point within the layers of the composite that will cause fatigue damage to initiate and propagate [4]. In addition, the flexural fatigue tests conducted on standard test coupons were found to be unreliable when trying to determine the fatigue life of a specimen since the specimens were found to delaminate at the edges [42]. To combat this problem, the half-sine clamp was developed by Drew and White. This is basically a cantilever clamp with a half-sine wave shape along the clamping edge which, when tested using CFRP test specimens, produced a more representative delamination failure within the test coupon [42].

Although not specifically developed for composite structures, an approximate analytical method for predicting the acoustic fatigue life of plates and shells using multi-modal analysis was developed recently by Blevins [43]. In his paper, Blevins extended the Miles approach to higher modes and complex shapes and developed methods for estimating the effects of finite acoustic wavelength on their excitation. Blevins method was a bridge between deterministic and statistical approaches and his approximations were most applicable to uniform plate and shell structures excited by a stationary (ergodic) sound field. The natural frequencies, mode shapes, and the relationship between modal deformation and modal stress are required as inputs in this method. Damping and the magnitude of the applied pressures are also required

although exact knowledge of the distribution of the applied surface pressures is not required, instead an estimate of this distribution was used. For this reason, the concept of joint acceptance was used in Blevins' formulation. Since the evaluation of joint acceptance requires an estimate of the surface acoustic pressure distributions, he suggested several approximations for the shape of these distributions [43]. Blevins used the mass-weighted structural mode shape approximation, from which the joint acceptance was calculated to be unity. A method was then given for calculating the acoustically induced displacements for any mode. In order to validate the method, Blevins compared his results with those produced by the AGARD [11] method, which is a design guide formulated primarily from the work of Miles [25] and Clarkson [8]. A flat plate and a singly curved plate loaded with broadband sound with an overall sound pressure level of 145.7dB were considered. Results from Blevins method agreed very closely with those from the AGARD method and he concluded that the former could be viewed as a generalization of the Miles/Clarkson/AGARD approach. For completeness, Blevins also compared predictions by his method with experimental data obtained from integrally stiffened, flat rectangular titanium panels tested in a Progressive Wave Tube (PWT). The experimental results agreed fairly well with the theoretical results within the bounds of uncertainty.

Recent developments in acoustic fatigue research have concentrated on combined thermal-acoustic environments, which are being driven by studies of new hypersonic vehicle designs such as NASP [44, 45], and there is now interest in understanding how these environments affect the non-linear response of aircraft structures [46, 47, 48].

1.3 Dynamic response prediction for sandwich structures subject to random acoustic excitation

Early investigations on the acoustic fatigue of sandwich structures were reported by Sweers [49] and Wallace [50] at one of the first conferences held on acoustic fatigue of aircraft structures [51]. Sweers [49] used simple panel theory to predict the natural frequencies of flat aluminium honeycomb panels, and compared the results with measurements obtained from shaker tests. Predictions for the lower natural frequencies were found to be more accurate than those of the higher modes. The apparent loss in accuracy for these higher modes was attributed to the reduction in plate stiffness due to the shear deformation of the core. Experimental investigations also showed that

the ratio of inner-to-outer [2] stress on the surface of the face plates in the centre of the panel was of the order of 2 to 2.5, which indicated possible fatigue failures in the inner face sheet. Failures were indeed reported in the inner face sheet, as well as along the bolt holes and the core-to-face sheet interface [49]. Prediction of the stress response to acoustic excitation was limited to the fundamental mode since the response at higher frequencies requires knowledge of the spatial correlation of the pressures. Wallace [50] presented an analysis of acoustically excited brazed steel honeycomb panels. Both jet noise and narrow band siren noise were considered in the analysis and stress and fatigue life were computed for variations in basic panel parameters. Damping was taken to be that due to radiation of acoustical energy away from the panel. Since the bending wavelength of the panel was greater than the corresponding wavelength of sound, the damping produced by acoustic radiation would be quite large. The fatigue life was calculated from the maximum value of face sheet stress, which was found to be at the centre of the panel which had simply supported boundary conditions.

Another early analytical and experimental programme was carried out by Jacobson and van der Heyde in order to obtain acoustic fatigue design information for honeycomb panels with fibre-reinforced facings [52]. The study was concerned with S-Glass fibre-reinforced, Boron fibre-reinforced, and aluminium alloy face plates, with a hexagonal cell honeycomb core. A PWT was used to excite the panels with broadband random acoustic waves at a Sound Pressure Level (SPL) of around 167dB (re 2×10^{-5} Pa, frequency bandwidth 1000 Hz). Fifty eight simply supported panels were tested to failure and the effects of various ply lay-ups on the panel life and mode of failure were reported. The authors found that facing failures at the centre of the panel predominated, although some core failures were reported.

Finally, Soovere investigated the dynamic response of acoustically excited carbon fibre reinforced and Kevlar honeycomb panels [15, 53]. He extended existing orthotropic honeycomb panel theory, through coupled normal mode analysis, in order to predict the overall strain at both the edges and the centre of the faces of the panels. His work was the first to investigate the effect of the bevelled edge closeout pan, an example of which is shown in figure 1.2, which was shown to increase the effective shear stiffness of the honeycomb core by an order of magnitude. Soovere showed both analytically and experimentally that, with laterally rigid edge supports, the rotation of the bevelled edge introduced a linear dynamic membrane strain into the inner face sheet. He also found that the dominant contribution to honeycomb panel damping

[2] It is generally accepted that, for flat sandwich panels with bevelled edges, the inner face incorporates the pan or bevelled edge. The definition of the inner and outer face is not dependent on which side is being driven, instead it is dependent on the geometry and configuration of the structure.

was due to acoustic radiation, and for the carbon fibre reinforced panels, the material damping was very low compared to the Kevlar reinforced panels. For singly curved sandwich panels, it has been suggested that the strains at the centre of the panel are higher on the convex face than on the concave face [15].

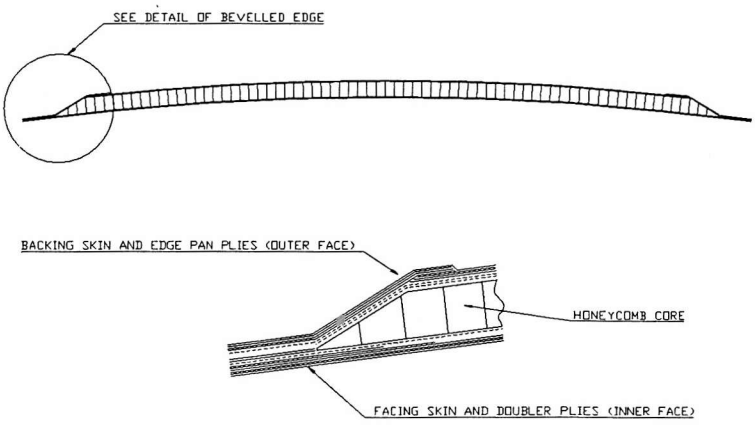

Figure 1.2: Example of a curved sandwich panel with detail of the bevelled edge

1.3.1 Current design techniques for sandwich structures

The Engineering Sciences Data Unit (ESDU) produce a large amount of design data using the results published in the open literature. The data series cover various aerospace related disciplines such as aerodynamics, fatigue, dynamics, structures, transonic aerodynamics, performance, and vibration and acoustic fatigue. The latter sub-series includes work on the prediction of natural frequencies, damping, and root mean square (RMS) stresses/strains in various structural elements such as flat and singly curved isotropic and laminated plates, shells and box structures under the action of random acoustic loading. Sandwich panels are included with both flat and singly curved geometries being considered. The data items which are relevant to the analysis of sandwich structures subject to random acoustic excitation are given in Table 1.1.

Item	*Description*
66013	Terms used in acoustic fatigue analysis.
86025	Practical background information relating to the nature of the acoustic fatigue problem. Includes a review of the acoustic and aerodynamic excitation sources.
74033	A method for estimating buzz-saw noise within the inlet duct of a supersonic fan.
66018	Relationship between Sound Pressure Level (SPL) and RMS fluctuating pressure.
83035	The estimation of the stiffness and apparent elastic properties of laminated flat plates.
72016	Natural frequencies of flat and curved sandwich panels with isotropic face plates (clamped and simply supported edge conditions).
85037	Natural frequencies of flat and curved sandwich panels with laminated face plates (All edges simply supported).
85012	Estimation of damping in laminated and fibre-reinforced plates.
72017	Response to acoustic loading of flat or shallow curved sandwich panels having isotropic face plates of equal thickness and honeycomb cores.
86024	Response to acoustic loading of flat or shallow curved sandwich panels having fibre-reinforced laminated face plates and honeycomb cores.

Table 1.1: ESDU International Data Items for Acoustic Fatigue Analysis of Sandwich Structures.

The general procedure adopted for estimating the in-service life of composite structures subject to acoustic pressure loading is itemised below.

- Estimate the orthotropic material properties of the structure from individual ply properties in the lay-up (Data Sheet 83035).
- Estimate the natural frequencies of the structure. This can be done using either ESDU data sheets (85037), or the finite element method (e.g. ANSYS). It is clear from this survey of the literature that further experimental work needs to be done in order to validate the theory for singly and doubly curved composite sandwich structures.
- Estimate the damping in the structure. Again, ESDU data sheets can be used (85012), but experimental validation is needed. White suggested that a 'bank'

of measured data for various types of structure is required [4].

- Estimate the RMS strain from a knowledge of the fundamental natural frequency, the excitation pressure spectral density at this frequency, the damping, and the stress at the point of interest due to a uniform static load, using equation 1.1.

In the USA, the Acoustic and Vibration Associates produced the "Sonic Fatigue Design Guide for Military Aircraft" [31]. Over 300 technical reports, papers, journal publications, and text books were reviewed to produce the guide which is a compilation, evaluation, and presentation of existing acoustic fatigue design methods, charts, nomographs, and related computer programs. The acoustic source of primary interest is the noise produced by the engine exhaust, although propeller noise, inlet duct noise for high bypass turbofan engines, noise from ducted rotors, ground reflection and aerodynamic noise were all considered. Many structural configurations were investigated in the study, including flat aluminium honeycomb and diffusion bonded titanium honeycomb panels. Curvature effects were also investigated but not in any great detail.

1.4 Principal failure mechanisms in sandwich structures

It is important to establish the principal failure mechanisms when developing response prediction methods for a structure subject to random acoustic excitation so that the model can be tailored to allow design against acoustic fatigue. For the case of sandwich structures which are subject to random acoustic excitation, the principal failure mechanisms are face plate cracking, core cracking, and face plate disbond. In order to establish which of these failure modes is most prevalent in doubly curved sandwich structures such as aircraft engine intake barrels, a survey was carried out in collaboration with the Nacelle Systems Division of Short Brothers plc [54].

1.4.1 Early failures in aircraft engine nacelles

Early intake barrels were manufactured with aluminium alloy face plates and a Nomex honeycomb core. The inner facing skin [3] was perforated in order to provide noise at-

[3]For intake barrel panels, and for the doubly curved sandwich panels considered in this thesis, the inner face or facing skin will be the concave surface, and the outer face, or backing skin will be the convex surface which incorporates the bevelled or panned down edge.

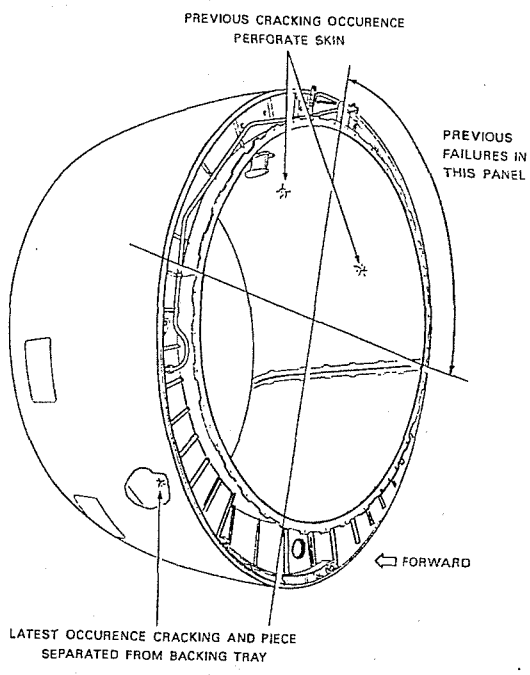

Figure 1.3: Early intake barrel failure locations [54].

tenuation properties and the majority of the early failures were due to face plate cracking, in particular the perforated facing skin [54]. The damage area was confined mostly to the upper left quadrant of the intake barrel (power plant radial (ppr) 0^o to 90^o) and the cracks appeared to grow through the panel thickness. Figure 1.3 shows the damage location on an intake barrel containing four segments. From subsequent flight tests on an instrumented nose cowl, peaks of strain response were observed at the blade passing frequency at 70-80% N1 engine speed (fan speed), which occurred during take-off and thrust reversal on landing. This indicated that the highest strains were associated with the fan blade passing frequency during acceleration as the tips went supersonic. A very narrow band response was observed which was of a much higher frequency (approximately 1200 Hz) than the fundamental frequency of the intake barrel [55]. This could explain why initial theoretical calculations based on the single mode method [8] did not indicate that there could be a potential problem, since this theory is based on the fundamental mode response to broad-band random loading. In addition, a mechanical fatigue approach was initially used to predict the life of the structure, whereas failure monitoring indicated slow growth under low stress conditions which suggested an acoustic fatigue problem. Following the initial failures, fleet inspections revealed that the honeycomb cores were cracking prior to the skin

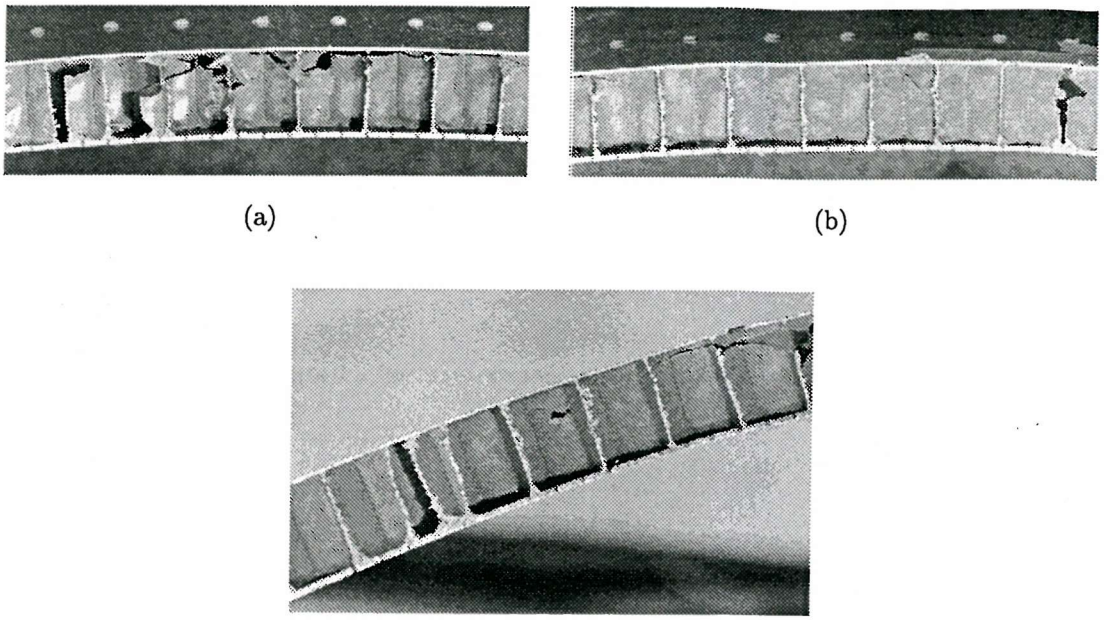

(a) (b)

(c)

Figure 1.4: Early examples of core failures in sandwich panels with aluminium alloy face plates and a Nomex core [54].

failures, which were thought to follow as a result of the breakdown in integrity of the structure. To overcome the problem, the core was replaced with a more robust variety having a higher density and shear strength [55], which resulted in a modest increase in the weight of the intake barrel segment panels. It is important to note at this point that only after the number of fan blades had been reduced did failures begin to occur [55]. Following the reported failures, a testing programme was carried out by the Materials Technology Department of Short Brothers plc in order to ascertain the initial failure mechanism and subsequent propagation through the structure. Defective intake barrel segments were subjected to Non-Destructive Testing (NDT) by Ultrasonic C-Scanning and Acoustic Flaw Detection (AFD) in order to ascertain the extent of the core damage prior to a more detailed examination of the structure. It was found that the Ultrasonic C-Scanning technique was able to map the extent of the damage by highlighting damage areas. The AFD method did detect the major damage area, but it was not possible to detect lesser damaged areas, such as small localised areas where the honeycomb had been compromised close to one of the face-plates. After this initial inspection, the damage areas where further inspected using an intrascope. Significant cracking was found in a number of cells in the damage area

highlighted by the C-Scan. Most of the cracks ran diagonally along one face of the cell and then grew into a horizontal crack along an adjacent face. Also, a number of faces contained cracks near, but above, the bond line with the backing skin [54]. This can clearly be seen in figure 1.4. Two important conclusions were drawn from these studies. First the testing indicated that the Nomex core had initially cracked with a substantial loss of core material in the middle of the section which disintegrated through subsequent erosion of the cell walls, and there was no evidence of disbond between the core and face plates. Secondly, examination of a portion of one of the crack faces using an electron microscope revealed the probability that the crack initiated close to the backing skin and propagated towards the facing skin [54].

One possible explanation for the cause of the core failures is connected with the use of the honeycomb cells as Helmholtz resonators via the perforated liner. It has been suggested that if the cells become distorted during the manufacture of the panels, thus changing the volume inside the cell, then this could cause a slight variation in the resonant frequency of that cell. During excitation at frequencies close to resonance, neighbouring cells could vibrate out of phase, thus causing cyclic pressure loading on adjoining cell walls and subsequent fatigue damage. This is a topic worthy of further investigation.

1.4.2 Recent testing of carbon fibre composite sandwich structures

More recently, carbon fibre composites have been introduced for the construction of the facing and backing skins of the intake barrel panels. The backing skin is formed from several plies of 8 Harness-Satin (8HS) pre-impregnated carbon fibre reinforced plastic (CFRP) while the facing skin consists of a wire mesh bonded to an open weave carbon fibre reinforced sheet. A special technique is employed to bond the facing skin to the honeycomb core to ensure that the perforations in the skin remain clear in order to provide the necessary noise attenuation properties. Since the introduction of these new materials there have been fewer reported skin failures, however, core failures have occurred in these new constructions [54, 55].

A recent test was carried out in the ISVR PWT facility at Southampton on a carbon composite honeycomb sandwich panel [56]. The panel was flat with overall dimensions of 1.42m x 0.83m and with a core thickness of 0.0254m, and was instrumented with 12 strain gauges and 2 accelerometers. Initial tests were carried out with a power spectral density of the applied loading constant over the 100 Hz to 500 Hz

range, giving an Overall Sound Pressure Level (OASPL) of 155 dB. The sound pressure levels and hence the strain response levels were further increased by reducing this bandwidth to 100 Hz. The loading was finally 1/3 octave centred on the predominant response frequency of the panel, which was 228 Hz, and an OASPL of 160 dB was acheived. During the tests the panel suffered major core failure which led to a breakdown of the structure, but there was no damage caused to the face plates since the tests were halted shortly after the panel failed. Following these tests, the panel was examined, and a large disbond was observed in the centre of the structure. However, this disbond did not extend to the panel edge where core cracking was also observed, and the opinion was given that the failure had not initiated in the disbond [56]. After analysis of the panel response using Blevin's Normal Mode method [43], Millar found that it was possible when using very light weight honeycomb cores, to generate core shear stresses of a similar order of magnitude to the allowable ultimate strength of the core material [56].

1.5 The aims of the work

There is a need for more advanced response prediction models for doubly curved composite honeycomb sandwich structures subject to random acoustic excitation. The aims of the work were therefore to use a commercially available finite element package to model this type of structure. A complementary experimental investigation was also carried out to determine the strain response of a set of doubly curved test panels to broadband random acoustic excitation using a PWT facility, and a critical appraisal of the results was made. In addition, the survey of principal failure mechanisms has highlighted the importance of the core in relation to the design of sandwich structures to resist acoustic fatigue. The majority of the work carried out so far has concentrated on measuring and estimating face plate strains in order to produce a fatigue resistant design. However, with the increasing use of lightweight resin impregnated paper cores, the issue of core durability and fatigue resistance should be considered in more detail. The use of carbon fibre reinforced composites for the manufacture of the face plates has lead to a decrease in the number of reported face plate failures. In any case, if the integrity of the core is compromised this can lead to a breakdown in the whole structure thus resulting in face plate cracking. It is for these reasons that the programme of work included a consideration of the core strain response to acoustic excitation. In addition, there is a need for a core strain measurement technique which will allow the estimation of core strain from surface face plate measurements, since the

direct measurement of core strain is difficult considering the the lack of accessibility and the usual size of the cells. This technique was developed and validated using a series of experiments, all of which are reported in a later chapter.

Overall, the approach taken in this thesis was one of carrying out complementary theoretical and experimental work to validate the former so that it may be used by designers. The work begins with details of the design and manufacture of a set of doubly curved test panels in chapter 2, after which a new experimental technique for estimating the core shear strain in closed sandwich structures is developed and validated in chapter 3. Details of the vibration testing of the set of doubly curved test panels is presented in chapter 4, and the results from these tests were used to validate the finite element models developed in chapter 6. The latter work was taken one stage further with the investigation of the effects of various design parameters on the vibration response of doubly curved sandwich panels. The dynamic response of the test panels to random acoustic excitation is investigated in chapter 5 using a Progressive Wave Tube facility. Overall RMS strains were recorded from the inner (facing) and outer (backing) skins in order to make comparisons with the theoretical prediction of the response, which is covered in chapter 7. Finally, in chapter 8, conclusions are drawn from the studies carried out and recommendations are made for further work.

Chapter 2

The design and fabrication of the experimental test panels

2.1 Introduction

The major part of this work involved the experimental investigation of the response of acoustically-excited composite honeycomb sandwich panels with double curvature. To this end, a range of experimental test panels with different radii of curvature were designed and manufactured at the University of Southampton. Three panels were designed with various radii of curvature and with identical ply orientation, thickness, plan area, and bevelled edge design. The sandwich lay-up in each case was symmetric with four carbon fibre reinforced plastic layers on either side of the core. A fourth panel was designed with an asymmetric lay-up having two layers in one face plate and six in the other. The radii of curvature of this panel were identical to that of one of the symmetric panels.

The face plates were made using an epoxy resin pre-impregnated (pre-preg) plain weave carbon fibre cloth. A lightweight, resin impregnated paper honeycomb was used for the core. Each panel was manufactured using an aluminium alloy mould tool with a convex mould surface to the specified radii of curvature. The panels were cured in a conventional temperature controlled oven which meant that a low temperature curing pre-preg was required.

The design and manufacture of the test panels is presented in this chapter. Details are given of material specifications, the design of the panels with particular attention to the bevelled edge, the design and manufacture of the mould tools and the panel fabrication procedure.

2.2 Panel design

The panels were designed with a constant plan area of 0.912 m x 0.525 m to fit the test aperture of the PWT facility. Three radii of curvature designs were employed; $R_x = 3.5m \times R_y = 1.0m$, $R_x = 1.2m \times R_y = 1.0m$, and $R_x = 3.5m \times R_y = 0.5m$, with x being the long side dimension and y being the short side dimension. Three "symmetric sandwich" panels and one "asymmetric sandwich" panel (with $R_x = 3.5m \times R_y = 0.5m$) were manufactured giving a total of four test panels.

The panel design can be broken into four main sections; the facing skin which forms the inner face of the panel, the core, the edge pan plies which enclose the edge of the core and form the attachment flange and bevelled edge, and the backing skin which forms the outer face of the panel. This design is typical of that used in the construction of aircraft type panels such as intake barrel panels and flap fairing panels, and a similar design was used by Soovere [15] during his investigation of flat honeycomb sandwich panels. The sandwich panel drawings, giving the geometry and lay-up details, are shown in figures 2.1, 2.2, and 2.3.

2.2.1 Bevelled edge details

Figure 2.4 shows the arrangement of the panned down edge, or bevelled edge, which is typical of in-service aircraft honeycomb sandwich panels. The honeycomb is chamfered to an angle of 25^o relative to the bottom face on one side along all four edges to form the pan, and edge pan plies are layed up over the honeycomb to totally enclose the core. The use of separate edge pan plies to enclose the core avoids excessive wastage of material when forming the backing skin. Doubler plies are incorporated in the lay-up in order to provide better load transfer in the bevelled edge region, and spacer plies are included in the edge pan to stiffen the attachment flange. In order to provide maximum lap shear and bearing strength, in addition to high panel edge and closeout pan stiffness, 0^o and $\pm 30^o$ fibre orientations (normal to the panel edge) are used for the doublers [15]. The backing skin and facing skin plies have fibre orientations of $\pm 45^o$ and $0/90^o$.

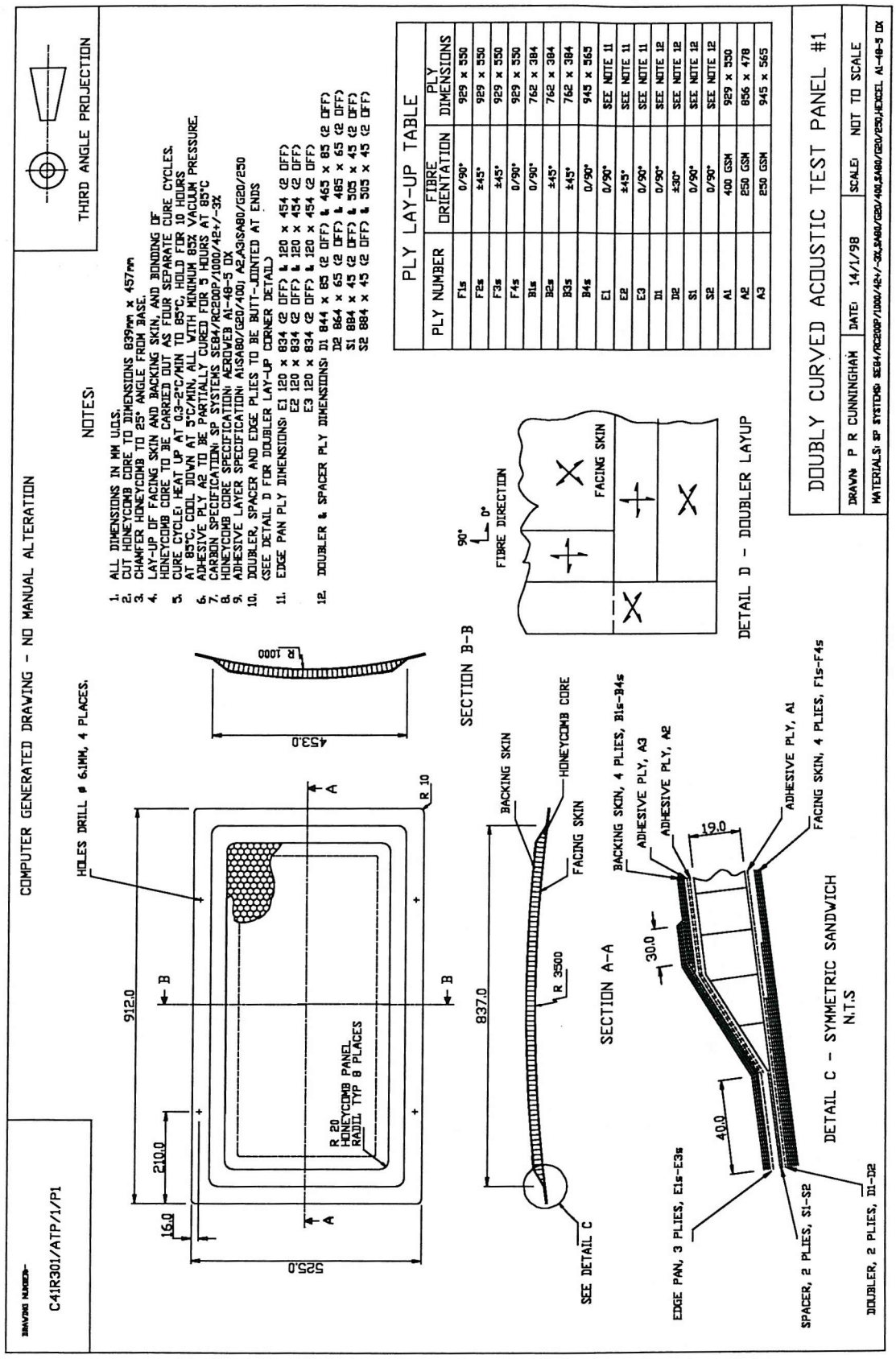

Figure 2.1: Panel 1 drawing.

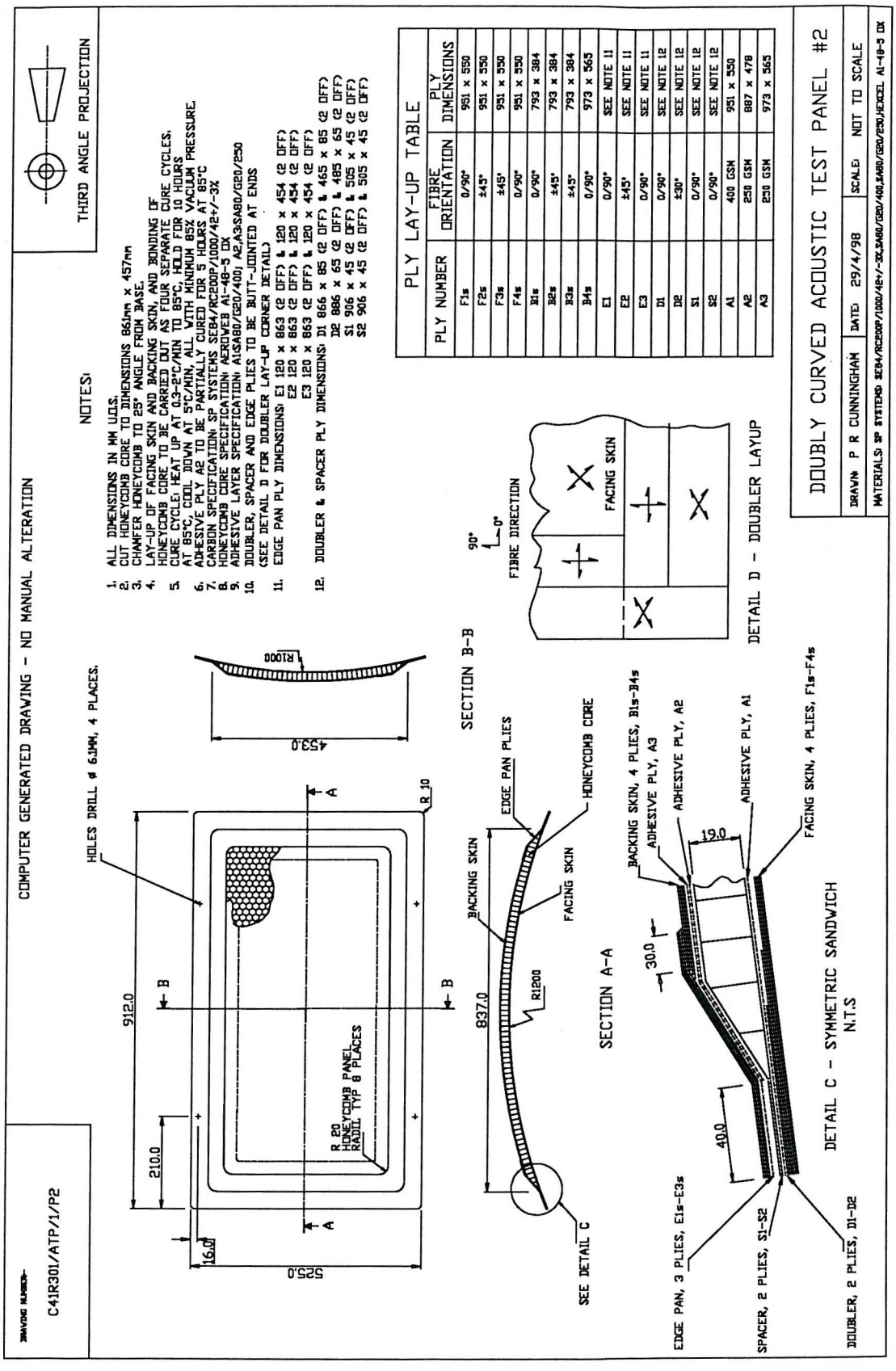

Figure 2.2: Panel 2 drawing.

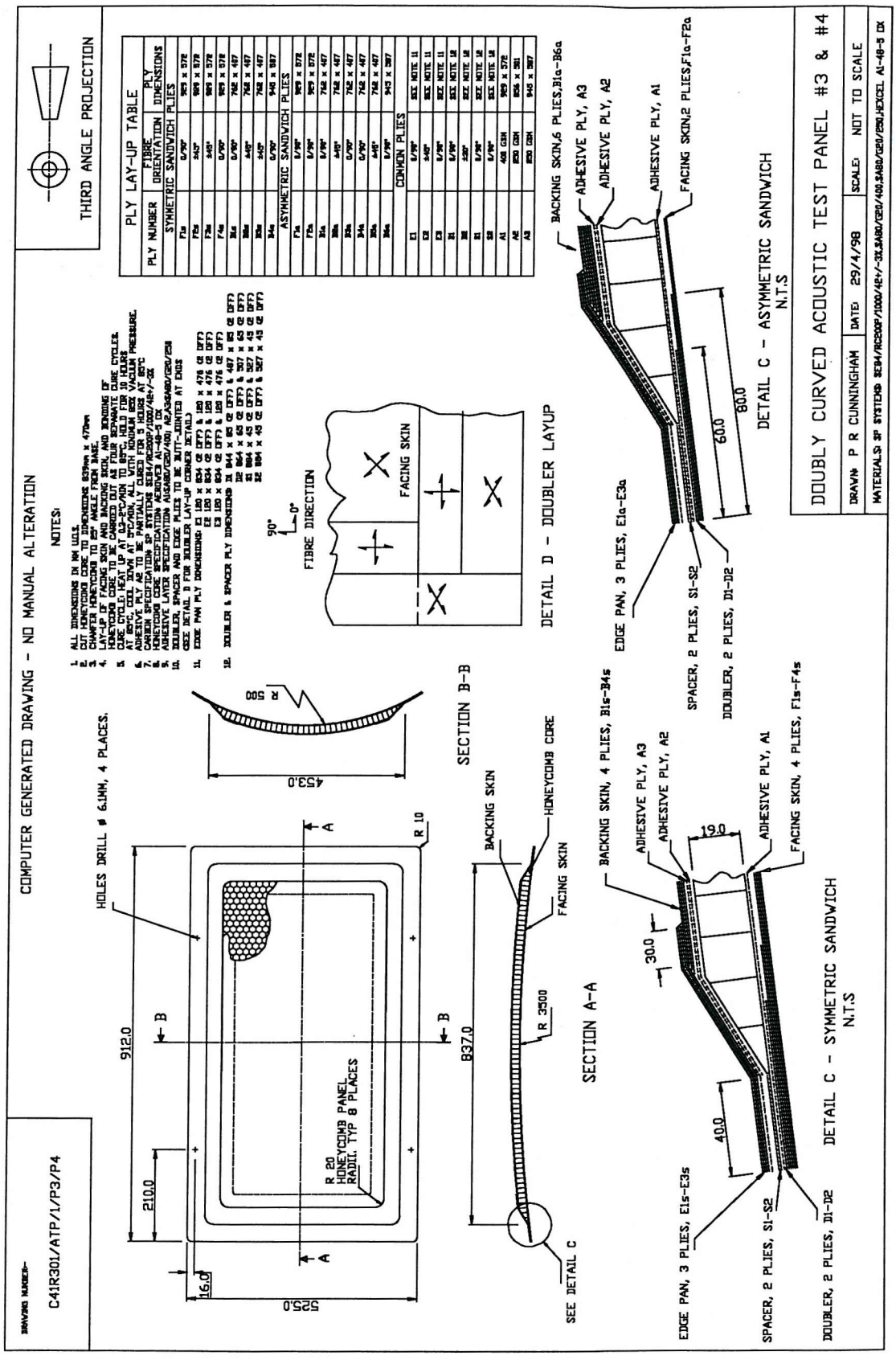

Figure 2.3: Panels 3 and 4 drawing.

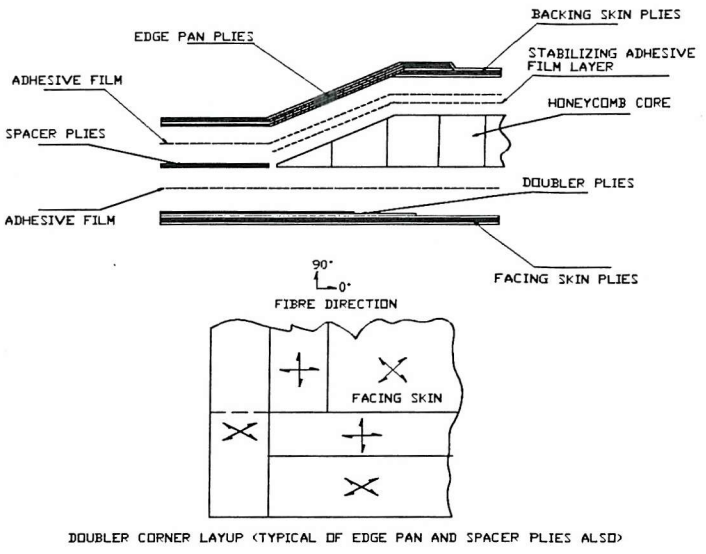

Figure 2.4: Panel lay-up and bevelled edge detail.

2.2.2 Material specifications

Each panel was manufactured using SP Systems SE84/RC200P pre-impregnated plain weave carbon fabric which is a low temperature cure epoxy pre-preg system processable with vacuum-only consolidation. The pre-preg has a fibre/volume fraction of $42\% \pm 3\%$ and comes in sheets of thickness $0.25mm$. It can be cured at temperatures as low as 80^oC, or for fast moulding of components at a temperature of 120^oC. A minimum vacuum pressure of 85% (650mm Hg) is recommended during the cure cycle. Full details of the cure procedure are given in section 2.4. Although SE84 is self-adhesive to Nomex honeycomb, an epoxy adhesive film was used to bond the face plates to the core. SP Systems SA80 was used for this purpose, being a toughened low energy cure epoxy adhesive film with a glass carrier and fully compatible with SE84 pre-pregs. The adhesive film is available in two area densities ($250gm^{-2}$ and $400gm^{-2}$), and in both cases the glass carrier area density is $20gm^{-2}$. Both types of adhesive film were used in the construction of the panels, which is discussed in section 2.4.

Hexcel composites Aeroweb®A1-48-5 OX honeycomb was used for the core, as shown in figure 2.5. The core is made from aramid paper which is coated in phenolic resin to give strength, toughness and chemical resistance. An over-expanded core was used for the doubly curved panels since the ordinary hexagonal core did not conform to the curvature. The over-expanded core, which is usually used for singly curved

geometries, was found to conform to the three doubly curved geometries with the minimum of cell distortion. Ideally, a special type of core called FlexCore®would have been preferred for this application since it conforms to doubly curved geometries without any cell distortion. However this type of core is extremely expensive. The over-expanded core had a thickness of $19mm$ and a cell size of $5mm$, the latter of which was measured across the flats of the hexagonal cell prior to being expanding to a rectangular shape, as shown in figure 2.5. Since the over-expanded core can easily conform to a tight curvature in one direction better than the other, the orientation of the core was changed for the panel with radii of curvature of $R_x = 1.2m \times R_y = 1.0m$. For this panel, the ribbon or 'L' direction was parallel to the short side, or y direction, whereas for the other three panels the ribbon direction was parallel to the long side, or x direction. A full set of material specifications for both the carbon fibre reinforced plastic and the Nomex core are given in table 6.1.

Layer	*Thickness* (m)	*Elastic Modulus* [Pa]		*Shear Modulus* [Pa]				*Density* $[kg/m^3]$	*Poisson's Ratio*
		E_{11}	E_{22}	E_{33}	G_{12}	G_{xz}	G_{yz}		
CFRP†	0.25e-3	57.93e9	57.93e9	-	3.7e9	-	-	1518.0	0.04
Honeycomb	19.0e-3	0	0	120e6	0	35e6	20e6	48.0	-

Table 2.1: Material specifications for the experimental test panels. † Properties obtained using cured test specimens with $[0_4]$ and $[45_4]$ ply lay-up and with 60% fibre volume fraction (see Appendix A for details of CFRP testing procedures).

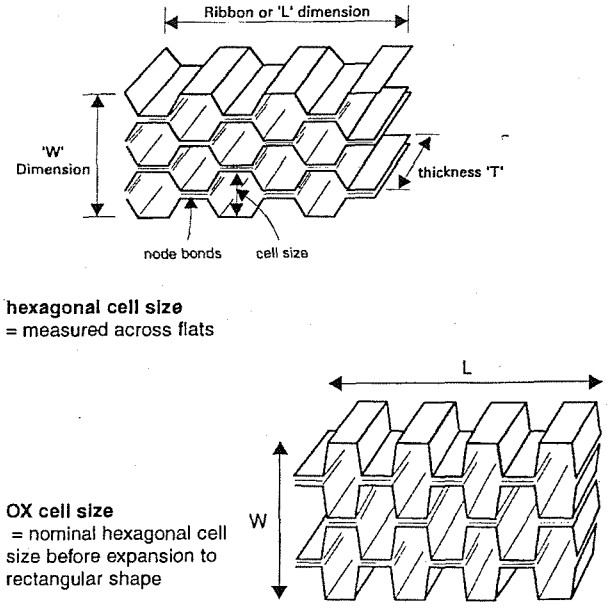

Figure 2.5: Hexagonal and over-expanded core [57] (W=direction of expansion, L=ribbon direction).

2.3 Mould tool design and manufacture

The tooling used to manufacture the panels was comprised of a doubly curved aluminium alloy skin which was stiffened using four aluminium alloy sheet frames riveted to an aluminium alloy base sheet. The convex surface of the aluminium alloy skin formed the mould face.

Each mould surface was rolled and wheeled to the specified radii of curvature using $1.6mm$ (16SWG) aluminium alloy sheet. The unsupported mould skin was then stiffened using four aluminium alloy sheet frames of $1.6mm$ thickness. The skin was attached to the frames and adjusted to the correct radii of curvature using 'L' brackets which were fastened using conventional aluminium pop rivets. The whole assembly was attached to an aluminium alloy base sheet, again using aluminium pop rivets. It is important to note that this method of fabricating the mould tools, although simple and inexpensive, cannot offer the best performance in terms of accuracy in geometry (radii of curvature) and compatibility of thermal expansion rates of the tool and part during cure. However, since the radii of curvature of the panels could be easily measured after fabrication, this was not considered a problem and was seen as the easiest solution to a rather complicated tooling requirement.

A complete set of drawings for the mould tool is shown in figure 2.6.

2.4 Panel fabrication procedure

There are two choices regarding the manufacture of honeycomb sandwich panels; co-cure or pre-cure. The co-cure process is much more simple and less time consuming than the pre-cure process. The facing skin, honeycomb core, and backing skin are consecutively consolidated under vacuum and the complete assembly is then cured in one stage, again under vacuum. The main drawback with this procedure is that the bond quality of the core to the skins, and the consolidation of the facing skin will not be as good as that which would be achieved using the pre-cure process. Pre-curing is the more involved of the two manufacturing procedures since each stage, facing skin, core, and backing skin manufacture, is carried out as an individual cure cycle. However, it has been shown to produce better results in terms of panel strength and bond quality [52]. It was for this reason that the pre-cure process was chosen as the manufacturing procedure for the doubly curved sandwich panels.

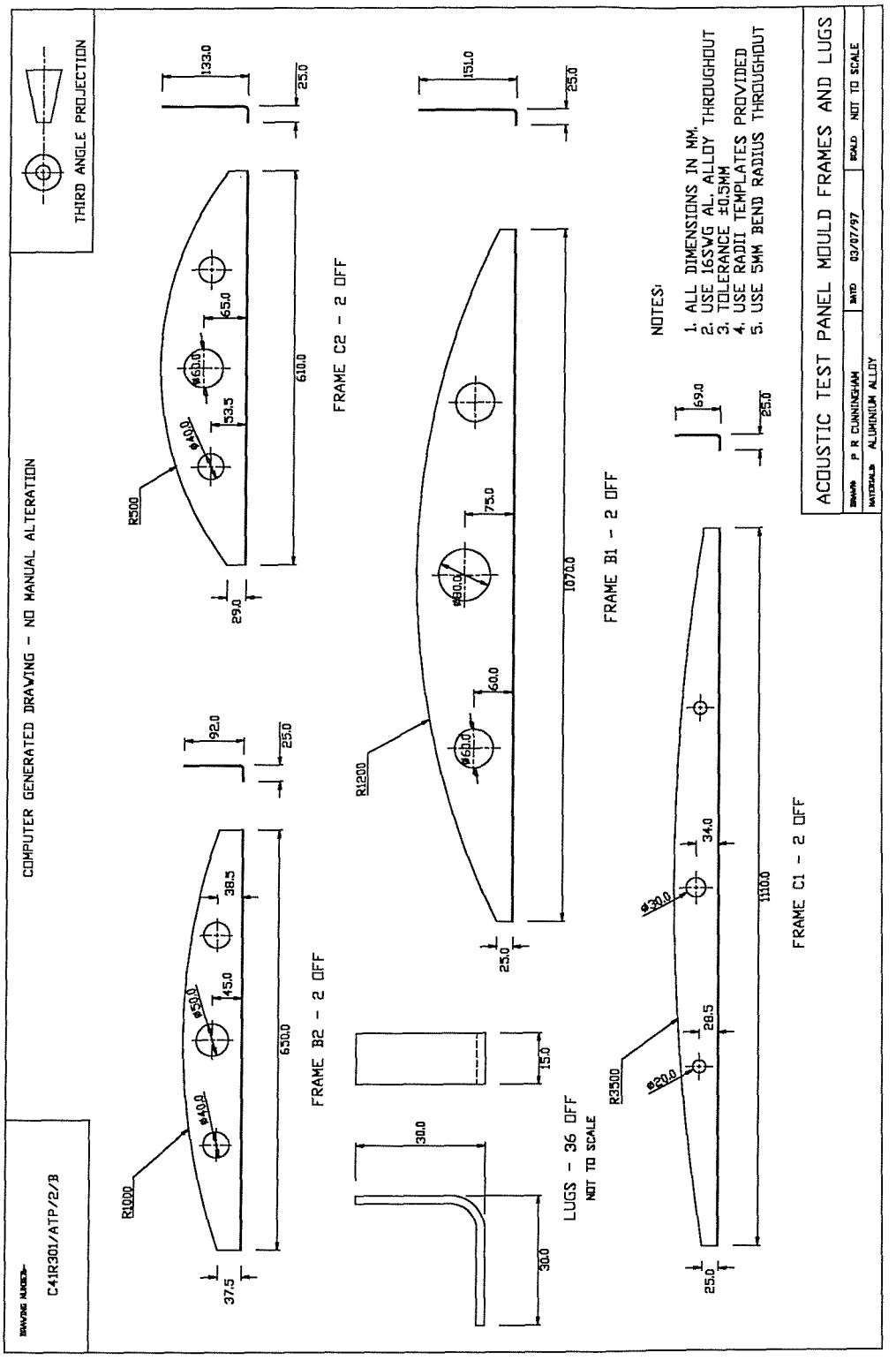

Figure 2.6: Drawing of mould tool frames and lugs.

2.4.1 Cure cycle

The cure cycle for the SE84 and SA80 epoxy systems is shown in figure 2.7. The recommended minimum cure cycle is at 85^oC for 10 hours. The most important aspect of the cure cycle is to ensure the part heats up at the correct rate and reaches the "Gel temperature", at which point the resin will begin to cure. During the heating phase the resin is able to flow so it is important to ensure that the rate is not too low, which would result in an excessive amount of resin being bled from the part giving a 'dry' component. It is therefore important to check that the oven is able to heat the part at the specified rate, which in this case was $0.3 - 2^oC/min$.

The oven heating rate was controlled by the set-point temperature. After repeated tests, it was found that the optimum oven performance was achieved by using an initial set-point temperature of 100^oC and then following the 100^oC cure cycle. Once the component had reached 100^oC, the set-point temperature was reduced to 80^oC to prevent excessive over-shoot. It was found that the oven maintained a relatively steady temperature of around $100^oC - 105^oC$ during the cure period which was 4 hours in this case. The cooling rate was achieved by simply switching the oven off and opening the door.

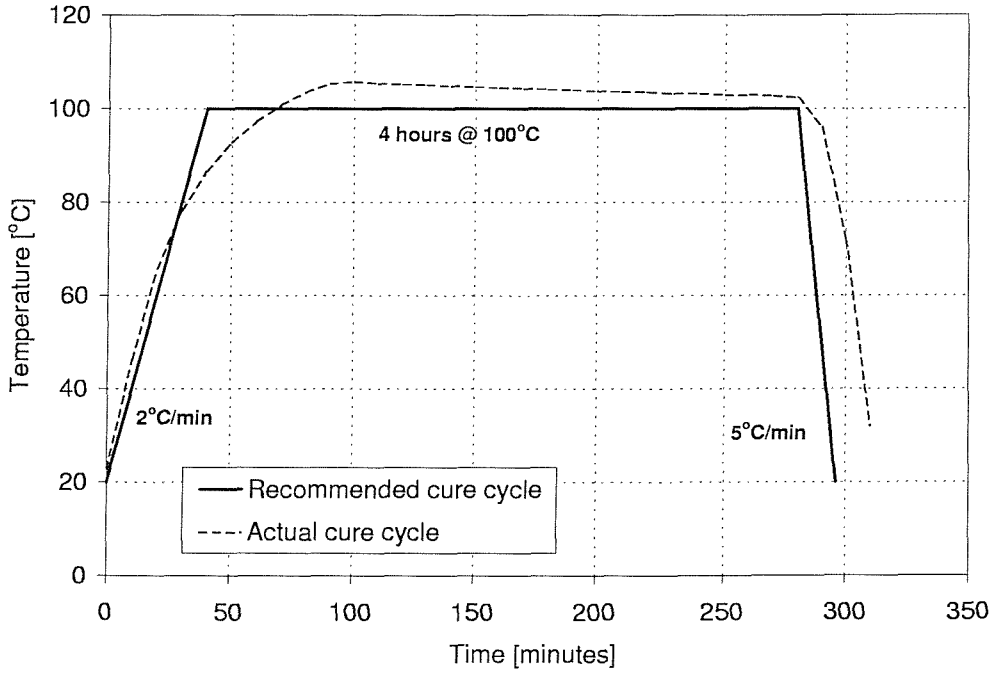

Figure 2.7: Recommended and actual cure cycle.

2.4.2 Lay-up procedure

Before manufacturing a panel, the mould tool was prepared to prevent the resin bonding to the surface of the mould. Frekote ®B15 sealant and 700C release agent were used for this purpose.

The lay-up procedure for each panel, which is shown in figure 2.8, was as follows:

Stage 1

The facing skin plies were laid in the centre of the clean and treated mould tool surface. A type 'K' thermocouple was inserted at the edge of the skins between the top and underlying layer and the facing skin plies were consolidated under vacuum pressure for half an hour. The doubler plies were applied, being butt-jointed as shown in the drawing and the whole assembly was consolidated under vacuum for one hour. After consolidation, which was carried out in-situ in the oven, the heat was turned on and the panel cured for four hours at 100^oC with a minimum vacuum of 85% (650 mm Hg).

Stage 2

The next stage involved bonding the honeycomb core to the cured facing skin. A $400gm^{-2}$ SE80 adhesive film layer was first laid up on the cured facing skin. The spacer plies were then laid to locate the core in the correct position. Butt joints were again used in the spacer plies. Heat was applied to soften the adhesive and 'tack' the core in place. The thermocouple was attached and the whole assembly was consolidated under vacuum for one hour before being cured at 100^oC for four hours with a minium vacuum of 85% (650 mm Hg).

Stage 3

The third stage was the quickest of the four stages, and involved the partial cure of an adhesive layer onto the core area. A $250gm^{-2}$ SE80 adhesive layer was cured for two hours at 100^oC with a maximum of 25-30% vacuum which prevents resin bleed and telegraphing occuring. The reason for this stage was to ensure a good bond between the backing skin and the core since the bond quality, in terms of distribution around the cells, can be checked prior to the final stage.

Stage 4

The backing skin was applied in this final stage to complete the sandwich panel construction. A $250gm^{-2}$ adhesive layer was first applied, which covered the entire area of the panel. The first three backing skin plies were then applied to the top area of the core, with the corner radii being trimmed in-situ. The three edge-pan plies were then applied. It was important to ensure that the plies were well bedded into the area where the honeycomb core ends and the flange begins. A small piece of perspex with a ball-nosed tip was used for this purpose. The edge pan plies were made from four separate strips (per layer) and were butt-jointed in the same manner as the doubler and spacer plies. The final layer was the fourth backing skin ply which covered the entire panel. Once all of the plies were laid-up, the thermocouple was attached and the whole assembly was consolidated under vacuum for one hour before curing at 100^oC for four hours with a minimum vacuum of 85%.

2.4.3 Non-Destructive Testing of panels

Following the manufacture of the test panels, the quality in terms of bond integrity and consolidation, was assessed using ultrasonic non-destructive testing. This was carried out by hand using an A-Scan machine. All of the panels were found to be satisfactory with a good bond and consolidation although a certain amount of porosity was found, particularly in the backing skin or outer faceplate. This is common with sandwich panels manufactured in this way where the backing skin is not formed within a mould, even when the panels are cured in an autoclave. To reduce the amount of porosity, the panels can be resin washed on the porous surface, however this was deemed unnecessary in this instance.

It is worth noting that a very simple and effective check of the quality of a finished panel can be carried out by tapping the entire outer surface with a two-pence piece whilst holding the panel by one corner. A clean, crisp "ring" is indicative of a good bond quality and consolidation, whereas a dull "thud" highlights areas where there may be disbonding or voids. This method follows the same principle as that used to check the quality of metal castings, and an automated version of this method has been proposed by Cawley and Adams [58] for the non-destructive testing of honeycomb structures.

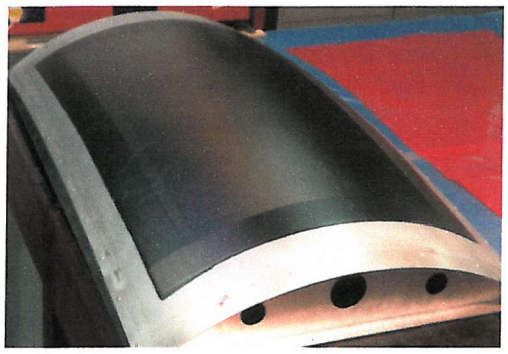

(a) Stage 1 - facing skin and doubler plies.

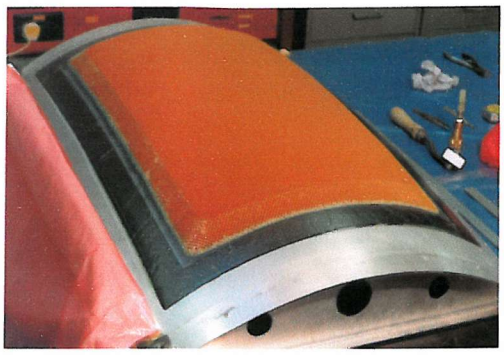

(b) Stage 2 - first adhesive film layer, core and spacer plies.

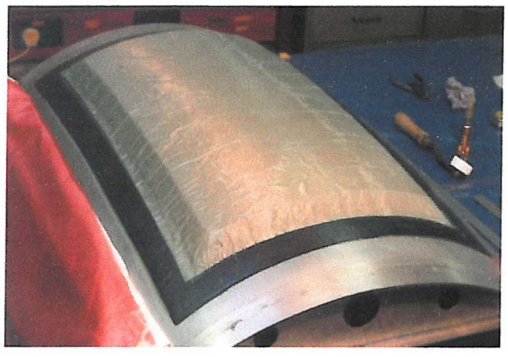

(c) Stage 3 - second adhesive film layer (partial cure).

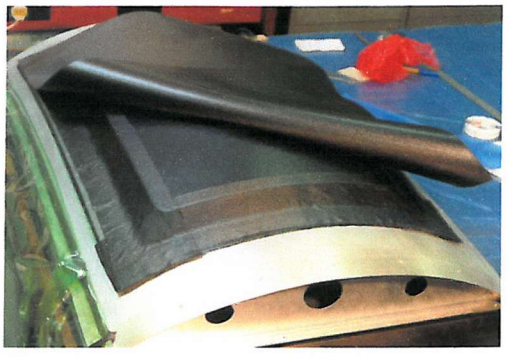

(d) Stage 4 - third adhesive film layer, backing skin and edge pan plies.

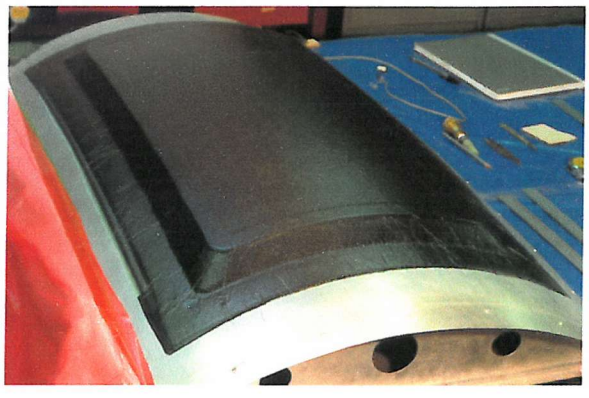

(e) Finished panel (prior to being trimmed to size).

Figure 2.8: Doubly curved CFRP/honeycomb sandwich panel manufacturing process.

2.5 Concluding summary

In this chapter, details of the design and manufacture of the test specimens have been given. The approach used represented the most efficient and economical use of the resources available with excellent results being obtained. A detailed description of the manufacture of a set of four doubly curved composite sandwich structures has been given, together with details of the mould tools used to form the geometry of the panels. The completed panels were scanned using an A-Scan machine, and they all were found to have satisfactory consolidation and bond quality.

Chapter 3

Development of a method for estimating the core shear strain in closed sandwich structures

3.1 Introduction

In order to establish whether a certain core is durable enough for a particular sandwich panel application, it would be useful if the engineer could directly measure the shear strain in the core in addition to the bending strain in the face plates, so that a more complete picture of the strain response of the structure can be established in relation to fatigue life assessment. In the majority of sandwich structures however, where the core is totally enclosed by the face plates and panned down edges (as is the case with the panels being used in this investigation), this task is not possible due to the lack of accessibility and size of the cells.

This chapter presents a new measurement technique whereby the shear strain in the core is estimated from surface face plate measurements using a linear finite difference approximation. The estimation method is presented and is supported by calculations on simple beam structures with various boundary conditions and loads. In order to validate the method, an experiment was designed using a simple honeycomb sandwich beam which was instrumented with strain gauges on the core and the face plates. Static and dynamic tests have been conducted and the results compared with those obtained from a Finite Element model of the structure. The results indicate that the method works well for sandwich structures with thin face plates, and the dynamic tests have shown that the method gave better results for the fundamental

bending mode compared to the other modes where an over-estimate of the core shear strain was observed.

3.2 Estimation procedure

The underlying assumptions of the theory presented in this section are as follows;

- The faceplates are very thin compared with the total thickness of the sandwich.
- The shear stress over the depth of the core is considered constant. Allen [59] highlighted that this assumption may be made if the core is too weak to provide a significant contribution to the flexural rigidity of the sandwich.
- The core is antiplane (i.e. $\sigma_x = \sigma_y = \tau_{xy} = 0$ [60]).
- The rotary inertia of the face plates about their own centroidal axes is negligable.
- The sandwich has equal thickness face plates (symmetric sandwich) and both face plates are of the same material with identical properties.

The total flexural rigidity of the sandwich beam element shown in figure 3.1 (a), is equal to the sum of the flexural rigidities of the faces and the core;

$$D = \frac{E_f b f^3}{6} + \frac{E_f b f (c+f)^2}{2} + \frac{E_c b c^3}{12} \tag{3.1}$$

By applying the assumptions made above, the expression for the flexural rigidity can be reduced. The first term represents the flexural rigidity of the faces bending separately about their own centroidal axes whilst the second term represents the bending stiffness of the faces bending about the neutral axis of the complete sandwich element. The third term represents the bending stiffness of the core on its own. If the sandwich element has a core which is much thicker than the face plates, then the error introduced by neglecting the first term is negligable provided that [59]

$$\frac{(c+f)}{f} > 5.77 \tag{3.2}$$

which assumes that the first term amounts to less than 1% of the second term in equation 3.1. The third term represents less than 1% of the second when [59]

$$6\frac{E_f}{E_c}\frac{f}{c}\left(\frac{(c+f)}{c}\right)^2 > 100 \tag{3.3}$$

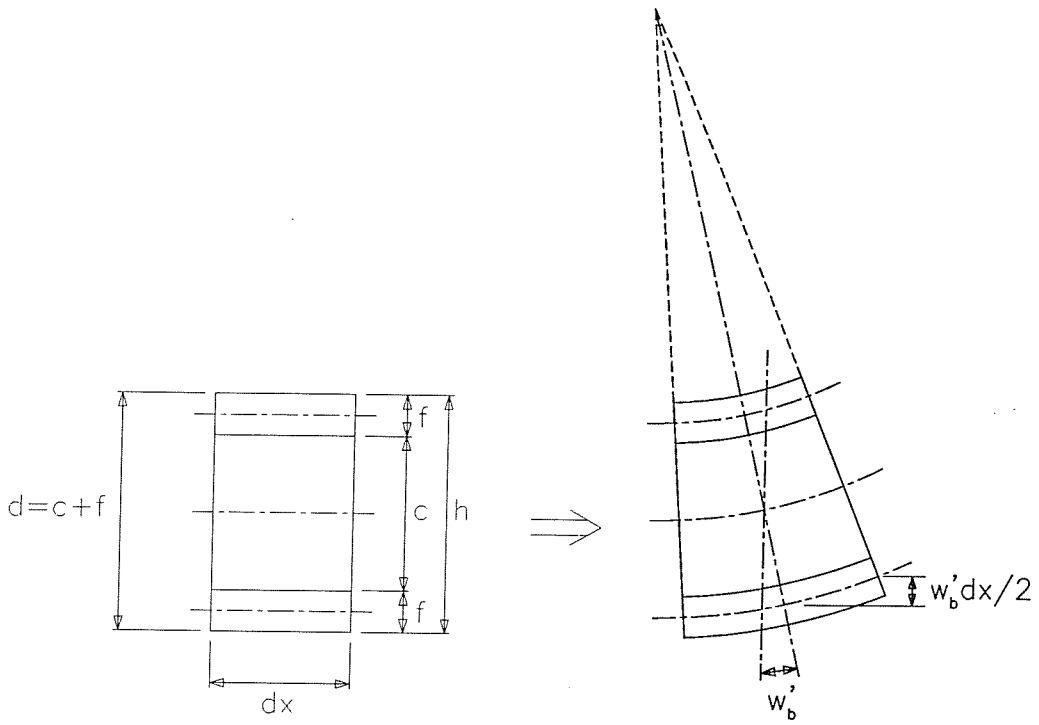

(a) Undeformed element.

(b) Bending partial deflection.

(c) Total deflection = bending + shear deflections.

Figure 3.1: Sandwich element deformation.

The sandwich structures being considered in this study have very thin faces compared with the core (assumption #1). Therefore, $(c+f)/c \approx 1$ and $(f/c) = 0.05$, and so the limiting value of the ratio between the Young's modulii of the face plates and the core is between 835 and 167 (317 in this case) which means that the third term can be neglected [59].

Following these assumptions, the expression for the flexural rigidity of the sandwich reduces to

$$D = \frac{E_f b f (c+f)^2}{2} \tag{3.4}$$

In order to outline the estimation method, it is necessary to discuss the fundamental bending theory of sandwich structures [59, 61]. Consider the sandwich element shown in figure 3.1(a). When the element deforms due to an applied load, the total deflection is comprised of two partial deflections, namely the bending or primary deflection and the shear or secondary deflection [59]. The bending deflection, w_b, is a result of the sandwich element bending about the neutral axis of the complete element as shown in figure 3.1(b). Since the core has a low transverse modulus of rigidity it undergoes a shear strain. This causes the face plates to bend about their own centroidal axes which results in the secondary deflection w_s. The total deflection of the sandwich is shown in figure 3.1(c), and is defined as

$$w = w_b + w_s \tag{3.5}$$

A relationship can be found between the shear strain in the core, γ_c and the secondary partial rotation, $w_s\prime$ using the geometry of deformation [59], which is illustrated in figure 3.2.

$$\gamma_c = \frac{(c+f)}{c}\frac{dw_s}{dx} \tag{3.6}$$

Now consider the sandwich element under load, with the normal forces and moments in the face plates and the shear force in the core as shown in figure 3.3 [61]. When the sandwich element deflects, the direct strains in the face plates are caused by both the bending and shear deflections;

$$\epsilon_x = -z\frac{d^2w_b}{dx^2} - z_f\frac{d^2w_s}{dx^2} \tag{3.7}$$

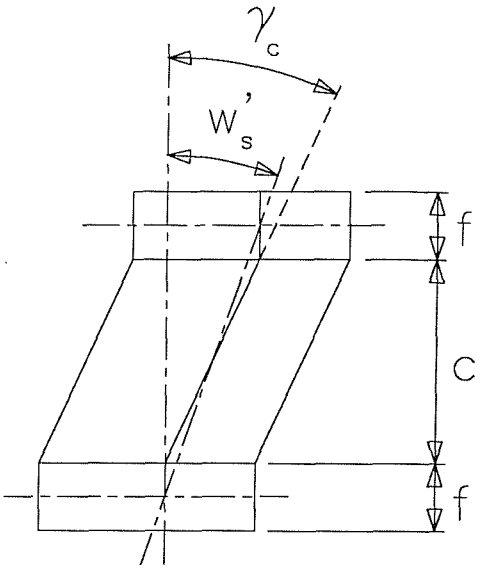

Figure 3.2: Secondary (shear) partial deflection.

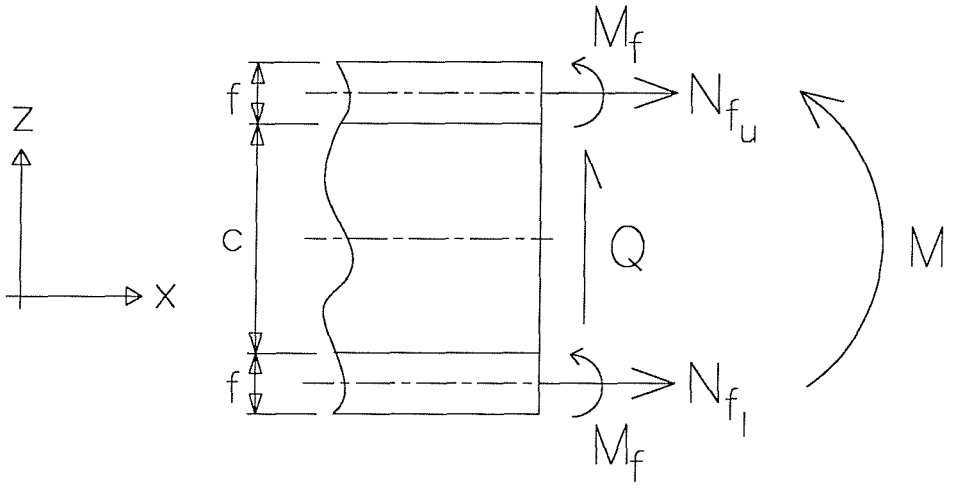

Figure 3.3: Moments and forces on the sandwich element.

where,

$$\frac{c}{2} \leq z \leq \left(\frac{c}{2} + f\right) \tag{3.8}$$

and, for the upper face plate.

$$z_f = z - \frac{1}{2}(c + f) \tag{3.9}$$

The normal force in each face plate is found by integrating the stress across the cross sectional area of each faceplate;

$$N_{f_u} = -E_f \int_0^b \int_{\frac{c}{2}}^{\left(\frac{c}{2}+f\right)} \left(z\frac{d^2w_b}{dx^2} + z_f\frac{d^2w_s}{dx^2} \right) dydz \tag{3.10}$$

where, b is the breadth of the beam and $b < (c+2f)$. Hence,

$$-N_{f_u} = E_f \frac{bf(c+f)}{2}\frac{d^2w_b}{dx^2} = N_{f_l} \tag{3.11}$$

The subscript u denotes the upper face plate, and l denotes the lower faceplate. Equation 3.11 implies that there are bending moments but no resultant normal forces produced in the face plates as a result of the secondary (shear) partial deflection [61]. The bending moment in each face is

$$M_f = E_f \frac{bf^3}{12}\left(\frac{d^2w_b}{dx^2} + \frac{d^2w_s}{dx^2}\right) = E_f \frac{bf^3}{12}\frac{d^2w}{dx^2} \tag{3.12}$$

From figure 3.3, the total bending moment in the sandwich element is

$$M = 2M_f - N_{f_u}\left(\frac{c+f}{2}\right) + N_{f_l}\left(\frac{c+f}{2}\right) \tag{3.13}$$

$$M = E_f \frac{bf^3}{6}\frac{d^2w}{dx^2} + E_f \frac{bf(c+f)^2}{2}\frac{d^2w_b}{dx^2} \tag{3.14}$$

and the total shear force is

$$Q = E_f \frac{bf^3}{6}\frac{d^3w}{dx^3} + E_f \frac{bf(c+f)^2}{2}\frac{d^3w_b}{dx^3} \tag{3.15}$$

Consider now the element of the upper face plate as shown in figure 3.4 [61]. For equilibrium in the x-direction

$$-N_{f_u} - b\tau_c dx + N_{f_u} + \frac{dN_{f_u}}{dx}dx = 0 \tag{3.16}$$

$$\tau_c = \frac{dN_{f_u}}{dx}\frac{1}{b} \tag{3.17}$$

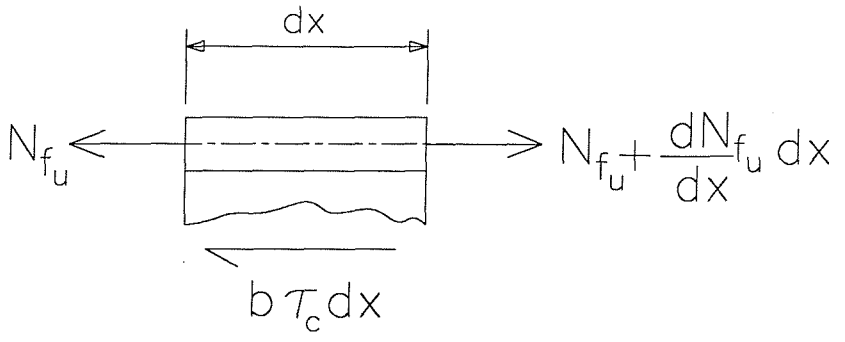

Figure 3.4: Force equilibrium of the upper face plate.

Now,

$$\frac{dN_{f_u}}{dx} = -E_f \frac{bf(c+f)}{2} \frac{d^3 w_b}{dx^3} \tag{3.18}$$

Therefore,

$$\tau_c = -E_f \frac{f(c+f)}{2} \frac{d^3 w_b}{dx^3} \tag{3.19}$$

and since

$$\gamma_c = \frac{\tau_c}{G_c} \tag{3.20}$$

then

$$\gamma_c = -\frac{E_f}{G_c} \frac{f(c+f)}{2} \frac{d^3 w_b}{dx^3} \tag{3.21}$$

From equations 3.7, 3.8, and 3.9, the total direct strain at the top surface of the upper face plate is

$$\epsilon_u = -\left(\frac{c}{2} + f\right) \frac{d^2 w_b}{dx^2} - \frac{f}{2} \frac{d^2 w_s}{dx^2} \tag{3.22}$$

Since the face plates are assumed to be very thin compared to the total thickness of the sandwich structure, the contribution from the secondary partial deflection (second term in equation 3.22) to the direct strain in the top surface of the upper faceplate will be negligable, therefore

$$\epsilon_u \approx -\left(\frac{c}{2} + f\right) \frac{d^2 w_b}{dx^2} \tag{3.23}$$

Now,

$$\frac{d\epsilon_u}{dx} = -\left(\frac{c}{2}+f\right)\frac{d^3w_b}{dx^3} \tag{3.24}$$

and substituting equation 3.24 into equation 3.21 gives

$$\gamma_c \approx \frac{E_f}{G_c}\frac{f(c+f)}{2}\left(\frac{c}{2}+f\right)^{-1}\frac{d\epsilon_u}{dx} \tag{3.25}$$

An expression has now been obtained relating the core shear strain to the rate of change of strain in the top surface of the upper face plate. In order to measure the rate of change of surface strain, a finite difference approximation technique can be applied,

$$\delta V(x) \approx \frac{V(x+\Delta x/2) - V(x-\Delta x/2)}{\Delta x} \tag{3.26}$$

Therefore the rate of change of direct strain can be approximated by

$$\frac{d\epsilon_u}{dx} \approx \frac{\left(\epsilon_{u_{(x+\Delta x/2)}} - \epsilon_{u_{(x-\Delta x/2)}}\right)}{\Delta x} \tag{3.27}$$

In this way, an estimate of the shear strain in the core can be obtained by measuring the direct strain from two strain gauges mounted Δx apart on the surface of one of the face plates and using the formula

$$\gamma_{est} \approx \frac{E_f}{G_c}\frac{f(c+f)}{2}\left(\frac{c}{2}+f\right)^{-1}\frac{\left(\epsilon_{u_{(x+\Delta x/2)}} - \epsilon_{u_{(x-\Delta x/2)}}\right)}{\Delta x} \tag{3.28}$$

3.2.1 Supporting calculations on simple beam structures

The method was initially verified using theoretical models of statically loaded beam structures. Equations are derived for the two partial deflections as a function of length along the beam for the structure under consideration, therefore allowing the direct strain in the face plates and the shear strain in the core at any position x to be readily estimated.

From equation 3.15, the total shear force in a sandwich beam is expressed as the sum of the shear stress produced by the bending deflection and that produced by the shear deflection,

$$Q = Q_b + Q_s = (D+D_f)\frac{d^3w_b}{dx^3} + D_f\frac{d^3w_s}{dx^3} \tag{3.29}$$

where,

$$D = \frac{E_f b f (c+f)^2}{2} \tag{3.30}$$

and,

$$D_f = E_f \frac{b f^3}{6} \tag{3.31}$$

Substituting equation 3.6 into equation 3.21, an expression relating the shear deflection to the bending deflection can be found [61, 59];

$$\frac{dw_s}{dx} = -\frac{D}{D_Q}\frac{d^3 w_b}{dx^3} \tag{3.32}$$

where,

$$D_Q = \frac{G_c b (c+f)^2}{c} \tag{3.33}$$

is the shear stiffness of the sandwich beam. Therefore,

$$\frac{d^2 w_s}{dx^2} = -\frac{D}{D_Q}\frac{d^4 w_b}{dx^4} \tag{3.34}$$

and,

$$Q_b = (D + D_f)\frac{d^3 w_b}{dx^3} \tag{3.35}$$

$$\Rightarrow \frac{d^4 w_b}{dx^4} = \left[\frac{1}{(D+D_f)}\right]\frac{dQ_b}{dx} \tag{3.36}$$

Hence,

$$Q = Q_b - \left[\frac{DD_f}{(D+D_f)D_Q}\right]\frac{d^2 Q_b}{dx^2} \tag{3.37}$$

Substituting

$$m^2 = \left[\frac{(D+D_f)D_Q}{DD_f}\right] \tag{3.38}$$

into equation 3.37, a differential equation relating the total shear force to the shear

force produced by the bending deflection only is obtained;

$$-m^2Q = \frac{d^2Q_b}{dx^2} - m^2Q_b \tag{3.39}$$

Consider the cantilevered sandwich beam shown in figure 3.5 with a point load P at the free end. The total shear force in the beam is P, so from equation 3.39;

$$-m^2P = \frac{d^2Q_b}{dx^2} - m^2Q_b \tag{3.40}$$

The general solution to which is

$$Q_b = C_1e^{mx} + C_2e^{-mx} + P \tag{3.41}$$

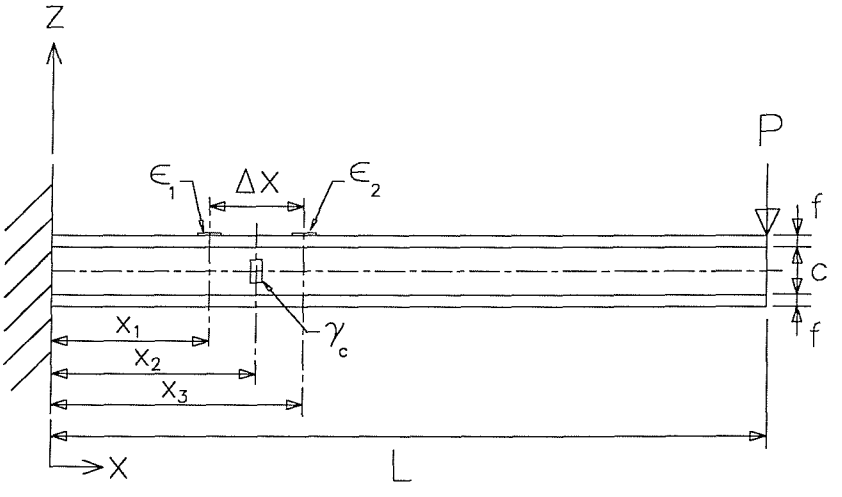

Figure 3.5: Cantilevered sandwich beam (theoretical case study).

Substituting equation 3.35 into equation 3.41, integrating three times and re-arranging results in an expression for the bending partial deflection:-

$$(D + D_f)w_b = \frac{C_1}{m^3}e^{mx} - \frac{C_2}{m^3}e^{-mx} + \frac{Px^3}{6} + \frac{C_3x^2}{2} + C_4x + C_5 \tag{3.42}$$

and integrating equation 3.34 twice and substituting into the second derivative of equation 3.42 results in an expression for the shear partial deflection:-

$$-D_fw_s = \frac{C_1}{m^3}e^{mx} - \frac{C_2}{m^3}e^{-mx} + \frac{Px}{m^2} + C_6 \tag{3.43}$$

where $C_1 ... C_6$ are arbitrary constants which are found by applying the following boundary conditions;

at $x = 0$; $w_b = 0$, $w_s = 0$, $w_b' = 0$, $w_s' = 0$, $M = -PL$

$$C_5 = C_6 = -\frac{1}{m^3}(C_1 - C_2) \tag{3.44}$$

$$C_4 = \frac{P}{m^2} \tag{3.45}$$

$$C_3 = -PL \tag{3.46}$$

at $x = L$; $M_s = M_b = 0$

$$C_2 = -P\left[\frac{e^{mL}}{e^{mL} + e^{-mL}}\right] \tag{3.47}$$

$$C_1 = -P\left[1 - \frac{e^{mL}}{e^{mL} + e^{-mL}}\right] \tag{3.48}$$

Therefore,

$$C_5 = C_6 = -\frac{P}{m^3} \tag{3.49}$$

Now,

$$\frac{e^{mL}}{e^{mL} + e^{-mL}} = \frac{e^{mL}}{e^{mL}(1 + e^{-2mL})} = \frac{1}{(1 + e^{-2mL})} \tag{3.50}$$

and,

$$(1 + e^{-2mL})^{-1} = 1 - e^{-2mL} + e^{-4mL} - .... \tag{3.51}$$

Therefore,

$$\frac{e^{mL}}{e^{mL} + e^{-mL}} \approx 1 - e^{-2mL} \approx 1 \tag{3.52}$$

to a first order approximation, and

$$1 - \frac{e^{mL}}{e^{mL} + e^{-mL}} = 1 - (1 - e^{-2mL}) \approx e^{-2mL} \tag{3.53}$$

again, to a first order approximation. So the constants C_1 and C_2 become

$$C_1 = -Pe^{-2mL} \tag{3.54}$$

$$C_2 = -P \tag{3.55}$$

Upon substituting the constants into equations 3.42 and 3.43 the final equations for the bending and shear deflections of a cantilevered sandwich beam with a point load are;

$$w_b = \frac{P}{(D + D_f)m^3}\left[e^{-mx} - e^{m(x-2L)} + \frac{x^3m^3}{6} - \frac{Lx^2m^3}{2} + xm - 1\right] \tag{3.56}$$

$$w_s = -\frac{P}{D_f m^3}\left[e^{-mx} - e^{m(x-2L)} + xm - 1\right] \tag{3.57}$$

The sandwich beam shown in figure 3.5 was modelled using equations 3.56 and 3.57 for loads from 10N to 100N. The direct strains in the top surface of the upper faceplate, ϵ_1 and ϵ_2, and the core shear strain, γ_c, were recovered. The beam was also modelled using the ANSYS finite element package. The solid model, shown in figure 3.6, was built using Solid73 elements for the core and Shell63 elements for the face plates. All of the nodes at the root of the beam were fully constrained in all degrees of freedom, as shown in the figure. The results from both the analytical and finite element models are given in table 3.2.1 together with the material properties used in both models. The results for the face plate strains were used to estimate the core shear strain, γ_{est}, using equation 3.28. Two different measurement positions on the beam with two different values for Δx were considered. At a point close to the root, both the finite element and the exact analytical results show that the core shear strain cannot be reliably estimated unless the distance between the two face plate strain gauges, Δx, is small. The reason for this is the high rate of change of strain at the root of the beam. In order to improve the estimate, Δx must be reduced, and the estimate is shown to improve considerably with a reduction in Δ_x from $0.04m$ to $0.01m$. In addition, Poisson's ratio effects cannot be neglected at the root, which will effect both the direct

face plate and core shear strain values in this region. Further away from the root, at $x_2 = 0.15m$, the estimate is shown to be in excellent agreement with the actual value for the core shear strain for both values of Δx.

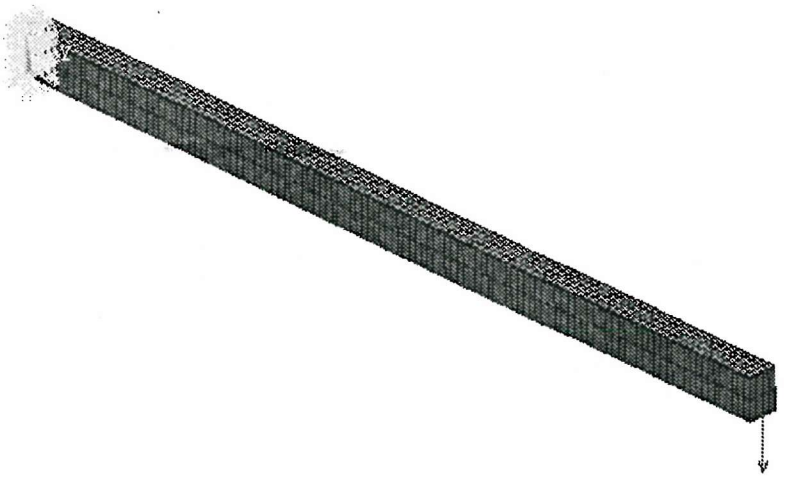

Figure 3.6: Finite Element model of a cantilevered sandwich beam (theoretical case study).

For the case of a beam subject to a three point bending load where the load is applied mid-way between the supports, the equations for the fully clamped cantilever case can be used by assuming symmetry about $L/2$ with the load equal to $P/2$.

P	w	$x_2 = 0.025m$							$x_2 = 0.15m$						
		$\Delta x = 0.04$m			$\Delta x = 0.01$m				$\Delta x = 0.04$m			$\Delta x = 0.01$m			
(N)	(mm)	ϵ_1 ($\mu\epsilon$)	ϵ_2 ($\mu\epsilon$)	γ_{est} ($\mu\epsilon$)	ϵ_1 ($\mu\epsilon$)	ϵ_2 ($\mu\epsilon$)	γ_{est} ($\mu\epsilon$)	γ_c ($\mu\epsilon$)	ϵ_1 ($\mu\epsilon$)	ϵ_2 ($\mu\epsilon$)	γ_{est} ($\mu\epsilon$)	ϵ_1 ($\mu\epsilon$)	ϵ_2 ($\mu\epsilon$)	γ_{est} ($\mu\epsilon$)	γ_c ($\mu\epsilon$)
Finite Element Model Results															
10	-1.59	171.9	144.4	**-1348.2**	151.4	148.2	**-627.5**	**-515.2**	122.3	111.9	**-509.8**	118.4	115.8	**-509.8**	**-514**
20	-3.18	343.7	288.9	**-2686.5**	303.1	296.5	**-1294.2**	**-1030.3**	244.6	223.8	**-1019.6**	236.8	231.6	**-1019.7**	**-1028**
30	-4.78	515.5	433.3	**-4029.8**	454.6	444.7	**-1941.3**	**-1545.5**	366.9	335.7	**-1529.5**	355.3	347.4	**-1549.2**	**-1542**
40	-6.37	687.4	577.8	**-5373.5**	606.1	529.9	**-2588.5**	**-2060.6**	489.3	447.6	**-2044.3**	473.7	463.3	**-2039.4**	**-2056**
50	-7.96	859.2	722.2	**-6718.2**	757.7	741.2	**-3235.6**	**-2575.8**	611.6	559.6	**-2549.2**	592.1	579.1	**-2549.2**	**-2570**
60	-9.55	1031.1	866.7	**-8059.5**	909.2	889.5	**-3863.1**	**-3090.9**	733.9	671.5	**-3059.1**	710.5	694.9	**-3059.1**	**-3084**
70	-11.15	1202.9	1011.1	**-9402.8**	1060.7	1037.8	**-4490.6**	**-3606.0**	856.3	783.4	**-3573.8**	828.9	810.7	**-3568.9**	**-3598**
80	-12.74	1374.8	1155.6	**-10746.0**	1212.3	1185.9	**-5176.9**	**-4121.2**	978.6	895.3	**-4083.7**	947.3	926.5	**-4078.8**	**-4122**
90	-14.33	1546.7	1300.0	**-12094.2**	1363.8	1334.2	**-5804.4**	**-4636.4**	1100.9	1007.2	**-4593.5**	1065.8	1042.4	**-4588.6**	**-4626**
100	-15.92	1718.5	1444.5	**-13432.5**	1515.4	1482.5	**-6451.5**	**-5151.5**	1223.2	1119.1	**-5103.4**	1184.2	1158.2	**-5098.5**	**-5140**
Analytical Results															
10	-1.49	165.2	139.4	**-1265.6**	145.8	143.1	**-525.9**	**-492.1**	118.0	107.9	**-492.4**	114.3	111.7	**-492.4**	**-492.4**
20	-2.98	330.4	278.7	**-2531.3**	291.6	286.3	**-1051.9**	**-984.3**	236.0	215.9	**-984.8**	228.5	223.5	**-984.8**	**-984.8**
30	-4.47	495.6	418.1	**-3796.9**	437.5	429.4	**-1577.9**	**-1476.4**	354.1	323.9	**-1477.2**	342.7	335.2	**-1477.2**	**-1477.2**
40	-5.96	660.7	557.5	**-5062.5**	583.3	572.6	**-2103.9**	**-1968.5**	472.1	431.9	**-1969.7**	457.0	446.9	**-1969.7**	**-1969.7**
50	-7.44	825.9	696.8	**-6328.2**	729.1	715.7	**-2629.8**	**-2460.6**	591.1	539.9	**-2462.1**	571.3	558.7	**-2462.1**	**-2462.1**
60	-8.93	991.1	836.2	**-7593.9**	874.9	858.9	**-3155.8**	**-2952.8**	708.1	647.9	**-2954.5**	685.5	670.5	**-2954.5**	**-2954.5**
70	-10.42	1156.3	975.6	**-8859.5**	1020.8	1001.9	**-3681.8**	**-3444.9**	826.2	755.8	**-3446.9**	799.8	782.2	**-3446.9**	**-3446.9**
80	-11.91	1321.5	1114.9	**-10125.2**	1166.6	1145.1	**-4207.7**	**-3937.0**	944.2	863.8	**-3939.3**	914.0	893.9	**-3939.3**	**-3939.3**
90	-13.40	1486.7	1254.3	**-11390.7**	1312.4	1288.3	**-4733.7**	**-4429.2**	1062.2	971.8	**-4431.7**	1028.3	1005.7	**-4431.7**	**-4431.7**
100	-14.89	1651.8	1393.7	**-12656.4**	1458.2	1431.4	**-5259.7**	**-4921.3**	1180.2	1079.8	**-4924.2**	1142.6	1117.4	**-4924.2**	**-4924.2**

Table 3.1: Theoretical results for a cantilevered sandwich beam with a point load at the tip. Geometric properties: $L = 0.6m$, $c = 0.028m$, $f = 0.001m$, $b = 0.02m$. Material properties: $E_f = 71e9Pa$, $G_c = 35e6Pa$, $E_c = 120e6Pa$, where the suffix f refers to the face plates and c refers to the core.

3.3 Static three point bending experiment on a simple honeycomb beam

A simple experiment was designed in order to validate the method thoroughly. A three point bending static test was carried out on a honeycomb sandwich beam. The beam was manufactured with aluminium alloy (DTD 5070 B) face plates which were $1mm$ thick, bonded to a Nomex honeycomb core (Hexcel Aeroweb HRH-10-3/8-3.0) using Cytec 753 ($400gm^{-2}$) adhesive film. The full specifications for the beam, including the material properties, are shown in table 3.2. Strain gauges were bonded to the face plates and the core at the positions shown in figure 3.7. Delta rosette gauges (TML FRA-1) with a nominal resistance of $120\Omega \pm 0.5$ and a gauge factor of 2.1 were used to measure the maximum shear strain in the core. The alignment of these gauges was not important since the readings from the three gauges were used to calculate the principal strains using a strain transformation relationship as shown in figure 3.8 and using the formula [62]

$$\epsilon_{P,Q} = \frac{\epsilon_1 + \epsilon_2 + \epsilon_3}{3} \pm \frac{\sqrt{2}}{3}\sqrt{(\epsilon_1 - \epsilon_2)^2 + (\epsilon_2 - \epsilon_3)^2 + (\epsilon_3 - \epsilon_1)^2} \tag{3.58}$$

The principal strains are then used to calculate the maximum shear strain using

$$\gamma_{max} = \epsilon_P - \epsilon_Q \tag{3.59}$$

Length (L)	0.728 m
Width (b)	0.02 m
Face plate thickness (f)	0.001 m
Core thickness (c)	0.028 m
Facing skin Youngs Modulus (E_f)	71e9 Pa
Core shear modulus (G_c)	35e6 Pa†

Table 3.2: Test beam specifications († value quoted by manufacturer [57]

Four stacked delta rosette gauges were bonded directly to the cell walls, two on the outer walls on opposing sides, and two on the inner walls on opposing sides. In this way an average reading could be calculated from the four gauges which would take into account any misalignments of the cell walls from the $x - z$ plane which might cause a higher or lower reading compared to the true shear strain in this plane.

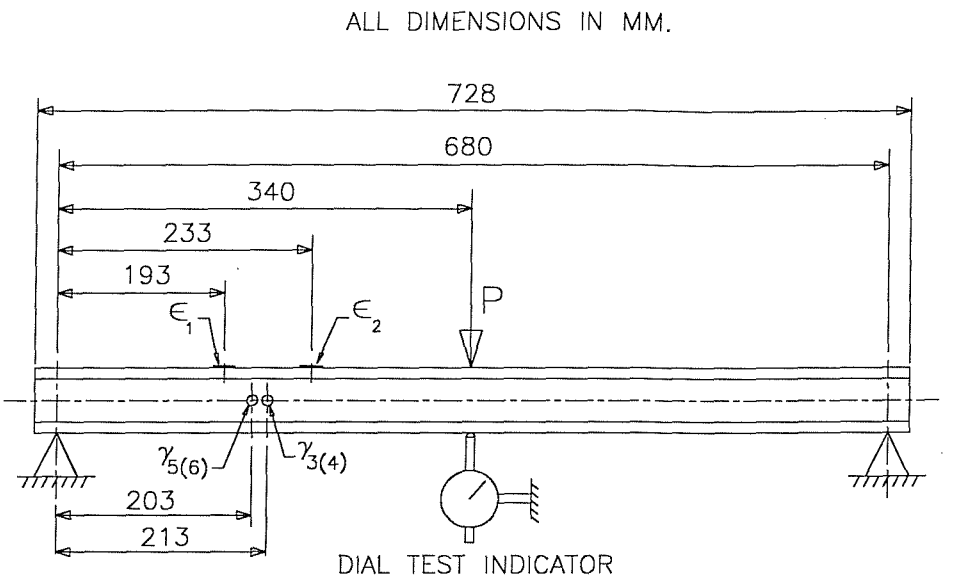

Figure 3.7: Set up of the static experiment. () refers to the rosette gauges on the opposite face.

Since the surface to which these gauges were bonded was very thin and made from a resin coated paper, the gauges were wired into a half bridge circuit with dummy gauges bonded to a similar piece of honeycomb core which was remote from the structure, to provide temperature compensation. Single element gauges (TML FLA-6) with a nominal resistance of $120\Omega \pm 0.5$ and a gauge factor of 2.1 were used to measure the direct strain in the face plates. These gauges were wired into a quarter bridge circuit. Figure 3.9 shows the location of the gauges on the face plates and the core. A Measurements Group Model 2200 signal conditioning amplifier was used for calibration and to amplify the signals from the strain gauges. The amplifier has a total of ten channels, so it was only possible to take measurements from two rosette gauges and the two face plate gauges at any one time. The readings were acquired using a National Instruments VXI A/D acquisition system over a time interval of two seconds. This was done to see if there was any drift in the strain readings, especially from the rosette gauges mounted on the core cell walls. When these gauges were wired into a quarter bridge circuit, there was considerable drift in the readings over a very short space of time, which again suggested that a half bridge circuit was needed.

The experimental arrangement for the static three point bending test is shown in figure 3.10. A loading plate was manufactured so that the load could be easily applied using $0.5kg$ weights. Each weight was numbered and accurately weighed prior to the test to give the value for the applied load, which included the loading tray. Prior to the test, each bridge was calibrated using an internal shunt resistor. The excitation

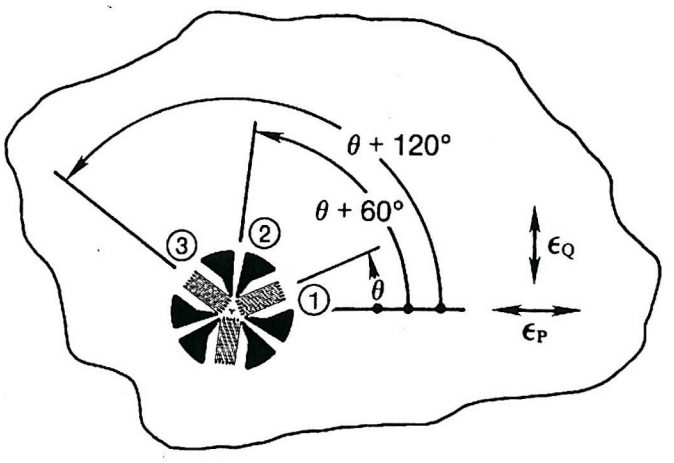

Figure 3.8: Delta rosette strain gauge configuration [62].

level was set to $2V$ and the bridge was balanced. A simulated strain of $1000\mu\epsilon$ was then applied using the "cal A" switch and the gain was adjusted to give $2V$ at the output. The calibrated strain was then obtained using the shunt resistor value, and the resistance and the gauge factor of the strain gauge as follows

$$\mu\epsilon_{cal} = \frac{R_g \times 10^6}{K\left(R_c + \frac{R_g}{2}\right)} \tag{3.60}$$

and the measured value of strain was obtained using the relationship

$$\mu\epsilon_{measured} = \frac{V_{loaded}}{(V_{cal} - V_{unloaded})}\mu\epsilon_{cal} \tag{3.61}$$

where: $\mu\epsilon_{cal}$ = calibrated strain,
R_g = resistance of shunted bridge arm (strain gauge resistance),
K = gauge factor of strain gauge,
R_c = calibration resistor = $59.94K\Omega$,
V_{loaded} = voltage reading from loaded strain gauge,
V_{cal} = calibration voltage = $2V$,
$V_{unloaded}$ = voltage reading from unloaded strain gauge (zero reading),

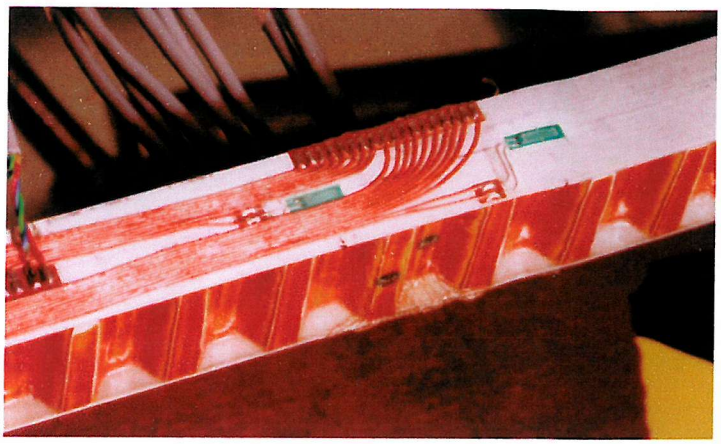

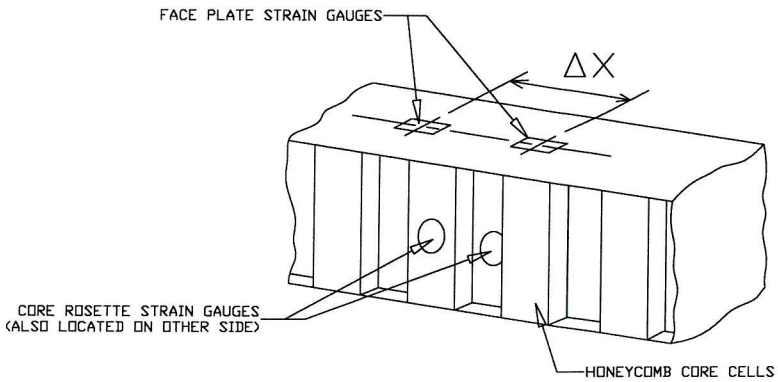

Figure 3.9: Strain gauge locations on the experimental test beam.

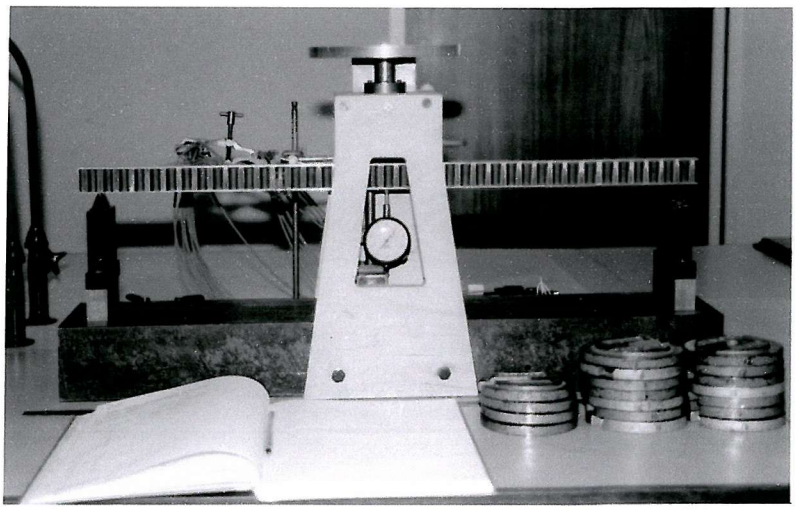

Figure 3.10: Static test set-up.

A set of five tests was carried out, loading from $12.77N$ to $101.27N$, to give an indication of the repeatability. The experimental results were initially found to disagree with the finite element and analytical model results. Not only did the core shear strains and the face plate direct strains not agree, but the central deflections were also in disagreement. The most possible explanation was that the value of the core shear modulus used in the theoretical models was incorrect since all of the other geometric/material specifications were known to be correct. It is known that the core shear modulus for honeycomb materials is a difficult property to obtain. The standard test method used is detailed in the ASTM standard C 273 [63]. In this standard test, a piece of core which has a width not less than twice the thickness and a length not less than twelve times the thickness of the core, is bonded between two thick steel face plates which are located in a special fixture and the specimen is subject to a standard tensile or compressive test. In the case of the core used in these experiments, the width was $20mm$, which included only two cells across the width. It was therefore thought that the "smeared" core shear modulus obtained from the manufacturer was not applicable to a specimen of the dimensions used in these tests. In order to verify this, a simple experiment was conducted whereby a honeycomb sandwich beam, with similar specifications to the one used in the strain measurement tests, was loaded in a three point bending test and the deflections were measured for each load step. The beam was manufactured using $290mm$ long $\times$ $70mm$ wide $\times$ $1mm$ thick aluminium alloy face plates (DTD 5070 B) which were bonded to a $25.4mm$ thick hexagonal honeycomb core (Hexcel Composites HRH-10-3/8-3.0) using Cytec 753 adhesive film. The distance between the two supports was $250mm$ and the manufactures quoted shear modulus for the honeycomb material was 38.6 MPa. After carrying out the load deflection test with loads from $13.6N$ to $209.8N$, the width of the beam was trimmed to $30mm$ and then $20mm$, repeating the test at each stage. The results from the experiment are shown in figure 3.11, and a comparison is made with the analytical solution for the mid-point deflection using equations 3.42 and 3.43 with symmetry about $L/2$ and with half the load applied. It can be seen that as the width of the beam was reduced, the value of the shear modulus needed to obtain an approximate agreement with the measured deflections increased. This therefore suggests that the effective core shear modulus should be obtained from a comparison between the experimental and theoretical load/deflection results. This was done for the original test using the instrumented honeycomb beam, and the results are shown in table 3.3, and in figures 3.12 and 3.13. The agreement between the experimental results and the finite element and analytical models, with a core shear modulus of

$66MPa$ (as opposed to the manufacturer's quoted value of core shear modulus, which is given in table 3.2), was very good. In addition, the estimated core shear strain is in very good agreement with the measured core shear strain, with a maximum of 14% difference.

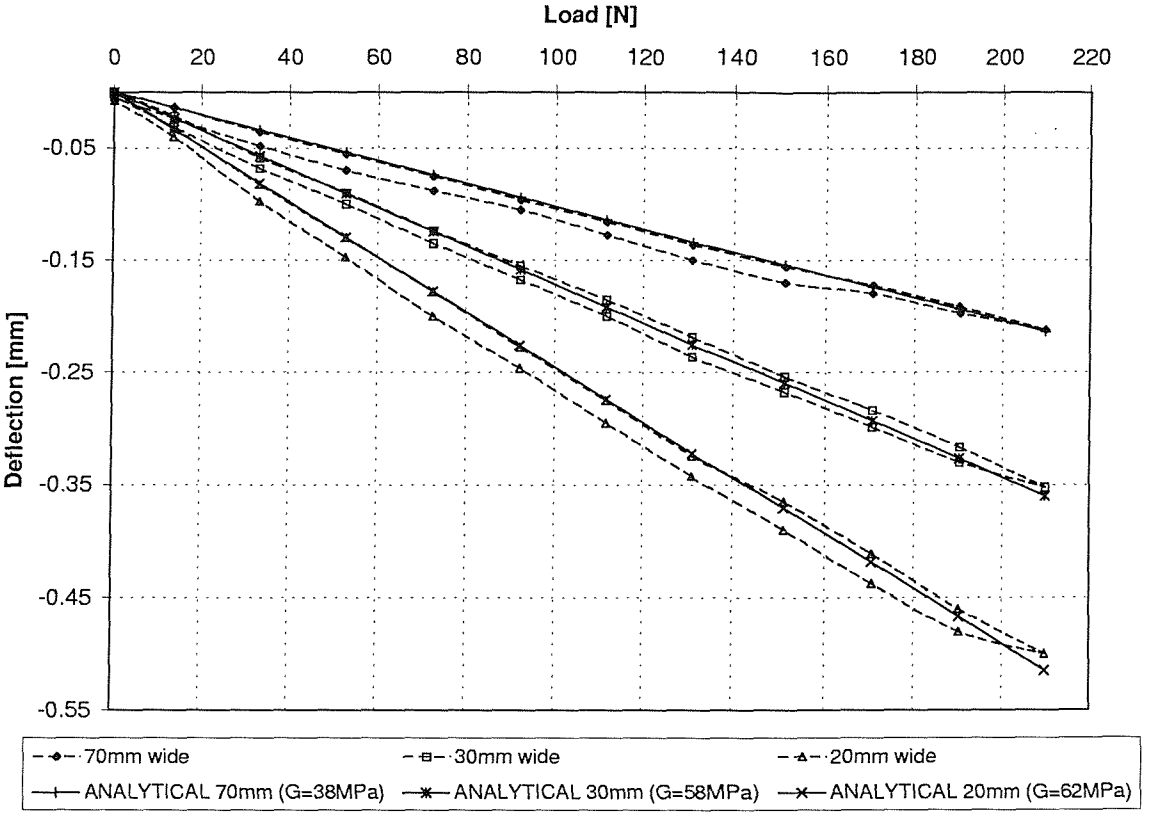

Figure 3.11: Variation of the effective core shear modulus with width of beam.

Load (N)	Deflection (mm)	ϵ_1 ($\mu\epsilon$)	ϵ_2 ($\mu\epsilon$)	γ_c ($\mu\epsilon$)	γ_{est} ($\mu\epsilon$)
Experiment					
12.77	-0.20	-27.35	-34.87	-170.67	-195.32
17.69	-0.27	-38.06	-48.27	-241.74	-265.27
22.69	-0.35	-48.78	-61.86	-314.36	-339.94
27.73	-0.42	-59.67	-75.63	-385.72	-414.98
32.68	-0.50	-70.34	-88.99	-456.65	-484.88
37.52	-0.57	-80.83	-102.27	-527.47	-557.36
42.45	-0.64	-91.59	-115.82	-599.98	-629.94
47.35	-0.72	-102.16	-129.07	-670.78	-699.48
52.19	-0.79	-112.83	-142.47	-743.08	-770.69
57.03	-0.86	-123.18	-155.50	-812.72	-840.19
61.94	-0.93	-133.62	-168.54	-884.30	-907.85
66.88	-1.01	-144.38	-182.12	-955.98	-981.20
71.84	-1.08	-155.32	-195.85	-1028.7	-1053.6
76.74	-1.15	-165.78	-209.02	-1099.9	-1124.3
81.67	-1.23	-176.49	-222.51	-1172.6	-1196.2
86.60	-1.30	-186.93	-235.64	-1246.2	-1266.2
91.54	-1.38	-198.02	-249.56	-1316.0	-1339.9
96.35	-1.45	-208.75	-262.95	-1386.3	-1408.9
101.3	-1.52	-218.81	-275.68	-1458.5	-1478.41
Finite Element Analysis					
12.77	-0.21	-27.75	-34.38	-176.22	-172.36
17.69	-0.29	-38.45	-47.63	-244.12	-238.66
22.69	-0.37	-49.32	-61.10	-313.18	-306.25
27.73	-0.45	-60.28	-74.68	-382.77	-374.36
32.68	-0.53	-71.03	-87.99	-451.01	-440.92
37.52	-0.61	-81.56	-101.04	-517.90	-506.43
42.45	-0.69	-92.26	-114.30	-585.87	-572.98
47.35	-0.77	-102.93	-127.51	-653.57	-639.02
52.19	-0.85	-113.44	-140.53	-720.32	-704.27
57.03	-0.92	-123.96	-153.56	-787.07	-769.53
61.94	-1.00	-134.64	-166.79	-854.90	-835.81
66.88	-1.09	-145.39	-180.11	-923.14	-902.63
71.84	-1.17	-156.16	-193.45	-991.52	-969.44
76.74	-1.25	-166.82	-206.65	-1059.2	-1035.5
81.67	-1.33	-177.52	-219.92	-1127.2	-1102.3
86.60	-1.41	-188.25	-233.20	-1195.3	-1168.6
91.54	-1.49	-198.97	-246.49	-1263.4	-1235.4
96.35	-1.56	-209.44	-259.46	-1329.9	-1300.4
101.3	-1.64	-220.13	-272.70	-1397.7	-1366.7
Analytical (3.42 and 3.43)					
12.77	-0.19	-30.94	-37.36	-166.73	-166.73
17.69	-0.27	-42.87	-51.75	-230.97	-230.97
22.69	-0.35	-54.98	-66.37	-296.25	-296.25
27.73	-0.42	-67.20	-81.12	-362.06	-362.06
32.68	-0.50	-79.19	-95.61	-426.69	-426.69
37.52	-0.57	-90.92	-109.76	-489.88	-489.88
42.45	-0.65	-102.87	-124.18	-554.25	-554.25
47.35	-0.72	-114.73	-138.51	-618.42	-618.42
52.19	-0.79	-126.47	-152.68	-681.42	-681.42
57.03	-0.87	-138.20	-166.84	-744.61	-744.61
61.94	-0.94	-150.09	-181.20	-808.72	-808.72
66.88	-1.02	-162.06	-195.65	-873.22	-873.22
71.84	-1.09	-174.08	-210.16	-937.98	-937.98
76.74	-1.17	-185.95	-224.50	-1002.0	-1002.0
81.67	-1.24	-197.90	-238.92	-1066.3	-1066.3
86.60	-1.32	-209.85	-253.34	-1130.7	-1130.7
91.54	-1.39	-221.82	-267.79	-1195.2	-1195.2
96.35	-1.47	-233.48	-281.87	-1258.0	-1258.0
101.3	-1.54	-245.40	-296.26	-1322.2	-1322.2

Table 3.3: Static experiment results.

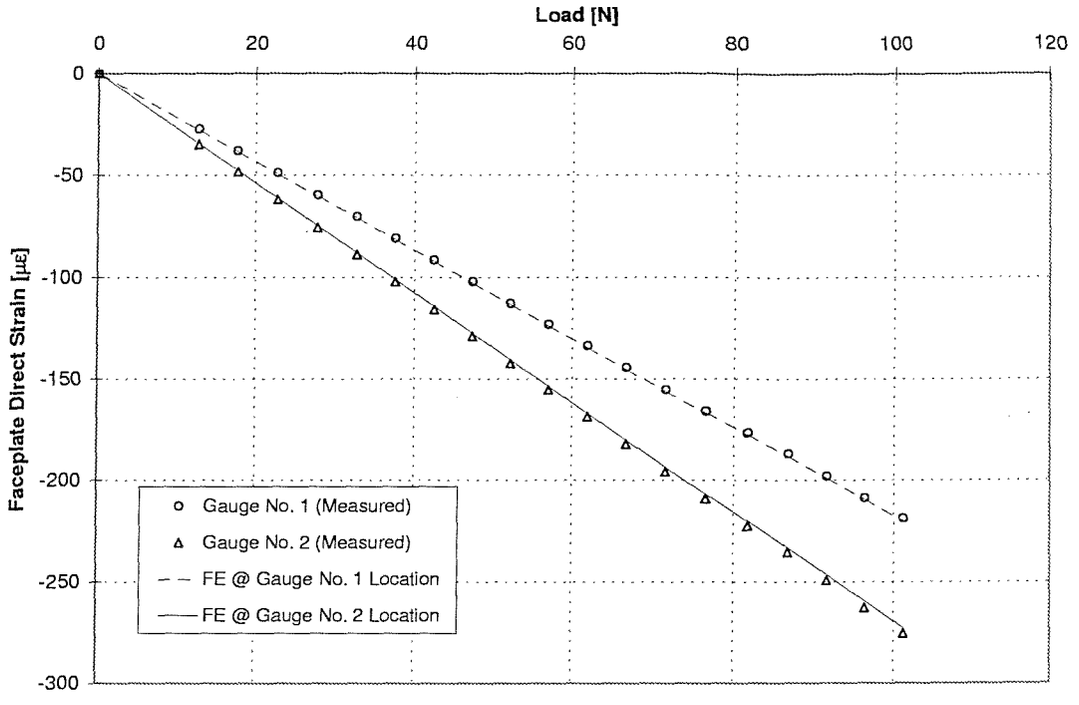

Figure 3.12: Measured and theoretical (FE) face plate strains for the static three point bending experiment.

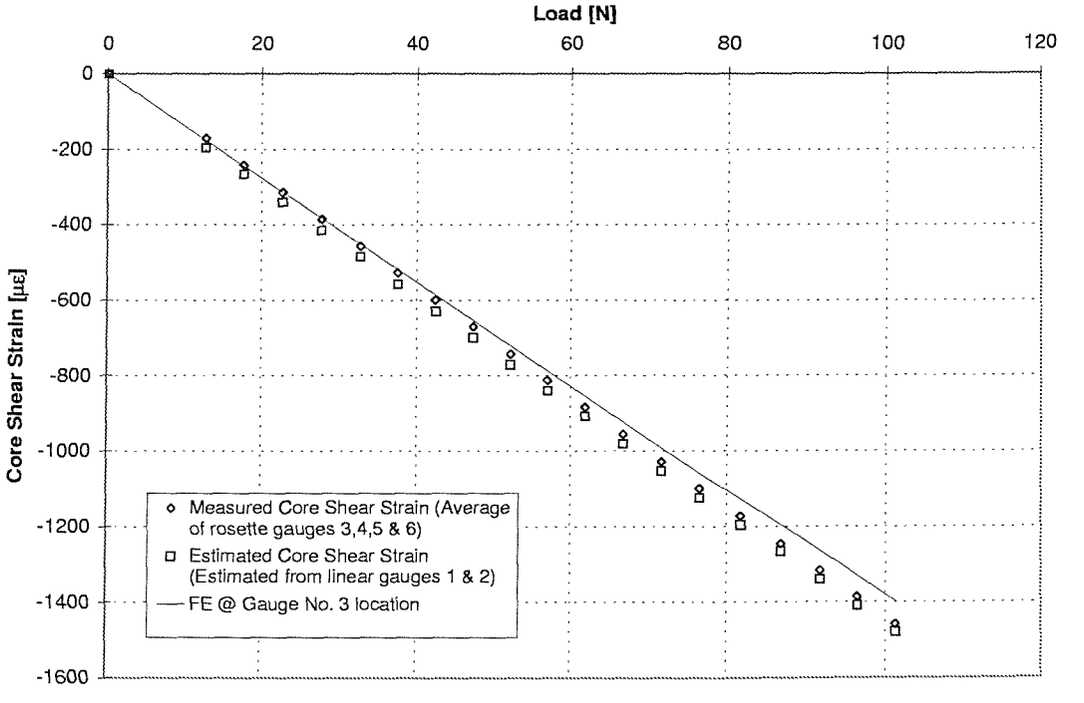

Figure 3.13: Measured, estimated, and theoretical (FE) core shear strains for the static three point bending experiment.

3.4 Dynamic experiment on a cantilevered beam

The same instrumented honeycomb sandwich beam was also used in a dynamic experiment. The objective of this experiment was to make sure that the technique worked just as well when measuring dynamic strains since this will be the ultimate use of the measurement technique.

3.4.1 Test set up and procedure

The beam was set up as a clamped cantilever as shown in figure 3.14 and figure 3.15. Two large steel blocks were machined with a groove into which the sandwich beam was located in order to give the best clamping arrangement possible. In order to prevent core crush, the honeycomb cells located in the area of the clamp were filled with a mixture of epoxy resin and phenolic micro-spheres. The experiment was set up on a concrete and steel vibration test bed and the sandwich beam was driven at one end with a small electrodynamic shaker which was coupled to the beam using a "stinger" via a B&K type 8200 piezoelectric force transducer. The acceleration was also measured at the driving point using a B&K type 4344 piezoelectric accelerometer. The Measurements Group series 2200 signal conditioning amplifier was again used for calibration and to amplify the signals from the strain gauges which were wired in the same bridge configurations as those used in the static test. A B&K type 1405 random signal generator was used to provide the input signal to the shaker via a power amplifier, and a band pass filter was incorporated in the circuit between the signal generator and the amplifier. The signals from the piezoelectric transducers and the strain gauges were directed, after being conditioned and amplified, to the VXI data acquisition suite via a low pass filter set.

Several tests were carried out in order to check the repeatability of the experiment with both broadband and narrow band excitation. For the broadband tests, a 55 Hz to 1500 Hz band limited signal was used to drive the shaker, whilst for the narrow band tests the signal was band limited between 55 Hz and 95 Hz, a frequency range which encompassed the first resonance frequency of the cantilevered test beam. The output signals from the accelerometer, force transducer, and strain gauges were filtered using low pass filters. For the broad band tests the cut-off frequency was 1 kHz, whereas for the narrow band tests it was 500 Hz.

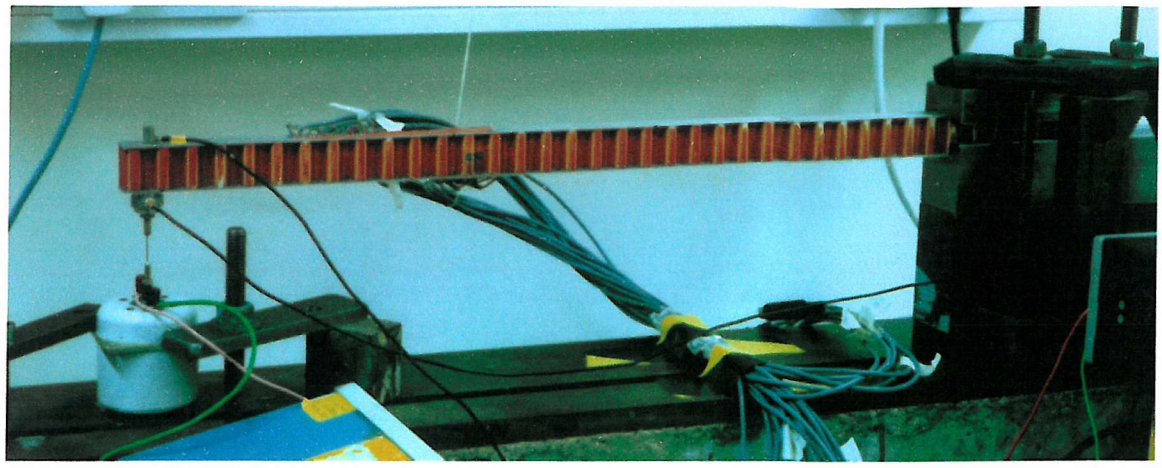

Figure 3.14: The dynamic experiment on a cantilevered honeycomb sandwich beam.

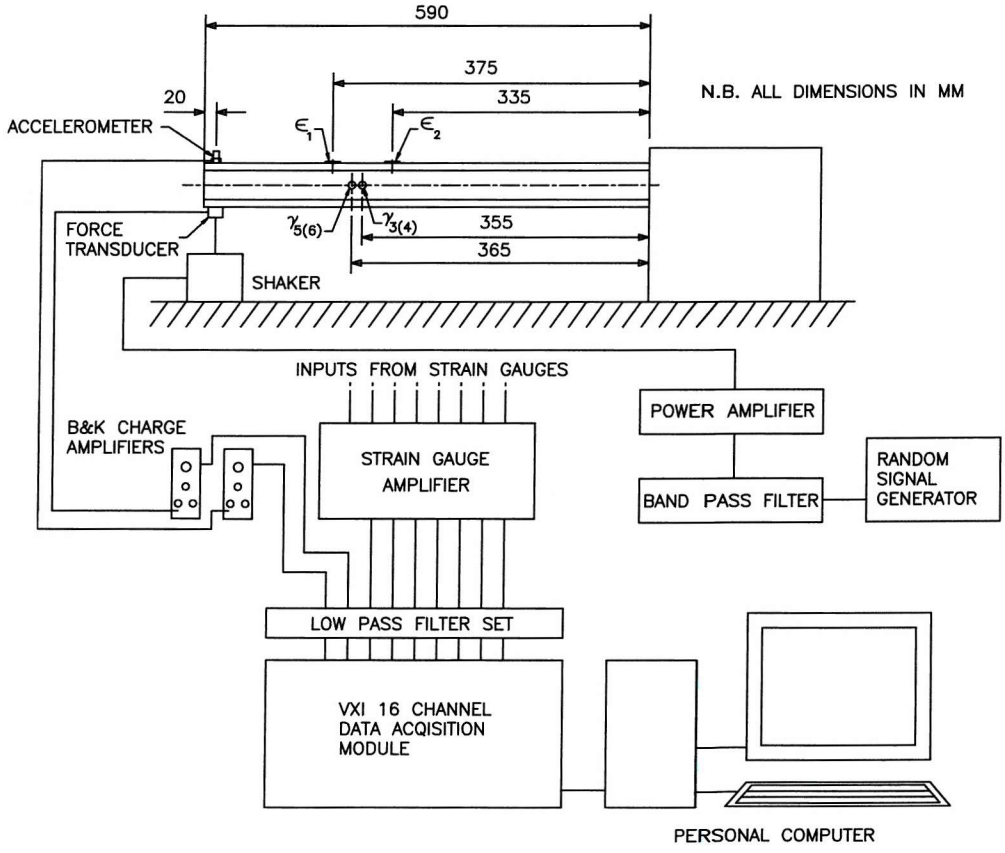

Figure 3.15: Experimental set up of the dynamic experiment.

Once the time signals had been acquired and the actual values of strain calculated using equations 3.60 and 3.61, they were transformed into the frequency domain using the MATLAB "spectrum" function which uses a radix-2 FFT algorithm. The next step was to process the frequency dependant data in order to calculate the core shear strain from the rosette gauge measurements using the strain transformation relationship 3.58, and to calculate the estimate of the core shear strain using the direct strain measurements from the two face plate gauges and equation 3.28. The maximum core shear strain can be calculated, in the time domain, using equations 3.58 and 3.59

$$\gamma_{max}(t) = \frac{2\sqrt{2}}{3}\sqrt{(\epsilon_{m1}(t) - \epsilon_{m2}(t))^2 + (\epsilon_{m2}(t) - \epsilon_{m3}(t))^2 + (\epsilon_{m3}(t) - \epsilon_{m1}(t))^2} \quad (3.62)$$

The measured strains from the face plates are denoted as ϵ_1 and ϵ_2, whilst the measured core strains from the rosette gauges are denoted as ϵ_{m1}, ϵ_{m2}, and ϵ_{m3}, where the suffix m denotes the rosette gauge number (3, 4, 5, or 6) and the suffix 1, 2, and 3 denotes the element number as shown in figure 3.8. When transformed into the frequency domain, these measured strains become complex numbers, and each of these complex strains can be expressed as a "single frequency" time history which has the form

$$\epsilon_{mn}(t) = \Re\{\underline{\epsilon}_{mn}(\omega)e^{i\omega t}\} \quad (3.63)$$

where the suffix mn denotes the element n of rosette gauge m as before, and the underscore denotes a complex number. For elements 1 and 2, for example

$$\epsilon_{m1}(t) - \epsilon_{m2}(t) = \Re\{(\underline{\epsilon}_{m1}(\omega) - \underline{\epsilon}_{m2}(\omega))e^{i\omega t}\} \quad (3.64)$$

and,

$$(\epsilon_{m1}(t) - \epsilon_{m2}(t))^2 = \Re\{(\underline{\epsilon}_{m1}(\omega) - \underline{\epsilon}_{m2}(\omega))e^{i\omega t}\}.\Re\{(\underline{\epsilon}_{m1}(\omega) - \underline{\epsilon}_{m2}(\omega))e^{i\omega t}\} \quad (3.65)$$

Using the identity

$$\Re\{\underline{a}\}.\Re\{\underline{b}\} = \frac{1}{2}\Re\{\underline{a}.\underline{b} + \underline{a}.\underline{b}^*\} \quad (3.66)$$

where * denotes the complex conjugate, equation 3.65 becomes

$$\begin{aligned}(\epsilon_{m1}(t)-\epsilon_{m2}(t))^2 &= \frac{1}{2}\Re\{(\underline{\epsilon}_{m1}(\omega)-\underline{\epsilon}_{m2}(\omega))^2 e^{2i\omega t} \\ &\quad + (\underline{\epsilon}_{m1}(\omega)-\underline{\epsilon}_{m2}(\omega))e^{i\omega t}.(\underline{\epsilon}_{m1}(\omega)^*-\underline{\epsilon}_{m2}(\omega)^*)e^{-i\omega t}\} \\ &= \frac{1}{2}\Re\{(\underline{\epsilon}_{m1}(\omega)-\underline{\epsilon}_{m2}(\omega))^2 e^{2i\omega t}\} \\ &\quad + \frac{1}{2}\Re\{(\underline{\epsilon}_{m1}(\omega)-\underline{\epsilon}_{m2}(\omega)).(\underline{\epsilon}_{m1}(\omega)-\underline{\epsilon}_{m2}(\omega))^*\}\end{aligned} \tag{3.67}$$

So

$$(\epsilon_{m1}(t)-\epsilon_{m2}(t))^2 = \frac{1}{2}\Re\{(\underline{\epsilon}_{m1}(\omega)-\underline{\epsilon}_{m2}(\omega))^2 e^{2i\omega t}\} + \frac{1}{2}|\underline{\epsilon}_{m1}(\omega)-\underline{\epsilon}_{m2}(\omega)|^2 \tag{3.68}$$

Hence the time history of the measured core shear strain can be reconstructed, and by taking the average of equation 3.68, an expression for the measured core shear strain in the frequency domain can be obtained;

$$<(\epsilon_{m1}(t)-\epsilon_{m2}(t))^2>=\frac{1}{2}|\underline{\epsilon}_{m1}(\omega)-\underline{\epsilon}_{m2}(\omega)|^2 \tag{3.69}$$

since

$$<e^{2i\omega t}>=0 \tag{3.70}$$

where <> denotes time averaging, hence in terms of the frequency, f, where $\omega = 2\pi f$,

$$\gamma_{max}(f) \leq \frac{2}{3}\sqrt{|\underline{\epsilon}_{m1}(f)-\underline{\epsilon}_{m2}(f)|^2+|\underline{\epsilon}_{m2}(f)-\underline{\epsilon}_{m3}(f)|^2+|\underline{\epsilon}_{m3}(f)-\underline{\epsilon}_{m1}(f)|^2} \tag{3.71}$$

A similar approach can be adopted for calculating the estimate of the core shear strain in the frequency domain. Using equation 3.28, the estimate in the time domain is

$$\gamma_{est}(t) \approx \frac{E_f}{G_c}\frac{f(c+f)}{2}\left(\frac{c}{2}+f\right)^{-1}\frac{\epsilon_2(t)-\epsilon_1(t)}{\Delta x} \tag{3.72}$$

and using equation 3.69, the estimate of the core shear strain in the frequency domain becomes

$$\gamma_{est}(f) \approx \frac{E_f}{G_c}\frac{f(c+f)}{2\sqrt{2}}\left(\frac{c}{2}+f\right)^{-1}\frac{\sqrt{|\underline{\epsilon}_2(f)-\underline{\epsilon}_1(f)|^2}}{\Delta x} \tag{3.73}$$

Equations 3.71 and 3.73 were used to obtained the measured and estimated values of the core shear strain from the measured complex values of strain in the frequency domain.

3.4.2 Experimental results

Broad band tests

For the broadband tests, data were acquired at a sampling rate of 8000 Hz. A total of 60000 samples (7.5 seconds of data) were taken for each strain gauge and the actual values of strain were calculated using equations 3.60 and 3.61. The raw time domain signals were then transformed into the frequency domain using the MATLAB "spectrum" function. The data were divided into segments containing 8192 samples, which gave a frequency resolution of 0.97 Hz, and a Hanning window was applied and overlapped by 70%. The measured core shear strain was then calculated using the frequency dependent strain data from the rosette gauges and equation 3.71 and the average was taken from the four gauges, whilst equation 3.73 and the strain data from the face plate gauges were used to estimate the core shear strain.

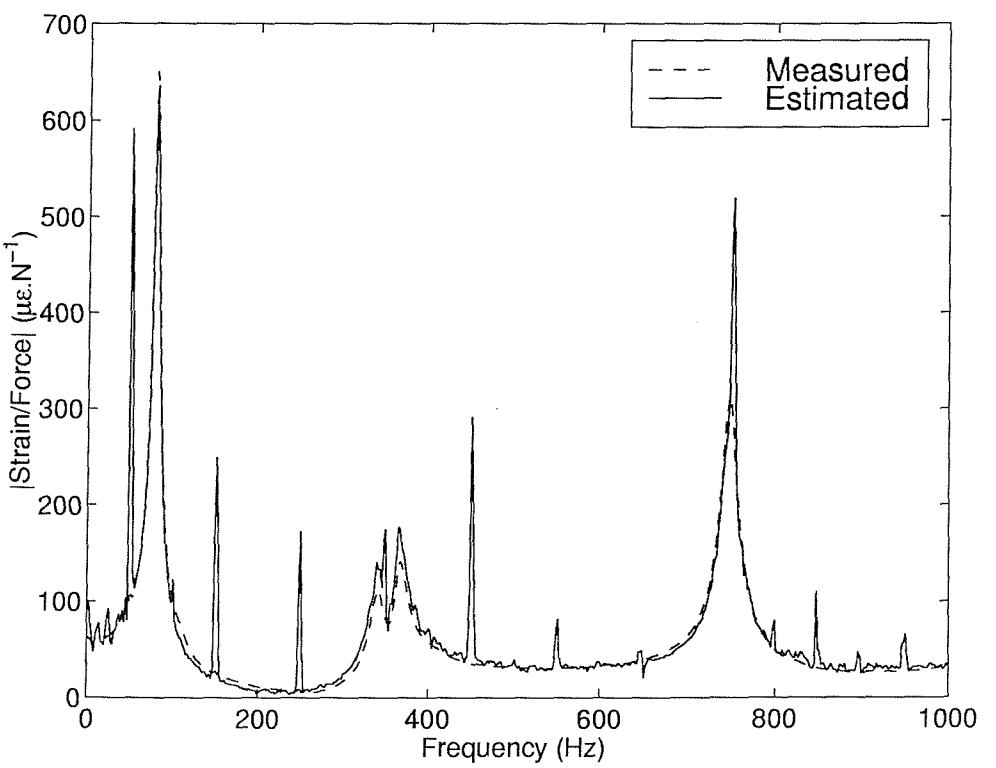

Figure 3.16: A comparison of measured and estimated core shear strains for a cantilevered honeycomb sandwich beam under broad band random point excitation at the tip.

Figure 3.16 shows the result from one of the broadband tests. The results indicated that a significant amount of noise was present, particularly in the estimate of core shear strain. This noise appears to be at multiples of 50 Hz over the entire spectrum, which suggests that it could not be purely "mains pick-up" since the amplitude of the noise is still quite strong at the higher harmonics where it should have reduced.

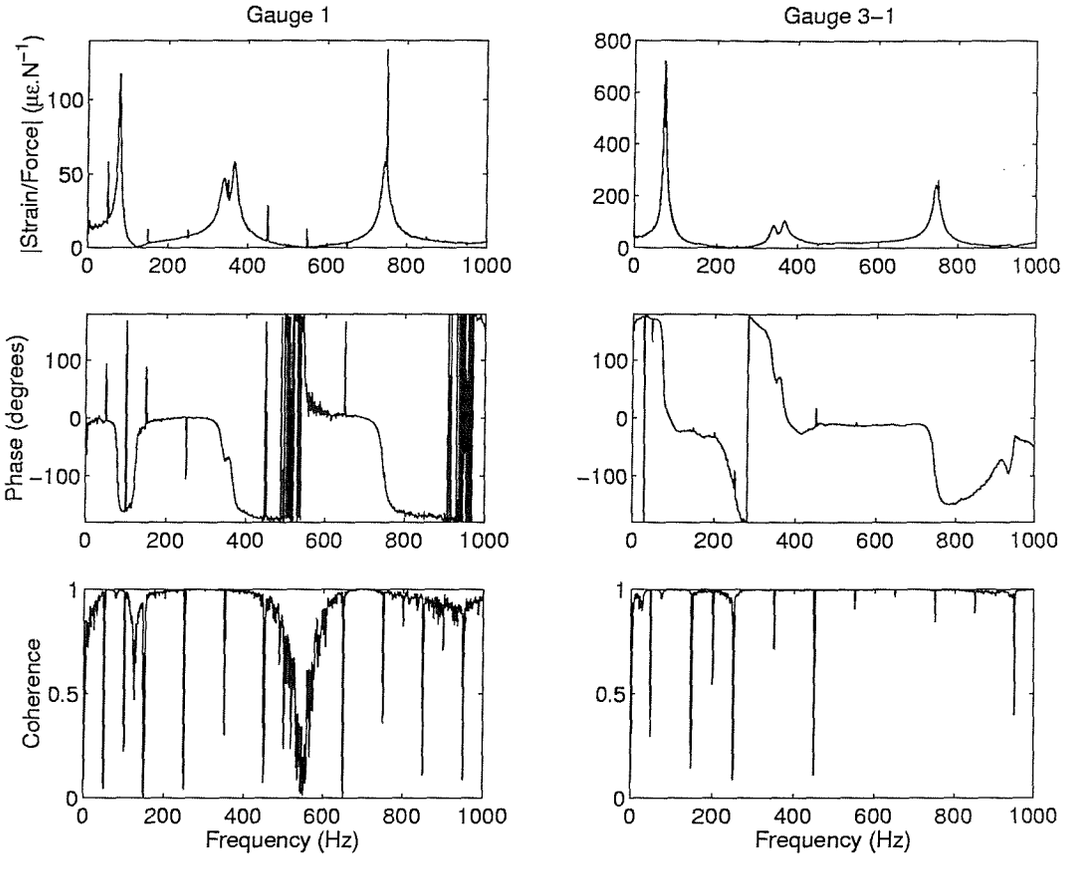

Figure 3.17: Measured strain per force, phase, and coherence in the face plate (gauge 1), and element 1 of rosette gauge 3 (gauge 3-1).

The left-hand side of figure 3.17 shows the linear magnitude of the transfer function of strain per force for gauge 1 (one of the face plate gauges) and the associated phase and coherence. Here, the noise is quite large in magnitude, particularly at 750 Hz whereas the right-hand side of figure 3.17 shows the same result but for one of the elements of gauge 3 (core rosette gauge), where the magnitude of the noise is seen to be much less. The direct strains in the face plates are lower than those measured in the core, therefore the face plate strains are much closer to the noise floor, hence the noisy estimated result for the core shear strain. A measurement was taken from strain gauge 1, with the same sampling rate and number of samples as for the dynamic test

but with no load applied, to see if the noise was still present. Figure 3.18 shows the measured signal-to-noise ratio for the two face plate gauges (1 and 2) and element 1 of rosette gauge 3, which was calculated using [64]

$$SNR = \frac{\gamma_{xy}^2}{1 - \gamma_{xy}^2} \tag{3.74}$$

where γ_{xy} is the coherence between the strain signal and the signal from the force transducer.

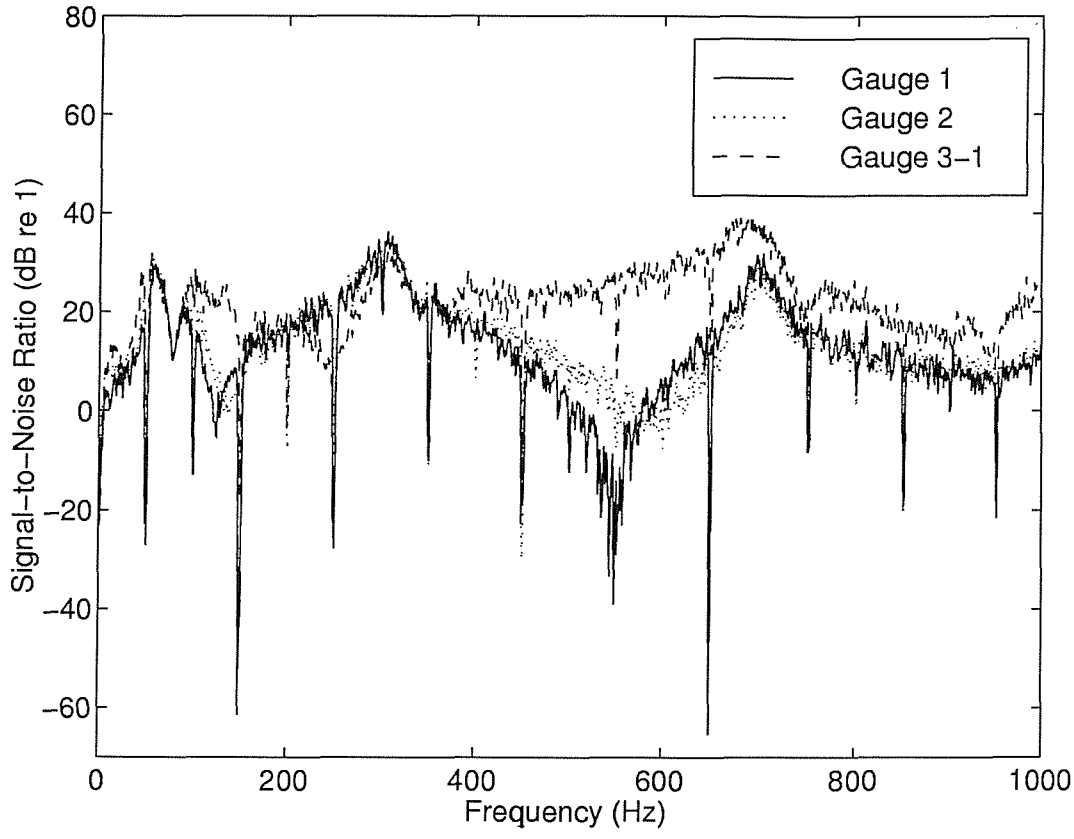

Figure 3.18: Measured signal-to-noise ratio for the face plate strains (gauges 1 and 2) and element 1 of rosette gauge 3.

There are considerable reductions in the signal-to-noise ratio at multiples of 50 Hz across the entire frequency band, the most notable at 150 Hz and 650 Hz for gauge 1. A signal was also recorded from gauge 1 in an unloaded condition, the result of which is shown in figure 3.19. Again, there is a considerable amount of noise present at multiples of 50 Hz. It is possible that this noise was a result of the DIN plug connections used in the lead wires connecting the gauges to the amplifier leads which are connected to the strain gauge amplifier using MIL-SPEC plugs. The manufacture

specifies a maximum noise, referred-to-input (RTI), of $3\mu V$ in the frequency range of interest, and the strain gauge amplifier was checked and found to be within specification. Following discussions with the manufacture it was recommended that the strain gauges be wired directly to the MIL-SPEC plugs with no breaks in the connection. Since there was no time to re-wire the gauges and repeat the test, and since the noise seemed to be uncorrelated with the strain signals from the test, the noise was simply subtracted from the estimated reading and the result is shown in figure 3.20. The estimate is very close to the measured core shear strain, particularly around the first resonant frequency.

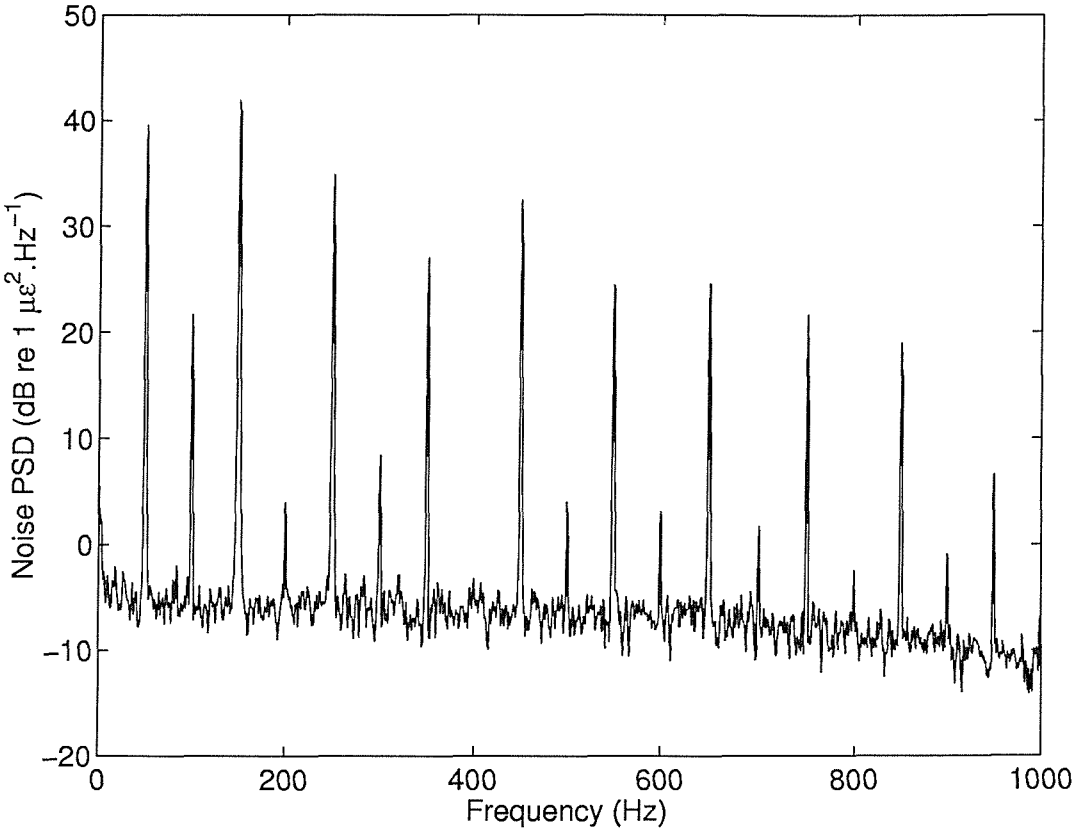

Figure 3.19: Measured noise signal from gauge 1 (unloaded).

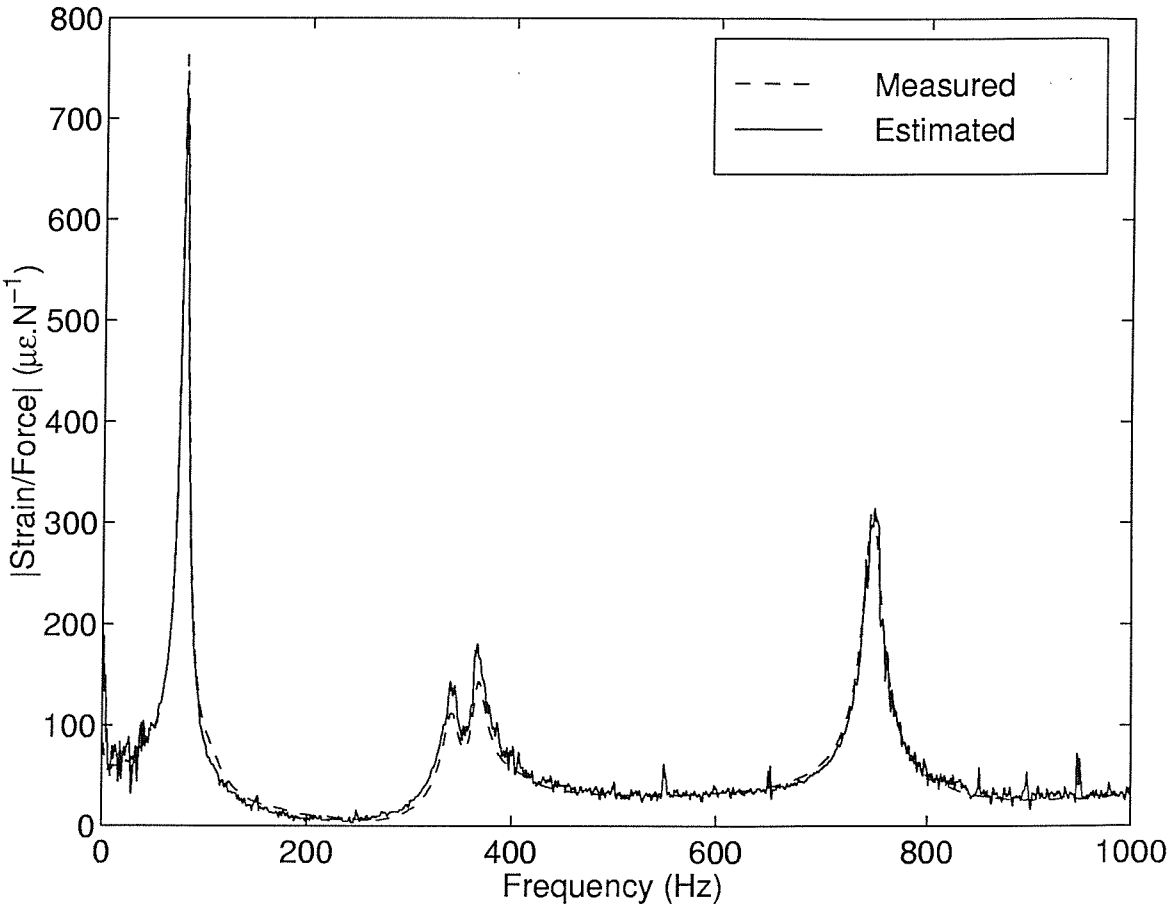

Figure 3.20: A comparison of measured and estimated core shear strains for a cantilevered honeycomb sandwich beam under broad band random point excitation at the tip - noise removed.

Narrow band tests

Several narrow band tests were also carried out. The data were acquired at a sampling rate of 800 Hz and a total of 8000 samples (10 seconds of data) were recorded. The results were processed in exactly the same way as those in the broad band tests but with a window size of 2048 samples giving a frequency resolution of 0.39 Hz. Since the frequency band of interest does not contain any multiples of 50 Hz, there was no noise present, and the result of one of these tests can be seen in figure 3.21. The result shows excellent agreement between measured and estimated core shear strains, and further tests confirmed that the experiment was repeatable.

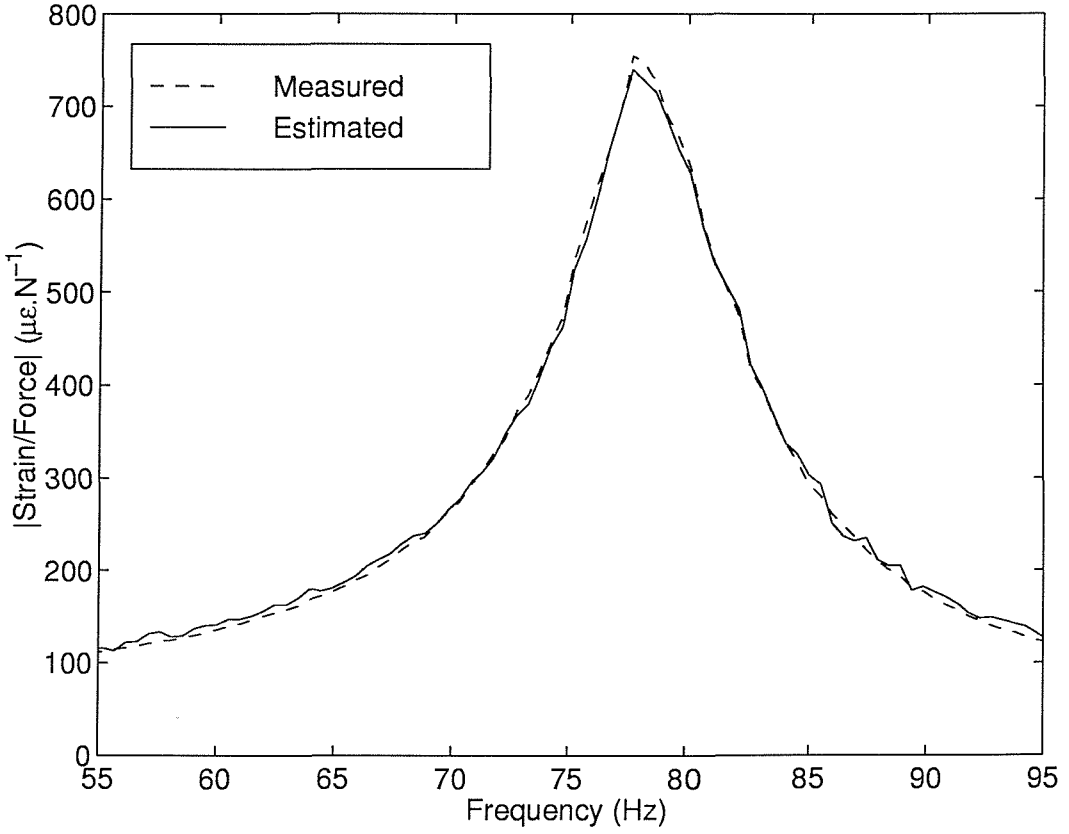

Figure 3.21: A comparison of measured and estimated core shear strains for a cantilevered honeycomb sandwich beam under narrow band random point excitation at the tip.

3.4.3 Finite Element model of the dynamic test

Comparison with theory was achieved by constructing a finite element model of the clamped cantilever sandwich beam used in the experiments and performing a harmonic analysis using this model. The model, which is shown in figure 3.22, was constructed using SOLID63 elements for the face plates and SOLID73 elements for the core. MASS21 elements were included at the positions shown in figure 3.22 to account for the accelerometer and that portion of the force transducer between the beam and the seismic mass, which had masses of 2.5 grams and 3 grams respectively. A unit force was applied at the node associated with the force transducer MASS21 element. A constant damping ratio of 4%, obtained from the experimental results shown in figure 3.21, was used in the finite element model, and all material properties were as given in table 3.2. ANSYS provides three options when carrying out a

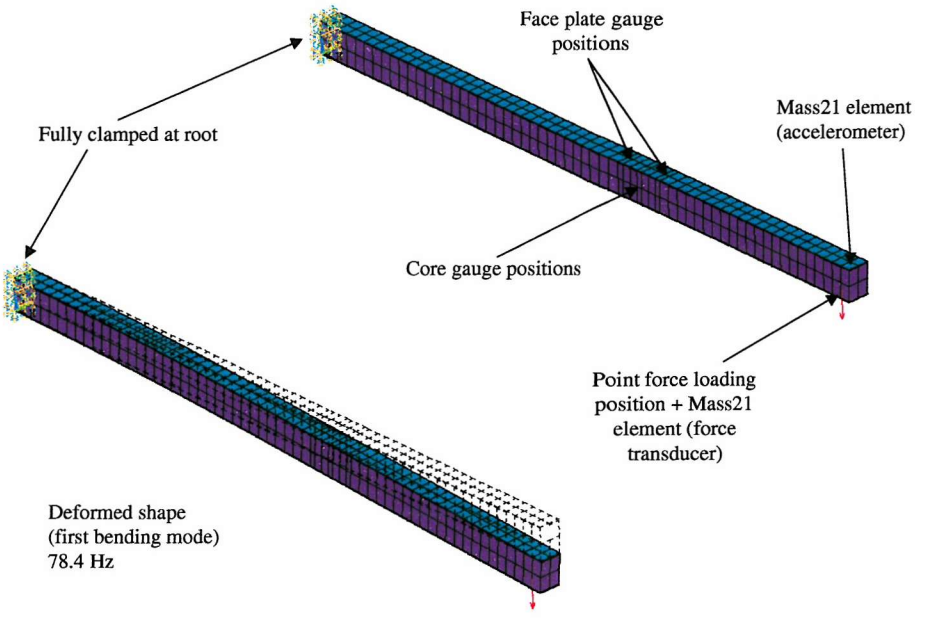

Figure 3.22: Finite element model and dynamic analysis result for the first mode of vibration

harmonic analysis; full method, reduced method, or modal superposition [65]. The modal superposition method of analysis was chosen since it is the fastest of the three methods. There are three solutions steps involved the modal superposition analysis; modal analysis, harmonic analysis, and an expansion pass in which the solution is

expanded to obtain element stress solutions. The analysis was carried out over the frequency range 55 Hz to 95 Hz, which included the first natural frequency of vibration. The first natural frequency was found to be 78.4 Hz, which is very close to the experimental value of 78.26 Hz, and the mode shape obtained from the finite element analysis is shown in figure 3.22. The strains at the positions shown in figure 3.22, which correspond to the strain gauge locations on the experimental test beam, were calculated together with the estimated core shear strain using the calculated face plate strains and equation 3.28, and the transfer function of strain/force was obtained.

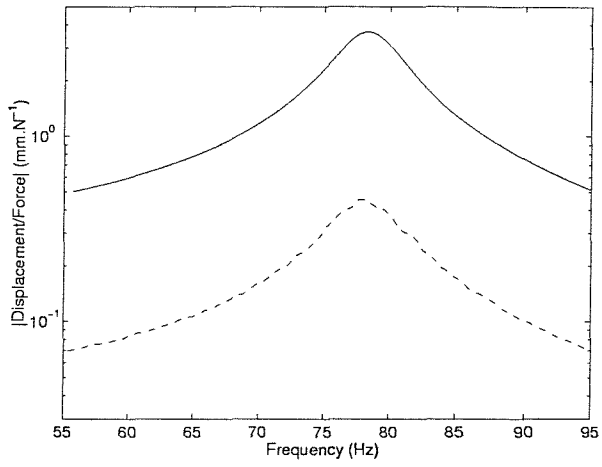

Figure 3.23: Measured driving point displacement (- -) and FE calculated driving point displacement (–) transfer functions.

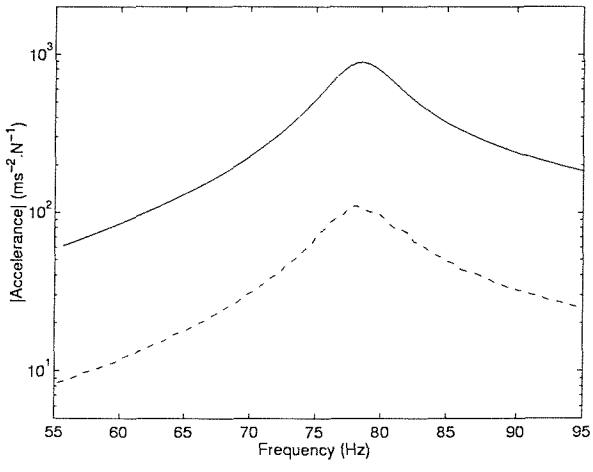

Figure 3.24: Measured driving point accelerance (- -) and FE calculated driving point accelerance (–).

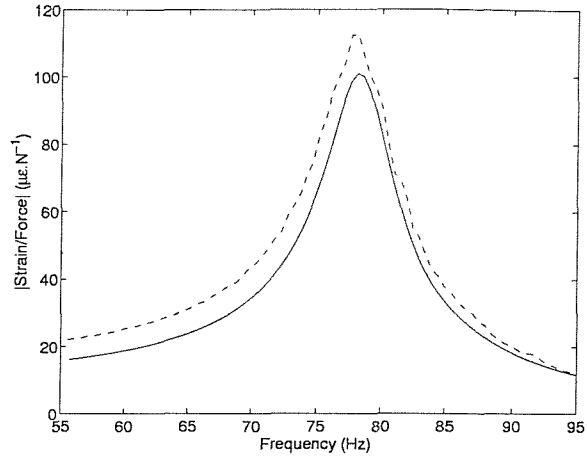

Figure 3.25: Transfer functions of measured face plate strain for gauge 1 (- -) and FE calculated face plate strain for gauge 1 (–).

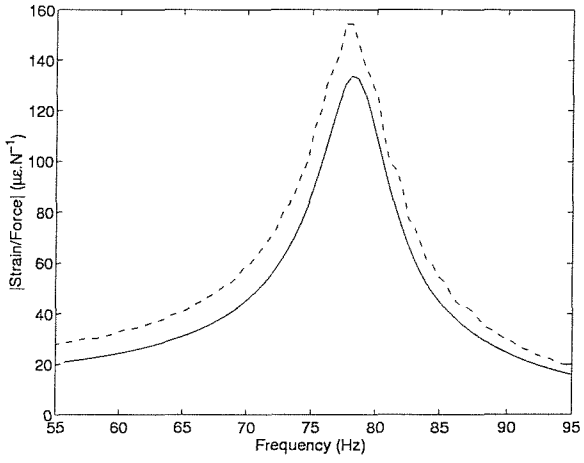

Figure 3.26: Transfer functions of measured face plate strain for gauge 2 (- -) and FE calculated face plate strain for gauge 2 (–).

The experimental results for driving point displacement and accelerance, and the transfer functions between the face plate strain and core shear strain measurements and the force, are compared with the FE model results in figures 3.23 to 3.27. The results show a disagreement between experiment and theory, despite the natural frequency of vibration being in agreement. The displacement and accelerance are much higher for the FE results whereas the strain calculations appear to be lower (the core shear strain should be $\sqrt{2}$ higher since this factor has been introduced in calculating the core shear strain from the rosette gauge measurements which can be seen in equation 3.71). These results appear to be rather paradoxical since the experimental beam was stiffer than the apparently equivalent FE model. A further check

was carried out by measuring the static deflection at two points on the cantilevered beam and comparing this with the FE model calculations, and theoretical calculations using equations 3.56 and 3.57. The results are shown in figure 3.28, and again the experimental beam appears to be stiffer than both the FE and theoretical calculations. Several approaches were adopted in an attempt to resolve this parodox, however it was not possible to conduct further experiments due to limitations in time and availability of the test equipment.

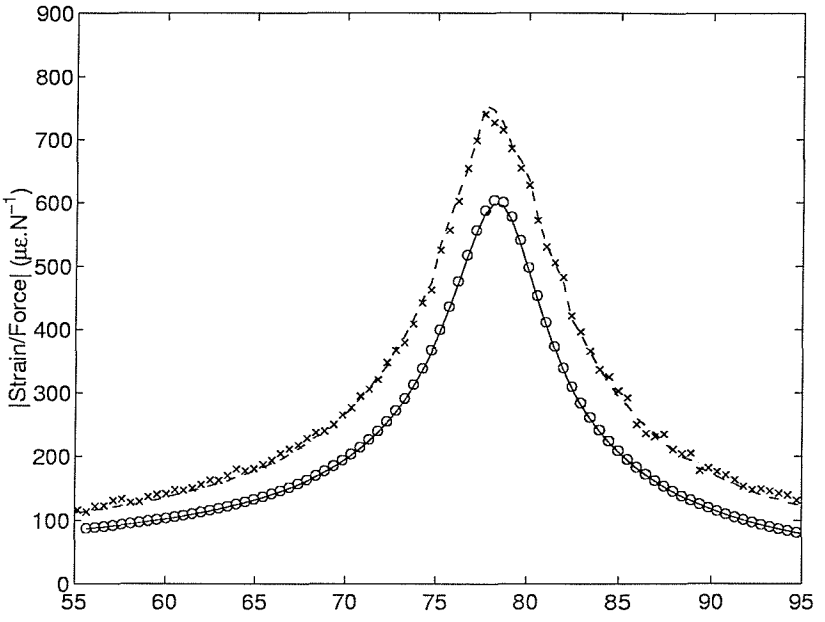

Figure 3.27: A comparison of measured core shear strain (- -), estimated core shear strain from face plate measurements (x), calculated core shear strain using FE (–), and estimated core shear strain from FE calculations (o) for a cantilevered honeycomb sandwich beam under dynamic loading at the tip.

First, the number of elements used in the FE model was increased to check that the solution had converged. This was found to have no effect on the results, hence verifying that the solution had indeed converged. Secondly, the FE model was used to investigate the effect of a combined force and moment dynamic load at the tip in order to ascertain whether a moment was being introduced in the experiments. A sensitivity analysis was carried out by applying a unit moment at 10mm, 20mm, 30mm and 40mm from the load point. This had very little effect on the displacement and the strains. Finally, it was noticed that two of the cells containing potting compound were located forward of the clamp, which meant that at this point the shear properties of the core would have been higher than those used in the FE model. The model was analysed

again with the element materials in this region changed to represent this effect, and the results indicated that this also had very little effect on the displacement or strains.

The only other possible reason for the discrepancy between the experimental and theoretical results is the supporting structure itself, i.e. the large steel blocks used to clamp the beam and the test bed to which this was attached. This fixture is effectively an added mass, and the assumption is that there must be a considerable impedence mismatch between the structure and its support. However, if there were any motion in this support this would result in differences between the experimental and theoretical results. It would have therefore proved beneficial to model the complete arrangement (including the fixture and test bed). If the acceleration levels from the fixture in the experiment were recorded, this would allow the FE model to be "tuned" in terms of the lateral and rotational stiffness at the support. In addition, it should be noted that a more ideal shaker location would have been toward the root rather than at the tip of the beam, since the interaction between the beam and shaker at the tip becomes more important at resonance (for the first bending mode) where the input force will be very low. All of these suggestions could be adopted in future investigations, however limitations in time did not allow them to be carried out here.

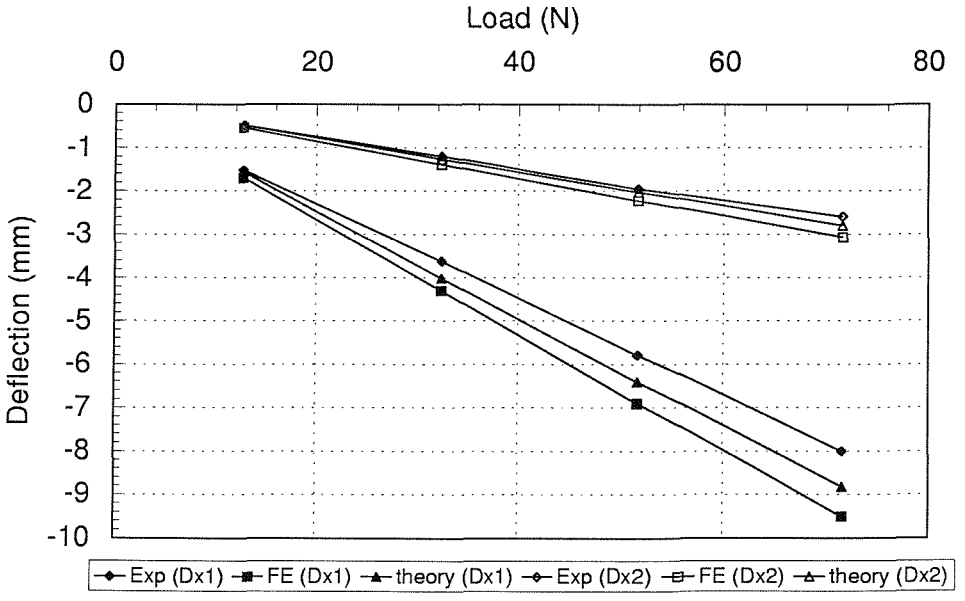

Figure 3.28: Experimental, analytical (equations 3.42 and 3.43), and theoretical (FE) static deflection versus load for the cantilevered beam experiment.

It is important to point out at this stage that, despite the disagreement between the experimental and theoretical results for the cantilevered beam test, this in no way detracts from the validity of the technique. This disagreement is purely a problem of modelling the global cantilevered beam system, whereas the concept of estimating the core shear strain from face plate strain measurements is only concerned with the local strain field around the point of interest, and not the global response of the structure. This concept has been fully validated from a point of view of local changes in strain for both the experimental and theoretical models. It is therefore worthy to suggest that further experiments could prove beneficial, allowing the technique to be investigated further by considering effects such as measurements close to discontinuities, asymmetric sandwich configurations, and the effects of various face plate thickness and core materials. A suggested approach would be to carry out experiments on tee-coupon sandwich beams using base excitation, such as that suggested by ESDU [41] for obtaining sandwich configuration S-N data. This approach would also obviate any problems that could be encountered when modelling the clamped boundary conditions. Another suggestion would be to incorporate a bevelled edge, allowing a more realistic design to be investigated.

3.5 Development of the technique for sandwich panels using a semi-empirical method

The technique has been fully validated for sandwich beams with thin face plates, however for sandwich panels with various boundary conditions, a semi-empirical method must be employed. In addition, the Young's modulus term in equation 3.73 must be factored by $(1-\nu_f^2)^{-1}$ to account for Poisson effects in the panel, which were neglected for the sandwich beam formulation due to the width of the beam being smaller than the total depth. In addition, the strain field in the panel problem is potentially more complex than that of the beam. By introducing semi-empirical constants in the x and y directions (say A_x and A_y), and assuming that the introduction of these constants allows the x and y strains in the panel to be uncoupled, equation 3.73 can be written in the form,

$$\gamma_{est_x}(f) \approx A_x \frac{E_f f(c+f)}{2\sqrt{2}\, G_{xz}(1-\nu_f^2)} \left(\frac{c}{2}+f\right)^{-1} \frac{\sqrt{|\underline{\epsilon}_{x2}(f)-\underline{\epsilon}_{x1}(f)|^2}}{\Delta x} \tag{3.75}$$

in the x direction, and

$$\gamma_{est_y}(f) \approx A_y \frac{E_f f(c+f)}{2\sqrt{2}\, G_{yz}(1-\nu_f^2)} \left(\frac{c}{2}+f\right)^{-1} \frac{\sqrt{|\underline{\epsilon}_{y2}(f) - \underline{\epsilon}_{y1}(f)|^2}}{\Delta y} \tag{3.76}$$

in the y direction. The semi-empirical constants, A_x and A_y, can be found by analysing an FE model of the structure under investigation, and equating the calculated core shear strain with the FE estimated core shear strain. Therefore,

$$A_x \approx \left(\frac{\gamma_x}{\gamma_{est_x}}\right)_{FE} \tag{3.77}$$

and,

$$A_y \approx \left(\frac{\gamma_y}{\gamma_{est_y}}\right)_{FE} \tag{3.78}$$

where γ_x and γ_y are the FE calculated core shear strains in the x and y directions, and γ_{est_x} and γ_{est_y} are the FE estimated core shear shear strains found using equations 3.75 and 3.76 and the FE calculated face plate direct strains in the x and y directions. In order to demonstrate the method, an example of a flat panel with fully clamped boundary conditions on all four edges was analysed. A constant pressure load of 10000 Pa was applied to one surface, and a harmonic analysis was carried out and a solution was obtained around the first natural frequency of vibration of the panel. Seven different result locations were chosen in order to assess the spatial variability of A_x and A_y. The geometric and material properties of the panel are given in table 3.4 and the seven 'gauge' locations are shown in figure 3.29.

Length, a	0.6 m	Width, b	0.44 m
f	0.001 m	c	0.019 m
E_f	71e9 Pa	G_{xz}	35e6 Pa
ν_f	0.33	G_{yz}	20e6 Pa
ρ_f	2770 kgm^{-3}	ρ_c	48 kgm^{-3}
Δx	0.02 m	Δy	0.02 m

Table 3.4: Geometric and material properties for the flat sandwich panel used in the demonstration of the semi-empirical method.

Fully clamped boundary conditions were applied on all four edges of the panel and a modal analysis was carried out in order to determine the first natural frequency of vibration of the panel, which was found to be 358 Hz. A unit surface pressure

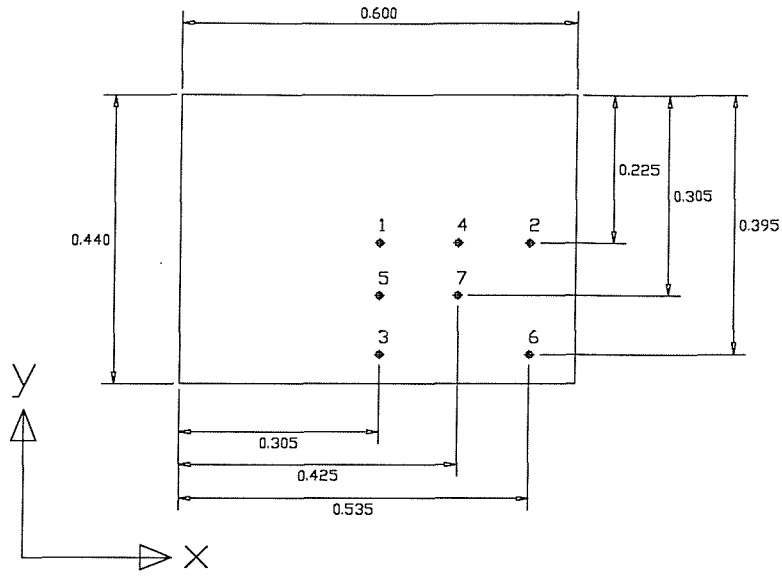

Figure 3.29: The seven result locations for the flat sandwich panel used in the demonstration of the semi-empirical method (all dimensions in metres).

was then applied to one surface of the panel and a harmonic analysis was conducted. An expansion pass was then performed and the core shear strain at each of the seven positions, along with the face plate strains in the x and y directions surrounding these positions, were recovered. Using equations 3.75 and 3.76, the estimated core shear strain was equated to the calculated core shear strain obtained from the middle layer (core) of the sandwich element, and the semi-empirical constants in both the x and y directions were recovered. The semi-empirical constants for each of the seven locations are given in table 3.5. Close consideration of these values in the x and y directions reveal that in the x direction, the values appear to decrease from the middle of the panel towards the edge. In the y direction, the values along the centre-line increase towards the edge, whereas the other two 'rows' (4 and 7, 2 and 6) show a decrease towards the edge. A plot of a typical response for the flat sandwich panel at one of these locations is shown in figure 3.30.

Position	A_x	A_y
1	1.3691	1.4873
2	1.3057	0.7724
3	1.2335	1.5158
4	1.3244	1.2692
5	1.3449	1.4898
6	0.9547	0.5950
7	1.3011	1.2674

Table 3.5: Semi-empirical constants for a flat sandwich panel with fully clamped boundary conditions on all four edges.

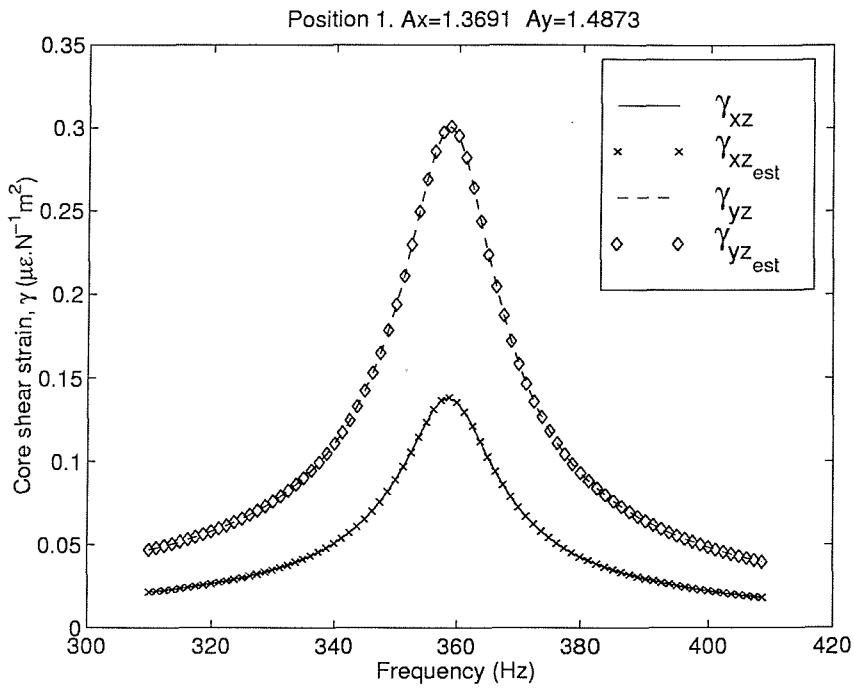

Figure 3.30: A plot of the core shear strain response of the flat sandwich panel with a unit pressure load applied on one face - position 1.

3.6 Concluding summary

A new measurement technique has been presented and fully validated using both experimental and theoretical results. The technique allows the test engineer to estimate the shear strain in a totally enclosed core of a sandwich structure using two strain gauges bonded to one of the face plates in a tandem configuration and at a certain distance apart. There are limitations to the technique, which are that it can only

be applied to sandwich panels with thin and equal thickness face plates. However, the sandwich panels used in the aircraft industry generally meet these requirements, specifically the former, which makes the technique applicable to this type of structure.

Both static and dynamic experiments have been conducted on a simple beam structure which was fully instrumented with strain gauges on the face plates and the core. Static results showed very good agreement with theory using both analytical equations and finite element analysis, and the estimated value of shear strain obtained from the face plate measurements was in good agreement with the actual measured values, therefore proving the method. An experiment has also been conducted using the same test beam but in a cantilevered configuration. Narrow-band and broad-band random excitation was applied using an electrodynamic shaker and stinger arrangement, and the results for the measured and estimated core shear strain agreed very well across both frequency bands. The results from the dynamic broad band tests showed the presence of noise, which was attributed to the connectors being used. This noise was removed from the results since it was completely uncorrelated with the actual strain signals. A finite element model of the dynamic experiment was analysed and although the predicted natural frequency of vibration agreed very well with the measured resonance frequency for the first bending mode, the deflections and strain did not. In fact, the experimental beam seemed to be stiffer than the theoretical beam, and this was verified by comparison between measured static deflections and calculated deflections using both the FE model and the analytical equations. The reason for this parodox was investigated, however an explanation could not be found. To this end, recommendations have been made for further work, however it is important to note that this does not detract from the validity of the technique, since the estimation of the core shear strain depends on measurements of the local strain field on the surface of the face plates, and not the global response of the cantilevered beam system.

For panel type structures with various boundary conditions, a semi-empirical method was applied in order to obtain a set of constants in both the x and y directions for the measurement position and panel under consideration. A finite element model with a unit surface pressure on one surface was analysed, and the harmonic response obtained for the frequency range of interest. To obtain the semi-empirical constants, the calculated core shear strain was equated to the estimated shear strain obtained from the calculated face plate strains in the x and y directions. Once obtained, these constants can then be used in the experimental measurements with any type of loading condition for panels with these dimensions, boundary conditions, and

form of construction.

In conclusion, it is clear that a new viable experimental technique has been established which has great potential for use in the assessment of the fatigue life of honeycomb sandwich aircraft structures.

Chapter 4

Vibration testing of the experimental test panels

4.1 Introduction

The vibration testing of the four test panels is presented in this chapter. The objective was to provide a set of data which could be used to validate the finite element model which is presented in a later chapter. The panels were tested under freely supported boundary conditions, since these are the simplest to model using the finite element method and also the only conditions which can be reasonably achieved in practice. In addition, the experiments will give an indication of the amount of damping present, which can be compared at a later stage with the amount of extra damping produced when the panels are placed in the PWT facility.

4.2 Experimental procedure

4.2.1 Calibration of the vibration test equipment

The vibration test equipment, which consisted of an ENDEVCO® impact hammer incorporating an ISOTRON® force sensor with a plastic tip and an ENDEVCO® Model 2256A piezoelectric accelerometer, was calibrated using a known rigid mass suspended on two light wires [66]. The accelerometer was secured to one end of the block using beeswax, and the other end was tapped ten times using the impact hammer. The resulting signals were captured using a NATIONAL INSTRUMENTS VXI^{TM} A/D converter and the accelerance FRF was obtained and averaged over the ten measurements. The overall sensitivity was found to be $0.453(Volts.N).(Volts.ms^{-2})^{-1}$,

and the ratio of the manufacturer's quoted sensitivities of the accelerometer and hammer was

$$\frac{10.112 \times 10^{-3}}{22.7 \times 10^{-3}} \left[\frac{Volts.(ms^{-2})^{-1}}{Volts.N^{-1}}\right] = 0.445 \left[\frac{(Volts.N)}{(Volts.ms^{-2})}\right]$$

giving a 1.8% difference. The results from the calibration experiment are shown in figure 4.1.

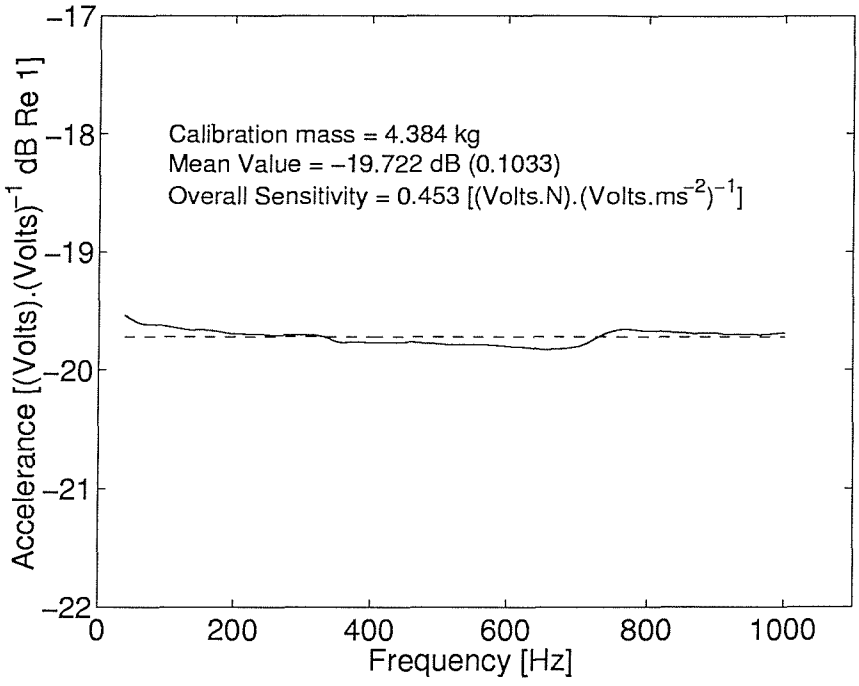

Figure 4.1: Overall sensitivity of the vibration test equipment.

4.2.2 Vibration testing

Each panel was freely supported using bungee cords attached to a stiff frame. A grid of forty measurement points was marked on each panel in order to recover the mode shapes from the test results. During the experiments, the hammer auto-power force spectrum was checked prior to saving the data to ensure a smooth spectrum with a reasonable input energy up to around 400 Hz. The cleanest hammer signal with a reasonably flat spectrum up to 400 Hz was produced by exciting the panels on the flange region, rather than in the main body of the panel. It was for this reason that the accelerometer was moved from point to point and the excitation position remained fixed. Five measurements were recorded per position and the hammer and

accelerometer signals were recorded simultaneously, after passing through low pass filters with a cut-off frequency of 1kHz, using a VXI^{TM} A/D converter. A sampling rate of 8000 Hz was used with a total number of 10000 samples being recorded, giving 1.25 seconds of data. Since the acceleration time domain signal decayed significantly in the sample window (the decay in amplitude was of the order of 50 - 60 dB) any possible errors which could be introduced by leakage were considered negligible. Therefore, a rectangular window was used over the entire 10000 samples (force and acceleration) giving a frequency resolution of 0.8 Hz. The digitised time histories were transformed to the frequency domain using the MATLAB^{TM} "spectrum" function [67] which uses a radix-2 FFT algorithm, and the accelerance frequency response function was obtained and averaged over the five measurements.

4.2.3 Experimental results

Typical plots of the real and imaginary parts of the accelerance for all four panels are shown in figures 4.2, 4.4, 4.6, and 4.8. The real and imaginary parts are shown to clearly indicate a resonance which is characterised by the real part crossing the zero axis accompanied by a sharp peak in the imaginary part at this point of crossing. As can be seen, the peaks are very sharp indicating a very low level of damping present. The equivalent viscous damping ratio was found using the half power point method and the linear magnitude of accelerance,

$$\zeta = \frac{\omega_2 - \omega_1}{2\omega_n} \tag{4.1}$$

where ω_n is the frequency which corresponds to the resonance peak amplitude A_{max} and ω_1 and ω_2 are the frequencies either side of ω_n which correspond to $A_{max}/\sqrt{2}$.

Panel	*Average critical damping ratio, ζ*		
	Mode 1	Mode 2	Mode 3
1	0.0040	0.0032	0.0030
2	0.0053	0.0039	0.0026
3	0.0035	0.0053	0.0029
4	0.0056	0.0044	0.0059

Table 4.1: Average measured damping ratios for the first three modes of the four test panels. Freely supported. (average of forty measurement points).

The damping ratio values, which were calculated for the first three resonance frequencies at each measurement position and then averaged, are shown in table 4.1,

for all four panels. As can be seen, the damping ratios are very small for the first three resonance frequencies. This allowed the resonant response of each of the first three modes to be treated as a single degree of freedom response, hence estimates of the deflected shape at resonance were obtained from the imaginary part of the accelerance at the resonant frequency. These deflected shapes are not strictly mode shapes since to obtain the latter would require either a complicated analysis procedure such as the phase separation approach, a multi-exciter forcing and "tuning" approach, or a combination of the two, such as that discussed by Wright and his co-workers [68, 69]. In addition, errors in the estimates of the deflected shapes at resonance would have been introduced due to the relatively large finite frequency resolution (0.8 Hz in this case), particularly at low frequency, which is why the deflected shapes presented here are not accurate measurements of the mode shapes. This source of error will also be introduced in the estimates of modal damping.

The first three experimental deflected shapes at resonance for all four panels are shown in figures 4.3, 4.5, 4.7, and 4.9. As can be seen, for panels 1, 2 and 3, the first mode of vibration is purely torsional, the second is a fundamental bending mode, and the third is a combination of bending and torsion. For panel 4, the second and third modes appear to have changed order. This panel was different from the other panels in that the sandwich lay-up is asymmetric, with two layers in the facing (inner) skin, and six layers in the backing (outer) skin. In addition, this panel had the highest modal damping ratios, and the first resonant frequency had also reduced by approximately 43% compared with panel 3, which had the same geometry but with a symmetric sandwich lay-up.

4.3 Concluding summary

The vibration experiments conducted using the doubly curved panels have produced very good results which show sharp resonances with a low value of damping. Since the resonance frequencies were well spaced, the resonant response of each of the first three modes could be treated as a single degree of freedom response thus allowing estimates of the deflected shapes at resonance to be obtained from the imaginary part of the accelerance at each measurement location. The damping values obtained from the experiments were very low, in all cases less than 1%, and the highest set of modal damping ratios were found to be those associated with panel 4, all being approximately 0.5%.

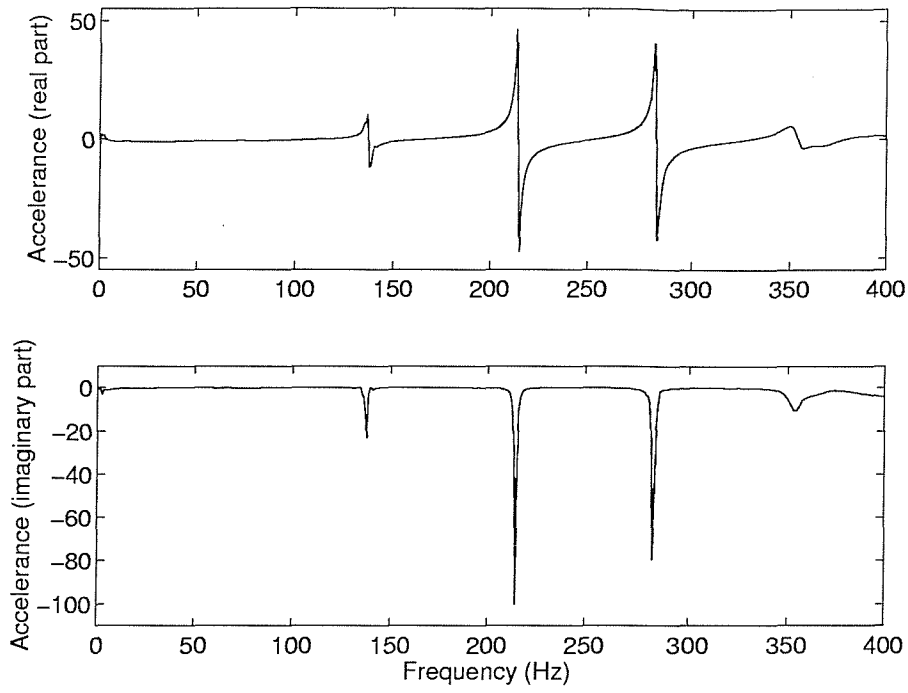

Figure 4.2: Real and imaginary parts of the accelerance for panel 1. Freely supported. (Excitation point: $x = 360mm$, $y = 48mm$. Accelerometer position: $x = 307mm$, $y = 90mm$). Excitation point and measurement locations given in arc lengths (x=long side, y=short side) from the bottom left hand corner of the panel on the inside (concave) face.

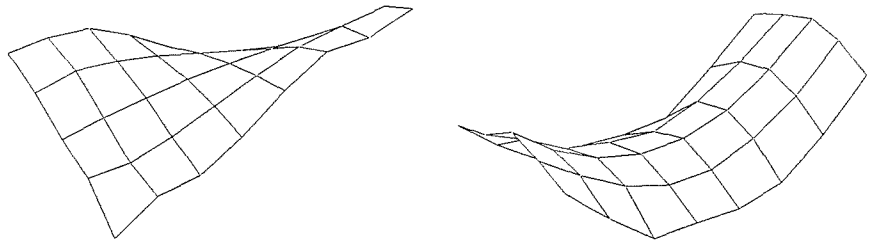

(a) Mode 1, 136.0 Hz

(b) Mode 2, 214.6 Hz

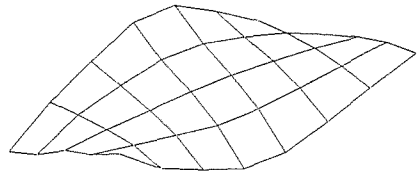

(c) Mode 3, 282.6 Hz

Figure 4.3: The first three deflection shapes at resonance for panel 1 (measured).

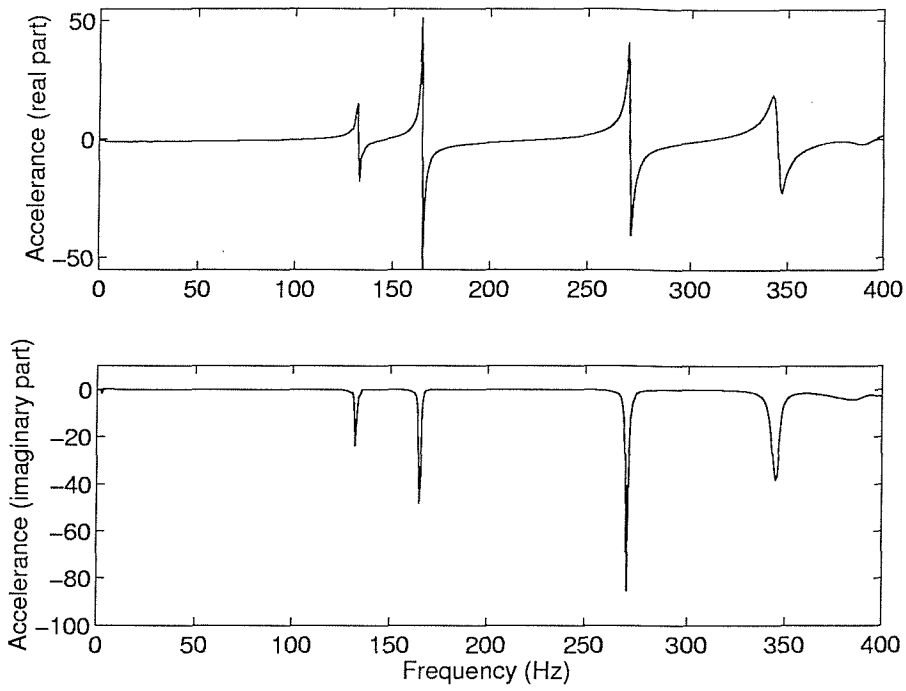

Figure 4.4: Real and imaginary parts of the accelerance for panel 2. Freely supported. (Excitation point: $x = 360mm$, $y = 48mm$. Accelerometer position: $x = 309mm$, $y = 85mm$). Excitation point and measurement locations given in arc lengths (x=long side, y=short side) from the bottom left hand corner of the panel on the inside (concave) face.

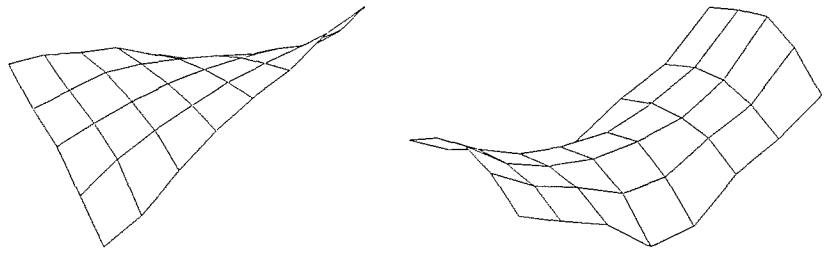

(a) Mode 1, 131.5 Hz

(b) Mode 2, 164.7 Hz

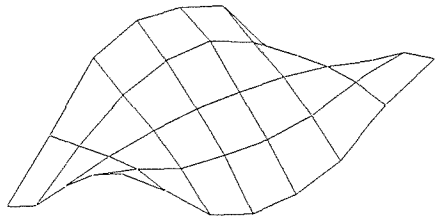

(c) Mode 3, 269.0 Hz

Figure 4.5: The first three deflection shapes at resonance for panel 2 (measured).

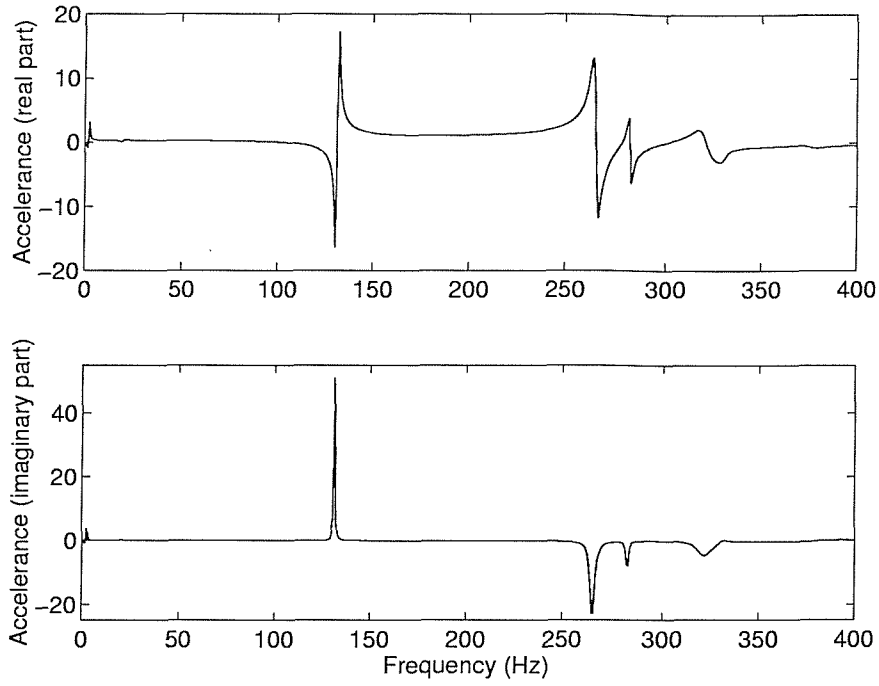

Figure 4.6: Real and imaginary parts of the accelerance for panel 3. Freely supported. (Excitation point: $x = 360mm$, $y = 48mm$. Accelerometer position: $x = 202mm$, $y = 464mm$). Excitation point and measurement locations given in arc lengths (x=long side, y=short side) from the bottom left hand corner of the panel on the inside (concave) face.

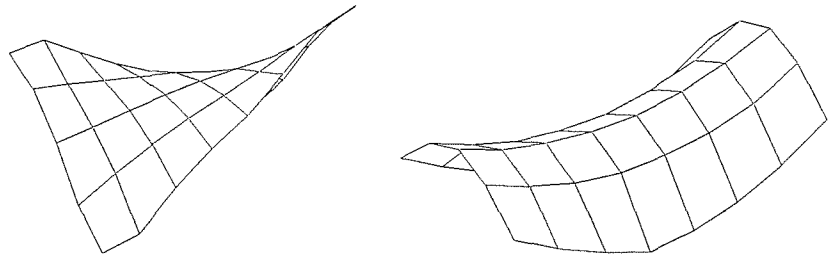

(a) Mode 1, 130.9 Hz

(b) Mode 2, 264.5 Hz

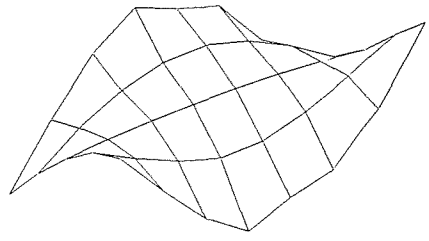

(c) Mode 3, 280.9 Hz

Figure 4.7: The first three deflection shapes at resonance for panel 3 (measured).

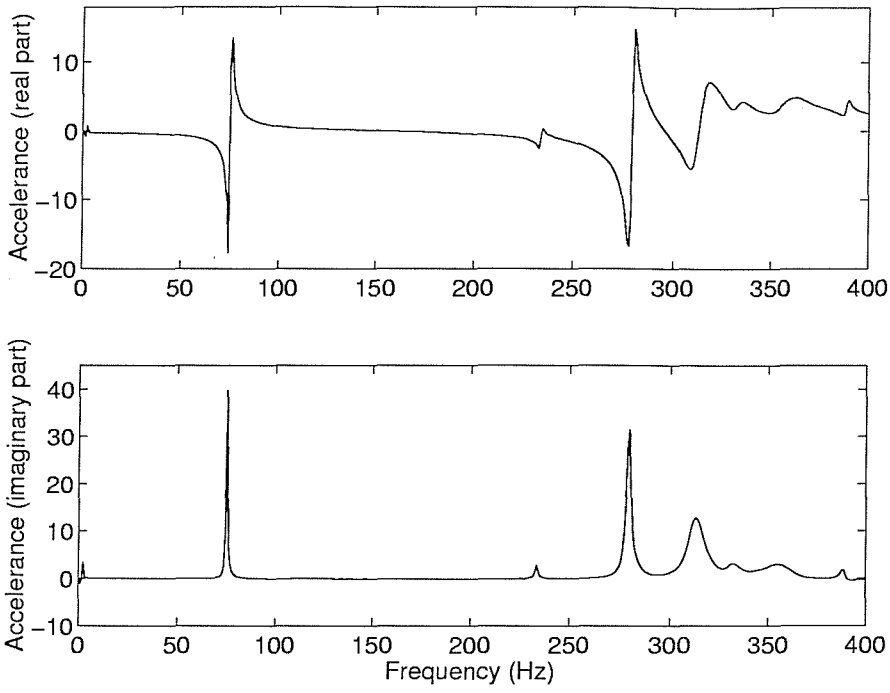

Figure 4.8: Real and imaginary parts of the accelerance for panel 4. Freely supported. (Excitation point: $x = 360mm$, $y = 48mm$. Accelerometer position: $x = 100mm$, $y = 372mm$). Excitation point and measurement locations given in arc lengths (x=long side, y=short side) from the bottom left hand corner of the panel on the inside (concave) face.

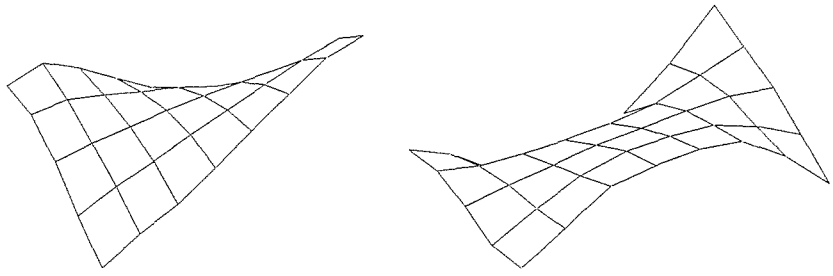

(a) Mode 1, 74.7 Hz

(b) Mode 2, 233.2 Hz

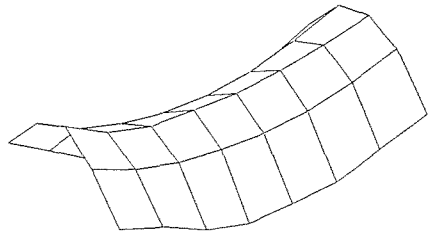

(c) Mode 3, 279.3 Hz

Figure 4.9: The first three deflection shapes at resonance for panel 4 (measured).

Chapter 5

High intensity acoustic testing of the experimental test panels using a progressive wave tube

5.1 Introduction

In this chapter, the high intensity acoustic testing of the four experimental test panels is presented. The progressive wave tube (PWT) facility is discussed in terms of its set-up, operation, specifications and characteristics with regard to the overall sound pressure level (OASPL), phase, and coherence response at various locations in the test aperture. Details of the experimental set-up of the panels in the PWT are given and the testing procedure is presented with information on the acquisition of strain and sound pressure data and the associated post-processing procedures used.

Experimental results are presented in terms of strain power spectral density (PSD) at each strain gauge location and the normalised integral across the PSD, which gives an indication of the percentage contribution of each resonant response to the total PSD over the measurement interval. Statistical results for the sampled data are also presented.

Conclusions are drawn with regard to the relative response of doubly curved sandwich panels to random acoustic excitation and comparisons are made with similar results for flat and singly curved geometries [49, 15].

5.2 The progressive wave tube facility

The ISVR progressive wave tube facility, shown in figure 5.1, uses a Wyle Labs WAS 3000 air modulator as the acoustic source. The WAS 3000 is an electro-pneumatic device which has a maximum acoustical power output of 30 kW over a frequency range of 25 Hz to 10 kHz. Air modulation is achieved by using the principle of a vibrating valve to produce pressure fluctuations in the supply air stream. When coupled to an exponential horn, maximum overall sound pressure levels of 167 dB (re 2×10^{-5} Pa) can be achieved with a frequency range of 60 to 600 Hz.

Figure 5.1: The ISVR progressive wave tube facility.

The PWT facility has a working section which is 1.2m long, 0.6m high, and 0.3m deep. Panels are secured in an appropriate test fixture which is then bolted into the test aperture to form one wall of this section. The panels are therefore excited by grazing incidence sound which propagates along the PWT where it is finally attenuated in the attenuation duct downstream of the test section.

5.2.1 Spatial variation of sound pressure level in the PWT facility

Before commencing tests in the PWT, sound measurements were taken at several points around the test section in order to ascertain the spatial variation in sound pressure level. This work was conducted by Xiao and White [70] as part of an investigation of the acoustic fatigue of box-type structures. A detailed description is given here for completeness since the results were used in the formulation of the response prediction methods presented in chapter 7. A 1 inch (25.4 mm) thick plywood board

was used to close the test aperture, and seven microphone locations were drilled into this board at positions shown in figure 5.2. A reference microphone, which was the permanent microphone used to monitor the overall sound pressure levels in the centre of the test aperture, was used to compare with the measurements from the panel microphone.

Seven measurements were taken using the reference microphone and the panel microphone, which was located in each of the seven positions shown in figure 5.2. Each test was carried out at five OASPL's from 140 dB to 160 dB in 5 dB steps. Unfortunately, only two microphones were available for the tests, one of which was permanently installed in the PWT and therefore in a different plane. It was therefore not possible to ascertain the level of coherence between two points on the panel. However, the level of coherence between the reference microphone and the panel microphone could be calculated for each measurement location on the board, and the OASPL recorded by the reference microphone was kept as constant as possible to enable a comparison to be made between each of the results from the seven tests.

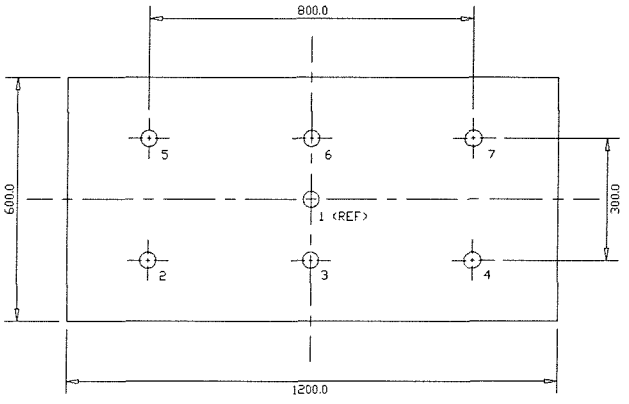

Figure 5.2: Microphone positions used to ascertain the spatial variation in sound pressure level.

The signals from the reference and panel microphones were filtered between zero and 1 kHz using a low pass filter, and then digitally sampled using a National Instruments VXI A/D converter coupled to a personal computer running in the LabView environment. A sampling rate of 6000 samples per second was used and 5 seconds of data were acquired for each sound pressure level [70]. All of the data were post-processed in the MATLAB environment, and the digitised time histories were transformed to the frequency domain using the "spectrum" function, which uses a radix-2 FFT algorithm and Welch's averaging method. A Hanning window was applied over 4096 samples which gave a frequency resolution of 1.5 Hz.

The test results showed that the spatial distribution of OASPL was fairly constant

over the test aperture, which can be seen in table 5.1. The maximum variation along the axis of the aperture was 3.1 dB and from the bottom to the top of the aperture the maximum variation was 2.9 dB. For all of the tests, a spectrum shaper was used to control[1] the spectrum over a frequency range of 60 to 600 Hz, which can be seen in figure 5.3 for all seven microphones and the reference microphone. The PWT

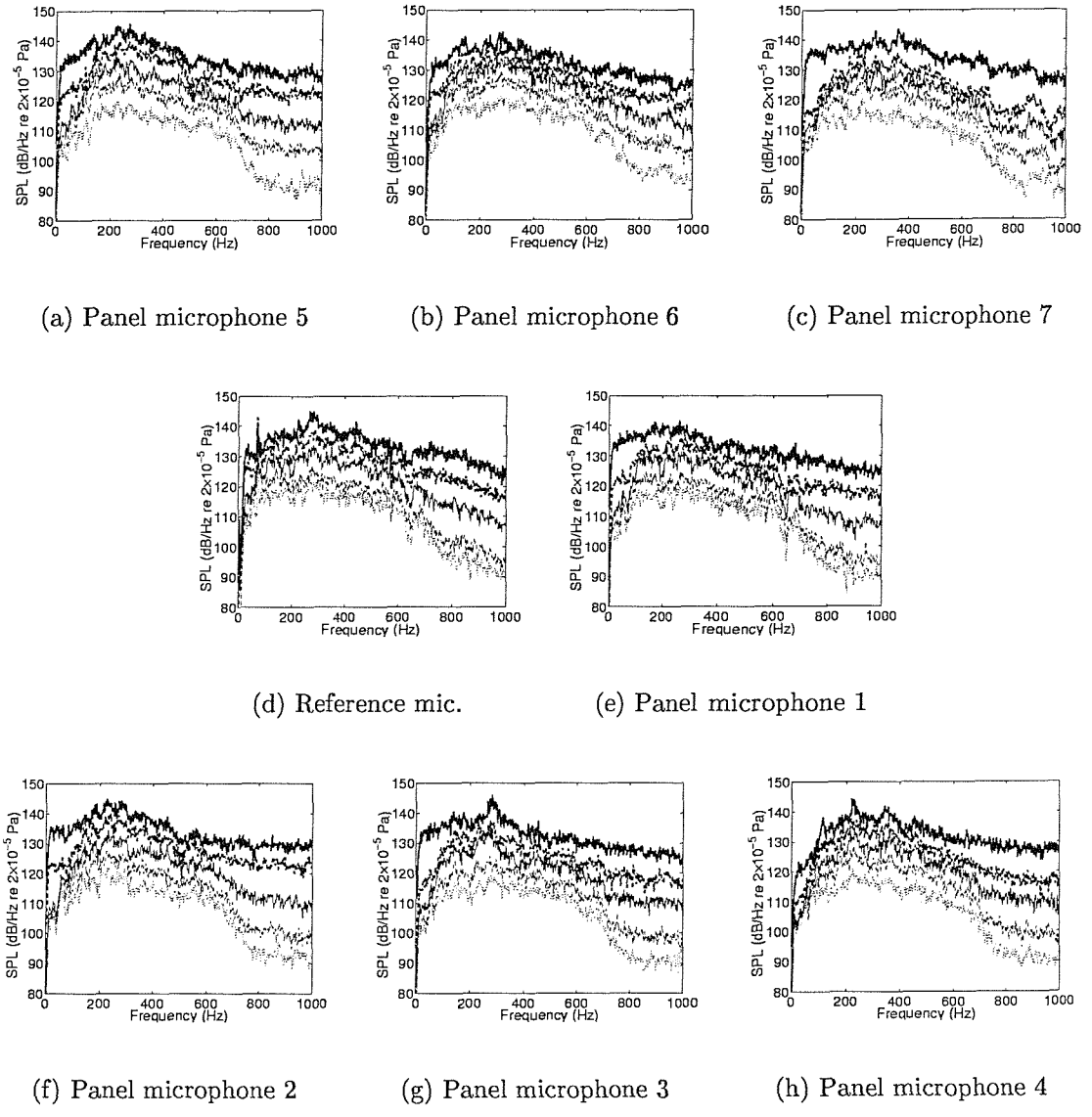

(a) Panel microphone 5 (b) Panel microphone 6 (c) Panel microphone 7

(d) Reference mic. (e) Panel microphone 1

(f) Panel microphone 2 (g) Panel microphone 3 (h) Panel microphone 4

Figure 5.3: Sound pressure level spectrum for each of the seven panel microphones and the reference microphone (OASPL ··· 140 dB, - - 145 dB, – 150 dB, - - 155 dB, - 160 dB).

[1]It is important to note that this was not closed-loop control. The spectrum shape was adjusted during a set of initial runs to give the required shape in the test aperture, and was left at this setting for the remainder of the tests.

facility exhibits a certain degree of non-linearity caused by distortion in the response of the siren to low frequency components in the driving signal. This means that the spectral characteristics of the drive signal will not necessarily correlate with the response measured at the aperture. For this reason, several test runs were carried out in order to obtain the flattest response spectrum over the 60 to 600 Hz frequency range.

OASPL (dB)	*Test Number/Panel microphone position*													
	1		**2**		**3**		**4**		**5**		**6**		**7**	
	Measured Overall Sound Pressure Level (dB)													
	Ref.	Panel	Ref.	Panel	Ref.	Panel	Ref.	Panel	Ref.	Panel	Ref.	Panel	Ref.	Panel
140	144.9	142.9	145.1	143.7	144.5	141.8	145.6	142.2	144.9	142.3	144.5	144.7	143.9	141.4
145	149.8	147.5	150.2	149.1	149.8	147.3	151.4	149.0	150.4	150.1	152.1	151.2	151.5	148.9
150	155.8	154.2	155.5	154.9	156.6	154.2	155.9	154.5	156.1	155.7	155.9	156.4	155.6	153.8
155	160.8	158.4	160.9	161.2	161.4	158.1	160.6	159.1	161.2	161.7	161.4	159.9	159.9	157.6
160	165.9	164.4	165.3	166.7	165.8	164.9	165.7	164.7	166.1	167.1	164.8	164.8	166.7	165.9

Table 5.1: Spatial variation of measured overall sound pressure level in the PWT aperture.

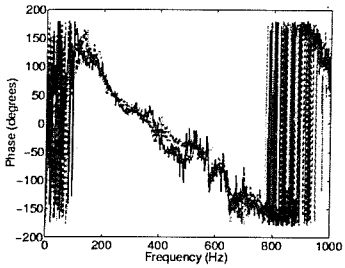

(a) Panel microphone 5

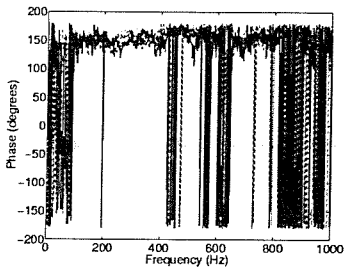

(b) Panel microphone 6

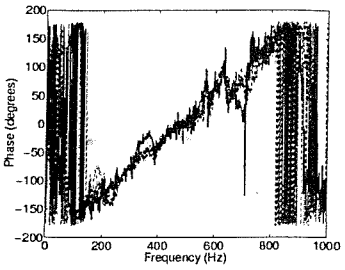

(c) Panel microphone 7

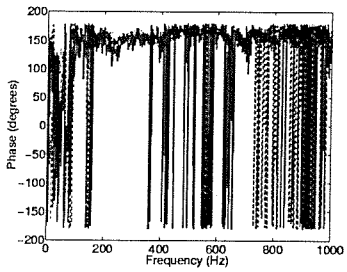

(d) Panel microphone 1

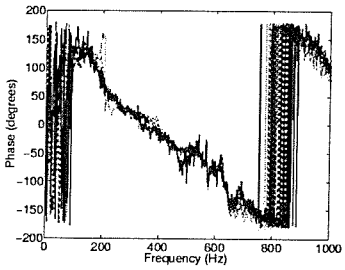

(e) Panel microphone 2

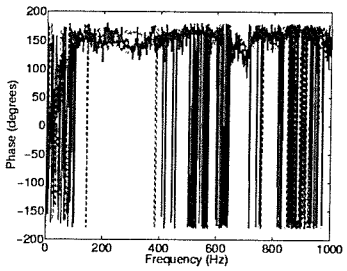

(f) Panel microphone 3

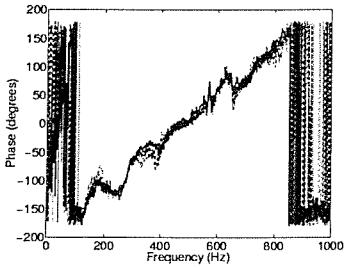

(g) Panel microphone 4

Figure 5.4: Phase relationship between each of the seven panel microphones and the reference microphone (OASPL ··· 140 dB, - - 145 dB, – 150 dB, - - 155 dB, - 160 dB).

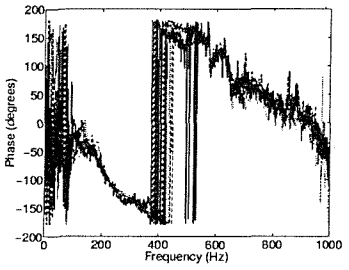

(a) Panel microphone 5

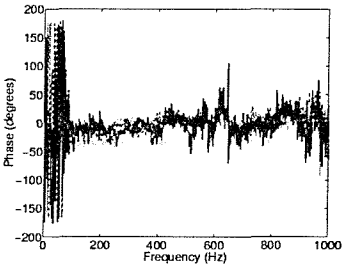

(b) Panel microphone 6

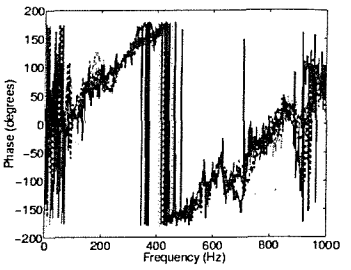

(c) Panel microphone 7

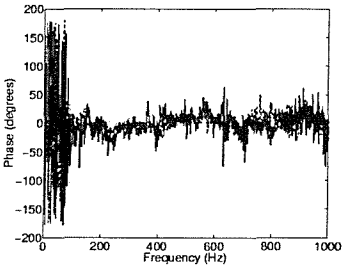

(d) Panel microphone 1

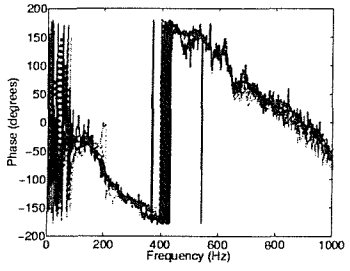

(e) Panel microphone 2

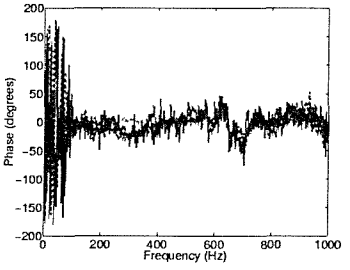

(f) Panel microphone 3

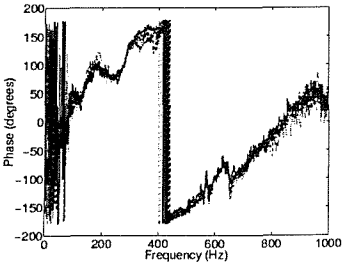

(g) Panel microphone 4

Figure 5.5: Corrected phase relationship between each of the seven panel microphones and the reference microphone (OASPL ··· 140 dB, - - 145 dB, – 150 dB, - - 155 dB, - 160 dB).

Figure 5.4 shows the relative phase between the reference microphone and the seven panel microphones, with the plots being arranged in such a way that they reflect the panel microphone position in the experiment. The phase was calculated using cross-spectral density analysis [71, 72] in MATLAB using the "spectrum" function. In figure 5.4 (d), which is the phase between panel microphone 1 and the reference microphone, there is a phase difference of approximately 160° between the two microphones. Assuming that these two microphones were coincident in space (although in a different plane), and assuming that there was no spatial lag across the width of the tunnel, then it can be concluded that the lag between the two microphones could be due to a mismatch between the microphones and measurement amplifiers (the two systems not being identical, unfortunately). This was not investigated in practice [70], which could have been done by positioning the microphones together and calculating the phase difference using the cross-spectral density method. In addition, if there were a phase lag between microphone 1 and the reference microphone, there would be a noticeable variation of phase with frequency, which was not apparent in figure 5.4, therefore the assumption of no phase lag across the width of the tunnel is reasonably valid. Figures 5.4(b) and (f) show that the phase is also relatively invariant along the height of the tunnel. Following these assumptions, the phase plots were corrected by subtracting 160° phase difference, and the result is shown in figure 5.5. The phase is relatively invariant at each section perpendicular to the axial direction of the PWT, shown by positions 2 and 5 at the downstream section, points 1, 3 and 6 at the middle section, and points 4 and 7 at the upstream section. However, each section has a different phase relative to the reference section. In addition, the phase at each section varies linearly with changing frequency for both the upstream and downstream section, whereas for the middle section, the phase is relatively invariant with changing frequency. The phase spectra relative to the reference microphone for panel microphones 5 and 7 are plotted together in figure 5.6. As can be seen, there is a frequency at which both microphones appear to be in phase relative to the reference microphone, which in this case is $\approx$ 428.5 Hz. The un-corrected phase plots have been used here since they illustrate this point more clearly. At this frequency, the wavelength should be equal to the distance between the two microphones, i.e. 0.8 m. Using the relationship between wavelength and frequency

$$c = \lambda f \tag{5.1}$$

where the wavespeed, c, is found to be equal to 342.8 m/s, which is approximately the

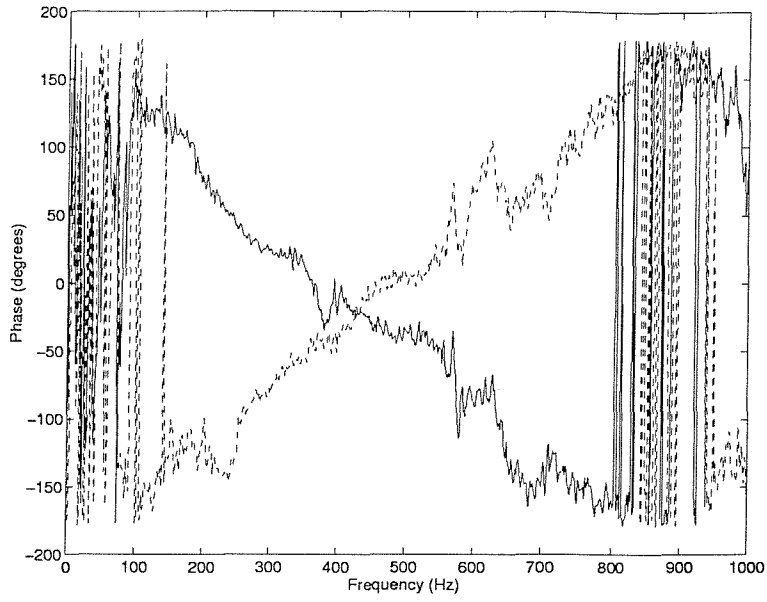

Figure 5.6: Phase spectra for panel microphones 5 (–) and 7 (- -) at 150 dB OASPL.

speed of sound in air. This fact, coupled with the linear relationship between phase and frequency indicates that the acoustic loading on the surface of a test structure which is mounted in the aperture of the PWT is caused by many sound waves travelling at the speed of sound in an axial direction across the aperture [70]. Although fairly obvious, this fact is very important since it suggests that for any theoretical predictions of the response of structures mounted in the PWT, the load should be treated as a travelling wave rather than an in-phase pressure load [70].

The level of coherence between the signals from the seven panel microphones and the reference microphone for all of the sound pressure levels is shown in figure 5.8. At low sound pressure levels, the coherence is fairly good in the 100 to 500 Hz frequency range. This is particularly true for the middle section of the PWT aperture. However, the coherence becomes very poor between the panel microphones and the reference microphone with increasing sound pressure level above 150 dB, with the most noticeable decrease in the level of coherence occurring at the higher frequencies.

A statistical analysis was carried out on the results and the probability density functions (pdf) were obtained for each of the seven tests for both the reference and panel microphone. In order to calculate the probability density function from the digitised time histories of pressure, an algorithm was written in MATLAB. The number of points falling within a band Δp, where p is the pressure, were counted, and the band was moved from the positive maximum value to the negative minimum value in

Δp steps (i.e., with no overlap). The probability density could then be calculated by considering the fraction of the total number of points which lie in the Δp band, as shown in figure 5.7 as dotted vertical lines [71],

$$p(x)dx = \frac{dn}{N} \tag{5.2}$$

where $p(x)$ is the probability density function of the random pressure signal $p(t)$. By normalising the result of equation 5.2 with respect to σ, the root mean square value, the pdf could be presented in its non-dimensional form. The main drawback with this method for estimating the statistics of a random signal is that the length of the sample and the spacing between the sampling points (determined by the original sampling frequency) must be such that the true characteristics of the random process are identified [71].

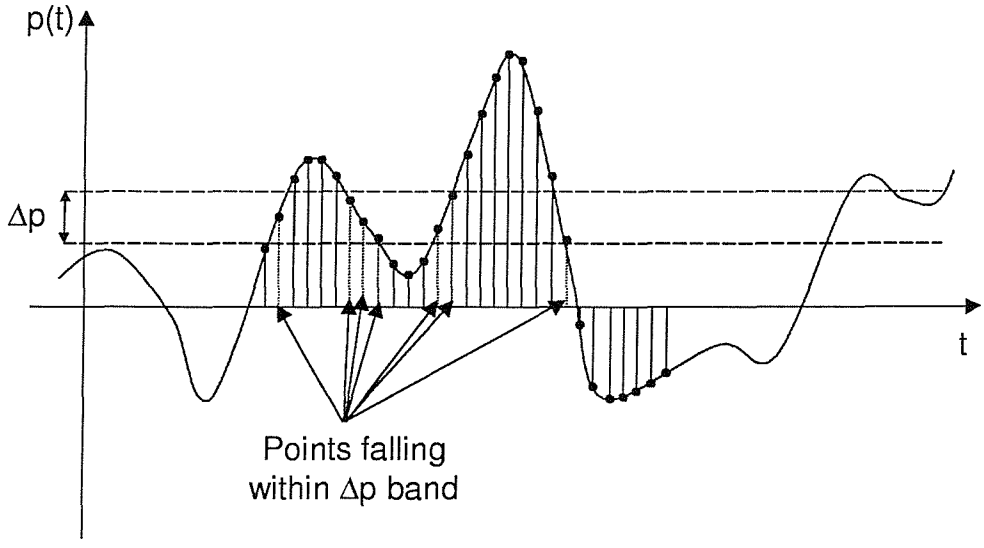

Figure 5.7: Estimating the probability density function of a digitised random process.

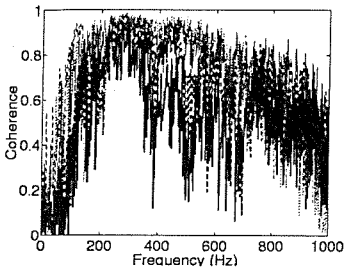

(a) Panel microphone 5

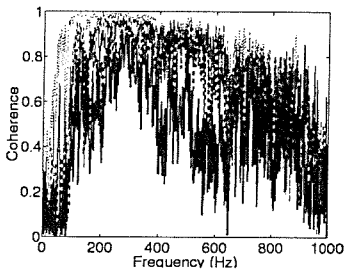

(b) Panel microphone 6

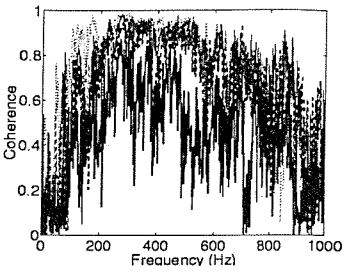

(c) Panel microphone 7

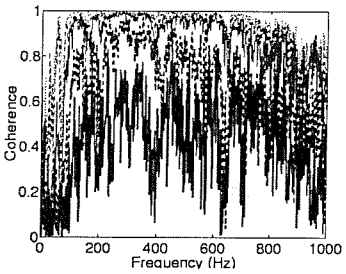

(d) Panel microphone 1

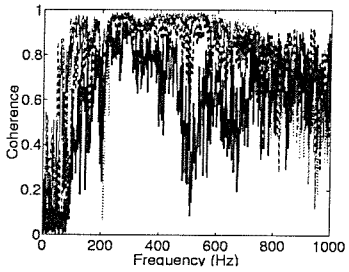

(e) Panel microphone 2

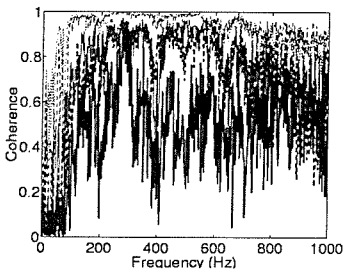

(f) Panel microphone 3

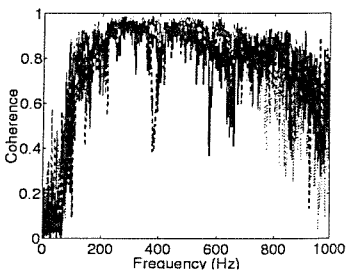

(g) Panel microphone 4

Figure 5.8: Level of coherence between each of the seven panel microphones and the reference microphone (OASPL ··· 140 dB, - - 145 dB, – 150 dB, - - 155 dB, - 160 dB).

In addition to the probability density function, mean, and root mean square values, higher moments of the random response were calculated in order to give some useful information about the pdf of the process. The third moment about the mean is termed the *skewness* and is given by the expression

$$\gamma_1 = \frac{E[(X - \mu_x)^3]}{\sigma_x^3} \tag{5.3}$$

where X is the random variable (i.e. $p(t)$ in the case of the measured random pressure time history), μ_x is the mean of the random time history, and σ_x is the standard deviation of the random time history. The skewness gives a measure of the departure from symmetry, and for a Gaussian distribution, $\gamma_1 = 0$. The fourth moment about the mean is termed the *kurtosis*, which gives a measure of the degree of flattening of the pdf. The kurtosis is given by the expression

$$\gamma_2 = \frac{E[(X - \mu_x)^4]}{\sigma_x^4} \tag{5.4}$$

For a Gaussian distribution, $\gamma_2 = 3$. A kurtosis value greater than 3 is indicative of a peaky distribution, whereas a value lower than three means that the distribution is more flattened than Gaussian. By monitoring the third and fourth moments of random response data it is possible to identify any non-linear behaviour, since non-linear systems are said to exhibit non-Gaussian responses [73].

Table 5.2 shows the results from the statistical analysis of the data. For each of the seven tests, the mean value, μ (Nm^{-2}), root mean square, σ (Nm^{-2}), skewness, γ_1, and kurtosis, γ_2, are given for both the reference and panel microphone at each OASPL. For all of the tests, and for both microphones, departure from Gaussianity was more evident in the kurtosis values than for the skewness values. In addition, the degree of non-Gaussian behaviour was not linked to increasing OASPL, and the majority of the data recorded from the PWT showed a peaky response distribution rather than a flattened distribution. It is interesting to note that the higher kurtosis values were associated with the lower OASPL's, when one would have expected the kurtosis values to be closer to three at the lower levels, with a greater departure from three at the higher levels, perhaps due to nonlinearity in the siren and nonlinear acoustic effects in the "throat" of the horn. However, at the 140 dB level, the sound is dominated by the airflow through the tunnel from the compressed air tanks, which could be the reason for the non-Gaussian behaviour. The probability density function plots for tests 1 to 7 are shown in figure 5.9 for the reference and panel microphones.

In relation to the tests carried out with the doubly curved panels located in the PWT, the information presented in this section and the statistical properties presented in table 5.2 all give a fair estimate of the spatial characteristics of the PWT, which can later be used as a guide when predicting the response. The spatial characteristics of the pressure loading are the most difficult to estimate in practice, particularly for response prediction purposes, therefore it is beneficial to the designer if these can be estimated for the practical case before prediction strategies are employed. However, it must be noted that the tests conducted here only give an approximate estimate of the characteristics of the PWT, and it must be borne in mind that these characteristics will be slightly different when the doubly curved panels are located in the aperture due to the geometry of the panels, the stiffness of the mounting and the properties of the doubly curved panels compared to the plywood board.

OASPL (dB)	*Test number/Panel microphone position*														Statistical Parameter
	1		**2**		**3**		**4**		**5**		**6**		**7**		
	Ref.	Panel	Ref.	Panel	Ref.	Panel	Ref.	Panel	Ref.	Panel	Ref.	Panel	Ref.	Panel	
140	-1.33	-1.49	-1.22	-1.88	-1.46	-2.02	-1.57	-1.83	-1.09	-1.76	-1.01	-1.51	-1.29	-1.96	μ (Pa)
	351.40	280.71	358.16	304.68	334.06	246.64	381.38	258.43	354.58	260.28	336.89	342.15	313.22	236.01	σ (Pa)
	-0.03	0.11	0.05	-0.001	-0.02	0.03	0.09	0.08	0.03	0.04	-0.08	0.14	0.01	-0.04	γ_1
	4.46	4.38	4.20	5.33	3.96	4.23	3.61	4.11	4.69	4.61	4.63	4.96	3.56	4.31	γ_2
145	-3.03	-4.95	-4.80	-6.15	-4.62	-6.28	-3.19	-5.73	-2.65	-5.69	-3.67	-4.92	-4.91	-5.72	μ (Pa)
	615.39	473.98	649.62	573.09	615.19	461.34	745.30	566.04	660.08	640.23	809.65	723.14	748.35	556.53	σ (Pa)
	-0.17	0.17	0.08	-0.02	0.02	0.01	-0.10	0.07	0.08	0.03	0.08	-0.01	0.01	0.02	γ_1
	5.57	5.04	4.23	4.30	4.08	4.19	4.05	3.68	5.32	4.43	4.19	4.29	3.73	4.57	γ_2
150	-3.66	-5.28	-4.75	-6.51	-2.43	-6.40	-3.94	-5.61	-3.78	-6.47	-5.13	-5.05	-5.12	-6.13	μ (Pa)
	1234.0	1024.8	1197.0	1111.9	1352.2	1029.4	1250.5	1067.4	1281.7	1232.4	1247.4	1314.0	1215.4	981.45	σ (Pa)
	0.07	0.19	0.19	-0.01	0.11	0.11	0.17	0.05	0.14	0.04	0.2	-0.001	0.07	0.05	γ_1
	4.01	3.77	4.06	4.39	3.51	3.72	3.72	3.36	4.14	3.77	3.77	3.86	3.53	3.97	γ_2
155	-12.76	-4.72	-16.43	-19.07	-13.87	-20.00	-11.37	-17.63	-11.23	-19.50	-11.68	-15.29	-14.96	-18.64	μ (Pa)
	2202.4	1672.0	2231.2	2288.3	2347.4	1603.1	2139.4	1812.9	2299.0	2449.9	2355.2	1983.9	1992.8	1524.4	σ (Pa)
	0.31	0.06	0.41	-0.12	0.23	0.15	0.28	0.03	0.39	-0.05	0.38	0.16	0.26	-0.03	γ_1
	4.08	3.70	3.40	3.84	3.46	3.48	3.78	3.37	3.85	3.20	3.68	3.47	3.71	3.44	γ_2
160	-13.08	-16.87	-12.42	-17.92	-7.97	-21.68	-13.18	-19.03	-9.48	-17.73	-4.94	-15.28	-15.20	-19.56	μ (Pa)
	3973.9	3336.2	3688.1	4312.7	3908.0	3543.8	3888.1	3424.9	4026.4	4534.1	3482.9	3491.5	4311.1	3948.3	σ (Pa)
	0.47	-0.08	0.42	-0.41	0.37	-0.09	0.39	-0.05	0.43	-0.02	0.39	0.004	0.49	0.20	γ_1
	3.41	3.75	3.09	3.81	3.16	4.29	3.31	2.90	3.29	2.71	3.28	3.54	3.32	3.93	γ_2

Table 5.2: Statistical parameters for the seven panel microphones and reference microphone used in the spatial variation tests.

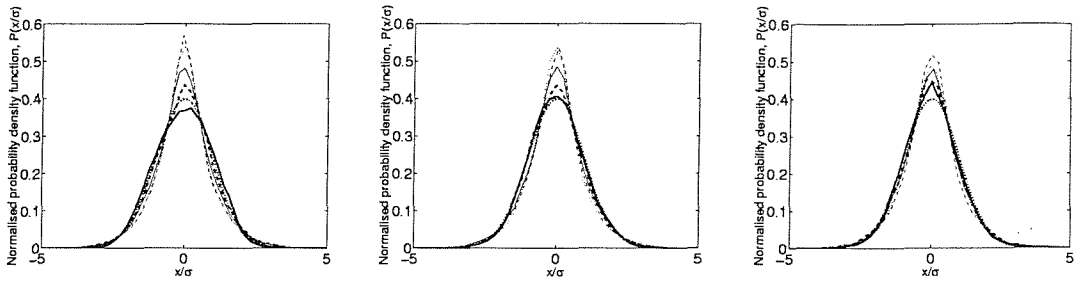

(a) Panel microphone 5 (b) Panel microphone 6 (c) Panel microphone 7

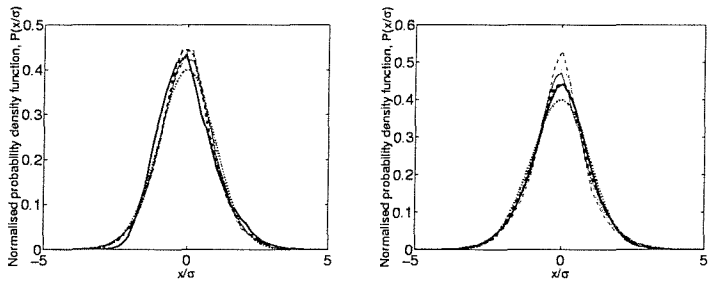

(d) Reference microphone (e) Panel microphone 1

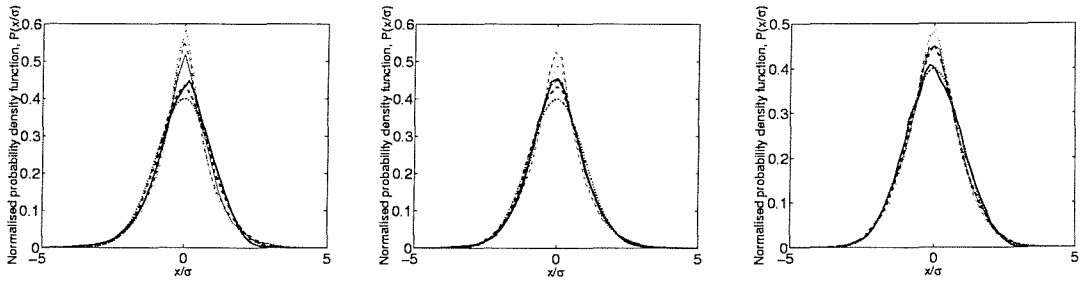

(f) Panel microphone 2 (g) Panel microphone 3 (h) Panel microphone 4

Figure 5.9: Probability density function for each of the seven panel microphones and the reference microphone (··· Gaussian, OASPL ··· 140 dB, - - 145 dB, – 150 dB, - - 155 dB, - 160 dB).

5.3 Experimental set-up

The experimental set-up is shown in figure 5.10. A B&K Type 1402 random signal generator was used to supply the drive signal, which was attenuated outside the 60 Hz to 600 Hz range using a B&K Type 5612 spectrum shaper. The signal from the shaper was amplified using a B&K Type 2608 measuring amplifier before being supplied to the LDS PA 500L power amplifier in order to give the required range to drive the WAS 3000 at the high sound pressure levels. The OASPL in the test section was monitored using a B&K Type 4136 condenser microphone coupled to a B&K Type 2609 measuring amplifier with the appropriate scale fitted.

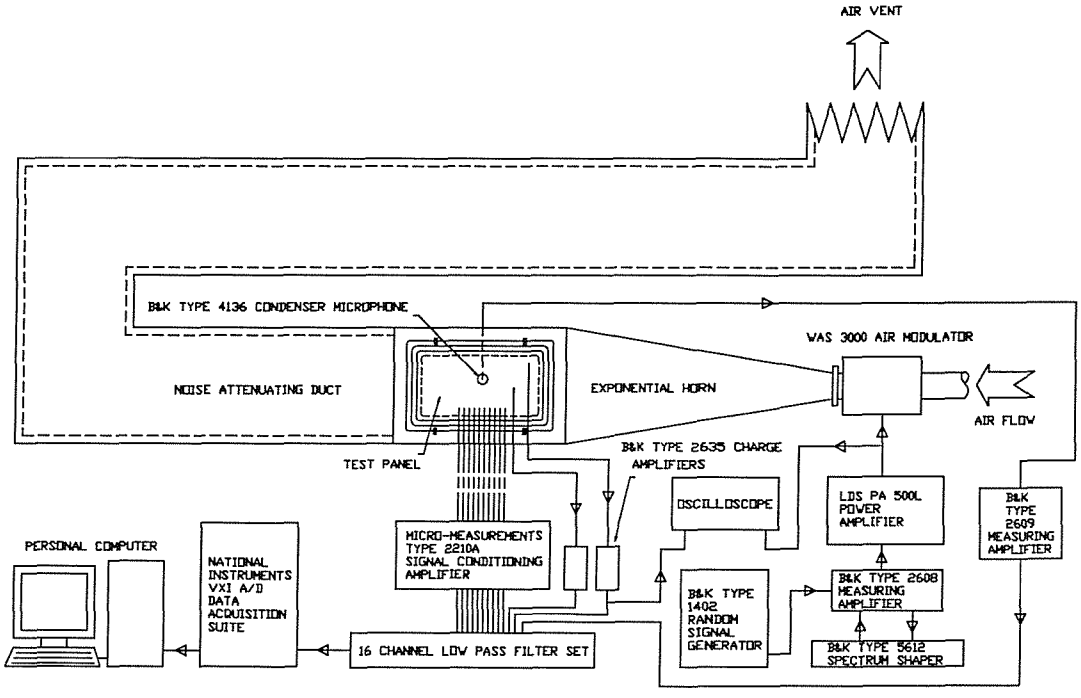

Figure 5.10: Experimental set-up of the panels in the PWT facility.

A Measurements Group model 2200 signal conditioning amplifier was used to calibrate and amplify the signals from the strain gauges, which were filtered at 1 kHz using a 16 channel low pass filter set. The signals were then digitally sampled using a National Instruments VXI data acquisition system coupled to a personal computer. In addition to the strain gauges, two B&K Type 4344 accelerometers were used to measure the dynamic response of the panels. The signals from the accelerometers were amplified using B&K Type 2635 charge amplifiers before being filtered and digitally sampled.

5.3.1 Panel attachment in the PWT aperture

The design and manufacture of a suitable test fixture for the doubly curved panels was a very difficult task when one considers the geometry and stiffness of the panel itself, and the need to accurately model the panels in the PWT using the finite element method. One of the main objectives of the work here was to predict the response of the test panels to random acoustic excitation and compare this with experimental results obtained from the PWT tests. It was important that the highest possible strain was achieved in order that potential non-linear effects could be investigated. In addition, the panels and associated boundary conditions in the PWT needed to be modelled as accurately as possible so that a representative comparison between test and theory could be made. Initial test fixture designs centred around moulding a

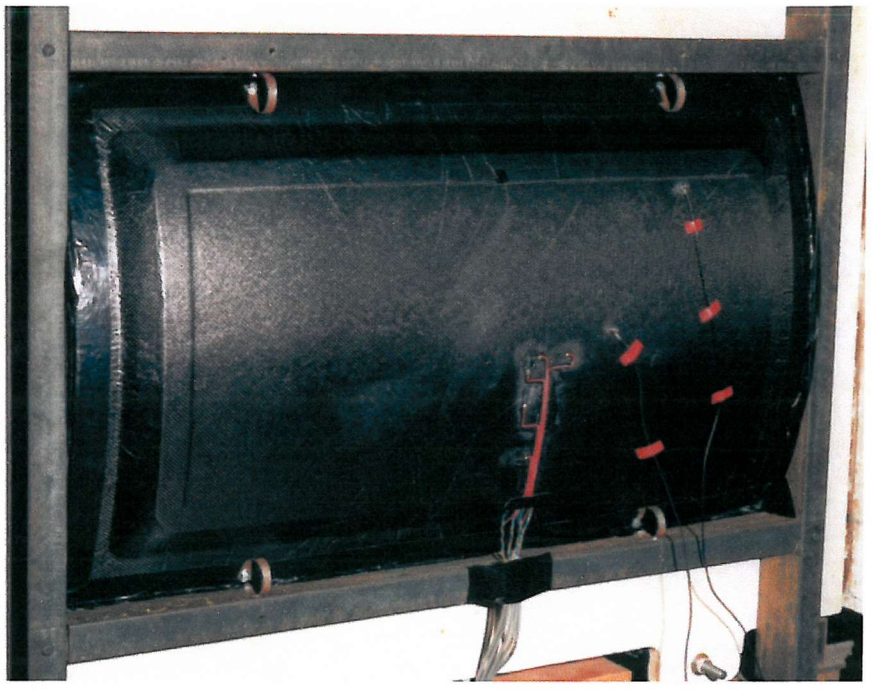

Figure 5.11: Panel 3 secured in the PWT aperture using four circular steel springs.

glass fibre/epoxy "picture" frame. The problem with this approach was two-fold. This type of test fixture would introduce extra stiffness which would result in a very low level strain response, and an increase in the predominant response frequency which could be outside the broad-band frequency limits of the PWT facility (80 to 800 Hz). Secondly, the best way to manufacture this fixture would be to use the panel as a mould and use the wet lay-up method. However, this method would produce a fixture with variable thickness and poor quality consolidation.

To this end, each panel was secured in the test aperture of the PWT using four circular steel springs, as shown in figure 5.11. The circular springs introduce very little extra stiffness to the panel, thus allowing the highest possible strain to be achieved. In addition, the natural frequencies of vibration and the associated modes were very close to that of the freely supported test panel, which was verified using a finite element model of the configuration and comparing this with the experimental results for the freely supported test panels, as shown in table 5.3. Note that details of the FE models used to obtain the ANSYS results in this table are given in chapter 6, and an example of one of these models (including the spring supports) is shown in figure 7.2.

5.3.2 Strain gauge locations

Single element gauges and tee-rosette gauges, each with a gauge length of 6mm and 5mm respectively, a nominal resistance of $120\Omega \pm 0.5$, and a gauge factor of 2.1, were used to measure the dynamic response of the test panels. All of the gauges were wired into quarter bridge circuits, which were incorporated in the Measurements Group 2200 signal conditioning amplifier. Since long leads were used from the strain gauges to the measuring amplifier situated in the control room, three wire connection was used to eliminate dc offset and balancing problems. For the spring-supported test panels, the gauges were located on the inner and outer face (concave and convex face respectively) of the test panels at the locations shown in figure 5.12. In addition to measuring the direct strain in the face plates, the gauges were arranged in such a way that the core shear strain could be estimated in both the x-wise (long side) and y-wise (short side) directions using the method covered in chapter 3. It was for this reason that the gauges were located slightly off-centre in one quadrant of each panel, away from the core shear strain nodal line, as shown in figure 5.12.

5.3.3 Calibration procedure

Before commencing testing in the PWT, the reference microphone was calibrated using a B&K Type 4220 pistonphone. This is essentially a device which is designed for the absolute calibration of precision sound measuring systems. The pistonphone produces a pure tone of 250 Hz, with an RMS sound pressure level of 124 dB (re 2×10^{-5} Pa), by the reciprocating action of two symmetrically mounted pistons with a floating spring arrangement [74]. The unit totally encloses the microphone during calibration, which allows correct calibration in noisy environments. The B&K Type 2609 measuring amplifier was fitted with a SA179 scale, suitable for use with the

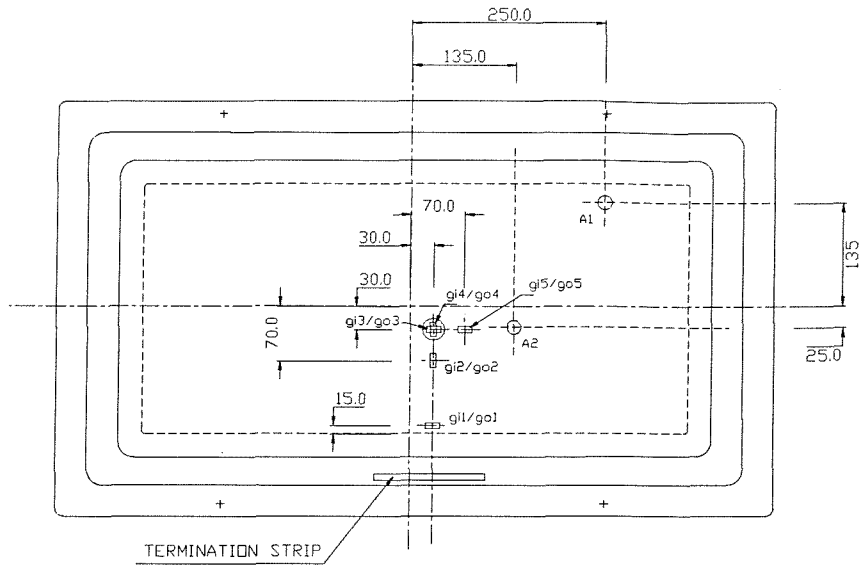

Figure 5.12: Strain gauge and accelerometer locations.

4136 microphone, which has an open circuit sensitivity of 1.24 mV/Pa. Calibration was carried out by setting the appropriate ranges on the measuring amplifier [75] and adjusting the sensitivity potentiometer to read 124 dB. The pistonphone was then removed, and the sensitivity of the sound measurement system, including the microphone pre-amplifier, was checked by selecting the internal reference voltage (50 mV RMS) and recording the level from the measuring amplifier. The overall sensitivity was found to be 0.764 mV/Pa. This was compared with the calculated sensitivity, S_{MP}, using the formula [76]

$$S_{MP} = S_{oc} + g + 20log_{10}\left(\frac{C_M}{C_P + C_M}\right) \tag{5.5}$$

where: S_{oc} = open circuit sensitivity of microphone
= 0.765 mV/Pa (-58.1 dB re 1 V/Pa),
g = gain of pre-amplifier (B&K Type 2615 + UA0035) = -0.8 dB,
C_M = microphone cartridge capacitance = 6.2 pF,
C_P = input capacitance of pre-amplifier = 3 pF.

Substituting these values into equation 5.5, an overall sensitivity of 0.7649 mV/Pa is obtained, which compares very well with the measured sensitivity.

Measured (Free) (Hz)	Measured (PWT) (Hz)	ANSYS Results (Chamfered edge Model with spring supports) (Hz)
Panel 1		
136.0	-	141.14
214.6	210.5	219.02
282.6	-	282.61
352.1	353.9	357.93
-	-	373.01
-	-	435.60
-	465.9	459.17
-	503.2	528.85
Panel 2		
131.5	-	136.49
164.7	163.1	164.30
269.0	-	267.28
343.1	330.8	338.22
-	403.7	410.64
-	431.3	414.55
-	-	453.37
-	493.5	524.14
Panel 3		
130.9	-	137.65
264.5	258.9	272.62
280.9	-	300.31
320.4	320.7	335.08
-	-	360.45
-	436.9	473.92
-	-	491.52
-	554.4	541.45
Panel 4		
74.65	-	82.39
233.2	-	251.13
279.3	269.6	288.67
312.4	315.2	319.28
-	387.7	349.19
-	-	433.72
-	-	457.89
-	497.1	522.78

Table 5.3: Comparison of measured (from the freely supported and PWT tests) and predicted resonance/natural frequencies of the four test panels.

5.4 Testing procedure

Testing was carried out at overall sound pressure levels from 140 to 160 dB in 5 dB steps. The driving signal to the WAS 3000 was attenuated outside the 60 Hz to 600 Hz frequency range using a B&K Type 5612 spectrum shaper [77] as previously mentioned. Five tests were carried out for each panel in order to assess the repeatability of the experiments.

Initial calibration of the strain gauges was carried out using the internal shunt circuit in the signal conditioning amplifier, which supplies a dummy strain of $1000\mu\epsilon$ across the bridge. An excitation voltage of 2V was used and the gauges were calibrated to give 2V output at $1000\mu\epsilon$. Before each test, the strain gauges were balanced.

During the operation of the PWT, the air pressure supply to the siren was kept constant at 15 psi for all OASPL's up to 160 dB, at which point the pressure was increased to 20 psi, which gave approximately an extra 2 dB needed to reach an indicated OASPL of 160 dB. The signals from the strain gauges, accelerometers, and microphone were digitally sampled using the National Instruments VXI acquisition suite coupled to a personal computer. A sampling frequency of 6000 Hz was used and 60000 samples were acquired giving 10 seconds of data per OASPL. The digital data were saved to disk, ready for post-processing in the MATLAB environment.

5.5 Experimental results

5.5.1 Statistics of the response

The statistical properties of the microphone, strain gauges, and accelerometer signals were evaluated from the digitised time histories, and the results for the four panels are shown in tables 5.4 to 5.7. For each of the four panels, and for each test, a very large mean strain signal was observed for all ten gauges. However, considerable variability in mean strain was observed between each test. Since the signals from the strain gauges were not filtered to remove any possible dc offset, it is possible that the large mean values were caused by either poor dc balancing, a static strain induced by the pressure on the inside face of the panels, considerable drift in the signals over time, or a non-linear panel response. The latter possibility can be ruled out since this was not observed during the tests, as can be seen from the statistics of the response in tables 5.4 to 5.7 and figures 5.13 to 5.16. An approximate assessment of the drift in the strain data was obtained by breaking the data into segments, calculating the mean for each segment, and plotting this value over the entire acquisition period, as shown

in figures 5.17 to 5.20. The drift in the strain signals for each gauge and across all four panel tests appears to be very slight (around 2–3$\mu\epsilon$), and in some cases non-existent. In addition, it should be noted that there were no trends either in the overall mean strain signal or the approximation of the drift in the signal for each panel and across all of the tests carried out. A comparison of the mean pressure signal between each panel test revealed a consistent mean value for each SPL setting, as can be seen from tables 5.4 to 5.7, and this was also consistent over all of the tests carried out. In order to assess whether a static strain was present during the tests, an FE model of each panel was analysed with a pressure load equal to the mean pressure measured in the tunnel, which was applied to the inner (concave) face of the panel. As expected, the computed static strain was negligible, as can be seen in table 5.8. This suggests, along with the fact that there was a considerable amount of variability in the measured mean strain results, that the large non-zero mean was not caused by a static strain in the faces of the test panels, but was instead due to poor dc balancing. Indeed, it was found that during the tests, the method of establishing whether each bridge was balanced by extinguishing a red/green light on the front of the signal conditioning amplifier was very difficult to gauge properly. In this case, a meter would have been much more effective.

OASPL (dB)	Mic. (Pa)	Acc.1 ($Nm^{-1}s^2$)	Acc.2 ($Nm^{-1}s^2$)	gi1 ($\mu\epsilon$)	gi2 ($\mu\epsilon$)	gi3 ($\mu\epsilon$)	gi4 ($\mu\epsilon$)	gi5 ($\mu\epsilon$)	go1 ($\mu\epsilon$)	go2 ($\mu\epsilon$)	go3 ($\mu\epsilon$)	go4 ($\mu\epsilon$)	go5 ($\mu\epsilon$)
	Mean												
143.29	-6.19	-0.0002	0.0003	5.45	2.28	14.18	17.80	8.46	0.91	13.59	10.39	5.57	5.14
149.97	-5.96	-0.0003	0.0003	0.42	-0.20	14.24	16.40	4.95	6.09	18.70	16.88	12.83	11.72
154.75	-5.91	-0.0002	0.0003	-5.42	-4.64	10.31	10.62	-1.01	4.71	15.68	13.39	9.63	10.48
159.28	-6.02	-0.0002	0.0005	-7.66	-5.72	9.28	9.25	-2.37	4.45	14.28	12.51	9.15	10.05
163.71	-5.95	-0.0002	0.0003	-3.14	2.06	16.32	14.09	3.78	7.97	14.16	12.37	12.90	13.49
	Standard Deviation (zero mean)												
143.29	292.33	0.005	0.011	8.99	11.95	12.73	6.78	5.63	15.75	9.77	10.97	16.53	14.72
149.97	630.51	0.011	0.022	18.27	26.47	28.31	13.49	10.90	34.58	21.25	24.10	36.57	31.39
154.75	1092.30	0.020	0.038	31.94	46.77	50.11	22.36	18.88	61.36	37.40	42.42	64.65	55.23
159.28	1842.24	0.034	0.065	55.38	80.90	86.62	36.53	32.63	107.22	64.31	73.04	112.11	95.55
163.71	3066.80	0.062	0.115	99.81	145.58	154.84	66.77	59.67	196.01	113.75	128.39	203.04	173.13
	Skewness (zero mean)												
143.29	0.023	-0.010	0.003	-0.053	0.008	0.010	0.160	0.003	-0.005	-0.013	-0.025	0.004	0.009
149.97	0.044	0.032	0.020	-0.015	0.007	-0.003	0.290	-0.026	0.011	-0.035	-0.026	-0.003	-0.015
154.75	-0.048	0.054	0.062	-0.056	-0.001	-0.016	0.298	-0.048	0.003	-0.005	-0.007	-0.012	-0.010
159.28	-0.059	0.067	0.047	-0.113	0.020	-0.007	0.163	-0.106	0.021	-0.037	-0.032	0.004	0.005
163.71	-0.065	0.138	0.077	-0.211	0.045	0.003	-0.050	-0.231	0.045	-0.069	-0.050	-0.003	0.004
	Kurtosis (zero mean)												
143.29	6.21	3.44	3.40	3.36	3.45	3.48	3.67	3.17	3.46	3.44	3.43	3.50	3.45
149.97	5.02	3.29	3.37	3.38	3.39	3.40	3.46	3.36	3.44	3.38	3.38	3.43	3.42
154.75	3.88	3.21	3.26	3.02	3.07	3.06	3.15	3.07	3.03	3.05	3.04	3.05	3.05
159.28	3.42	3.23	3.31	2.98	2.99	3.00	3.14	3.02	2.96	2.99	2.99	2.98	2.99
163.71	2.71	3.11	3.07	3.22	3.22	3.20	3.35	3.26	3.17	3.20	3.18	3.20	3.20

Table 5.4: Statistical properties for panel 1 subject to random acoustic excitation in the PWT.

OASPL (dB)	Mic. (Pa)	Acc.1 ($Nm^{-1}s^2$)	Acc.2 ($Nm^{-1}s^2$)	gi1 ($\mu\epsilon$)	gi2 ($\mu\epsilon$)	gi3 ($\mu\epsilon$)	gi4 ($\mu\epsilon$)	gi5 ($\mu\epsilon$)	go1 ($\mu\epsilon$)	go2 ($\mu\epsilon$)	go3 ($\mu\epsilon$)	go4 ($\mu\epsilon$)	go5 ($\mu\epsilon$)
	Mean												
143.88	-7.20	-0.0004	0.0004	2.80	-4.59	-1.41	7.49	10.40	-0.25	8.58	-1.30	-6.35	-3.95
149.91	-6.96	-0.0004	0.0003	15.67	6.90	9.45	19.61	22.28	-2.36	5.31	-5.78	-9.73	-5.93
154.92	-6.95	-0.0004	0.0003	25.22	14.86	17.30	28.85	31.37	-2.53	4.52	-6.04	-9.76	-5.87
159.00	-6.90	-0.0004	0.0003	34.19	22.65	24.82	37.03	39.33	-2.05	4.44	-5.51	-8.35	-4.73
163.09	-7.12	-0.0004	0.0003	49.81	35.02	37.02	52.63	54.80	-2.25	4.89	-4.12	-7.10	-3.90
	Standard Deviation (zero mean)												
143.88	313.01	0.005	0.007	7.44	8.49	8.02	6.63	7.02	10.21	7.27	6.25	9.06	9.29
149.91	625.59	0.011	0.014	13.11	16.87	15.88	12.77	13.34	20.46	14.29	12.27	17.92	16.94
154.92	1114.26	0.022	0.027	20.73	27.27	25.64	20.60	21.59	33.09	23.29	20.18	28.71	26.70
159.00	1783.04	0.039	0.049	35.27	46.85	44.02	35.37	37.11	57.13	40.60	35.26	49.47	45.72
163.09	2857.02	0.067	0.082	59.50	78.95	74.15	59.63	62.14	96.65	69.03	60.26	83.62	76.81
	Skewness (zero mean)												
143.88	-0.029	0.031	-0.006	-0.058	-0.002	-0.001	0.023	0.028	-0.012	-0.006	-0.004	-0.009	0.031
149.91	-0.113	0.100	-0.012	-0.035	0.011	0.005	-0.010	-0.046	0.018	0.018	0.028	0.013	0.035
154.92	-0.147	0.077	-0.025	-0.013	-0.017	-0.019	0.005	0.017	-0.006	0.034	0.045	0.003	-0.004
159.00	-0.127	0.061	-0.036	-0.051	0.037	0.034	-0.043	-0.073	0.040	-0.009	0.004	0.031	0.050
163.09	-0.221	0.009	-0.035	-0.032	-0.011	-0.015	-0.034	-0.022	0.003	0.013	0.025	0.000	-0.016
	Kurtosis (zero mean)												
143.88	5.31	3.58	3.40	3.14	3.26	3.23	3.18	3.13	3.24	3.23	3.21	3.19	3.17
149.91	4.41	3.40	3.24	3.11	3.12	3.11	3.14	3.14	3.12	3.15	3.16	3.13	3.15
154.92	3.76	3.24	3.23	3.02	3.01	3.01	3.02	3.06	3.00	3.05	3.08	2.96	2.98
159.00	3.35	3.17	3.24	3.18	3.19	3.19	3.17	3.12	3.20	3.17	3.16	3.21	3.18
163.09	3.10	3.07	3.20	3.21	3.24	3.24	3.22	3.20	3.24	3.23	3.22	3.26	3.24

Table 5.5: Statistical properties for panel 2 subject to random acoustic excitation in the PWT.

OASPL (dB)	Mic. (Pa)	Acc.1 ($Nm^{-1}s^2$)	Acc.2 ($Nm^{-1}s^2$)	gi1 ($\mu\epsilon$)	gi2 ($\mu\epsilon$)	gi3 ($\mu\epsilon$)	gi4 ($\mu\epsilon$)	gi5 ($\mu\epsilon$)	go1 ($\mu\epsilon$)	go2 ($\mu\epsilon$)	go3 ($\mu\epsilon$)	go4 ($\mu\epsilon$)	go5 ($\mu\epsilon$)
	Mean												
143.51	-6.92	-0.0004	0.0003	-1.85	-2.52	5.63	8.71	6.84	6.84	6.57	13.24	3.02	-2.87
149.93	-6.91	-0.0004	0.0003	9.33	7.08	15.13	20.00	18.61	11.36	10.22	16.01	5.48	-3.80
154.18	-6.73	-0.0003	0.0003	17.52	13.79	21.66	27.84	26.99	12.13	11.48	17.80	6.80	-3.48
158.84	-6.73	-0.0003	0.0003	24.45	19.82	27.36	34.81	34.26	12.84	14.01	21.18	9.65	-1.32
162.82	-6.25	-0.0003	0.0002	35.49	29.09	35.80	46.26	46.77	14.31	17.32	26.01	12.80	0.46
	Standard Deviation (zero mean)												
143.51	299.76	0.004	0.015	5.06	11.25	11.76	4.57	4.72	8.74	9.95	10.51	10.64	10.51
149.93	627.57	0.009	0.031	8.01	23.74	24.92	9.00	8.80	18.51	21.28	22.66	22.29	20.89
154.18	1023.49	0.016	0.049	12.55	41.13	43.19	14.41	14.02	31.44	36.54	39.23	36.00	33.57
158.84	1751.63	0.028	0.084	21.02	70.72	74.10	24.08	23.67	54.97	61.85	66.87	61.72	56.87
162.82	2768.33	0.047	0.134	34.68	121.65	126.48	38.42	37.78	92.83	103.62	112.50	100.67	92.00
	Skewness (zero mean)												
143.51	-0.103	0.031	0.010	-0.054	-0.024	-0.031	0.048	0.052	0.020	0.050	0.055	0.008	0.024
149.93	-0.092	0.030	0.015	-0.046	-0.012	-0.017	0.029	0.034	-0.008	0.042	0.045	-0.020	-0.010
154.18	-0.074	0.080	0.012	-0.017	0.004	0.000	0.004	0.016	0.005	0.020	0.016	0.002	0.009
158.84	-0.111	0.079	0.019	-0.054	-0.019	-0.029	0.042	0.065	-0.014	0.050	0.054	-0.026	-0.018
162.82	-0.161	0.037	0.031	-0.070	-0.018	-0.025	0.031	0.057	-0.013	0.034	0.040	0.004	0.008
	Kurtosis (zero mean)												
143.51	6.06	3.95	3.67	3.24	3.48	3.50	3.45	3.23	3.40	3.55	3.58	3.48	3.32
149.93	4.71	3.52	3.34	3.11	3.18	3.19	3.35	3.30	3.04	3.21	3.22	3.25	3.23
154.18	4.09	3.32	3.29	3.05	3.10	3.11	3.20	3.19	3.11	3.12	3.14	3.12	3.11
158.84	3.48	3.16	3.18	3.03	3.10	3.11	3.12	3.14	3.04	3.11	3.13	3.07	3.05
162.82	3.05	3.04	2.97	2.90	2.88	2.88	2.99	2.99	2.85	2.89	2.89	2.96	2.95

Table 5.6: Statistical properties for panel 3 subject to random acoustic excitation in the PWT.

OASPL (dB)	Mic. (Pa)	Acc.1 ($Nm^{-1}s^2$)	Acc.2 ($Nm^{-1}s^2$)	gi1 ($\mu\epsilon$)	gi2 ($\mu\epsilon$)	gi3 ($\mu\epsilon$)	gi4 ($\mu\epsilon$)	gi5 ($\mu\epsilon$)	go1 ($\mu\epsilon$)	go2 ($\mu\epsilon$)	go3 ($\mu\epsilon$)	go4 ($\mu\epsilon$)	go5 ($\mu\epsilon$)
	Mean												
143.20	-7.46	-0.0004	0.0003	9.87	6.86	8.58	12.90	15.74	-2.11	-1.12	-8.91	-6.75	-3.77
149.49	-7.34	-0.0004	0.0003	18.45	14.61	15.47	20.99	24.71	-3.53	-2.59	-11.68	-9.84	-5.92
154.69	-7.64	-0.0004	0.0003	24.27	20.46	20.46	26.91	30.97	-4.05	-2.91	-12.28	-10.80	-6.62
159.49	-7.66	-0.0004	0.0003	32.14	27.90	26.90	34.15	39.31	-3.50	-2.62	-12.00	-10.73	-6.28
163.71	-7.44	-0.0004	0.0003	45.20	41.07	39.07	50.54	57.45	-3.86	-2.37	-11.30	-10.70	-6.00
	Standard Deviation (zero mean)												
143.20	289.34	0.004	0.014	5.91	15.17	18.15	4.11	4.86	5.76	7.28	7.47	9.91	10.13
149.49	596.34	0.009	0.032	10.70	36.11	43.36	8.54	9.83	12.58	16.42	17.09	21.36	20.43
154.69	1085.57	0.018	0.057	19.31	70.07	83.84	15.62	18.65	24.16	30.73	32.22	38.10	35.90
159.49	1887.95	0.034	0.102	35.73	134.35	158.96	28.37	35.29	46.13	56.52	59.39	65.95	62.24
163.71	3069.39	0.058	0.163	57.99	218.45	255.68	45.48	56.74	75.09	90.54	95.36	102.92	97.08
	Skewness (zero mean)												
143.20	-0.087	-0.022	0.045	-0.031	0.059	0.029	0.056	0.072	0.000	-0.023	-0.017	0.004	-0.009
149.49	-0.098	0.014	0.106	0.002	0.035	-0.008	-0.036	0.038	-0.001	0.017	0.019	0.009	0.009
154.69	-0.037	0.031	0.117	-0.017	0.055	-0.002	-0.031	0.014	-0.012	-0.007	-0.004	-0.003	-0.017
159.49	-0.046	0.009	0.111	-0.053	0.041	-0.011	-0.020	0.000	0.023	-0.005	-0.009	-0.005	-0.016
163.71	-0.078	-0.001	0.111	-0.033	0.033	-0.001	-0.021	-0.020	0.005	-0.035	-0.031	-0.022	-0.028
	Kurtosis (zero mean)												
143.20	4.76	3.63	3.54	3.20	3.40	3.35	3.25	3.00	3.21	3.35	3.37	3.39	3.32
149.49	4.40	3.33	3.42	3.17	3.24	3.21	3.32	3.22	3.20	3.25	3.23	3.14	3.14
154.69	3.71	3.28	3.28	3.10	3.11	3.09	3.12	3.06	3.10	3.12	3.12	3.05	3.05
159.49	3.16	3.10	3.13	2.93	2.87	2.89	2.95	2.89	2.94	2.92	2.92	2.92	2.92
163.71	2.94	3.05	3.16	3.07	3.02	3.04	2.98	2.97	3.01	3.05	3.05	2.98	3.00

Table 5.7: Statistical properties for panel 4 subject to random acoustic excitation in the PWT.

Panel	Mean static	Calculated strain - inner ($\mu\epsilon$)				
	pressure (Pa)	gi1	gi2	gi3	gi4	gi5
1	-6.00	0.013	0.112	0.136	-0.048	-0.061
2	-7.03	-0.021	0.080	0.097	-0.115	-0.130
3	-6.71	0.010	0.128	0.155	-0.018	-0.028
4	-7.51	0.025	0.124	0.151	-0.103	-0.099
		Calculated strain - outer ($\mu\epsilon$)				
		go1	go2	go3	go4	go5
1	-6.00	-0.032	-0.160	-0.170	0.010	0.015
2	-7.03	-0.041	-0.068	-0.079	-0.018	-0.0045
3	-6.71	-0.040	-0.174	-0.197	0.033	0.034
4	-7.51	-0.032	-0.084	-0.093	0.046	0.041

Table 5.8: Finite element estimation of the static strain produced by a mean static pressure measured during the PWT tests.

Higher moments of the pressure loading and random response were calculated and are again shown in tables 5.4 to 5.7. The probability density functions for gauges gi3 (y-wise) and gi4 (x-wise) on the inner surface, and gauges go3 (y-wise) and go4 (x-wise) on the outer surface for all four panels are shown in figures 5.13 to 5.16. As can be seen, the measured strain moments were very close to that of a Gaussian distribution with the skewness close to zero and the kurtosis close to three at all sound pressure levels. This was further evidence that the response of the panels was linear at all loading levels. For the measured pressure loading, departure from Gaussianity was evident at the lower sound pressure levels with a high kurtosis values around 4.4 to 6.2, however the skewness values were still quite low.

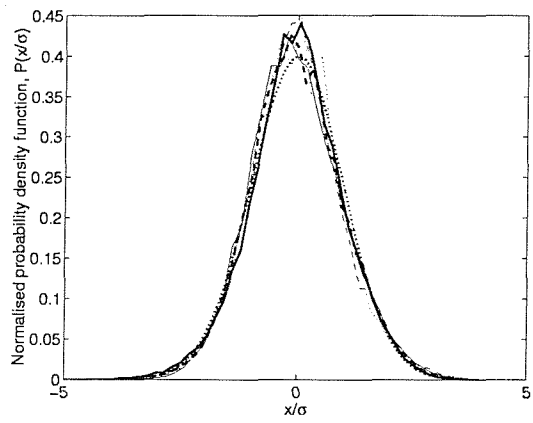

(a) PDF (inner gauge gi4 - x-wise).

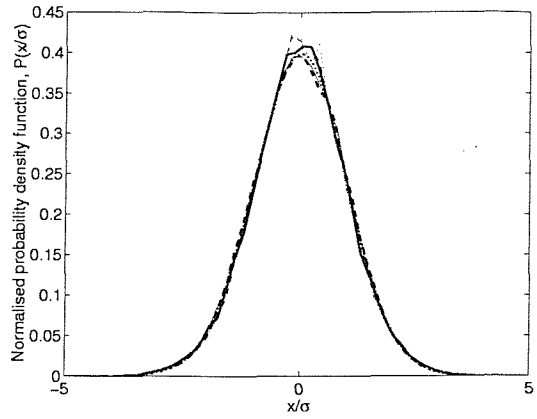

(b) PDF (inner gauge gi3 - y-wise).

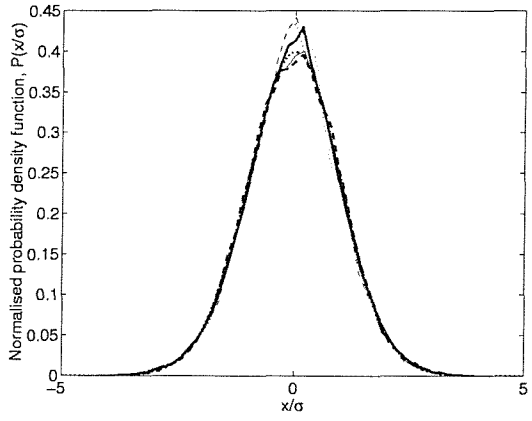

(c) PDF (outer gauge go4 - x-wise).

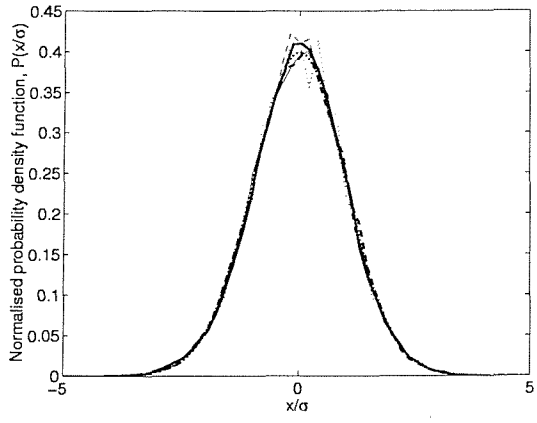

(d) PDF (outer gauge go3 - y-wise).

Figure 5.13: Probability density function for inner strain gauges gi3 and gi4, and outer strain gauges go3 and go4, panel 1 (··· Gaussian, ··· 140 dB, - - 145 dB, – 150 dB, - - 155 dB, – 160 dB).

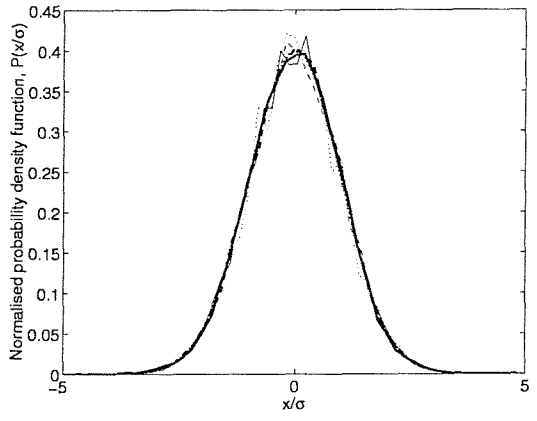

(a) PDF (inner gauge gi4 - x-wise).

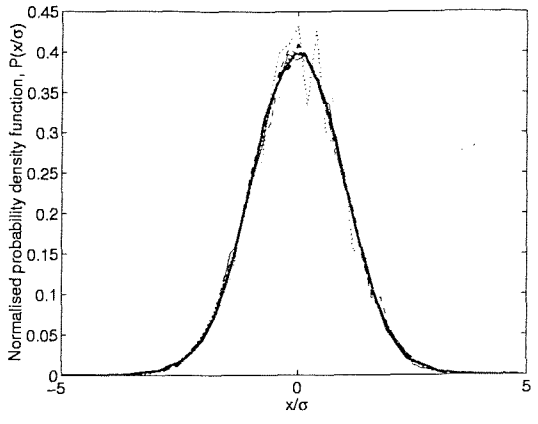

(b) PDF (inner gauge gi3 - y-wise).

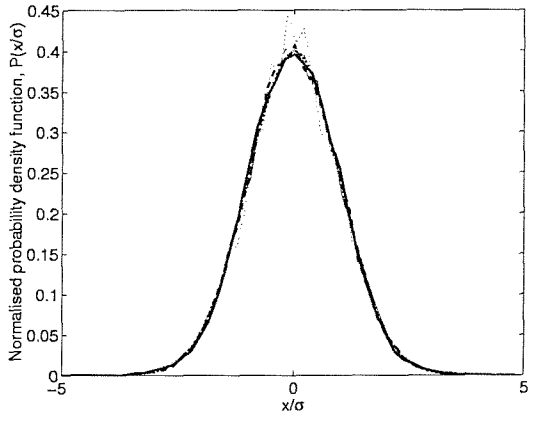

(c) PDF (outer gauge go4 - x-wise).

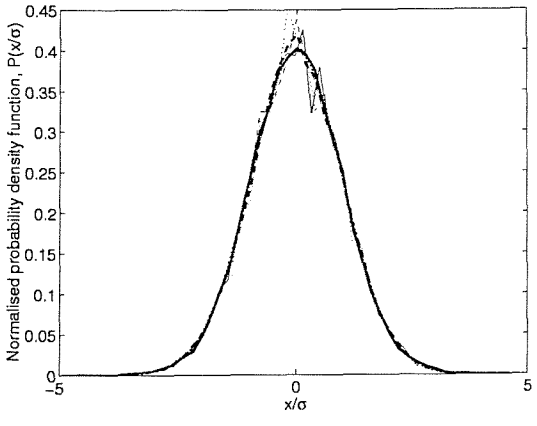

(d) PDF (outer gauge go3 - y-wise).

Figure 5.14: Probability density function for inner strain gauges gi3 and gi4, and outer strain gauges go3 and go4, panel 2 (··· Gaussian, ··· 140 dB, - - 145 dB, – 150 dB, - - 155 dB, – 160 dB).

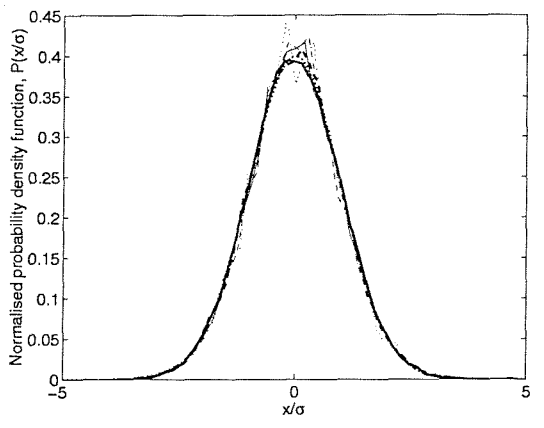

(a) PDF (inner gauge gi4 - x-wise).

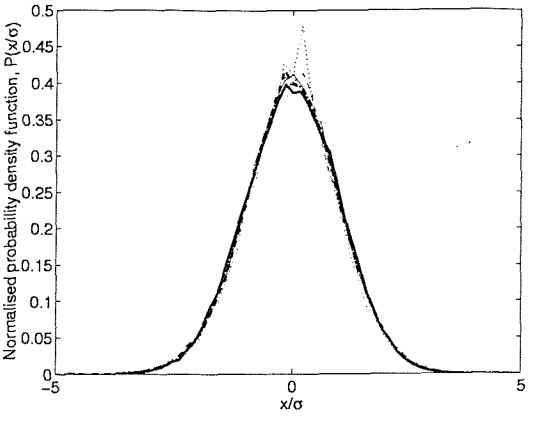

(b) PDF (inner gauge gi3 - y-wise).

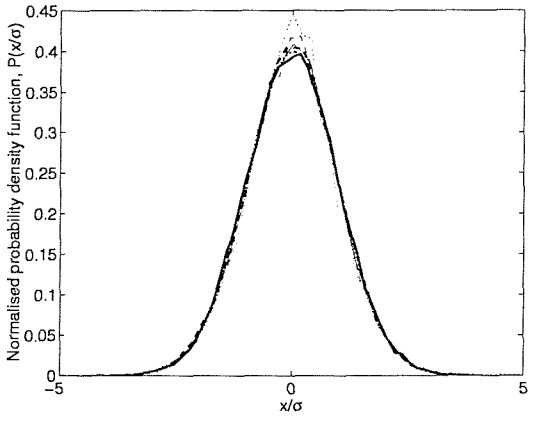

(c) PDF (outer gauge go4 - x-wise).

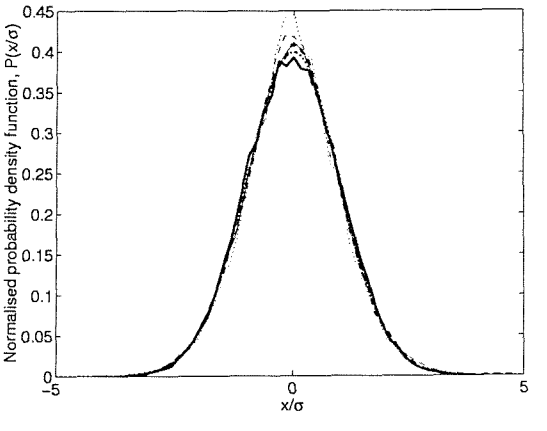

(d) PDF (outer gauge go3 - y-wise).

Figure 5.15: Probability density function for inner strain gauges gi3 and gi4, and outer strain gauges go3 and go4, panel 3 (··· Gaussian, ··· 140 dB, - - 145 dB, – 150 dB, - - 155 dB, – 160 dB).

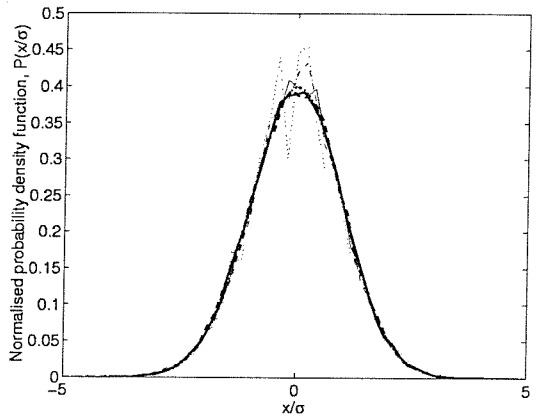

(a) PDF (inner gauge gi4 - x-wise).

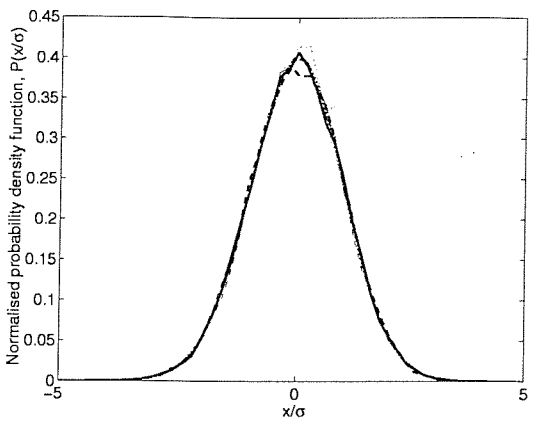

(b) PDF (inner gauge gi3 - y-wise).

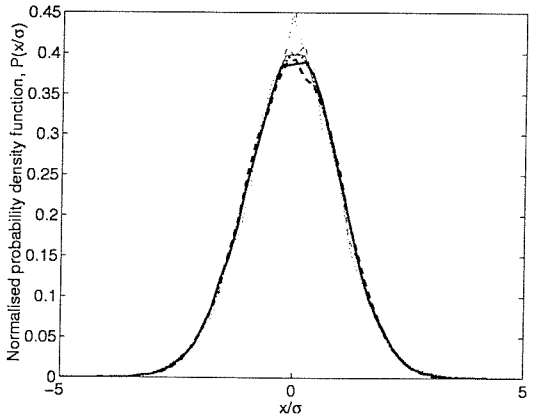

(c) PDF (outer gauge go4 - x-wise).

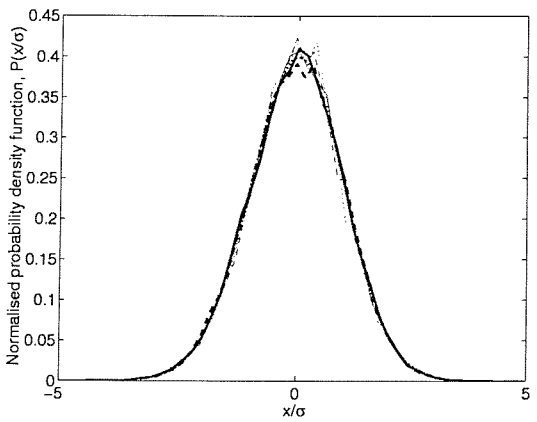

(d) PDF (outer gauge go3 - y-wise).

Figure 5.16: Probability density function for inner strain gauges gi3 and gi4, and outer strain gauges go3 and go4, panel 4 (··· Gaussian, ··· 140 dB, - - 145 dB, – 150 dB, - - 155 dB, – 160 dB).

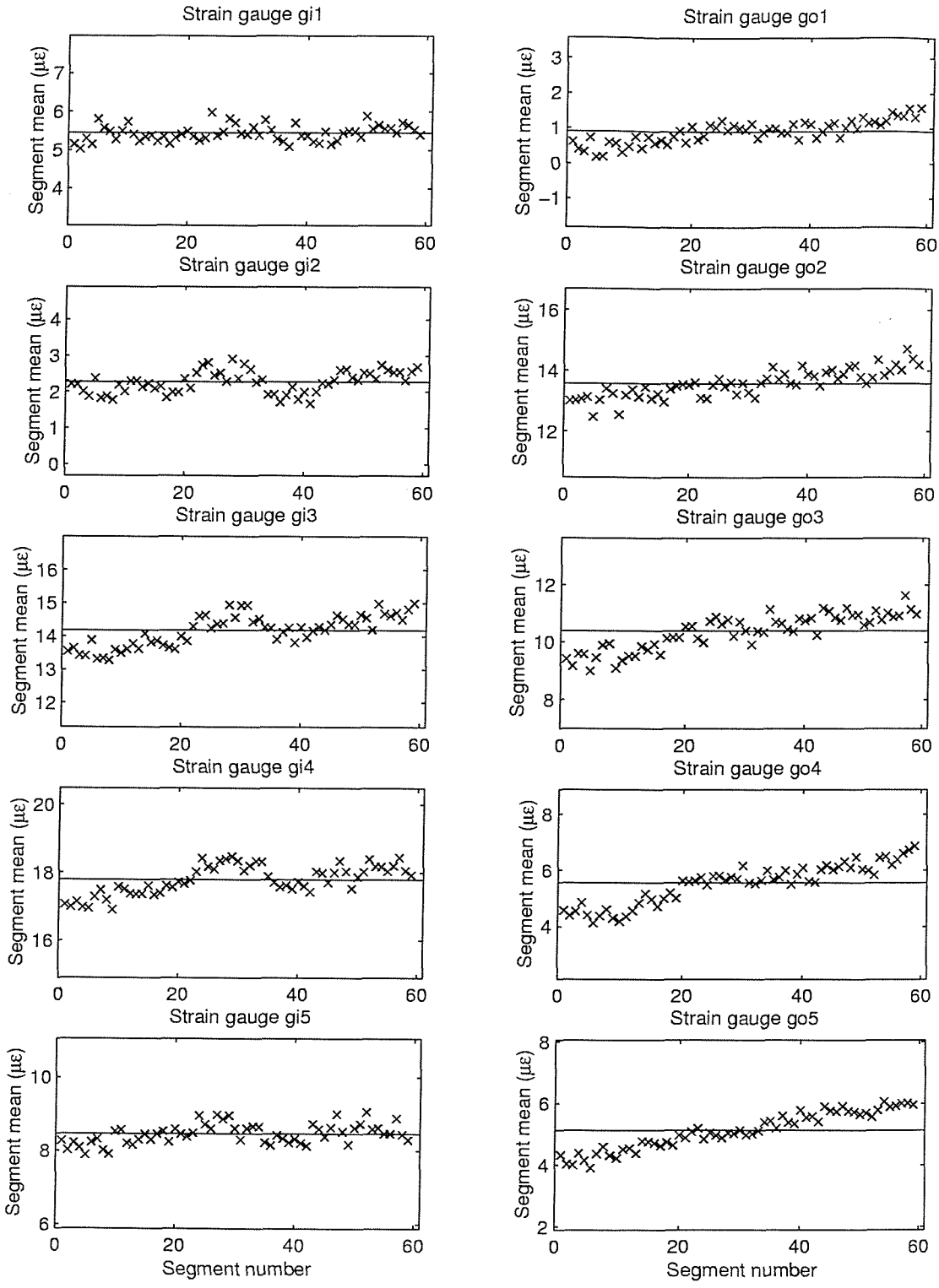

Figure 5.17: Drift in the mean strain time history for panel 1.

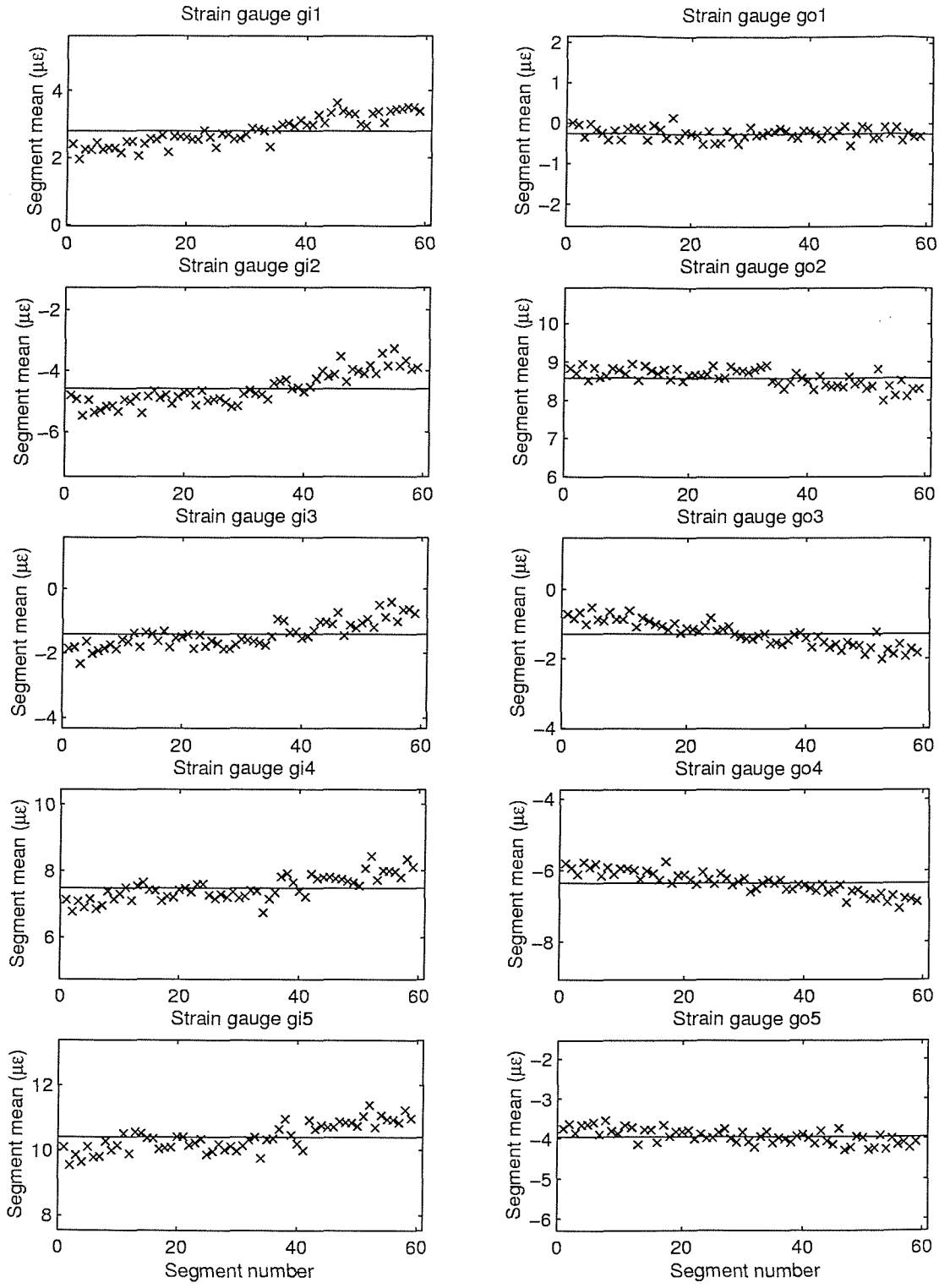

Figure 5.18: Drift in the mean strain time history for panel 2.

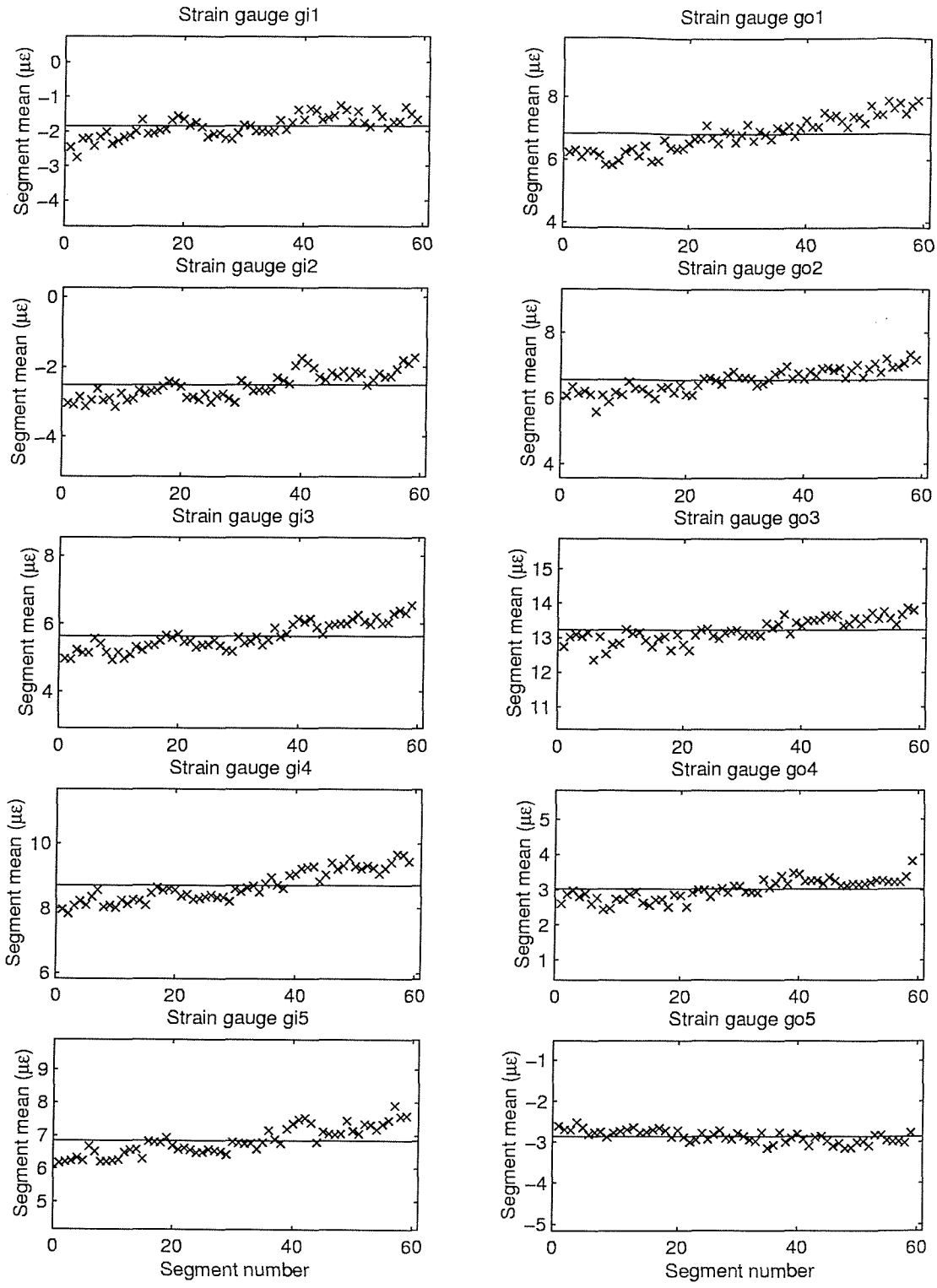

Figure 5.19: Drift in the mean strain time history for panel 3.

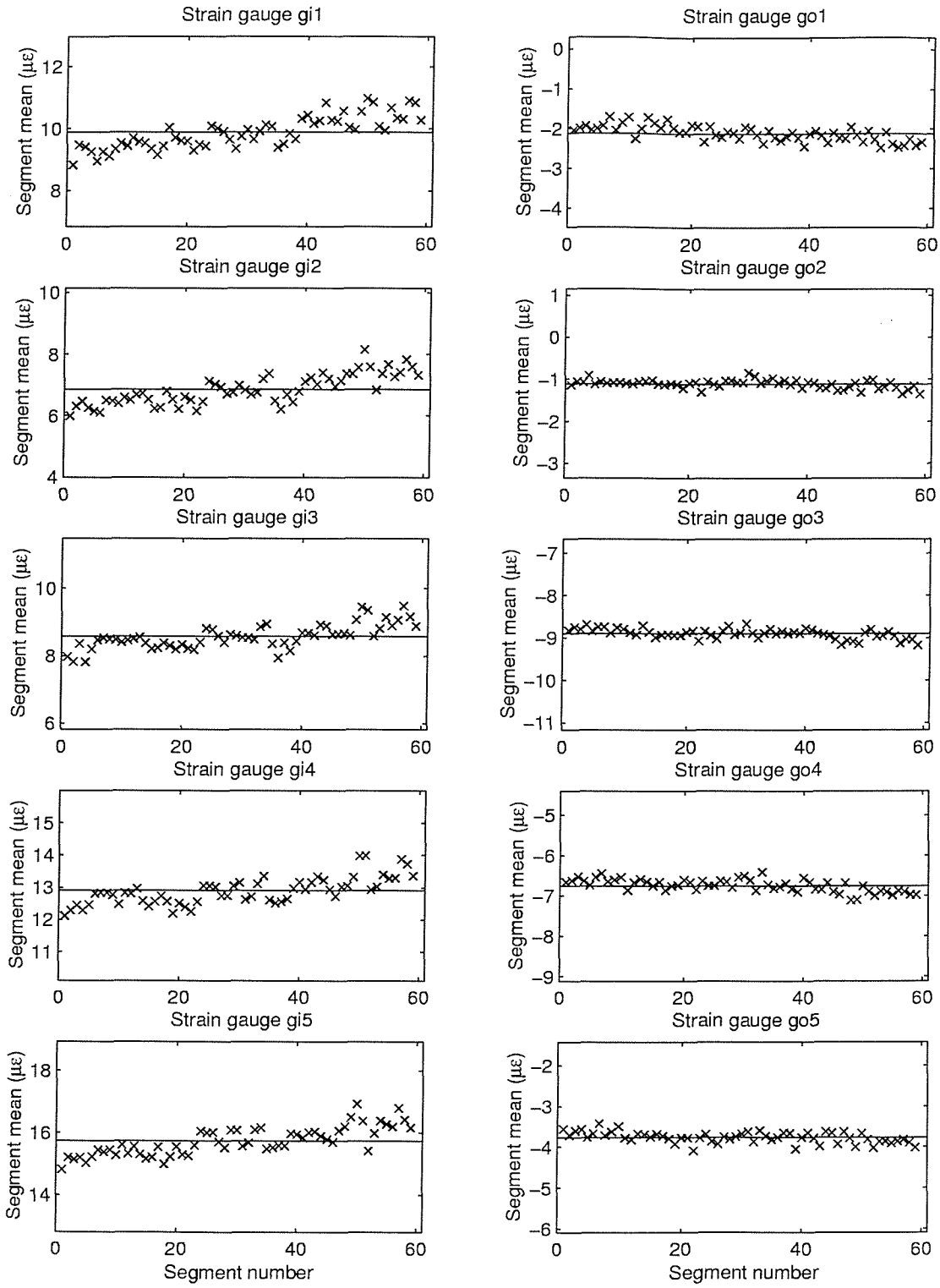

Figure 5.20: Drift in the mean strain time history for panel 4.

5.5.2 Pressure spectrum levels and strain power spectral density

The digitised time histories of strain, acceleration, and pressure were factored to take account of the gains introduced by the respective measurement amplifiers. The resulting data were then transformed to the frequency domain using the "spectrum" function in the MATLAB environment. A Hanning window was applied to the segmented data, which consisted of 8192 samples, prior to applying the FFT algorithm which gave a frequency resolution of 0.73 Hz, and an overlap of 70% was used.

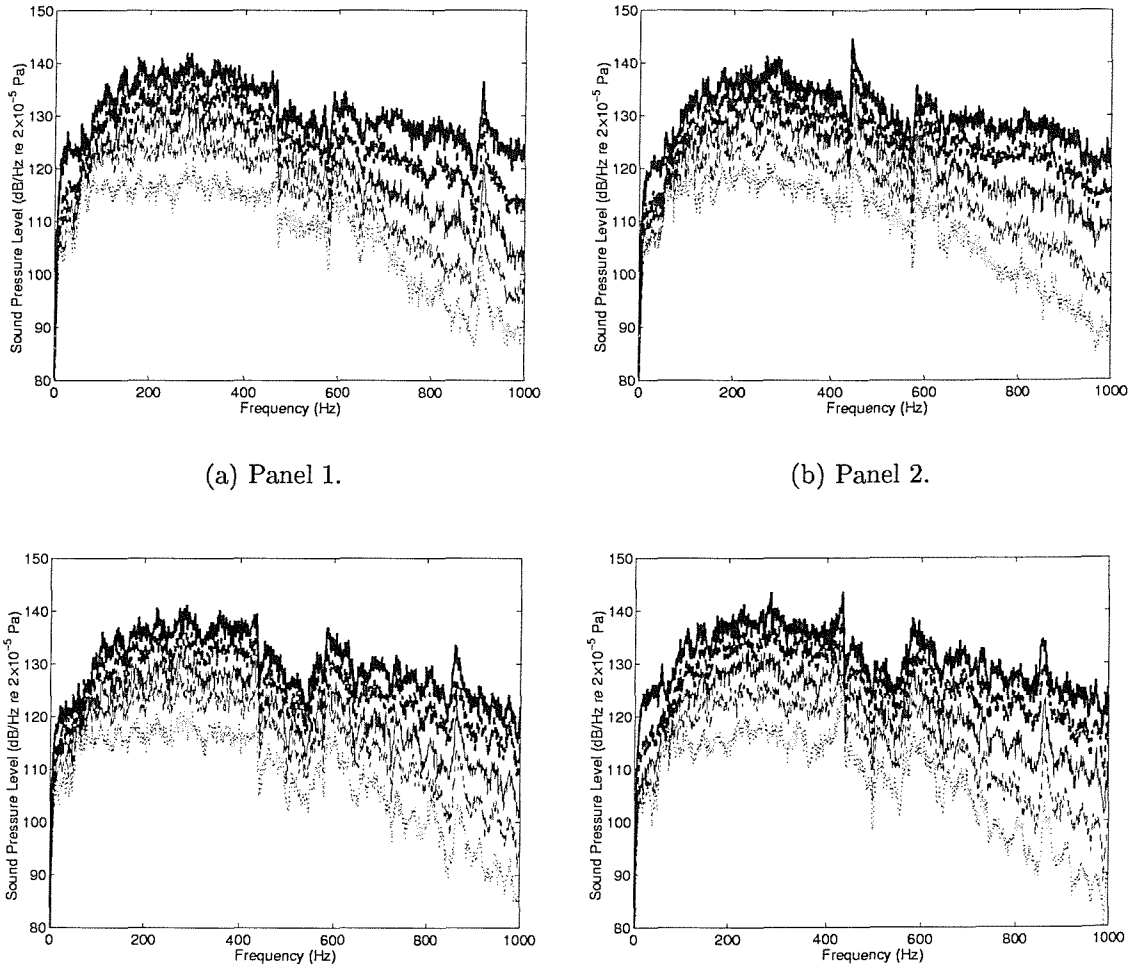

(a) Panel 1.

(b) Panel 2.

(c) Panel 3.

(d) Panel 4.

Figure 5.21: Sound pressure level spectrum for each of the four test panels (OASPL runs ··· 140 dB, - - 145 dB, – 150 dB, - - 155 dB, – 160 dB).

The spectrum levels of sound pressure for each of the four panels located in the PWT using spring supports are shown in figure 5.21. The results are from one test out of the total of five carried out for each panel, and the levels for each test and for all four panels were found to be within 3 dB OASPL, indicating a high degree of consistency. In each case the spectrum level, as opposed to the OASPL, was calculated using [3]

$$S(f) = 10log_{10}\frac{p^2_{\Delta f}/\Delta f}{p^2_{ref}} \tag{5.6}$$

where $p^2_{\Delta f}/\Delta f$ is the average spectral density of pressure in the band Δf, and p_{ref} is the reference pressure equal to $2 \times 10^{-5} Pa$ (the threshold of human hearing). As can be seen from figure 5.21, the spectrum levels are fairly constant, particularly across the 60 Hz to 600 Hz band, where shaping was applied to the input spectrum to the siren. It is interesting to note that a spike in the measured sound pressure appears at approximately 900 Hz for panel 1, which then shifts to 450 Hz for panel 2, and then back to around 850 Hz for panels 3 and 4. At first thought, this could be a cross sectional (width-wise) acoustic mode of the aperture, which is changing due to the change in width of the duct introduced by the different radii of curvature of the panels. However, since the duct walls are by no means rigid (particularly that formed by the panel, which is supported by springs) it is not possible to estimate the duct response using simple theory, and the response here is potentially more complicated.

The power spectral density (PSD), phase and coherence (with respect to the reference microphone measurement) are shown for gauges gi3, gi4, go3 and go4 (the middle gauges) and for all four panels in figures 5.22 to 5.32. Each resonance is indicated by a peak in the PSD response accompanied by a change in phase of approximately 180° . For all four panels, the first and third non-rigid body modes of vibration, which were recorded during the vibration tests, have not been measured in the PWT. This is to be expected since these modes were associated with the torsional vibration of the panel, which is not being excited in the PWT due to the symmetric pressure loading on the panels. With reference to table 5.3, the measured response frequencies agree very well with the estimated natural frequencies obtained using the finite element models of the panels with spring supports included.

For the majority of the strain gauge measurements, the predominant response was in the fundamental mode (excited in the PWT), which was further highlighted when one plots the integral of the PSD versus frequency [38], as shown in figures 5.24 to 5.33. In this case, the integral across the PSD has been normalised with respect to the mean

square response. These plots provide a very useful tool for the engineer interested in acoustic fatigue work, since they provide a means of assessing the percentage response of each of the measured modes of vibration. For the middle gauges of panels 1 and 2, approximately 80% to 90% of the total response was in the fundamental mode (first bending mode), whereas for panel 3, gauges gi4 and go4 (x-wise gauges) show that the fundamental mode accounts for approximately 40% of the response over the frequency band, and for panel 4, gauge go4, the fundamental mode accounts for approximately 20% of the total response. Panels 3 and 4 are particularly stiff in the x-direction due to the high curvature along the short side (y-direction), which could account for the lower response peak in the fundamental bending mode of vibration.

The overall root mean square strains for each of the ten gauges, and for all four panels, are given in tables 5.4 to 5.7 as the standard deviation, which is equal to the RMS value when the mean value is zero. These values are also plotted against the OASPL's as shown in figure 5.34. The highest RMS strain was measured at position gi3 on panel 4, which has an asymmetric lay-up with two face plate layers and six backing skin layers, in addition to which it is stiffer in the x-direction due to the high curvature in the y-direction. This result also corresponds with the result shown in figure 5.33 where for gauge go4, the fundamental bending mode only accounts for 20% of the total response, as mentioned previously. For panels 1 and 2, the highest strains were recorded at gauge locations go1 and go4, both x-wise gauges on the outer or backing skin. For panels 3 and 4, which are stiffer in the x-direction, the highest strains were recorded by the two y-wise gauges gi2 and gi3, located on the inner or facing skin. Sweers [49] suggested that the strain at the centre of the backing skin will invariably be higher than that at the centre of the facing skin due to the extra membrane strain introduced by the panned down or bevelled edge. This was proved following tests carried out on flat honeycomb panels with aluminium face plates, and was later shown to be the case in a study conducted by Soovere on flat honeycomb panels with CFRP face plates [15]. However, introducing double curvature into a panel can have a profound effect on the strains at the centre of the panel. The experiments conducted here have shown that for rectangular panels with a small radius on the short side (panels 3 and 4), the greatest strains were at central locations on the inner (facing) skin (referred to as the outer skin by both Sweers and Soovere).

The outer-to-inner (convex-to-concave) RMS strain ratios are plotted in figure 5.35. The ratio for gauges 2 and 3 (the middle y-wise gauges) is between 0.8 and 0.9 for panels 1, 2, and 3, whereas for panel 4 this ratio drops to between 0.4 and 0.5, possibly due to the asymmetric lay-up of the sandwich. For the x-wise gauges

4 and 5, the ratio is between 2.5 and 3 for panel 1, 1.2 and 1.4 for panel 2, 2.2 and 2.6 for panel 3 and 1.8 and 2.5 for panel 4. For flat rectangular honeycomb sandwich panels, a typical ratio of 2 to 2.5 has been quoted [49, 53]. The ratios were found to be fairly constant with increasing OASPL, particularly for gauges 1 and 2.

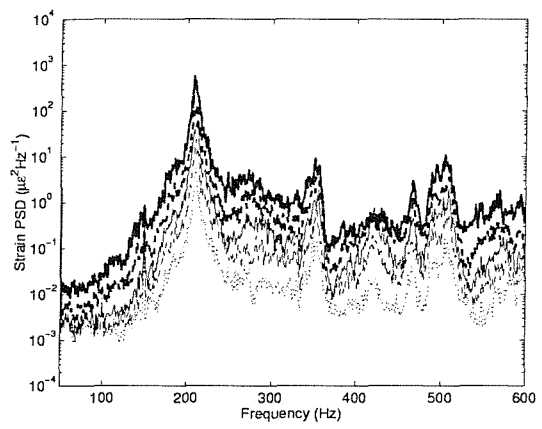

(a) PSD (gauge gi4 - x-wise).

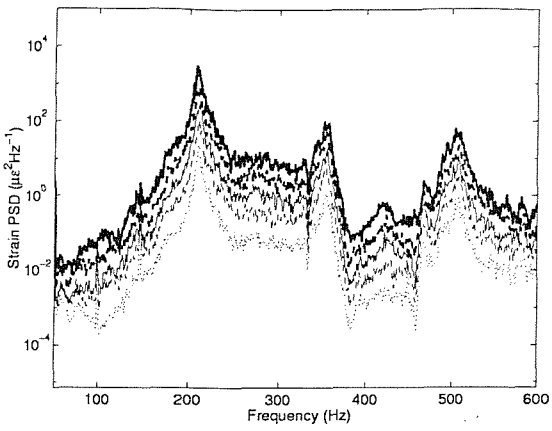

(b) PSD (gauge gi3 - y-wise).

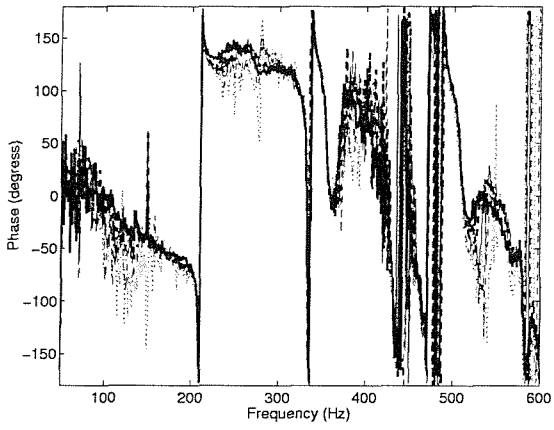

(c) Phase (gauge gi4).

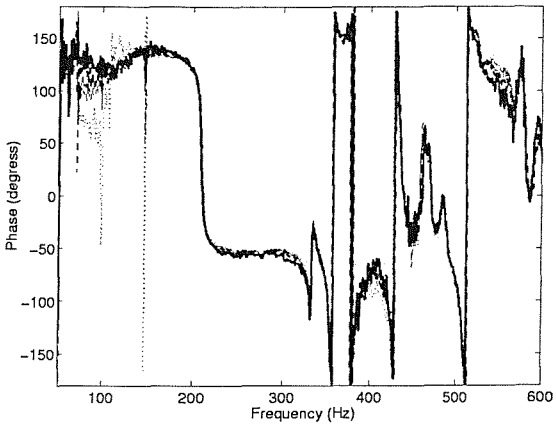

(d) Phase (gauge gi3).

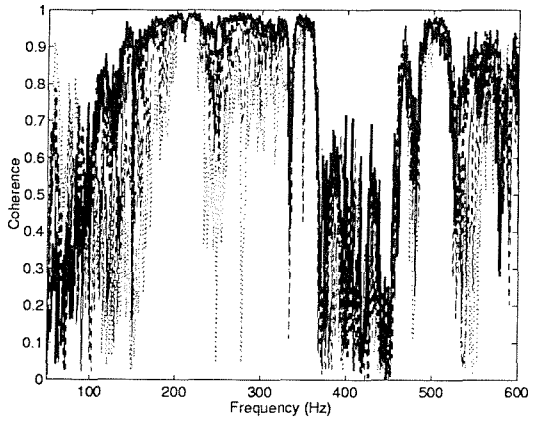

(e) Coherence (gauge gi4).

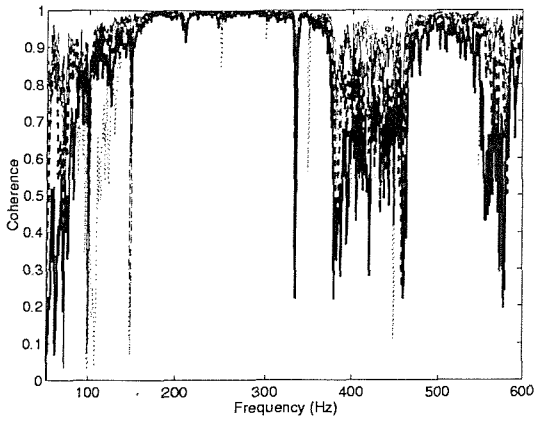

(f) Coherence (gauge gi3).

Figure 5.22: Power spectral density, phase (w.r.t ref. mic.), and coherence (w.r.t ref. mic.) for inner strain gauges gi3 and gi4, panel 1 (OASPL runs ··· 140 dB, - - 145 dB, – 150 dB, - - 155 dB, - 160 dB).

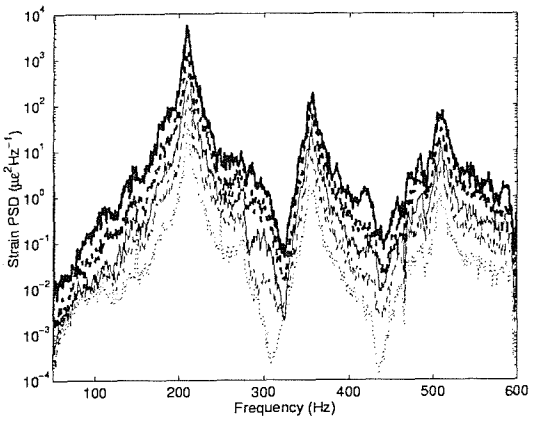

(a) PSD (gauge go4 - x-wise).

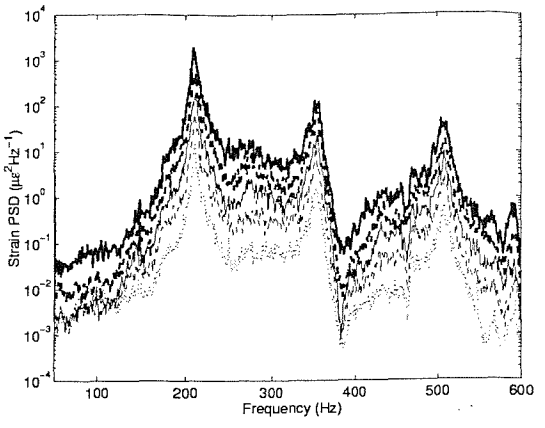

(b) PSD (gauge go3 - y-wise).

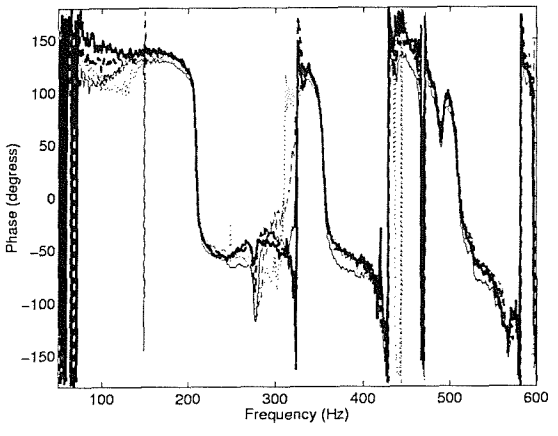

(c) Phase (gauge go4).

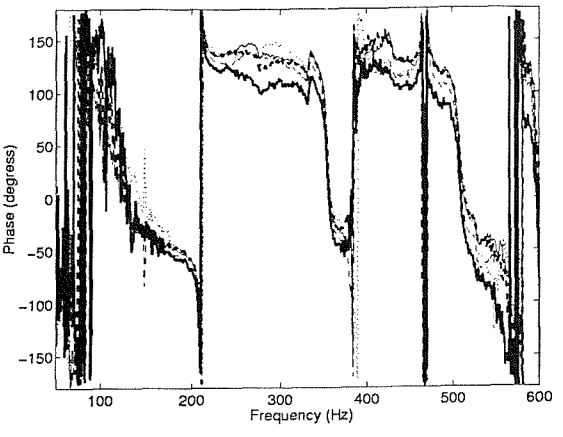

(d) Phase (gauge go3).

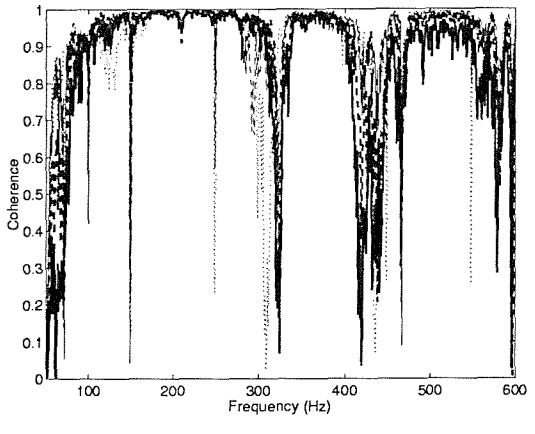

(e) Coherence (gauge go4).

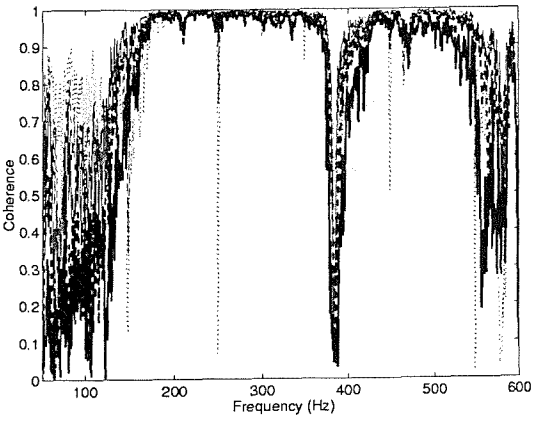

(f) Coherence (gauge go3).

Figure 5.23: Power spectral density, phase (w.r.t ref. mic.), and coherence (w.r.t ref. mic.) for outer strain gauges go3 and go4, panel 1 (OASPL runs ··· 140 dB, - - 145 dB, – 150 dB, - - 155 dB, - 160 dB).

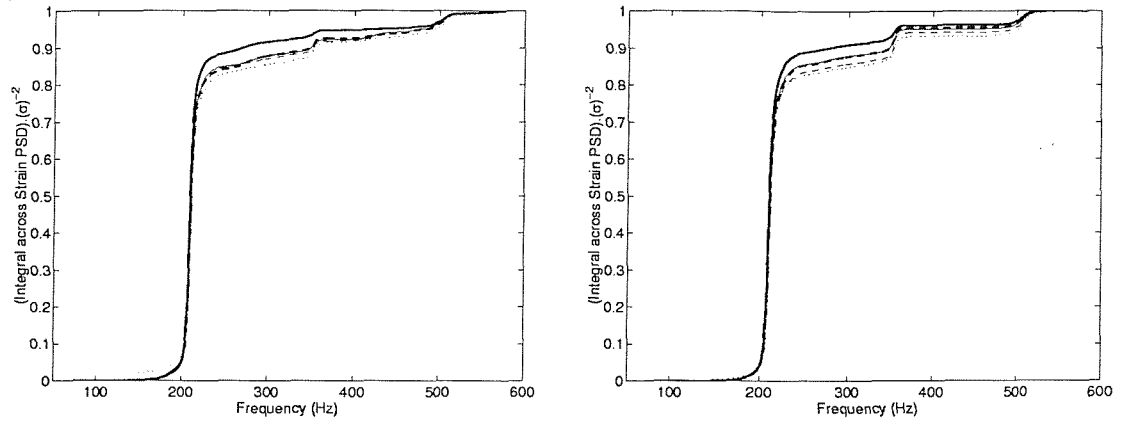

(a) Inner gauge gi4 - x-wise.

(b) Inner gauge gi3 - y-wise.

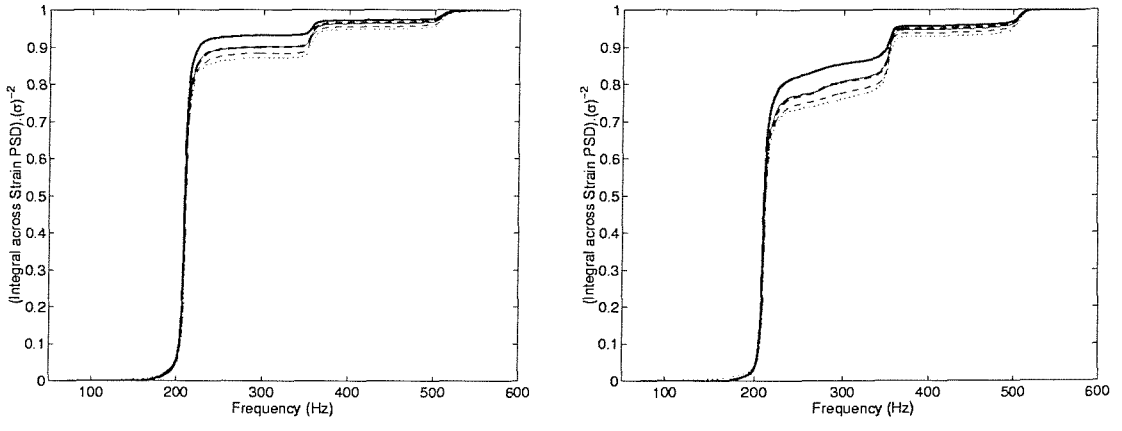

(c) Outer gauge go4 - x-wise.

(d) Outer gauge go3 - y-wise.

Figure 5.24: Integral across the PSD for the inner strain gauges gi3 and gi4, and outer gauges go3 and go4,for panel 1 (OASPL runs ··· 140 dB, - - 145 dB, – 150 dB, - - 155 dB, - 160 dB).

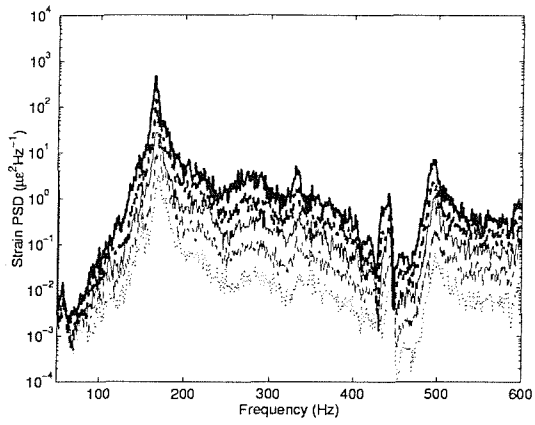

(a) PSD (gauge gi4 - x-wise).

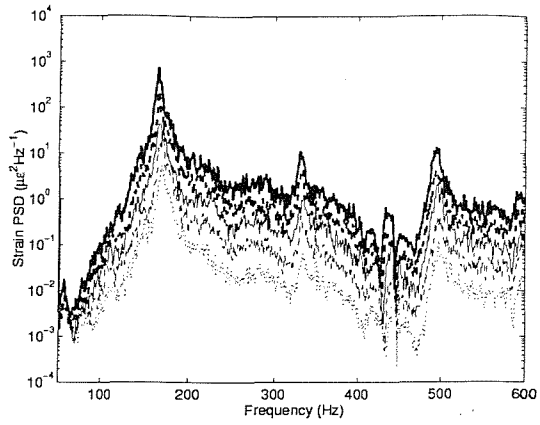

(b) PSD (gauge gi3 - y-wise).

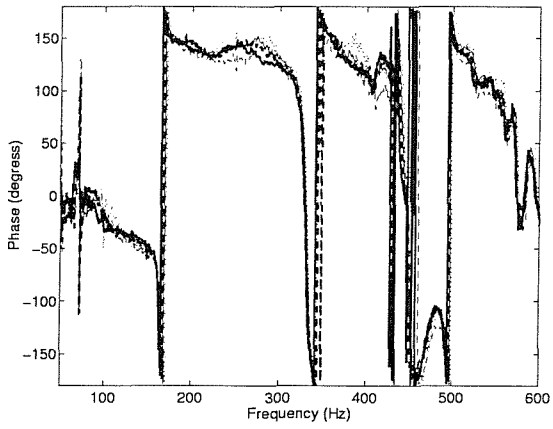

(c) Phase (gauge gi4).

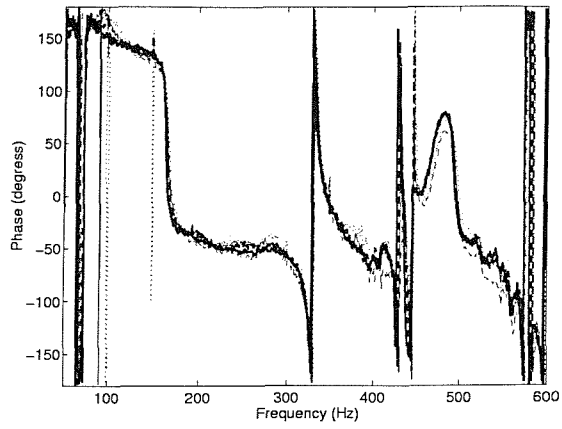

(d) Phase (gauge gi3).

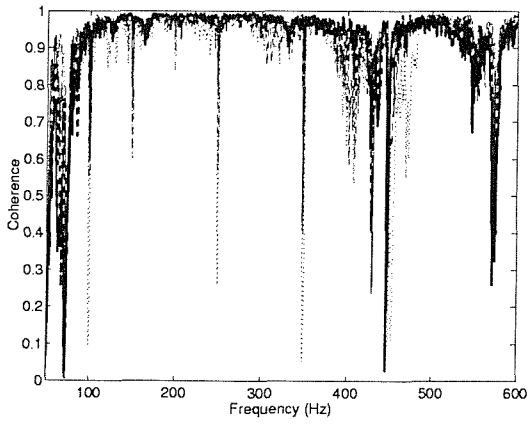

(e) Coherence (gauge gi4).

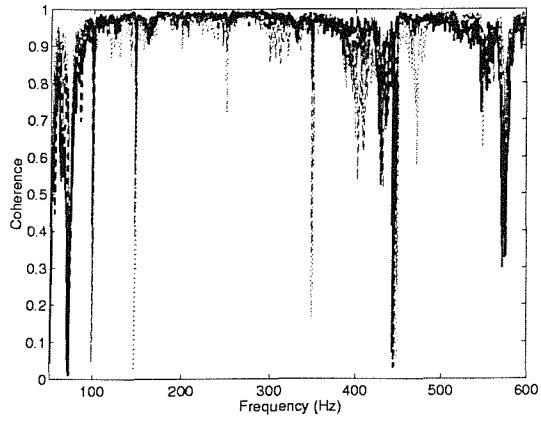

(f) Coherence (gauge gi3).

Figure 5.25: Power spectral density, phase (w.r.t ref. mic.), and coherence (w.r.t ref. mic.) for inner strain gauges gi3 and gi4, panel 2 (OASPL runs ··· 140 dB, - - 145 dB, – 150 dB, - - 155 dB, - 160 dB).

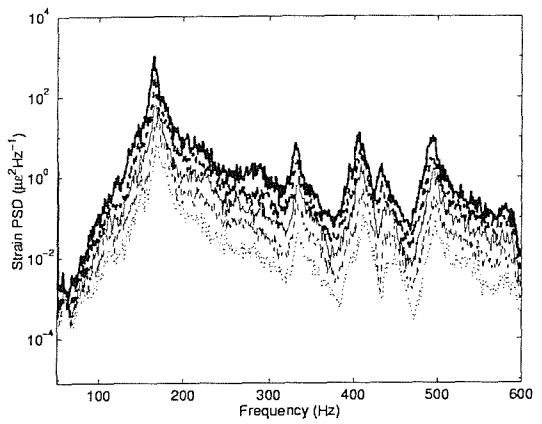

(a) PSD (gauge go4 - x-wise).

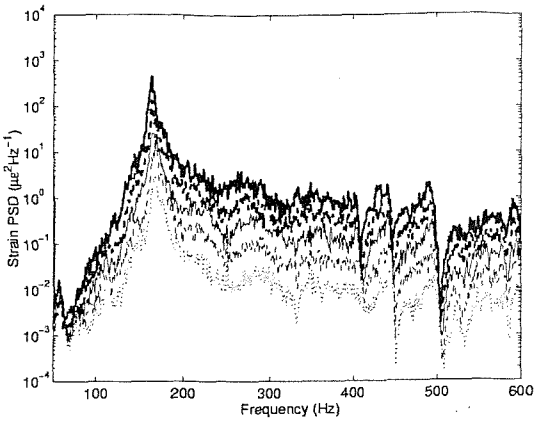

(b) PSD (gauge go3 - y-wise).

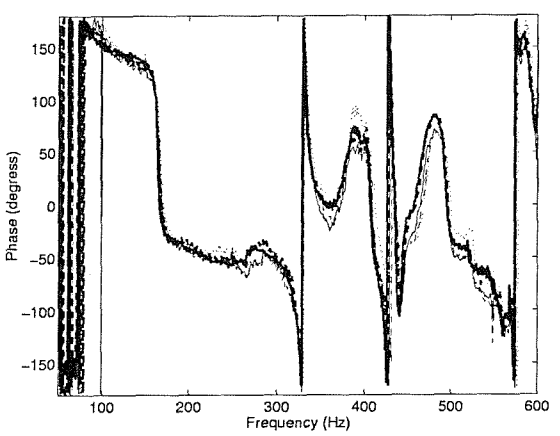

(c) Phase (gauge go4).

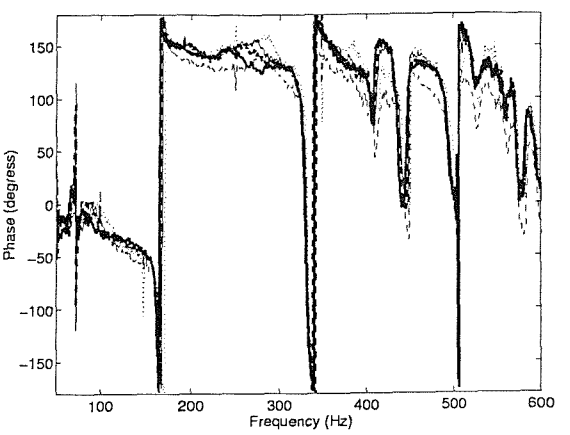

(d) Phase (gauge go3).

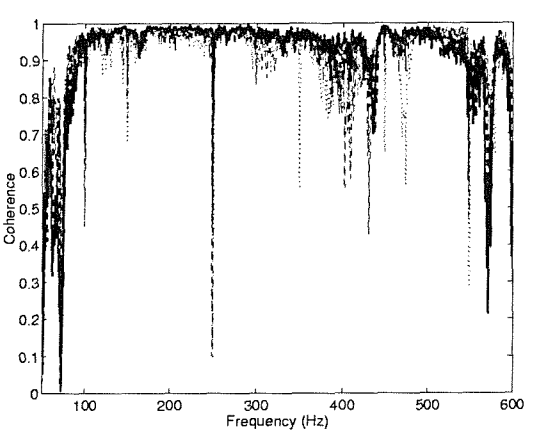

(e) Coherence (gauge go4).

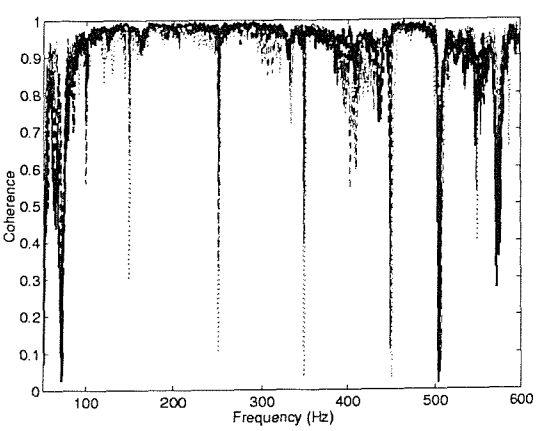

(f) Coherence (gauge go3).

Figure 5.26: Power spectral density, phase (w.r.t ref. mic.), and coherence (w.r.t ref. mic.) for outer strain gauges go3 and go4, panel 2 (OASPL runs ··· 140 dB, - - 145 dB, – 150 dB, - - 155 dB, - 160 dB).

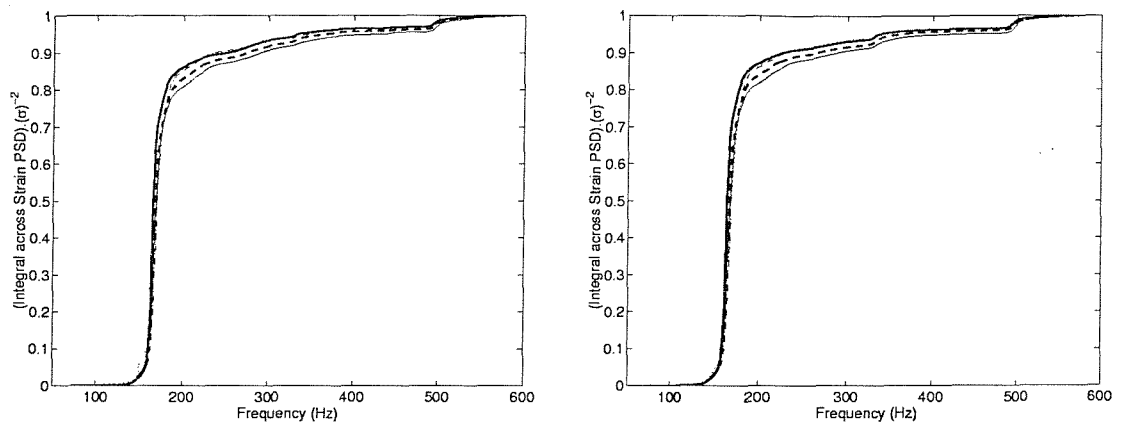

(a) Inner gauge gi4 - x-wise.

(b) Inner gauge gi3 - y-wise.

(c) Outer gauge go4 - x-wise.

(d) Outer gauge go3 - y-wise.

Figure 5.27: Integral across the PSD for the inner strain gauges gi3 and gi4, and outer gauges go3 and go4,for panel 2 (OASPL runs ··· 140 dB, - - 145 dB, – 150 dB, - - 155 dB, - 160 dB).

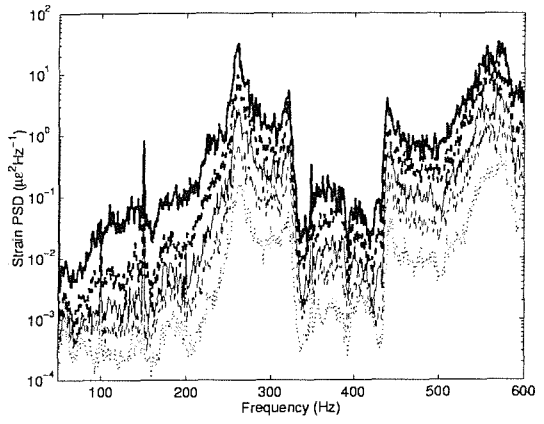

(a) PSD (gauge gi4 - x-wise).

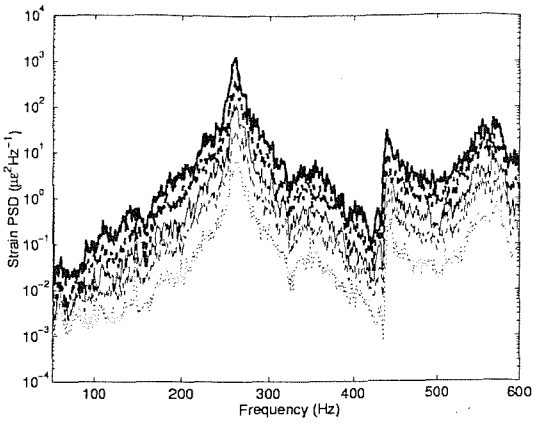

(b) PSD (gauge gi3 - y-wise).

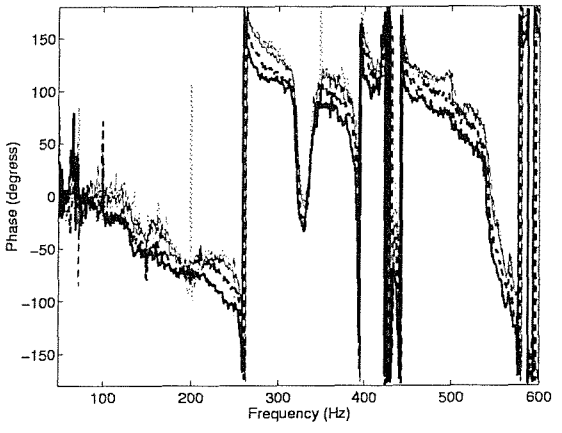

(c) Phase (gauge gi4).

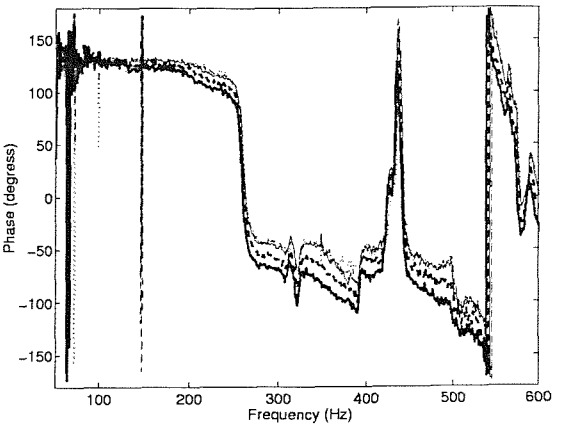

(d) Phase (gauge gi3).

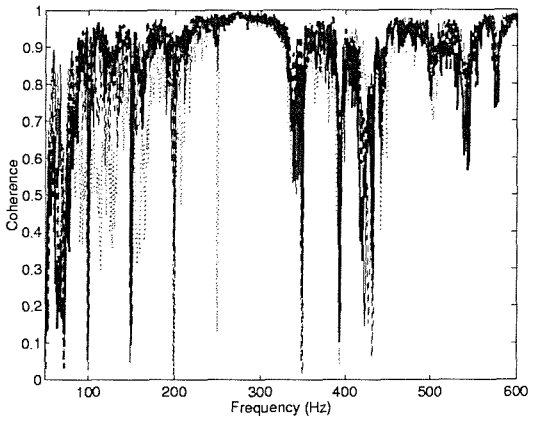

(e) Coherence (gauge gi4).

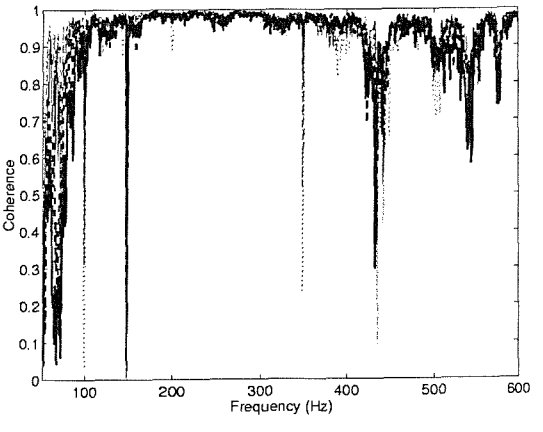

(f) Coherence (gauge gi3).

Figure 5.28: Power spectral density, phase (w.r.t ref. mic.), and coherence (w.r.t ref. mic.) for inner strain gauges gi3 and gi4, panel 3 (OASPL runs ··· 140 dB, - - 145 dB, – 150 dB, - - 155 dB, - 160 dB).

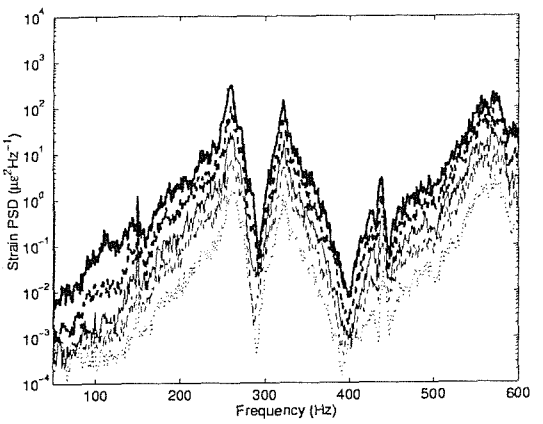

(a) PSD (gauge go4 - x-wise).

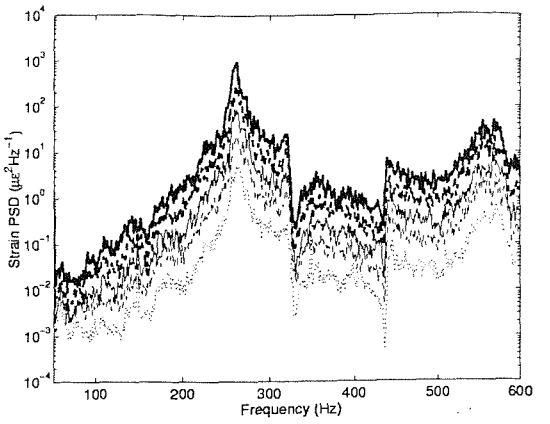

(b) PSD (gauge go3 - y-wise).

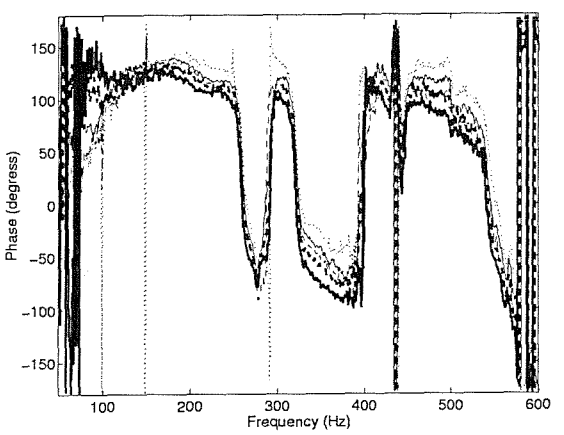

(c) Phase (gauge go4).

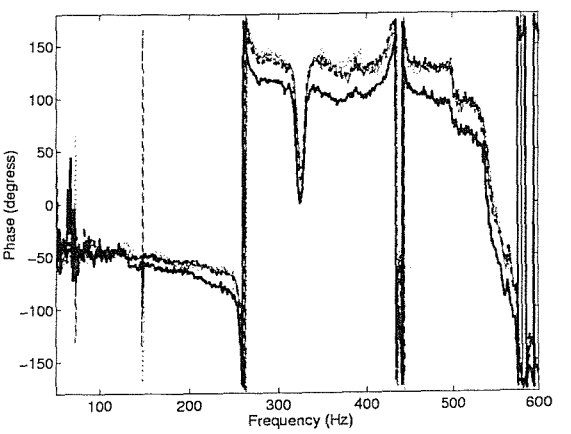

(d) Phase (gauge go3).

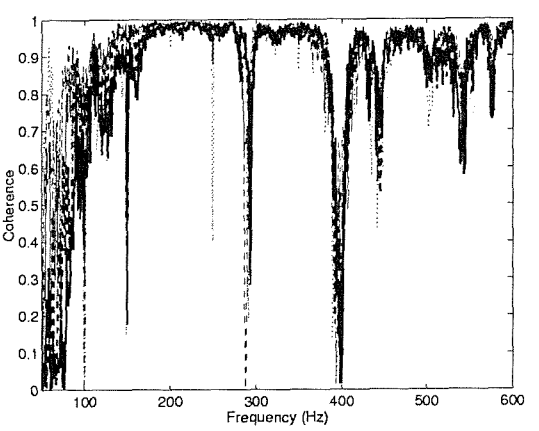

(e) Coherence (gauge go4).

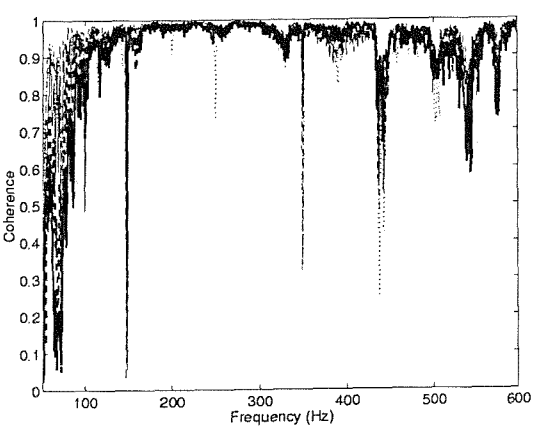

(f) Coherence (gauge go3).

Figure 5.29: Power spectral density, phase (w.r.t ref. mic.), and coherence (w.r.t ref. mic.) for outer strain gauges go3 and go4, panel 3 (OASPL runs ··· 140 dB, - - 145 dB, – 150 dB, - - 155 dB, - 160 dB).

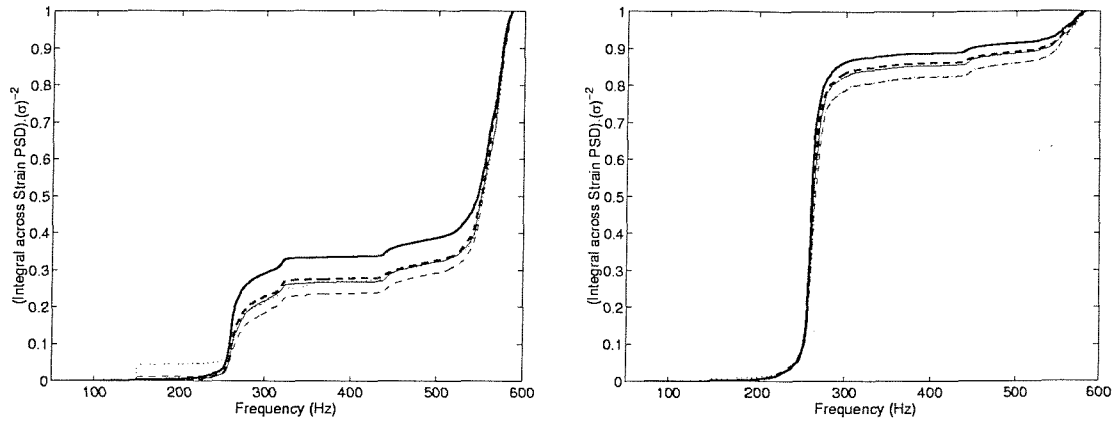

(a) Inner gauge gi4 - x-wise.

(b) Inner gauge gi3 - y-wise.

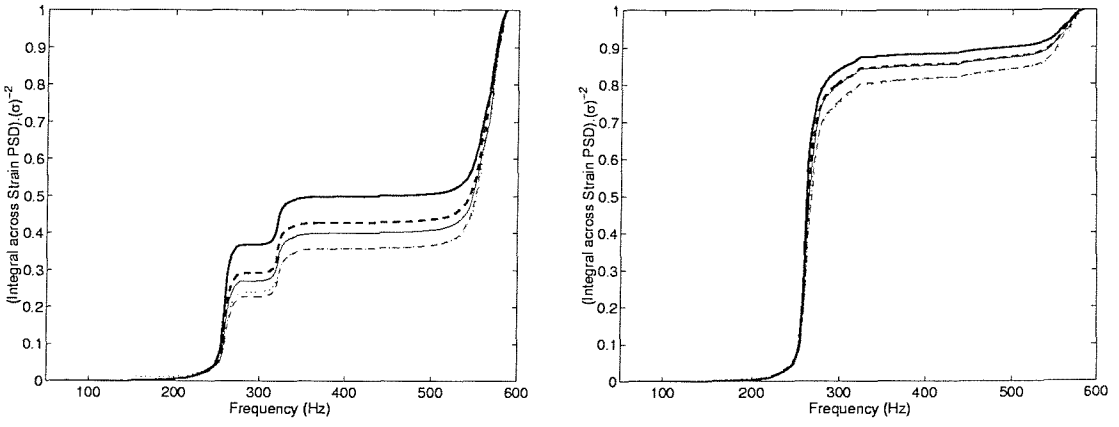

(c) Outer gauge go4 - x-wise.

(d) Outer gauge go3 - y-wise.

Figure 5.30: Integral across the PSD for the inner strain gauges gi3 and gi4, and outer gauges go3 and go4,for panel 3 (OASPL runs ··· 140 dB, - - 145 dB, – 150 dB, - - 155 dB, - 160 dB).

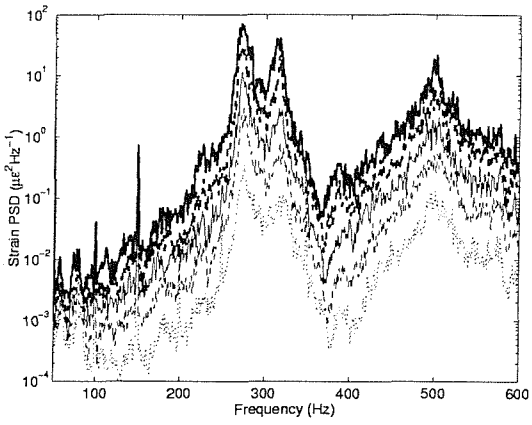

(a) PSD (gauge gi4 - x-wise).

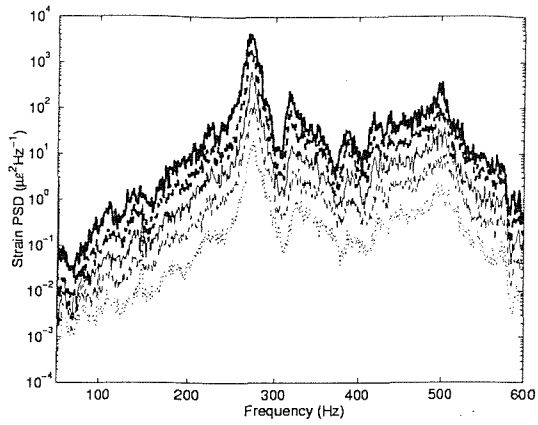

(b) PSD (gauge gi3 - y-wise).

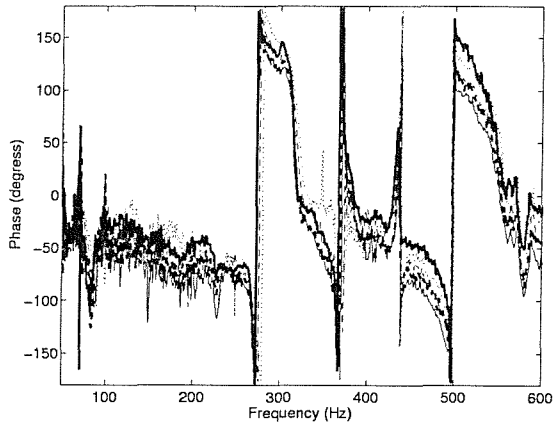

(c) Phase (gauge gi4).

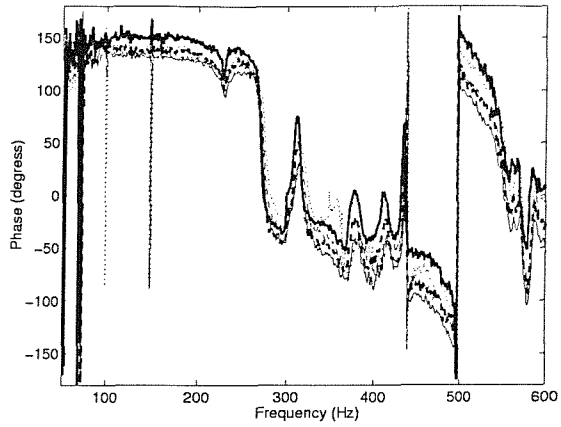

(d) Phase (gauge gi3).

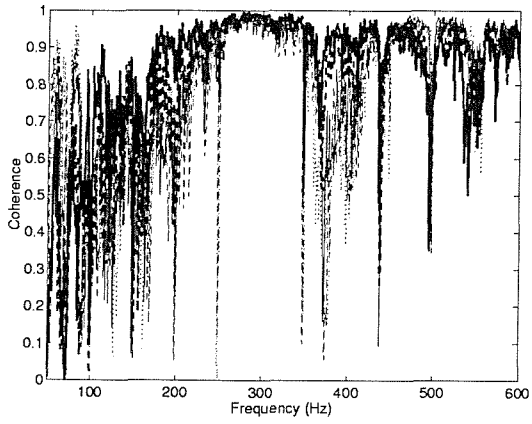

(e) Coherence (gauge gi4).

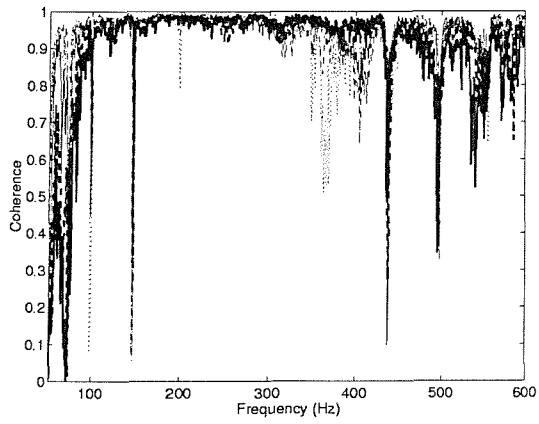

(f) Coherence (gauge gi3).

Figure 5.31: Power spectral density, phase (w.r.t ref. mic.), and coherence (w.r.t ref. mic.) for inner strain gauges gi3 and gi4, panel 4 (OASPL runs ··· 140 dB, - - 145 dB, – 150 dB, - - 155 dB, - 160 dB).

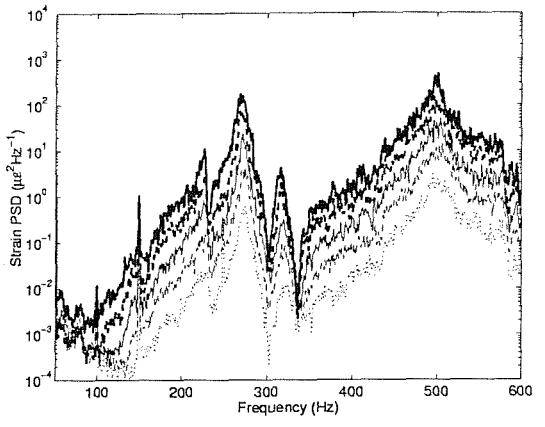

(a) PSD (gauge go4 - x-wise).

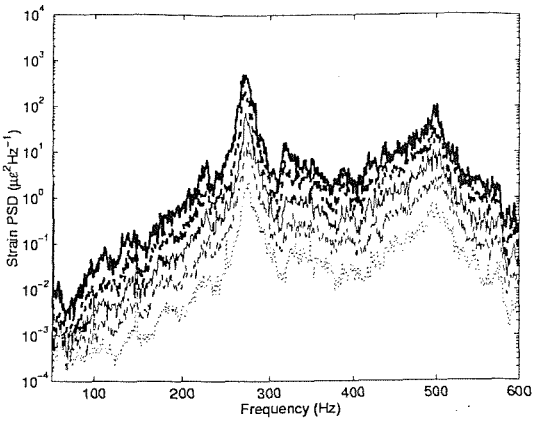

(b) PSD (gauge go3 - y-wise).

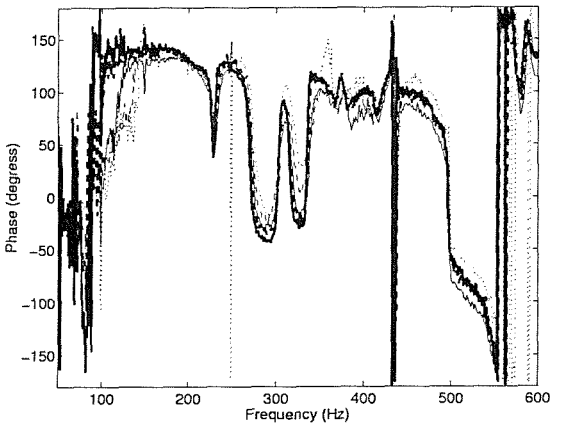

(c) Phase (gauge go4).

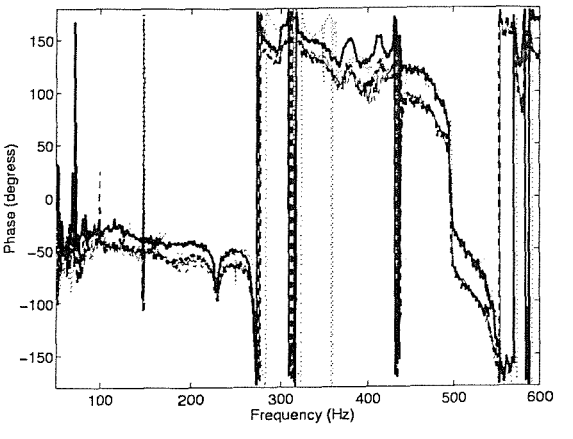

(d) Phase (gauge go3).

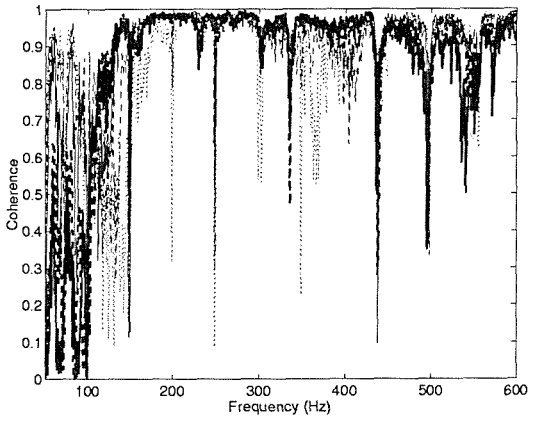

(e) Coherence (gauge go4).

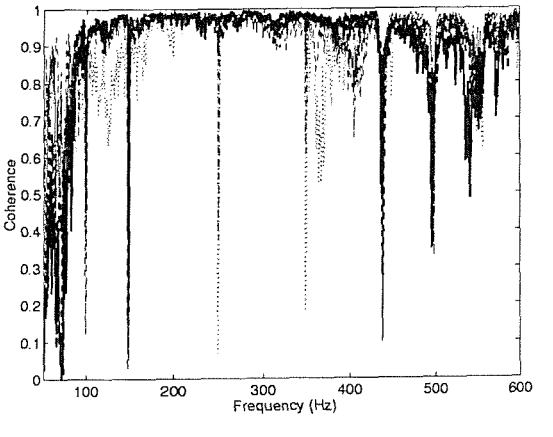

(f) Coherence (gauge go3).

Figure 5.32: Power spectral density, phase (w.r.t ref. mic.), and coherence (w.r.t ref. mic.) for outer strain gauges go3 and go4, panel 4 (OASPL runs ··· 140 dB, - - 145 dB, – 150 dB, - - 155 dB, - 160 dB).

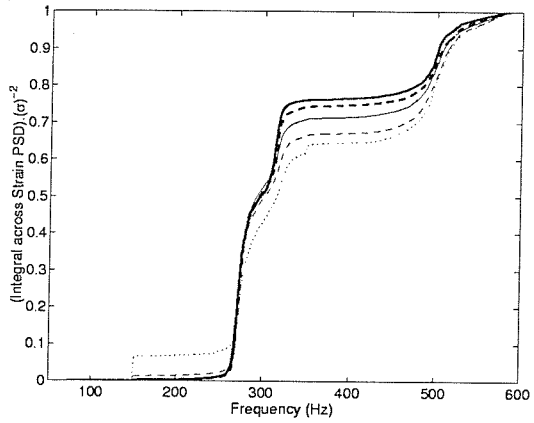

(a) Inner gauge gi4 - x-wise.

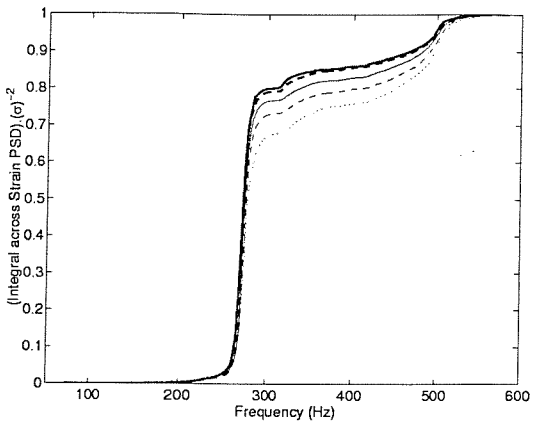

(b) Inner gauge gi3 - y-wise.

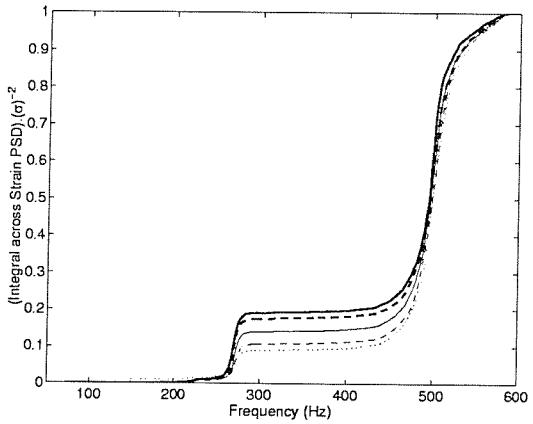

(c) Outer gauge go4 - x-wise.

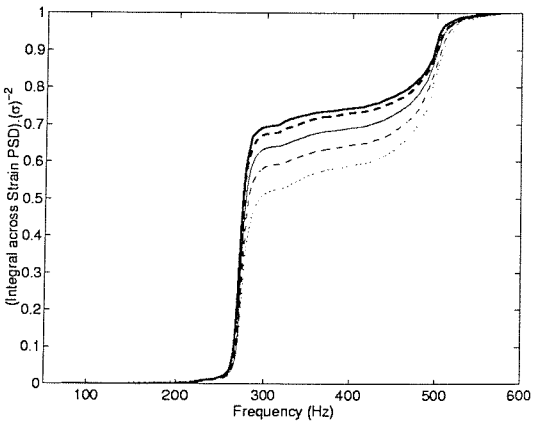

(d) Outer gauge go3 - y-wise.

Figure 5.33: Integral across the PSD for the inner strain gauges gi3 and gi4, and outer gauges go3 and go4,for panel 4 (OASPL runs ··· 140 dB, - - 145 dB, – 150 dB, - - 155 dB, - 160 dB).

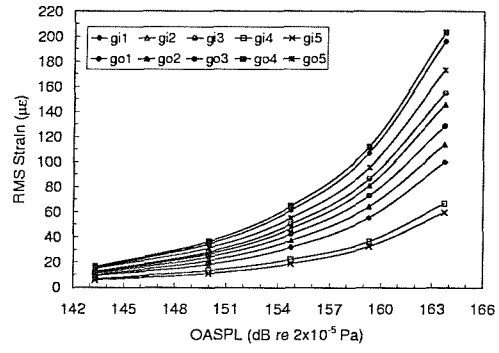

(a) Panel 1.

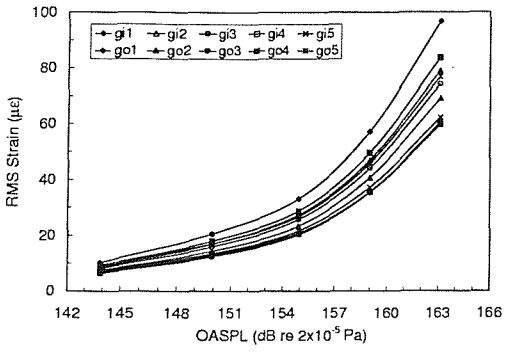

(b) Panel 2.

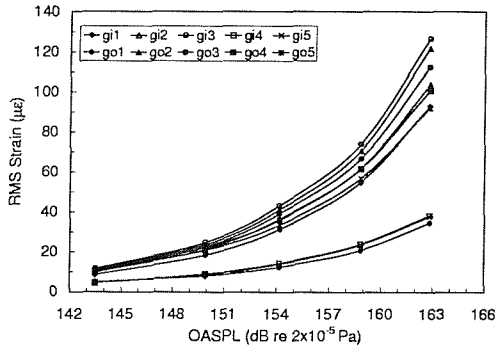

(c) Panel 3.

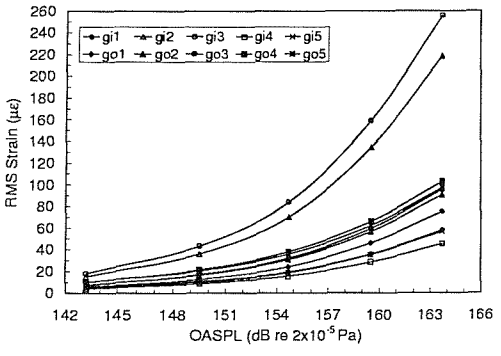

(d) Panel 4.

Figure 5.34: Measured RMS strain versus OASPL for the ten strain gauges on all four panels.

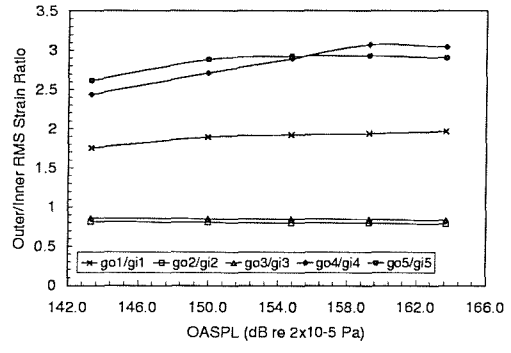

(a) Panel 1.

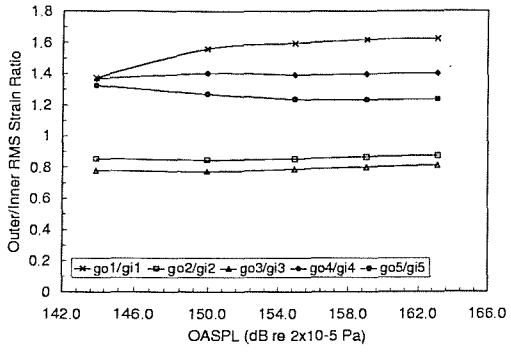

(b) Panel 2.

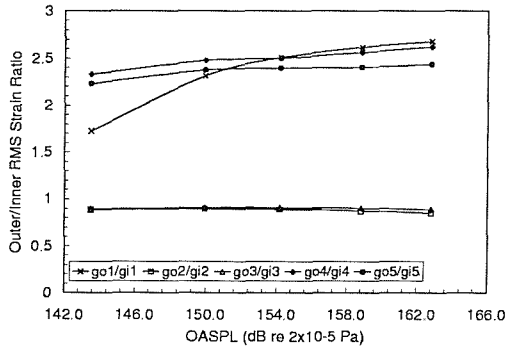

(c) Panel 3.

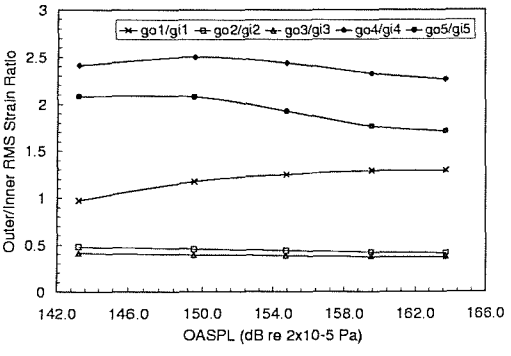

(d) Panel 4.

Figure 5.35: Ratio of Outer-to-Inner (convex-to-concave) RMS strain for all four panels.

5.5.3 Modal damping measurements

The modal damping ratios for each of the four panels were obtained from the transfer function of strain/pressure PSD using the half power point method. The values are presented in table 5.9, and will later be used in the forced response finite element models. These values are also compared with those obtained from the free vibration tests. The damping ratios for the fundamental mode obtained from the PWT tests are substantially higher than those obtained from the vibration experiments. The nature of damping in composite honeycomb panels has been shown to be primarily due to acoustic radiation [15]. It has also been suggested that the influence of the PWT can result in an increase in the damping ratio of the fundamental mode due to acoustic impedence effects [15], particularly if the panel surface area exceeds that of the PWT cross-sectional area, which is certainly the case here. A certain amount of extra damping would have been introduced by the attachment of the panels in the aperture and the application of duct tape around the periphery of the panels in order to provide a seal. However, the significant increase in the damping of the fundamental mode suggests that the impedence effects are the main contributory factor in this increase.

Panel	Frequency (Free) (Hz)	ζ_{free}	Frequency (PWT) (Hz)	ζ_{PWT}
1	214.6	0.0032	210.48	0.0105
	352.1	0.0098	353.9	0.0093
2	164.7	0.0039	163.1	0.0120
	343.1	0.0065	330.8	0.0084
3	264.5	0.0053	258.9	0.0125
	320.4	0.0148	320.7	0.0103
4	279.3	0.0059	269.6	0.0102
	312.4	0.0131	315.2	0.0124

Table 5.9: Comparison of measured modal damping values obtained from the PWT tests and the vibration tests.

5.5.4 Estimation of the dynamic core shear strain

An estimate of the core shear strain was obtained using gauge pairs 2 and 3 (for γ_{yz}) and pairs 4 and 5 (for γ_{xz}). Since the strains on the inner and outer face plates differed, this suggested that there were membrane strains, as well as the bending strain, on one or both faces. Soovere [53] suggested that the panned down edge was

responsible for the introduction of a membrane strain in the inner face plate (the face with the panned down edge for flat panels, but referred to as the outer, convex or backing skin here). In addition, it is possible that the double curvature could also introduce a linear membrane strain. In order to remove this effect and provide an estimate of the core shear strain from the measured face plate bending strains, both inner and outer skin gauge pairs must be used. This is possible since the gauges were located in the same position on both faces. Taking a cross section through the panel, the arrangement of the gauges is shown in figure 5.36. The strain measured by any

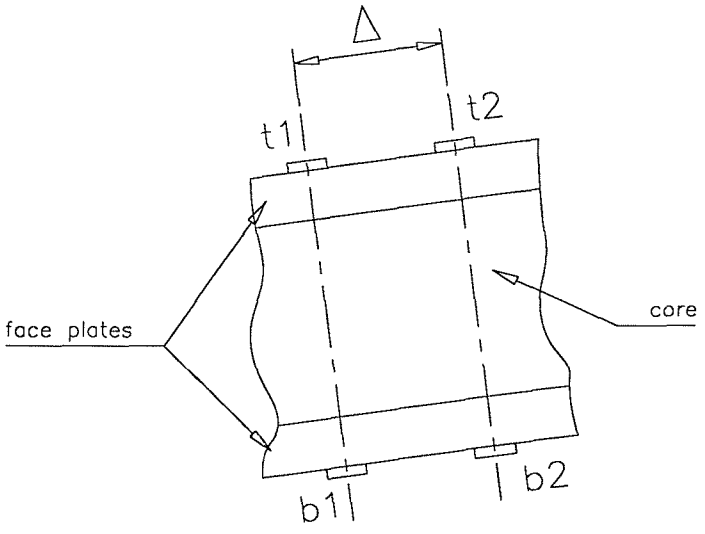

Figure 5.36: Arrangement of inner and outer strain gauges on the doubly curved test panels.

one of the four gauges will be a sum of the bending and membrane strain. Since the gauge pairs are in close proximity with each other, the membrane strain measured by each gauge can be said to be equal. Therefore for the upper face plate in figure 5.36,

$$\epsilon_{t1_{mem}} = \epsilon_{t2_{mem}} = \epsilon_{mem_t} \tag{5.7}$$

where $\epsilon_{t1_{mem}}$ is the membrane strain at location t1, $\epsilon_{t2_{mem}}$ is the membrane strain at location t2, and ϵ_{mem_t} is the membrane strain in the region of locations t1 and t2. For the lower face plate in figure 5.36,

$$\epsilon_{b1_{mem}} = \epsilon_{b2_{mem}} = \epsilon_{mem_b} \tag{5.8}$$

Also, assuming that the bending strains in the facing and backing skins are equal and opposite,

$$|\epsilon_{t1_{bend}}| = |\epsilon_{b1_{bend}}| \tag{5.9}$$

and,

$$|\epsilon_{t2_{bend}}| = |\epsilon_{b2_{bend}}| \tag{5.10}$$

Now,

$$\Delta\epsilon_1 = \epsilon_{t1} - \epsilon_{b1} = \epsilon_{t1_{bend}} + \epsilon_{mem_t} - \epsilon_{b1_{bend}} - \epsilon_{mem_b} \tag{5.11}$$

and,

$$\Delta\epsilon_2 = \epsilon_{t2} - \epsilon_{b2} = \epsilon_{t2_{bend}} + \epsilon_{mem_t} - \epsilon_{b2_{bend}} - \epsilon_{mem_b} \tag{5.12}$$

Subtracting equation 5.11 from equation 5.12 and substituting 5.9 and 5.10, an expression for the finite difference approximation using four gauges where the strains in the two face plates differ due to the presence of membrane strains is obtained,

$$(\epsilon_{t1} - \epsilon_{t2})_{bend} = \frac{1}{2}[(\epsilon_{t2} - \epsilon_{b2}) - (\epsilon_{t1} - \epsilon_{b1})] \tag{5.13}$$

An estimate of the core shear strain can be obtained by substituting the transfer functions of the measured strain signals and the microphone signal into equation 5.13, which will account for any phase differences in the signals. The face plate strain PSD finite difference approximation, $G_{\Delta_{bend}}(f)$ is then found by calculating the magnitude squared value and multiplying this by the power spectral density (auto-spectral density) of the pressure signal, $G_p(f)$:-

$$G_{\Delta_{bend}}(f) = \left|\frac{1}{2}[(\epsilon_{t2} - \epsilon_{b2}) - (\epsilon_{t1} - \epsilon_{b1})]\right|^2 G_p(f) \tag{5.14}$$

In order to obtain the semi-empirical constants for the three symmetric-sandwich panels used in the tests, a finite element model of each panel with a unit pressure load on one surface was analysed. The strain response over a bandwidth from 60 Hz to 600 Hz was calculated at locations corresponding with gauges gi2, gi3, gi4, gi5 on the inner surface, and gauges go2, go3, go4, and go5 on the outer surface. The core shear strain mid-way between each gauge pair was also calculated. Since the output from the

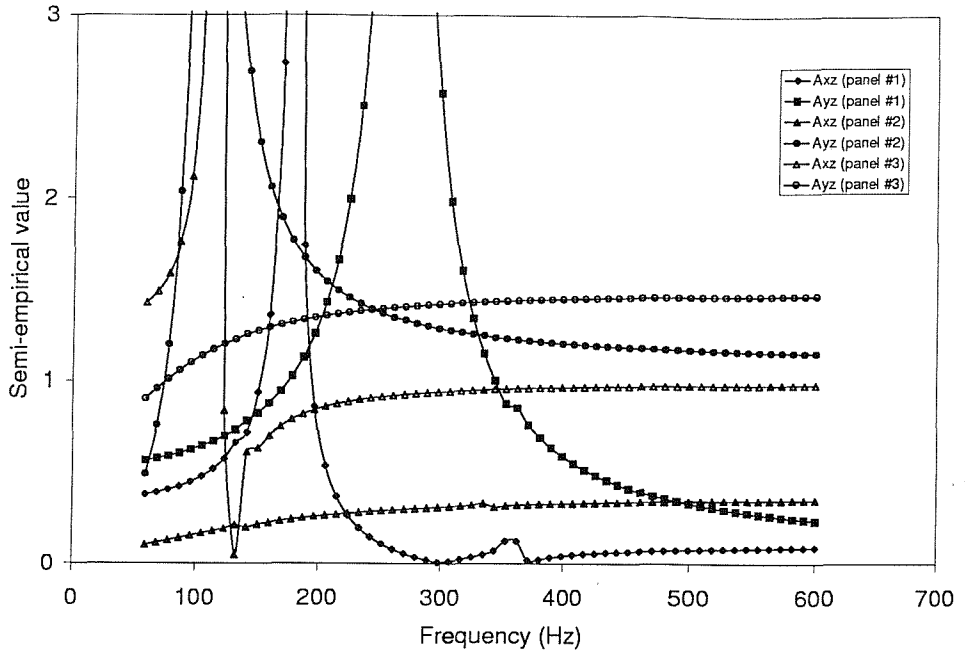

Figure 5.37: Semi-empirical values used in the estimates of core shear strain for the three doubly curved sandwich panels, spring supported, unit pressure applied on inner face.

finite element model was in units of $(\mu\epsilon).(Pa)^{-1}$, i.e. the transfer function and hence a complex quantity, equation 5.13 was used to remove the membrane strain element and the resulting finite difference approximation was substituted into equations 3.75 and 3.76 in order to obtain the estimate of core shear strain. The semi-empirical constants were then obtained by equating these results to the calculated (FE) core shear strains in each direction. The results for panels 1 to 3 are shown in figure 5.37. It is clear that there is variability in the calculated semi-empirical values A_{xz} and A_{yz} with frequency, particularly for panel 1. This variability was not apparent for the flat sandwich panel used to verify the method in chapter 3, although this panel was about half the size of the doubly curved panels. Another flat panel model with a surface area similar to that of the doubly curved was therefore analysed, and the results for the semi-empirical values again showed variation, as can be seen in figure 5.38.

It appears, upon closer inspection of this variability, that the semi-empirical values are tending to infinity at a particular frequency, depending on the panel being analysed. These constants are calculated by equating the actual calculated core shear strain to the estimated shear strain using four calculated values of face plate direct strain (two on the upper face plate, and two on the lower face plate). The rapid increase in the semi-empirical values at a particular frequency suggest that the es-

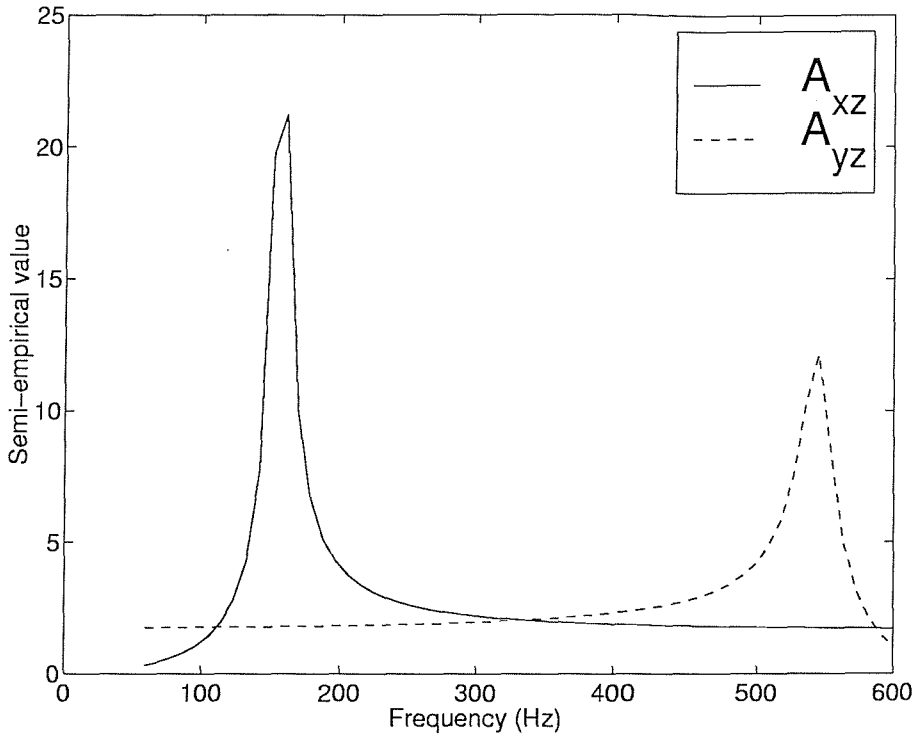

Figure 5.38: Semi-empirical values used in the estimates of core shear strain for the flat sandwich panel, fully clamped, unit pressure applied on inner face.

timated core shear strain is tending to zero, which will only occur when the finite difference approximation of the rate of change of direct strain with distance equals zero. For the flat sandwich panel model, the phase of the two calculated direct strains in the x direction from one of the face plates are plotted in figure 5.39 (lower plot), along with the phase of the difference between this pair of calculated values (lower plot) and the absolute value of strain (upper plot). As can be seen, there is a frequency at which the values of direct strain are equal, which can be clearly seen in the change in phase of the difference between them. For these strain values to be equal, there must exist a condition whereby either the bending strain is constant along the distance Δx, or the bending strain contribution to the total direct strain is so small that the assumption of neglecting the contribution to the total direct strain from the secondary (shear) partial deflection is no longer valid. In any case, it is clear at this point that further work needs to be done to investigate the possibility of separating out the bending and shear deflection contributions to the dynamic direct strain in the analysis, which unfortunately could not be done here due to limitations in time.

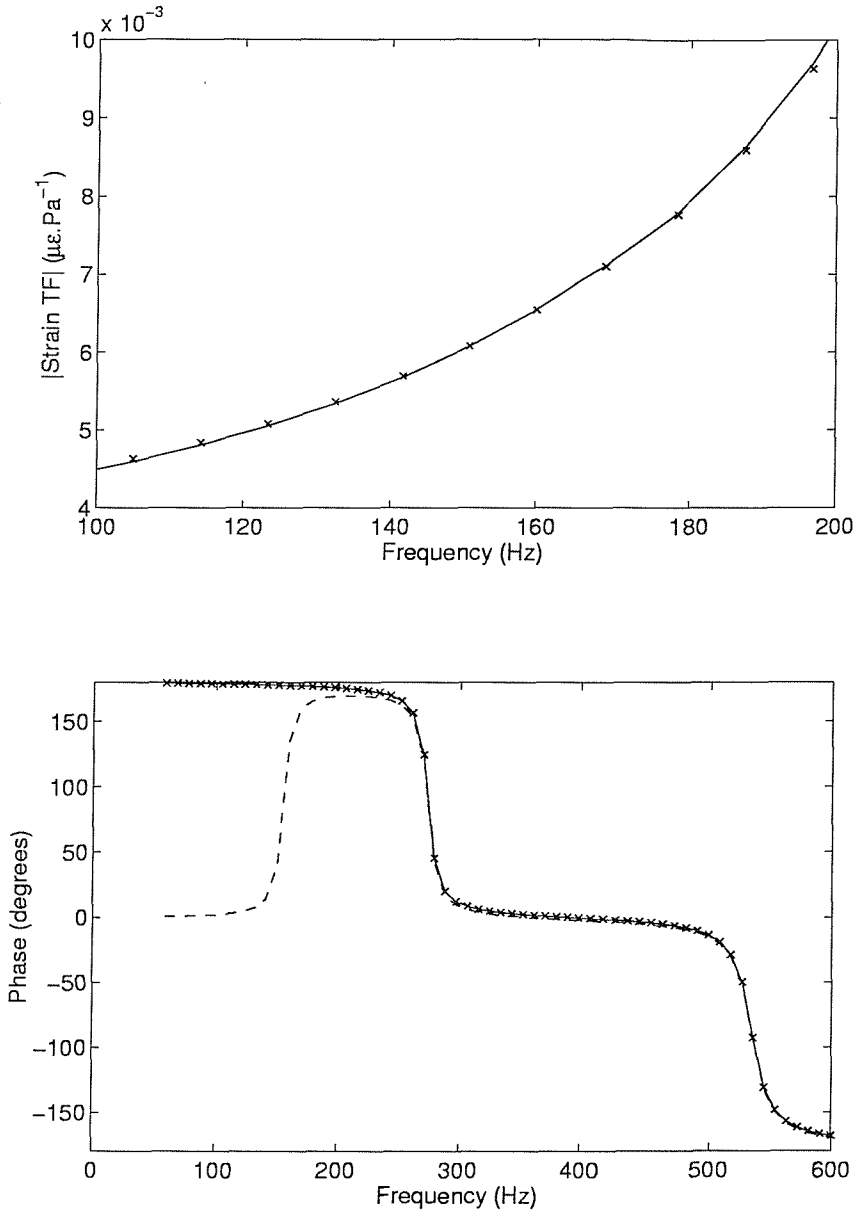

Figure 5.39: Absolute value of strain transfer function (upper plot - direct strain position 1 (-), direct strain position 2 (×), $\Delta x = 0.04m$), and phase (lower plot - position 1 (-), position 2 (×), difference between position 1 and 2 (- -)) for a flat sandwich panel, fully clamped along all four edges, a=0.9m, b=0.5m, all other specifications as per chapter 3, section 3.5.

In order to arrive at an estimate of the core shear strain in the experiments, the semi-empirical constants were calculated over a smaller bandwidth (30 Hz), centred on the predominant response frequency, and with a constant damping value equal to that given in table 5.9 for the three test panels. The results of the FE analyses are shown in figure 5.40, where the semi-empirical values are seen to be fairly constant with frequency over the reduced bandwidth, as expected. Estimates of the RMS core

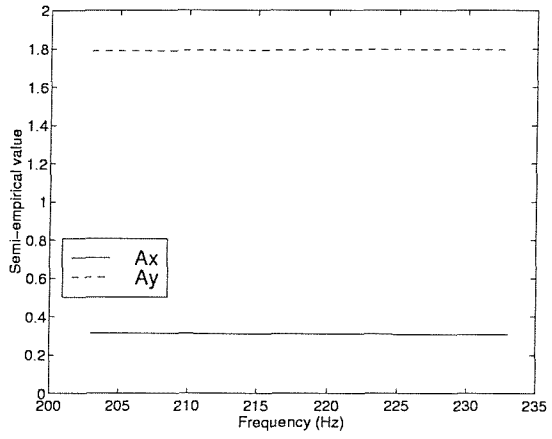

(a) Panel 1.

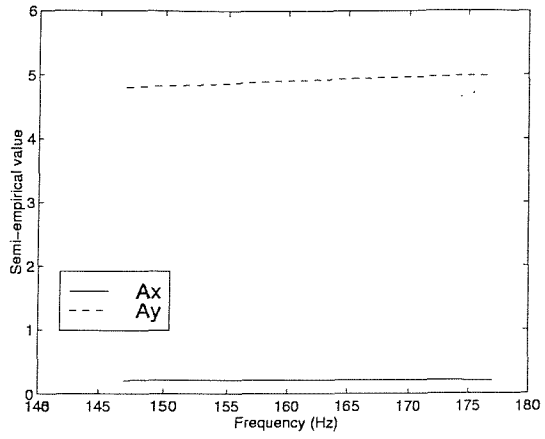

(b) Panel 2.

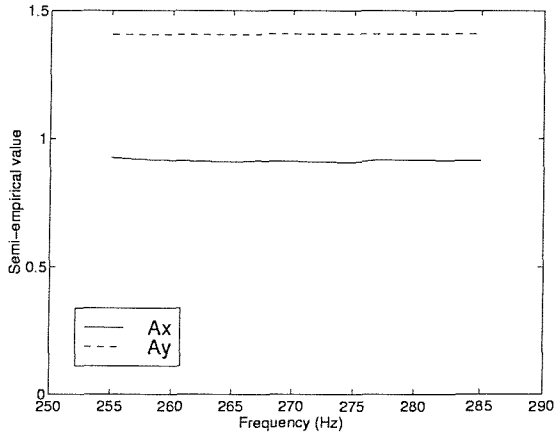

(c) Panel 3.

Figure 5.40: Semi-empirical values used in the estimates of core shear strain for each of the three test panels, calculated over a 30 Hz bandwidth centred on the fundamental resonant response frequency excited by the PWT.

shear strain were then obtained from the measured face plate strains. The transfer functions of the strain response for gauges gi2, gi3, gi4, and gi5 on the inner face

plate and go2, go3, go4, and go5 on the outer face plate were used in equation 5.13 to calculate the finite difference approximation, and equations 3.75 and 3.76 were used to estimate the RMS core shear strain using the calculated semi-empirical values given in table 5.10. The results are presented in table 5.10 for each of the three test panels. In addition to the average semi-empirical values, the percentage variation in these values over the 30 Hz bandwidth are given, which, as can be seen, are very small.

OASPL (dB)	$\overline{A_{xz}}$	Average % variation	$\overline{A_{yz}}$	Average % variation	RMS $\gamma_{est_{xz}}$ ($\mu\epsilon$)	RMS $\gamma_{est_{yz}}$ ($\mu\epsilon$)
Panel 1						
143.29					16.10	63.65
149.97					32.60	147.08
154.75	0.31	±0.24	1.79	±0.3	56.45	273.05
159.28					81.66	450.79
163.71					149.71	797.52
Panel 2						
143.88					7.29	117.93
149.91					9.38	187.88
154.92	0.21	±0.14	4.91	±6.1	15.50	295.21
159.00					25.21	498.81
163.09					45.44	892.15
Panel 3						
143.51					3.85	29.17
149.93					4.65	62.16
154.18	0.91	±0.48	1.41	±0.04	8.69	122.62
158.84					24.34	211.29
162.82					61.47	363.87

Table 5.10: Estimated core shear strain in the x and y directions at each OASPL (dB re 2×10^{-5} Pa), and the calculated semi-empirical values for the three doubly curved, symmetric-sandwich panels over a 30 Hz bandwidth centred on the first resonant response frequency.

In all three cases, the highest core shear strain was estimated for γ_{yz}, along the short side. The estimate of γ_{yz} was the greatest for panel 2, followed by panel 1 then 3, whilst the highest γ_{xz} was estimated for panel 1. The RMS values were calculated for a bandwidth centred on the fundamental response frequency, which is the first bending mode with a nodal line in the centre of the panel running along the y (short) dimension. This suggests that the high values of γ_{yz} are caused by the panels flattening out during this mode of response (since they are not fully constrained along the edges). The shear strains estimated in the core were found to be too low to cause

damage [56], since the shear strength of the core is 0.85MPa in the xz plane, and 0.8MPa in the yz plane. For the worst case of $892.15\mu\epsilon$ in the yz plane of panel 2, the stress is approximately 0.03MPa, which is well below the limit.

5.6 Concluding summary

In this chapter, the details of the high intensity testing of a set of four doubly curved sandwich panels has been presented. Measurements of the spatial variation of overall sound pressure levels across the length of the aperture of the ISVR progressive wave tube facility have been presented, and the presence of travelling waves along the aperture have been clearly shown.

The four test panels have been tested at levels from 142 dB to 164 dB, and the dynamic response has been measured using ten strain gauges located on the inner (facing) skin and the outer (backing) skin, near to the centre and the edge of the panels. The results clearly show a linear response, at all sound pressure levels, and the statistics of the recorded signals have been shown to be Gaussian with skewness values close to zero and kurtosis values close to three. This is an interesting result when one considers that the experiments conducted to determine the spatial characteristics on the PWT indicated non-Gaussian behaviour, particularly at the lower sound pressure levels. Not all of the modes excited during the free vibration experiments were excited during the PWT tests due to the symmetric pressure load on the panels. Much of the response of the four panels was in the fundamental mode, which was clearly highlighted by the plots of the integral of the PSD across the frequency band. However, for panels 3 and 4, the fundamental mode accounted for between 20% and 40% of the total response for the outer x-wise near-centre gauge. It is important to note at this stage that as long as the fundamental mode accounts for a large percentage of the overall RMS response, then this mode alone can confidently be used in calculations of the fatigue life of the structure. However, if higher modes account for a fair percentage of the overall response compared with the fundamental mode, or indeed if they predominate the overall response, then a multi-modal analysis will need to be conducted in order to calculate the fatigue life. This is where techniques such as Statistical Energy Analysis would be particularly useful.

The highest strains were recorded on the outer (backing) skin of panels 1 and 2. However, for panels 3 and 4, the highest strains were found to be on the inner (facing) skin. It follows that the introduction of double curvature, in this case a small short-side radius, can have a profound effect on the centre, or near-centre strains.

Outer-to-inner RMS strain ratios have also been presented, and have been found to be fairly constant with changing excitation level, particularly for gauges 1 and 2. The ratios for the symmetric sandwich configurations varied considerably from panel to panel. However for panel 1, which is the least curved of the panels, this ratio was between 2.5 and 3, which is consistent with the value of 2.5 quoted for flat rectangular sandwich panels [49, 15].

Measured modal damping values have been presented and compared with those obtained from the vibration experiments. The damping values for the fundamental mode were found to be substantially higher than the corresponding free vibration values, which has been attributed to the acoustic impedence effects introduced by the PWT aperture [15].

Finally, the semi-empirical method described in chapter 3 has been used to estimate the core shear strains developed in the core as a result of the random acoustic loading. The calculation of the finite difference approximation was modified in this chapter to take account of the additional membrane strains which were introduced as a result of the curvature of the panels. A finite element model of the panels supported by four circular springs (details of which can be found in the following chapter) was analysed with a unit pressure loading on one face over a frequency range from 60 Hz to 600 Hz and the resulting semi-empirical values obtained. These values were found to vary considerably over the frequency range, particularly for panel 1 at one frequency where the value seemed to tend asymptotically towards infinity. This variation was due to the FE estimate of the core shear strain tending to zero which was caused by the finite difference approximation approaching zero. One possible explanation was that the contribution to the total direct strain from the bending partial deflection was so small that the assumption of a negligible contribution from the shear partial deflection was no longer valid, hence the finite difference approximation at this frequency was not accurate enough to estimate the core shear strain. All of this suggests that further work needs to be done to separate the bending and shear partial deflections in the analysis. In addition, there is scope for refining the technique to take into account the shear deflection in the finite difference approximation, possibly using a combination of strain gauges and accelerometers which would enable the rate of change of direct strain and the rotation of the face plates to be measured. In order to arrive at an estimate for the core shear strain using the experimental measurements, the semi-empirical values were obtained over a smaller bandwidth centred on the fundamental response frequency. There was less variation in these values over this bandwidth, and estimates were obtained for the range of OASPLs tested using RMS face plate strains

over the reduced bandwidth. The greatest core shear strain was estimated close to the centre of the panels for γ_{yz} (along the short side) for all three panels, with panel 2 giving the highest strain levels, whereas the highest core shear strain γ_{xz} (along the long side) was estimated for panel 1.

Chapter 6

Development of the theoretical model using the finite element method

6.1 Introduction

The development of the finite element model used to analyse the doubly curved panels is presented in this chapter. The ANSYS^{TM} finite element package was used to construct the model and analyse the free vibration response of the doubly curved panels. The model developed here was then used to analyse the response of the panels to grazing incidence acoustic excitation in an attempt to predict the strain response of the panels when subject to random acoustic excitation in the PWT facility, which is presented in the next chapter.

6.2 Development of the model

The ANSYS^{TM} [65] finite element package was used to analyse the doubly curved panels. Due to the geometry of the panels and the complex lay-up details, particularly around the bevelled edge, the model was built by constructing the doubly curved surface in the global cartesian coordinate system and meshing this with SHELL91^{TM} elements. This is a layered element which offers the choice of a "sandwich option", whereby the middle layer is assumed to be thick (greater than 5/7 of the total thickness) and orthotropic, and is assumed to carry all of the transverse shear. The SHELL91^{TM} element has eight nodes with six degrees of freedom per node with the

option of nodal location at the top, middle or bottom surface. The complex bevelled edge region was initially modelled by modifying the real constants (specifically the lay-up details) for the elements [78], and the nodes where located along the bottom surface ($z = 0$) of each element to ensure that the flange and associated constraint nodes were located in the correct position, as shown in figure 6.1(a). The detail of the chamfer was not initially included since the influence of this detail on the natural frequencies of vibration for a panel having freely supported boundary conditions was deemed to be small. However, for any other boundary condition (simply supported or fully clamped), this chamfered region could have a profound effect [53], particularly in terms of the panel edge strains for a forced response analysis. The model was therefore made more representative by introducing the chamfer which was achieved by altering the element thickness real constants for the elements in this region. Both the initial and chamfered edge models, and the chamfer detail, are shown in figure 6.1 where the models have been plotted in terms of their real constant (thickness) values. The material properties used in the models are given in table 6.1, and the lay-up details are given in table 6.2.

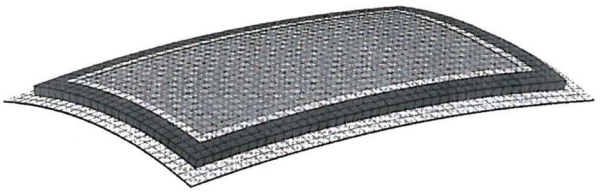

(a) Initial model (panel 1).

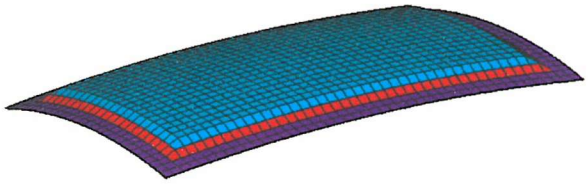

(b) Chamfered edge model (panel 1).

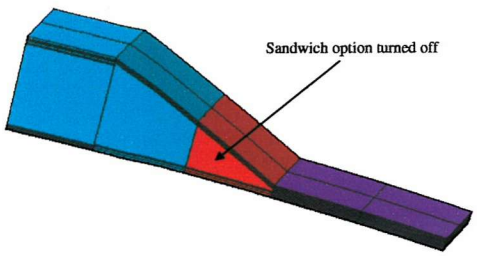

(c) Detail of the chamfer region.

Figure 6.1: Development of the Finite element model.

Layer	*Thickness* (m)	*Elastic Modulus* [Pa]		*Shear Modulus* [Pa]				*Density* $[kg/m^3]$	*Poisson's Ratio*
		E_{11}	E_{22}	E_{33}	G_{12}	G_{xz}	G_{yz}		
CFRP†	0.25e-3	57.93e9	57.93e9	-	3.7e9	-	-	1518.0	0.04
Honeycomb	19.0e-3	0	0	120e6	0	35e6	20e6	48.0	-

Table 6.1: Material specifications for the experimental test panels. † Properties obtained using cured test specimens with $[0_4]$ and $[45_4]$ ply lay-up and with 60% fibre volume fraction.

Layer	Panels 1, 2, and 3		Panel 4	
	Number of plies	*Ply orientation*	*Number of plies*	*Ply orientation*
Facing skin	4	$[0/45]_s$	2	$[0]_2$
Doublers	2	[0/30]	2	[0/30]
Spacers	2	$[0_2]$	2	$[0_2]$
Edge pan	3	[0/45/0]	3	[0/45/0]
Backing skin	4	$[0/45]_s$	6	$[0/45/0]_s$

Table 6.2: Ply lay-up details for the experimental test panels.

6.3 Finite element results

Both models were analysed with freely supported boundary conditions, using a networked Sun machine which was one of eight 60 MHz processors (each with floating point unit) controlled by a SunSPARC Server 1000. The predicted natural frequencies for the first four non rigid body modes are shown in table 6.3 for both the initial and chamfered edge models and for all four panel geometries. These results are compared with resonance frequencies obtained from the experiments and the percentage difference is indicated, although the difference values do not take into account uncertainties in the experiment and FE analysis. The results obtained do however show excellent agreement when compared with the experimental results for the lower natural frequencies of vibration. All of the models had approximately 23000 active degrees of freedom (DOF's) with $\sim$ 1200 elements, and the CPU time to obtain the first four non-rigid body modes was $\sim$ 1080 seconds (total elapsed time $\sim$ 2100 seconds). In order to check the convergence of the results, a finer mesh was used giving 90000 to 93000 active DOF's ($\sim$ 5000 elements). This resulted in a change in the predicted natural frequencies of $\approx 0.7\%$ compared with the coarser mesh model. The processing time however was significantly increased (CPU time $\sim$ 14600 seconds, total elapsed time $\sim$ 17700 seconds) and it was highly probable that the limits of the solver were being reached with so many active DOF's. Therefore, the models with approximately 23000 active DOF's were considered accurate enough for use in further investigations. Comparison is also made between the initial and chamfered edge model. The main

drawback with the chamfered edge model is that when using SHELL91^{TM} elements, the "sandwich option" cannot be used where the core is less than 5/7 of the total thickness. Therefore the "sandwich option" had to be turned off in part of the chamfered region, as shown in figure 6.1(c). This had the effect of introducing extra stiffness into the model since the middle core layer of the elements in this region cannot carry all of the transverse shear. This effect is seen in table 6.3 where the predicted natural frequencies are slightly higher than those obtained using the initial model. The main drawback with the initial model is the discontinuity introduced in the layup around the bevelled edge region. Although not necessarily a problem in terms of predicting natural frequencies of vibration for panels with freely supported boundary conditions, the model would produce a discontinuous strain distribution around the bevelled edge region for any other boundary condition when conducting a forced response analysis. It can be said, therefore, that the chamfered edge FE model can be used with confidence for predicting the natural frequencies of vibration of the doubly curved sandwich panels, which is reinforced when one compares the first three mode shapes obtained from the FE analysis with those obtained experimentally, as shown in figures 6.2 and figures 4.3 to 4.9 respectively. The chamfered edge FE model will be validated further by comparing strains obtained from PWT tests at a later stage in the study.

Measured (Hz)	ANSYS Results (Initial Model) (Hz)	Difference (%)	ANSYS Results (Chamfered edge Model) (Hz)	Difference (%)
Panel 1				
136.0	134.4	-1.2	139.3	-2.4
214.6	217.4	1.3	221.7	-3.2
282.6	275.8	-2.4	284.5	-0.67
352.1	367.2	4.3	370.8	-5.04
Panel 2				
131.5	130.5	-0.75	134.2	-2.0
164.7	166.0	0.75	169.3	-2.7
269.0	260.2	-3.3	270.2	-0.44
343.1	347.8	1.4	349.7	-1.9
Panel 3				
130.9	127.9	2.3	132.7	-1.4
264.5	278.1	-4.9	279.7	-5.4
280.9	294.0	-4.4	302.8	-7.2
320.4	340.7	-5.9	345.0	-7.1
Panel 4				
74.7	75.0	0.4	76.6	2.5
233.2	245.6	5.3	250.9	7.6
279.3	291.5	4.4	290.0	3.8
312.4	322.7	3.3	322.3	3.2

Table 6.3: Comparison of measured and predicted resonance/natural frequencies of the four freely supported test panels.

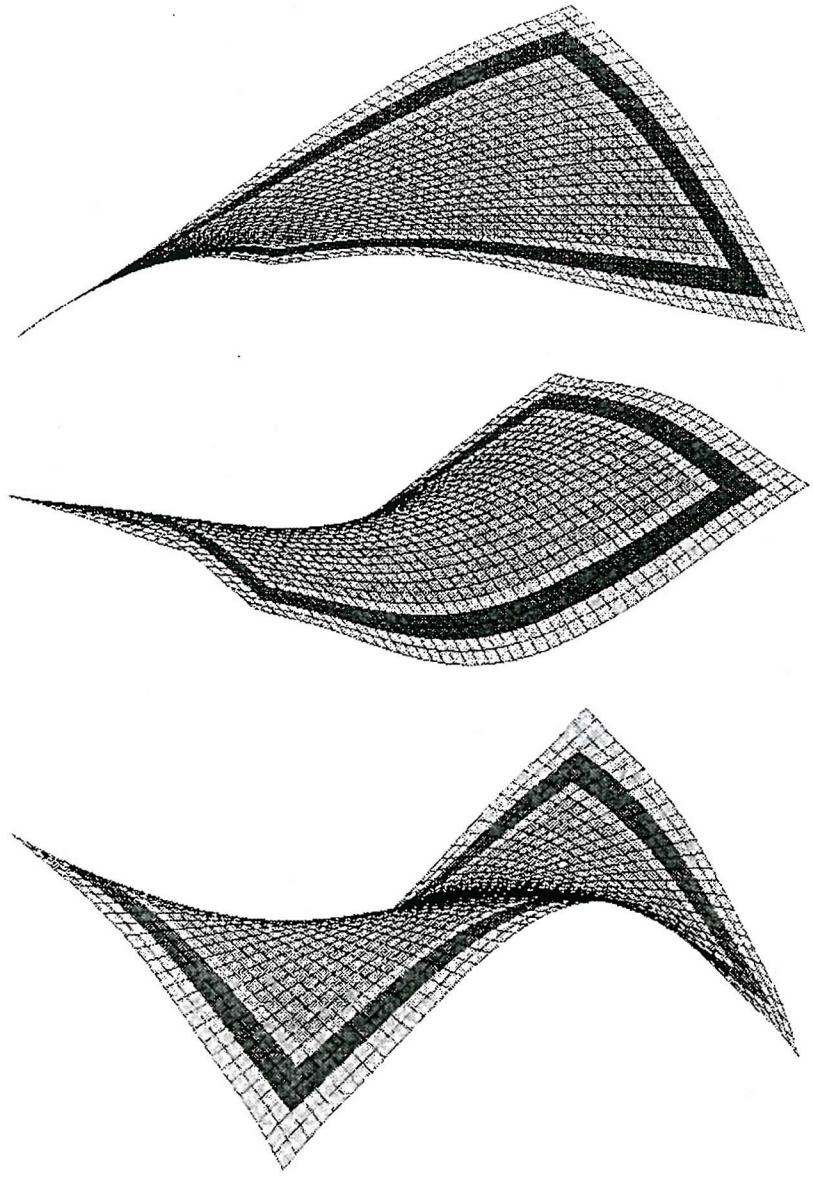

Figure 6.2: The first three mode shapes (FE), panel 1.

6.4 Parameter studies using the finite element model

The chamfered edge FE model was used to investigate the effects of various design parameters on the natural frequencies of vibration of doubly curved rectangular sandwich panels with various boundary conditions. In all cases the surface area of the panels was kept constant along with the number of plies, ply thicknesses, Young's modulii, and the ply and core densities.

6.4.1 The effect of the radii of curvature on the first four natural frequencies of vibration

The effect of changing radii of curvature on the natural frequencies of vibration was investigated for a panel having the dimensions $a = 0.915m \times b = 0.531m$, material properties as shown in table 6.1, and a lay-up as shown in table 6.2. Three boundary conditions were considered; freely supported, fully clamped along all four edges, and "pinned" whereby the translational degrees of freedom were constrained along all four edges (the nodes were aligned with the global cartesian coordinate system, hence in plane motion was not constrained in this case). Four long side radii cases, $R_x = 0.5m$, $R_x = 1.0m$, $R_x = 2.0m$, and $R_x = 10.0m$ were considered, and the short side radius was varied between 0.4m and 4m for each of these four cases.

The results for the freely supported boundary condition are shown in figure 6.3. For all of the long side radii cases considered here the fundamental natural frequency is relatively invariant with changes in the short side radius of curvature, which is understandable since the surface area has been kept constant and this frequency corresponds to the first torsional mode of vibration, as indicated on the figure. A slight decrease in the fundamental frequency is observed for short side radii smaller than 0.8m for all four long side radii cases, whereas the second and third natural frequencies exhibit an increase in frequency with decreasing short side radius. The second natural frequency is associated with the first bending mode of vibration, and the effect of decreasing the short side radius of curvature results in a rapid increase in the frequency of vibration which is more apparent for $R_x = 10.0m$, a case which tends towards to that of a singly curved panel. In fact, as the panels become more doubly curved, the effect of changing the radii of curvature appears less pronounced for the freely supported boundary condition. For the case of $R_x = 0.5m$, the fundamental frequency corresponds with the first bending mode of vibration for short side radii down to $R_y = 1.2m$, at which

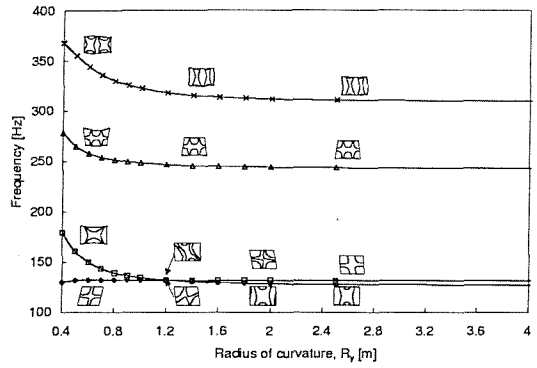

(a) R_x=0.5 m

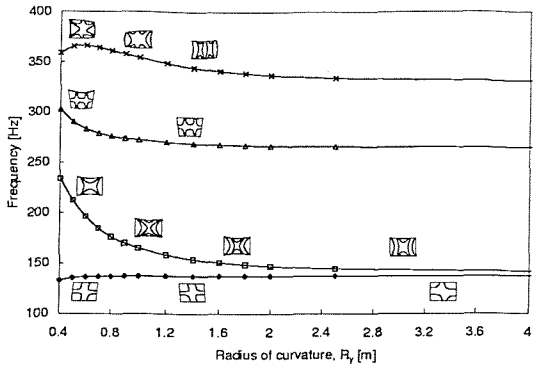

(b) R_x=1.0 m

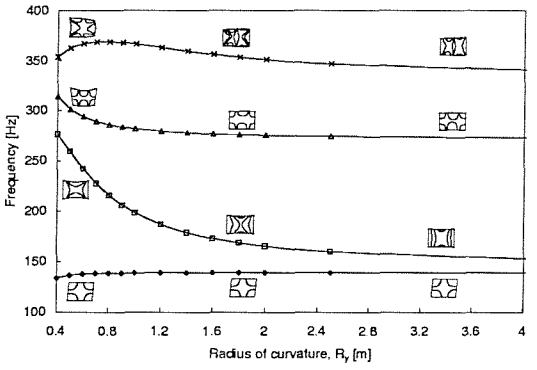

(c) R_x=2.0 m

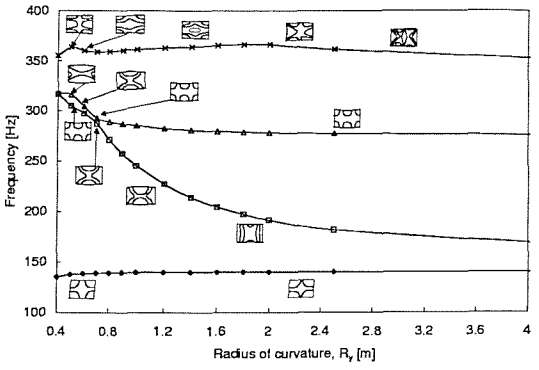

(d) R_x=10.0 m

Figure 6.3: Effect of changing radius of curvature (R_y - short side) on the first four natural frequencies. Freely supported. (Key to natural frequency number: ◇: I, □: II, △: III, ×: IV).

point the curves for the first and second natural frequency appear to almost touch and after which the torsional and bending modes appear to interchange as the curves veer away from each other. This phenomenon, known as "curve veering", has been well reported by many authors [79, 80, 81, 82, 83], and can be clearly seen for the "pinned" and fully clamped cases, as shown in figures 6.4 and 6.5 respectively. Here, reducing the short side radius of curvature has the effect of increasing the natural frequencies of vibration, although it is interesting to note that for $R_x = 2.0m$ and $R_x = 10.0m$, and for both boundary conditions, the frequency of vibration of the (1,2) mode seems to be relatively invariant with decreasing R_y down to $1.2m$, after which it increases. For the case of $R_x = 0.5m$ and for both "pinned" and fully clamped boundary conditions, the first four natural frequencies increase at approximately the same rate with very little

interchange of the mode shapes occurring. At lower values of R_y, the fundamental frequency tends to decrease with reducing short side radius of curvature, which does not occur for the other three long side radius cases. In addition, the mode shapes become more complicated at lower values of R_y, especially for the $R_x = 0.5m$ case.

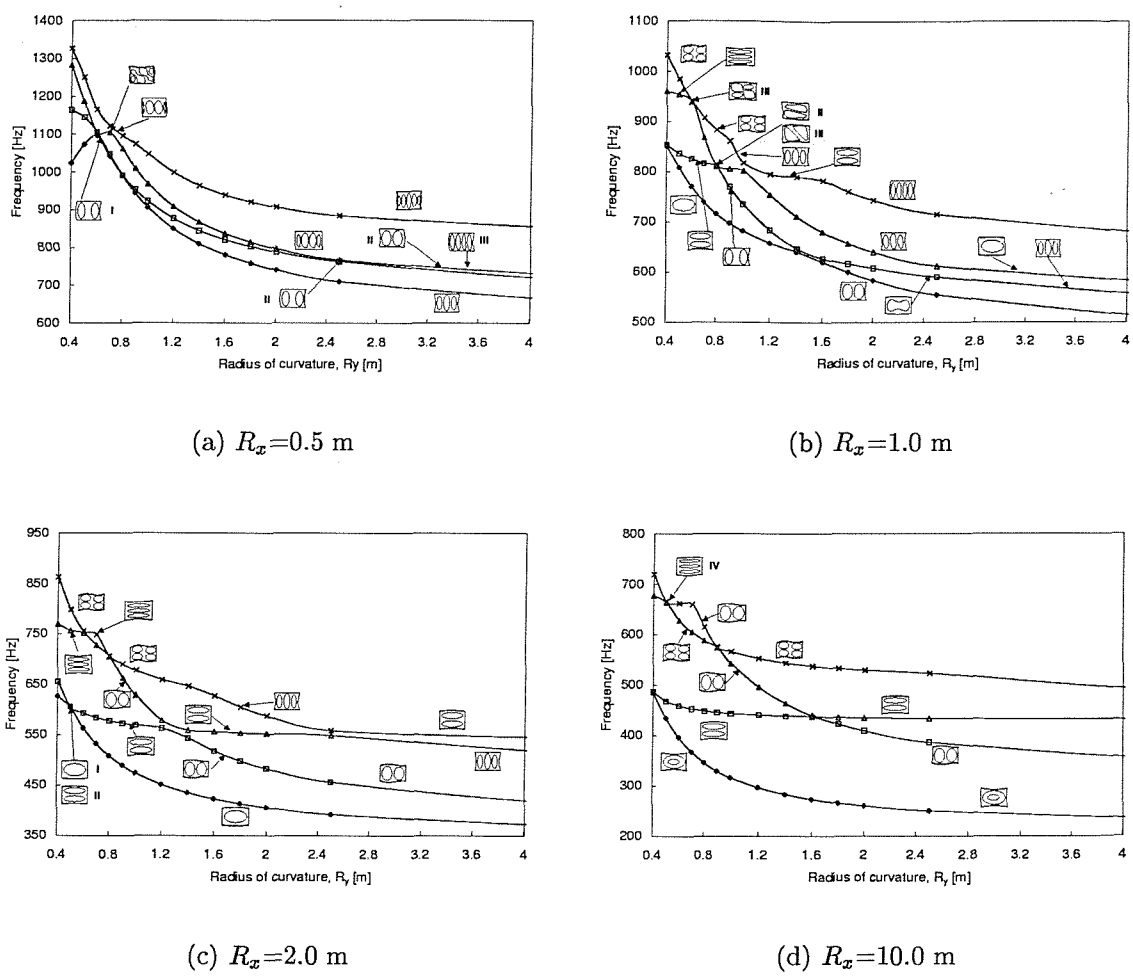

(a) R_x=0.5 m

(b) R_x=1.0 m

(c) R_x=2.0 m

(d) R_x=10.0 m

Figure 6.4: Effect of changing radius of curvature (R_y - short side) on the first four natural frequencies. "Pinned" along all four edges. (Key to natural frequency number: ◇: I, □: II, △: III, ×: IV).

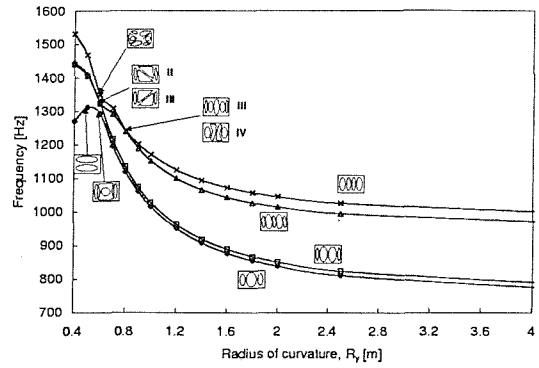

(a) R_x=0.5 m

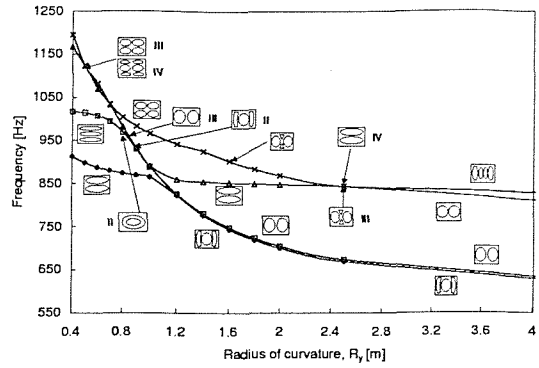

(b) R_x=1.0 m

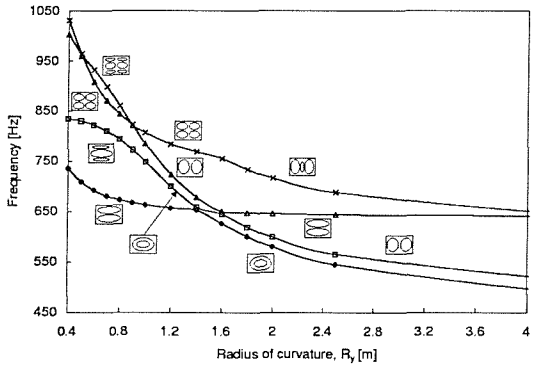

(c) R_x=2.0 m

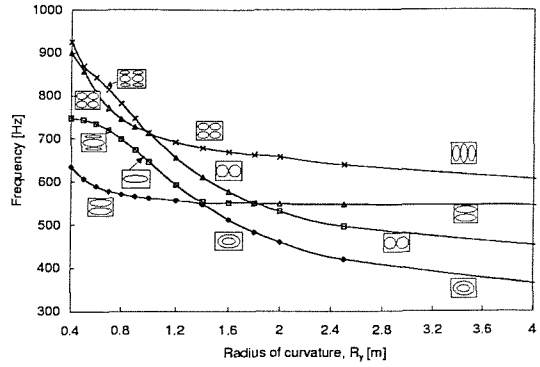

(d) R_x=10.0 m

Figure 6.5: Effect of changing radius of curvature (R_y - short side) on the first four natural frequencies. Fully clamped on all four edges. (Key to natural frequency number: ◇: I, □: II, △: III, ×: IV).

6.4.2 The effect of the orthotropy of the core on the first four natural frequencies of vibration

A sensitivity study was carried out to study the effect of changing the orthotropy of the core, which is represented by the ratio G_{xz}/G_{yz}, on the natural frequencies of vibration. The ratio was varied between 0.1713 and 1.256 (corresponding to -70% to +120% change about the original ratio of $G_{xz}/G_{yz} = 20/35 = 0.571$) by keeping the value G_{xz} constant whilst varying G_{yz}. Both low and high shear stiffnesses were considered; G_{xz}=20 MPa and G_{yz} varying between 15.92 MPa and 116.75 MPa, and with both G_{xz} and G_{yz} reduced by an order of magnitude respectively. Three panel cases were investigated; $R_x = 3.5m \times R_y = 1.0m$, $R_x = 1.2m \times R_y = 1.0m$, and

$R_x = 3.5m \times R_y = 0.5m$ with the dimensions $a = 0.915m \times b = 0.531m$ and with "pinned" and fully clamped boundary conditions. All other lay-up details and material properties were as detailed in tables 6.2 and 6.1 respectively. Figure 6.6 shows the

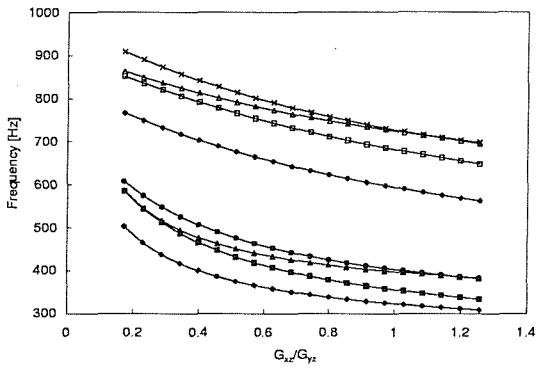

(a) R_x=3.5 m, R_y=1.0 m

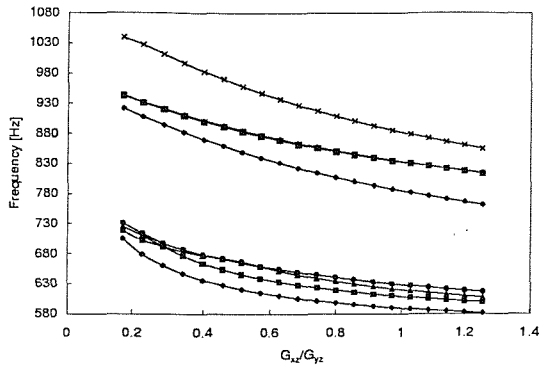

(b) R_x=1.2 m, R_y=1.0 m

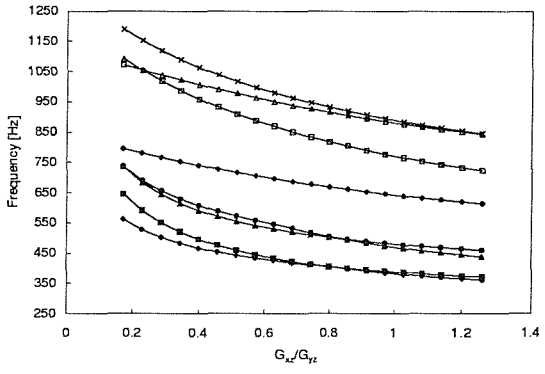

(c) R_x=3.5 m, R_y=0.5 m

Figure 6.6: Effect of changing orthotropy on the first four natural frequencies. Fully clamped along all four edges. (Key to natural frequency number: High shear stiffness: ◇: I, □: II, △: III, ×: IV. Low shear stiffness ($G_{xz}/10$, $G_{yz}/10$): ♦: I, ■: II, ▲: III, •: IV).

result for the fully clamped boundary condition and for all three panel cases. The natural frequencies of vibration are seen to increase as the orthotropy varied between $0.1713 < G_{xz}/G_{yz} < 1.256$, i.e. as G_{yz} is increased. In all three cases, the rate of change of frequency with changing orthotropy is moderate, so from the point of view of sensitivity, small changes in the orthotropy about a certain value do not produce large changes in the frequencies of vibration. This rate of change is approximately the same for the high and low shear stiffness cases for othotropic ratio values above

approximately 0.6. Below this, the lower shear stiffness core creates a sharper increase in frequency with decreasing orthotropy. Very little veering is observed with the fully clamped boundary condition, compared with the "pinned" boundary condition which is shown in figure 6.7. The veering phenomenon can be clearly seen in figure 6.7(c) (inset), where a larger set of results have been obtained between $G_{xz}/G_{yz} = 0.86$ and $G_{xz}/G_{yz} = 0.9$ for the fourth and fifth natural frequencies of vibration. The effect of changing orthotropy appears to be less pronounced for the "pinned" case than for the fully clamped case, particularly for the fundamental natural frequency and for both high and low shear stiffness cores. In addition, the first four frequencies for the higher shear stiffness case are spread over a greater frequency band compared to the lower shear stiffness case, which can also be observed for the fully clamped boundary condition.

6.4.3 The effect of ply orientation on the first four natural frequencies of vibration

The final parameter study was concerned with investigating the effect of changing ply orientation on the first four natural frequencies of vibration for the same three panel cases as those considered in the previous sub-section and for the "pinned" and fully clamped boundary conditions. The material properties used were those as given in table 6.1, and the panel dimensions were again $a = 0.915m \times b = 0.531m$. Due to the large number of possible ply lay-ups, it was decided to investigate the change in orientation of the middle two layers of both the facing and backing skin, which were varied between 0° and 90° in 5° steps, whilst keeping the outer plies at 0° . The results for the "pinned" case are shown in figure 6.8. As expected the results are symmetric about 45° due to the use of a balanced plain weave material which has identical properties in the two orthogonal directions E_x and E_y. The greatest change in frequency with ply orientation is for the $R_x = 1.2m \times R_y = 1.0m$ case, where changes in mode shape are observed for the third and fourth natural frequencies of vibration, which could probably be ascribed to veering with a much higher frequency, or the well known phenomenon of nodal lines aligning with the direction of dominant fibre reinforcement. In addition, it is interesting to note that the second natural frequency of vibration which again corresponds to the (1,2) mode, shows very little variation in frequency with the change in the parameter between 30° and 45° , particularly for the $R_x = 3.5m \times R_y = 1.0m$ case which shows little variation between 0° and 45° . Slight changes in the mode shape are observed with changes in the parameter,

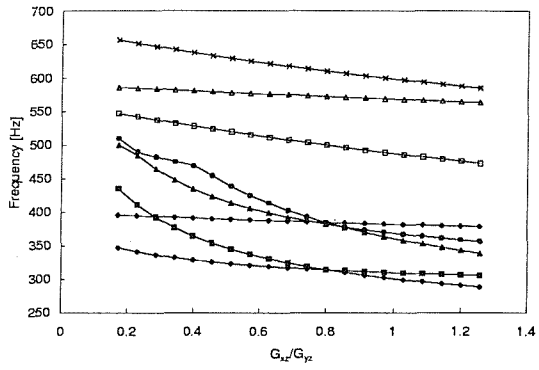

(a) R_x=3.5 m, R_y=1.0 m

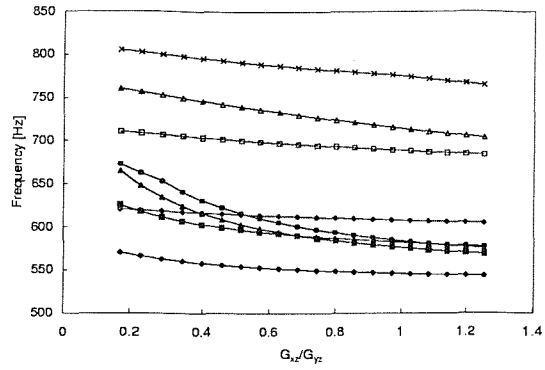

(b) R_x=1.2 m, R_y=1.0 m

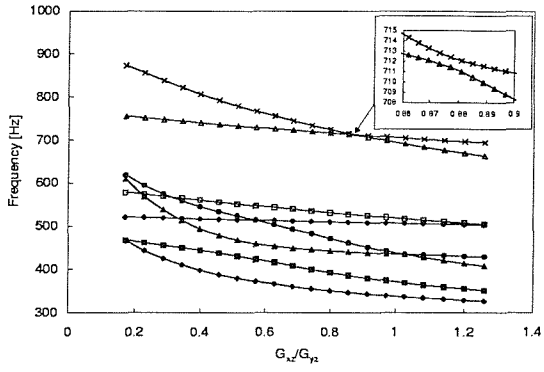

(c) R_x=3.5 m, R_y=0.5 m

Figure 6.7: Effect of changing orthotropy on the first four natural frequencies. "Pinned" along all four edges. (Key to natural frequency number: High shear stiffness: ◇: I, □: II, △: III, ×: IV. Low shear stiffness ($G_{xz}/10$, $G_{yz}/10$): ♦: I, ■: II, ▲: III, •: IV).

but no veering occurs, except for the fourth natural frequency of vibration for the $R_x = 3.5m \times R_y = 0.5m$ case. The results for the fully clamped boundary condition are shown in figure 6.9. The results are again symmetric about the 45° ply orientation. The greatest change in frequency with variation in ply angle is observed for the $R_x = 3.5m \times R_y = 0.5m$ case, and the second natural frequency of vibration corresponding to the (1,3) mode is seen to show very little variation with changes in the parameter. Veering occurs more readily in all three cases, especially in the $R_x = 1.2m \times R_y = 1.0m$ case, compared with figure 6.8.

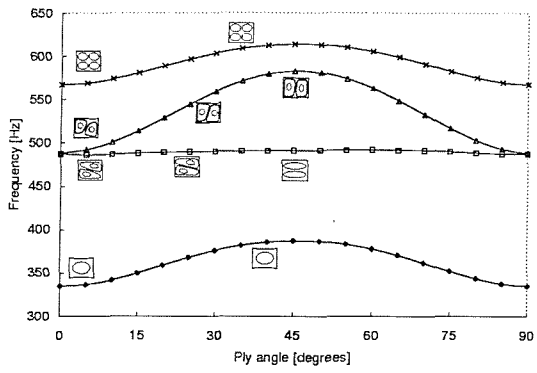

(a) R_x=3.5 m, R_y=1.0 m

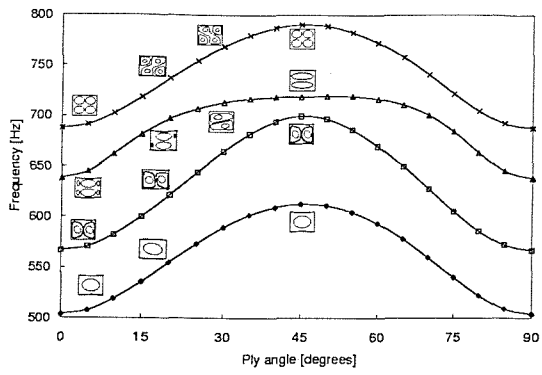

(b) R_x=1.2 m, R_y=1.0 m

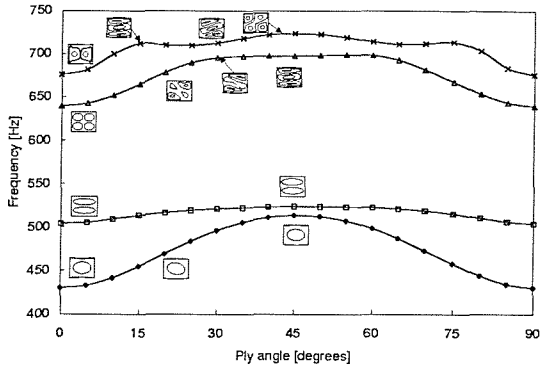

(c) R_x=3.5 m, R_y=0.5 m

Figure 6.8: Effect of changing ply angle (middle two plies in the facing and backing skins) on the first four natural frequencies. "Pinned" along all four edges. (Key to natural frequency number: ◇: I, □: II, △: III, ×: IV).

6.4.4 A summary of the major sensitivities

A relatively large amount of information has been presented concerning the effects of the various design parameters on the first four natural frequencies of vibration of doubly curved composite sandwich panels. Therefore, a brief summary of the major sensitivities is given below:

- For both the "pinned" and fully clamped boundary conditions, the panels with a long side radius of $R_x = 0.5m$ show the greatest overall change in frequency with variation in the short side radius R_y.
- The natural frequency associated with the (1,2) mode of vibration appears to be

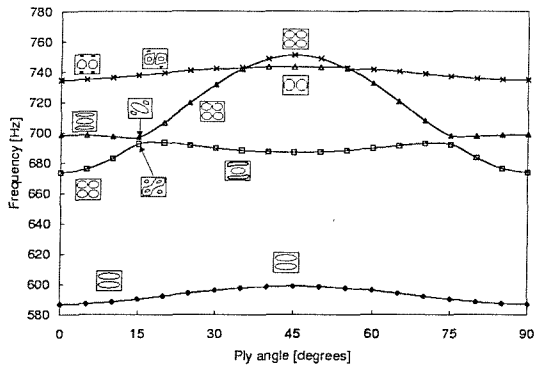

(a) R_x=3.5 m, R_y=1.0 m

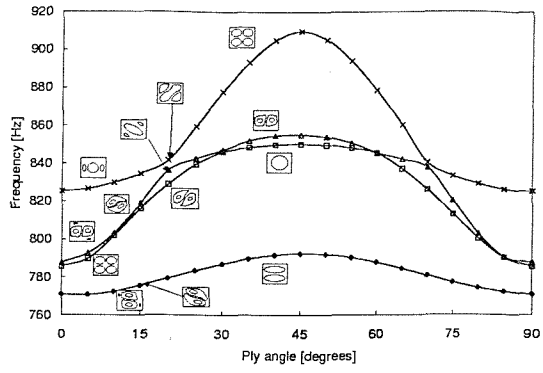

(b) R_x=1.2 m, R_y=1.0 m

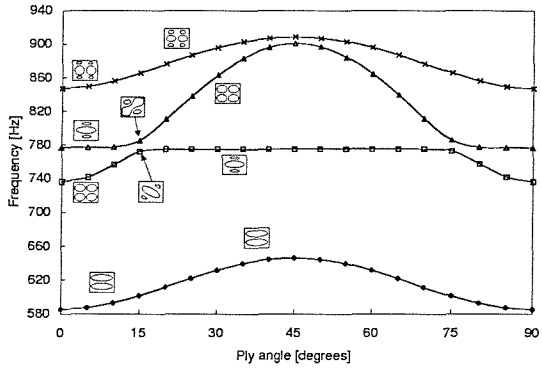

(c) R_x=3.5 m, R_y=0.5 m

Figure 6.9: Effect of changing ply angle (middle two plies in the facing and backing skins) on the first four natural frequencies. Fully clamped along all four edges. (Key to natural frequency number: ◇: I, □: II, △: III, ×: IV).

relatively insensitive to changes in both the radius of curvature and ply orientation parameters for both the "pinned" and fully clamped boundary conditions.

- For the structures investigated, as the short side radius of curvature is reduced below $R_y \approx 2.0m$, the rate of change of frequency increased with decreasing short side radius for all long side radii cases for both "pinned" and fully clamped boundary conditions. Therefore the natural frequency appears to become more sensitive to changes in the parameter below $R_y \approx 2.0m$. From a practical point of view, considering the engine intake barrel panel, the smaller engine intakes would be more sensitive to changes in the geometry in terms of the radii of curvature compared to the larger engine intakes.

- The natural frequencies of vibration appear to be less sensitive to changes in the orthotropy of the core for the range of core shear modulii considered for both "pinned" and fully clamped boundary conditions.

- For the "pinned" boundary condition case, the high shear stiffness core is less sensitive to changes in orthotropy than the low shear stiffness core. This effect was reported by Jacobson [84] for studies carried out on flat sandwich panels with orthotropic cores and simply supported boundary conditions. In addition, the fundamental mode appears to be least sensitive to changes in the parameter for the $R_x = 1.2m \times R_y = 1.0m$ case with "pinned" boundary conditions.

- A comparison between fully clamped and "pinned" boundary conditions shows that the former case results in an increased sensitivity to changes in the orthotropy, particularly for the high shear stiffness core.

- For "pinned" boundary conditions, the $R_x = 1.2m \times R_y = 1.0m$ case shows the greatest sensitivity to changes in the ply orientation in terms of the fundamental natural frequency of vibration. For fully clamped boundary conditions, it is the $R_x = 3.5m \times R_y = 0.5m$ case which results in the greatest overall change in the fundamental natural frequency with changing ply orientation. For both boundary conditions, the $R_x = 3.5m \times R_y = 1.0m$ case shows the least sensitivity to changes in ply orientaion in terms of the fundamental natural frequency.

6.5 Concluding summary

The development of the finite element models which will be used to analyse the response of the doubly curved sandwich panels to random acoustic excitation has been presented here. The initial models were analysed with freely supported boundary conditions, and the comparison of natural frequencies with measured resonance frequencies was very good.

Parameter studies have been carried out using the finite element model to investigate the effects of changing radii of curvature, orthotropy of the core, and ply orientation on the natural frequencies of vibration for several boundary conditions, and a summary of the major sensitivities has been presented. The curve veering phenomenon has been observed when changing these parameters, particularly in the case of changing radii of curvature and ply orientation. As a certain parameter is varied, the system eigenfunctions are said to be coupled when this variation produces curve

veering [80]. It has been demonstrated that veering can occur in continuous systems as well as those represented by a discretized (approximate) model [81, 80], indicating that it is not always a result of the approximation method or errors in numerical calculations [79]. For the case presented here, it is not clear whether veering is a result of the approximation method used or is actually occuring in the physical system.

The work presented in this chapter has clearly demonstrated the effects of various design parameters on the first few natural frequencies of vibration of doubly curved composite honeycomb sandwich panels. There is scope for further work here which could include the application of curve-fitting techniques such as least-squares to the curves presented in this chapter. It would then be possible to derive numerical formulae that would relate the fundamental frequencies of this type of panel to the design parameters such as the radius of curvature and orthotropic properties of the core. Although approximate, these formulae could be useful for the designer to outline the dynamic performance of a doubly curved sandwich panel.

Chapter 7

Dynamic response prediction of the acoustically excited, doubly curved sandwich panels

7.1 Introduction

Three methods which were used to predict the dynamic response of doubly curved composite honeycomb sandwich structures to random acoustic excitation are presented in this chapter. The first is based on the single-degree-of-freedom approach where the modes of vibration are assumed to be lightly damped and well separated. The predominant mode of vibration, which is usually the fundamental mode, is therefore treated as a single-degree-of-freedom system. The equations for a system subject to random excitation are developed in this chapter, and are applied to the case of the doubly curved sandwich panels. Three different solution cases are investigated, which involve estimating the spatial characteristics of the pressure loading. The finite element model, presented in the preceding chapter, was then used to provide the modal inputs to the equations from which the RMS response was calculated. The results are compared with the RMS measured response as presented in chapter 5. Comparisons are also made with the solution using Blevins method [43]. Finally, the finite element model is used to predict the response by considering the load as a series of travelling harmonic waves at grazing incidence to the surface of the structure. The harmonic solution is then used, together with the measured pressure spectrum, to arrive at an estimate of the strain power spectral density, which is again compared with the measured strain PSD. In addition to comparing the predicted and measured face plate

strain results, the predicted core shear strain is compared with the estimates made in chapter 5 using the technique developed in chapter 3. At the end of the chapter, conclusions are drawn with regard to the advantages and disadvantages of the three dynamic response prediction methods, and recommendations are made for further work.

7.2 The single-degree-of-freedom approximation

The classical approach used to predict the response of plate-type structures to random acoustic loading is based on the method originally developed by Miles [25], and subsequently refined by Powell [27] and Clarkson [8]. At low frequencies, the modes of vibration of a structure are generally well separated in frequency, and assuming the modal damping is small, approximations can be made to model each mode of vibration as a single-degree-of-freedom system. The response of a system in a single mode to a distributed pressure, $p(\mathbf{x}, t)$, where $\mathbf{x} = (x, y, z)$ is the spatial vector, is given by:-

$$y(\mathbf{x}, t) = w(t)\phi_n(\mathbf{x}) \tag{7.1}$$

where $w(t)$ is the modal amplitude, and $\phi_n(\mathbf{x})$ is the mode shape. Now, for a single-degree-of-freedom system, the equation of motion is:-

$$m_n\ddot{w}(t) + c_v\dot{w}(t) + k_s w(t) = f(t) \tag{7.2}$$

At resonance, the stiffness $k_s = \omega_n^2 m_n$ and the viscous damping $c_v = 2\zeta_n\omega_n m_n$, therefore,

$$\ddot{w}(t) + 2\zeta_n\omega_n\dot{w}(t) + \omega_n^2 w(t) = F_n(t) \tag{7.3}$$

where ω_n is the radian frequency of the n^{th} mode of vibration, and ζ_n is the modal damping ratio, m_n is the modal mass, and,

$$F_n(t) = \frac{\int p(\mathbf{x}, t)\phi_n(\mathbf{x})d\mathbf{x}}{\int m\phi_n^2(\mathbf{x})d\mathbf{x}} \tag{7.4}$$

Here, the numerator is the generalised force and the denominator is the generalised mass, with m being the mass per unit area. Assuming $F_n(t) = e^{i\omega t}$ and $w(t) = \mathbf{H}(\omega)e^{i\omega t}$, then the substitutions $\dot{w}(t) = i\omega\mathbf{H}(\omega)e^{i\omega t}$ and $\ddot{w}(t) = -\omega^2\mathbf{H}(\omega)e^{i\omega t}$ can be

made in equation 7.3 to give [71]:-

$$(-\omega^2 + (2\zeta_n\omega_n)i\omega + \omega_n^2)\mathbf{H}(\omega) = 1 \tag{7.5}$$

where t is the time, i is a complex number, and $\mathbf{H}(\omega)$ is the frequency response function. In general, where x is the system input, and y is the system output, the mean square response is given by [71, 72]:-

$$E[y^2] = \int_{-\infty}^{\infty} S_{yy}(\omega)d\omega = \int_{-\infty}^{\infty} |\mathbf{H}(\omega)|^2 S_{xx}(\omega)d\omega \tag{7.6}$$

It should be noted that the input auto-spectral density, $S_{xx}(\omega)$ and the output auto-spectral density, $S_{yy}(\omega)$ are both two-sided, that is they range from $-\infty$ to $+\infty$. In practice, the frequency range is from 0 to $+\infty$, therefore a physically measurable one-sided spectral density must be substituted, where [72]:-

$$S_{xx}(\omega) = \frac{G_{xx}(\omega)}{2} \tag{7.7}$$

Hence, in general,

$$\sigma_y^2 = E[y^2] = \frac{1}{2}\int_{-\infty}^{\infty} |\mathbf{H}(\omega)|^2 G_{xx}(\omega)d\omega \tag{7.8}$$

Therefore, the mean square response of the single-degree-of-freedom system to a broadband random excitation becomes:-

$$\sigma_w^2 = \frac{1}{2}\int_{-\infty}^{\infty} \left| \frac{1}{-\omega^2 + (2\zeta_n\omega_n)i\omega + \omega_n^2} \right|^2 G_n(\omega)d\omega \tag{7.9}$$

where $G_n(\omega)$ is defined as the input random excitation spectrum which is defined by both the spatial and temporal aspects of the excitation pressure. A set of closed form solutions to this type of integral can be found in [71], and are of the form,

$$\int_{-\infty}^{\infty} \left| \frac{i\omega B_1 + B_0}{-\omega^2 A_2 + i\omega A_1 + A_0} \right|^2 d\omega = \frac{\pi(A_0 B_1^2 + A_2 B_0^2)}{A_0 A_1 A_2} \tag{7.10}$$

Hence, the solution to equation 7.9 is:-

$$\sigma_w^2 = \frac{\pi G_n(\omega)}{4\zeta_n\omega_n^3} \tag{7.11}$$

Now, consider a pressure loading applied to the structure whose response is being approximated to that of a single-degree-of-freedom system,

$$p(\mathbf{x},t) = p(t)\psi(\mathbf{x}) \tag{7.12}$$

where $\psi(\mathbf{x})$ defines the spatial distribution of the loading, which will equal unity for a uniform pressure loading. The assumption of a pressure field with separable spatial and temporal characteristics in equation 7.12 is only true for certain pressure fields such as travelling waves, where the spatial characteristics are deterministic at each frequency. That is to say, the pressure field has a frequency dependent transfer function that exists between the pressure at point $\mathbf{x}$ and the pressure at a reference point. Defining $G_p(\mathbf{x},\omega)$ as the spectrum of $p(\mathbf{x},t)$, and $G_0(\omega)$ as the spectrum of the pressure $p(t)$, then equation 7.12 becomes,

$$G_p(\mathbf{x},\omega) = G_0(\omega)\psi^2(\mathbf{x}) \tag{7.13}$$

and taking the space average of this equation leads to,

$$< G_p(\mathbf{x},\omega) >_x = G_0(\omega) < \psi^2(\mathbf{x}) >_\mathbf{x} \tag{7.14}$$

Defining $G_p(\omega) =< G_p(\mathbf{x},\omega) >_x$, an expression for the spectrum of the pressure, $p(t)$ can be written,

$$G_0(\omega) = \frac{G_p(\omega)}{< \psi^2(\mathbf{x}) >_\mathbf{x}} \tag{7.15}$$

In the special case of a homogeneous pressure field, $G_p(\omega)$ is equal to the pressure spectrum measured as a single point. In other cases it is defined as the space average of the measured pressure spectrum, with the measurements being taken over a range of points on the panel.

Now substituting equation 7.12 into 7.4, an expression for the generalised force as a function of the pressure loading, mode shape and generalised mass is obtained:-

$$F_n(t) = \frac{\int p(\mathbf{x},t)\phi_n(\mathbf{x})d\mathbf{x}}{\int m\phi_n^2(\mathbf{x})d\mathbf{x}} = p(t)\left[\frac{\int \psi(\mathbf{x})\phi_n(\mathbf{x})d\mathbf{x}}{\int m\phi_n^2(\mathbf{x})d\mathbf{x}}\right] \tag{7.16}$$

From which the excitation spectrum is,

$$G_n(\omega) = \frac{G_p(\omega)}{< \psi^2(\mathbf{x}) >_{\mathbf{x}}} \left[\frac{\int \psi(\mathbf{x}) \phi_n(\mathbf{x}) d\mathbf{x}}{\int m \phi_n^2(\mathbf{x}) d\mathbf{x}} \right]^2 \tag{7.17}$$

Here, $G_p(\omega)$ is the measured pressure spectrum, $\phi_n(\mathbf{x})$ is the response mode shape obtained from the eigenvectors, and m is the mass per unit area, as before. It therefore remains to specify $\psi(\mathbf{x})$ in order to fully define the broadband random excitation spectrum $G_n(\omega)$. There are several possibilities here, and each will be covered as separate cases.

7.2.1 Case 1, $\psi(\mathbf{x}) = 1$

This is the case of uniform pressure loading which was assumed by Miles [25]. Substituting $\psi(x) = 1$ into equation 7.17 produces:-

$$G_n(\omega) = G_p(\omega) \left[\frac{\int \phi_n(\mathbf{x}) d\mathbf{x}}{\int m \phi_n^2(\mathbf{x}) d\mathbf{x}} \right]^2 \tag{7.18}$$

The response of the single-degree-of-freedom system to a uniform unit static pressure can be found by substituting $\ddot{w}(t) = 0$ and $\dot{w}(t) = 0$ into equation 7.2 and solving for $w(t)$ to give:-

$$\omega_n^2 w(t) = F_n(t) = \left[\frac{\int \phi_n(\mathbf{x}) d\mathbf{x}}{\int m \phi_n^2(\mathbf{x}) d\mathbf{x}} \right] \Rightarrow w_{stat}(t) = \frac{1}{\omega_n^2} \left[\frac{\int \phi_n(\mathbf{x}) d\mathbf{x}}{\int m \phi_n^2(\mathbf{x}) d\mathbf{x}} \right] \tag{7.19}$$

Therefore,

$$G_n(\omega) = G_p(\omega) \omega_n^4 w_{stat}^2 \tag{7.20}$$

which leads to the well known result [25, 8],

$$\sigma_w^2 = \frac{\pi \omega_n G_p(\omega)}{4\zeta_n} w_{stat}^2 \tag{7.21}$$

and in terms of the static strain due to a unit static pressure, ϵ_{stat}, and frequency, f_n,

$$\sigma_\epsilon^2 = \frac{\pi f_n G_p(f)}{4\zeta_n} \epsilon_{stat}^2 \tag{7.22}$$

since $\omega = 2\pi f$ and $G_p(\omega) = G_p(f)/2\pi$. From equation 7.19, the static strain due to a unit static pressure is:-

$$\epsilon_{stat} = \frac{\bar{\epsilon}}{\omega_n^2}\left[\frac{\int \phi_n(\mathbf{x})d\mathbf{x}}{\int m\phi_n^2(\mathbf{x})d\mathbf{x}}\right] \tag{7.23}$$

where $\bar{\epsilon}$ is the modal strain obtained from the modal analysis. Since the assumption of unit generalised mass has been made (i.e. $\int m\phi_n^2(\mathbf{x})d\mathbf{x} = 1$), then:-

$$\epsilon_{stat} = \frac{\bar{\epsilon}}{4\pi^2 f_n^2}\int_A \phi_n(\mathbf{x})d\mathbf{x} \tag{7.24}$$

The integral of the mode shape, ϕ_n, can be found by summing the element displacements ($i = 1..N$) for the mode of interest, obtained from the finite element modal analysis, and multiplying by the panel area divided by the number of elements (which is approximately equal to the area of each element, A_e). The displacements from the FE model are given per node, therefore it is necessary to estimate the displacement per element by averaging the nodal displacements, as shown in figure 7.1. Following this, the estimate of the RMS strain response for the case where $\psi(x) = 1$ becomes:-

$$\sigma_{\epsilon_{RMS}} = \left(\frac{\pi f_n G_p(f)}{4\zeta_n}\right)^{1/2}\frac{A_e\bar{\epsilon}}{4\pi^2 f_n^2}\sum_{i=1}^{N}\{\phi_n\}_i \tag{7.25}$$

7.2.2 Case 2, $\psi(\mathbf{x}) = \phi_n(\mathbf{x})$

In the case, the pressure loading is assumed to be perfectly matched to the structural mode shape, $\phi_n(\mathbf{x})$. This assumption is equivalent to stating that the joint acceptance function equals unity [43]. From equation 7.17,

$$< \psi^2(\mathbf{x}) >_{\mathbf{x}} = \frac{1}{A}\int \psi^2(\mathbf{x})d\mathbf{x} = \frac{1}{A}\int \phi_n^2(\mathbf{x})d\mathbf{x} \tag{7.26}$$

where A is the panel area. It follows that,

$$\left[\frac{\int \psi(\mathbf{x})\phi_n(\mathbf{x})d\mathbf{x}}{\int \phi_n^2(\mathbf{x})d\mathbf{x}}\right]^2 = \left[\frac{\int \phi_n^2(\mathbf{x})d\mathbf{x}}{m\int \phi_n^2(\mathbf{x})d\mathbf{x}}\right]^2 = \left[\frac{1}{m}\right]^2 \tag{7.27}$$

Assuming the modes of vibration are normalised to unit generalised mass, i.e.,

$$\int m\phi_n^2(\mathbf{x})d\mathbf{x} = 1 \Rightarrow \int \phi_n^2(\mathbf{x})d\mathbf{x} = 1/m \tag{7.28}$$

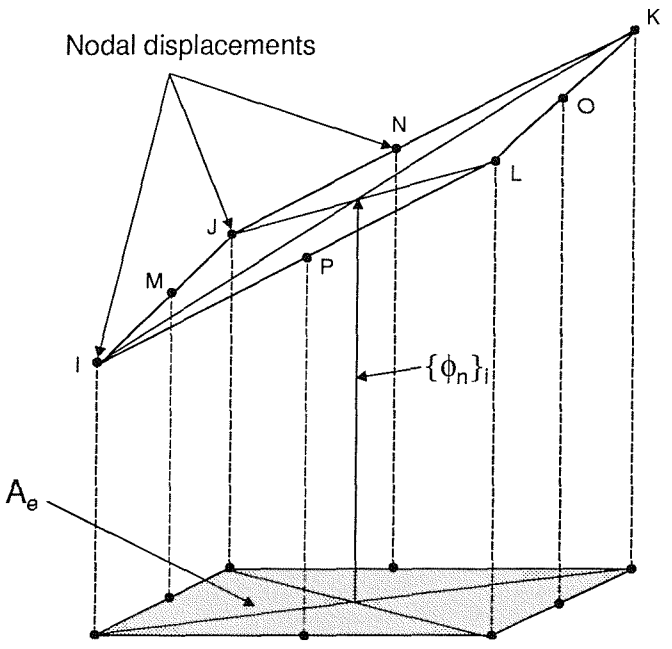

Figure 7.1: Estimation of the displacement of each element from the nodal displacements given by the FE model for the mode of interest.

therefore,

$$G_n(\omega) = (mA)G_p(\omega)[1/m]^2 = G_p(\omega)[A/m] \tag{7.29}$$

Substituting this into equation 7.11 results in the mean square strain response to a broadband random excitation where the pressure loading is assumed to be perfectly matched to the response mode shape:-

$$\sigma_\epsilon^2 = \frac{G_p(f)}{64\pi^3\zeta_n f_n^3}\left(\frac{A}{m}\right)\bar{\epsilon}^2 \tag{7.30}$$

from which the RMS strain response is:-

$$\sigma_{\epsilon_{RMS}} = \left(\frac{AG_p(f)}{64m\pi^3\zeta_n f_n^3}\right)^{1/2}\bar{\epsilon} \tag{7.31}$$

where $\bar{\epsilon}$ is the strain associated with the mode shape (when the shape is scaled to unit generalised mass).

7.2.3 Case 3, $\psi(\mathbf{x}) \neq \phi_n(\mathbf{x})$

For the final case, the spatial distribution of the loading, $\psi(\mathbf{x})$ is assumed to be neither uniform or equal to the mode shape, $\phi_n(\mathbf{x})$. However, assuming that the modes of vibration are still scaled to unit generalised mass (equation 7.28), and the space average mean squared spatial distribution of the loading is:-

$$< \psi^2(\mathbf{x}) >_{\mathbf{x}} = \frac{1}{A} \int \psi^2(\mathbf{x}) d\mathbf{x} \tag{7.32}$$

Then the excitation spectrum becomes:-

$$G_n(\omega) = \frac{AG_p(\omega)}{\int \psi^2(\mathbf{x}) d\mathbf{x}} \left[\frac{\int \psi(\mathbf{x}) \phi_n(\mathbf{x}) d\mathbf{x}}{m \int \phi_n^2(\mathbf{x}) d\mathbf{x}} \right]^2 \tag{7.33}$$

$$\Rightarrow G_n(\omega) = \left(\frac{A}{m} \right) \frac{G_p(\omega)}{\int \psi^2(\mathbf{x}) d\mathbf{x} \int \phi_n^2(\mathbf{x}) d\mathbf{x}} \left[\frac{(\int \psi(\mathbf{x}) \phi_n(\mathbf{x}) d\mathbf{x})^2}{m \int \phi_n^2(\mathbf{x}) d\mathbf{x}} \right] \tag{7.34}$$

and since,

$$m \int \phi_n^2(\mathbf{x}) d\mathbf{x} = 1 \tag{7.35}$$

Then,

$$G_n(\omega) = \left(\frac{A}{m} \right) G_p(\omega) \frac{(\int \psi(\mathbf{x}) \phi_n(\mathbf{x}) d\mathbf{x})^2}{\int \psi^2(\mathbf{x}) d\mathbf{x} \int \phi_n^2(\mathbf{x}) d\mathbf{x}} \tag{7.36}$$

and defining,

$$J_n = \frac{\int \psi(\mathbf{x}) \phi_n(\mathbf{x}) d\mathbf{x}}{\sqrt{\int \psi^2(\mathbf{x}) d\mathbf{x} \int \phi_n^2(\mathbf{x}) d\mathbf{x}}} \tag{7.37}$$

as the joint acceptance, which is the degree to which the spatial distribution of the pressure loading matches the mode shape of the n^{th} mode of vibration, then the estimate of the mean square strain response becomes:-

$$\sigma_\epsilon^2 = \frac{G_p(f)}{64\pi^3 \zeta_n f_n^3} \left(\frac{A}{m} \right) J_n^2 \bar{\epsilon}^2 \tag{7.38}$$

from which the estimated RMS strain is:-

$$\sigma_{\epsilon_{RMS}} = \left(\frac{AG_p(f)}{64m\pi^3\zeta_n f_n^3} \right)^{1/2} J_n\bar{\epsilon} \tag{7.39}$$

which as can be seen, is basically equation 7.30 multiplied by the joint acceptance. In this case, assuming the joint acceptance can be determined, equation 7.38 should provide the most accurate estimate of the response. However, in practice, estimation of the joint acceptance for a broadband random pressure loading is very difficult, as will be explained in section 7.3.

7.2.4 Estimation of the RMS strain response using the single-degree-of-freedom approximation

In order to estimate the RMS strain response of the four test panels using the single-degree-of-freedom approximations developed previously, calculation of the mode shapes and natural frequencies of vibration was required, whilst the applied pressure spectrum and damping are measured quantities.

Natural frequency of vibration, mode shapes, and modal strains

A modal analysis was performed in order to determine the natural frequencies of vibration, the mode shapes, and associated modal strains, and the latter two quantities were normalised with respect to the unit generalised mass matrix, which is a default option in ANSYS when conducting a modal analysis. This was done using the FE models developed in the previous chapter with spring supported boundary conditions, as shown in figure 7.2 for panel 1. The panels were modelled as described in chapter 6, while the springs were modelled using SHELL63 elements with material properties equal to that of steel (i.e. $E = 210GPa$, $\nu = 0.3$, and $\rho = 7800kg/m^3$). The modal direct strains were recovered for each of the five inner and outer strain gauge locations, and the modal shear strains were recovered for two locations mid-way between gauges gi2/go2 and gi3/go3 in the y-direction, and between gauges gi4/go4 and gi5/go5 in the x-direction in order to estimate the core shear strain. All of the modal strains were calculated for the fundamental mode of vibration excited by the PWT, in this case mode 2 for panels 1 to 3, and mode 3 for panel 4, and are given in table 7.1.

Panel	*Modal Strain* ($\epsilon \times 10^3$)									
	gi1	gi2	gi3	gi4	gi5	go1	go2	go3	go4	go5
1	126.6	221.7	233.4	87.4	84.1	287.9	171.3	176.3	294.9	284.1
2	162.9	163.3	168.8	164.0	160.0	237.2	130.9	131.2	204.2	198.3
3	53.0	312.3	349.6	64.1	63.5	199.0	257.4	278.8	144.9	140.3
4	86.6	446.7	501.7	93.1	93.3	155.3	160.8	176.1	101.5	98.7

Table 7.1: Calculated (FE) modal strains for each strain gauge location and for each test panel (the modal strains have been normalised with respect to unit generalised mass in the FE calculations).

Pressure spectrum level, $G_p(f)$ and modal damping, ζ_n

The RMS acoustic pressure applied to the panels was obtained from the measurements taken using the microphone located in the aperture of the PWT. The spectrum levels at each OASPL were averaged over the mean-square bandwidth centred on the fundamental response frequency excited by the PWT. For the case of a single-degree-of-freedom system, the mean-square bandwidth is [71]:-

$$B_{\sigma^2} = \pi \zeta_n \omega_n \tag{7.40}$$

The measured broadband spectrum levels versus frequency at each OASPL for panel 1 are shown in figure 7.3. The measured spectrum levels for each panel were very noisy, therefore the levels were smoothed by averaging over n adjacent spectral lines using the method presented by Newland [71]:-

$$\hat{G}_p(f_k) = \frac{1}{2n+1} \sum_{m=-n}^{n} \tilde{G}_p(f_{k+m}) \tag{7.41}$$

Both the noisy and smoothed spectra are presented, and as can be seen there is a certain degree of variability in the spectrum levels, which was obviously not as apparent in the decibel plots presented in chapter 5 due to the logarithmic scale. This variability will introduce a certain amount of uncertainty in the predicted response, and to this end the standard deviation in the spectrum level over the mean-square bandwidth is presented along with the average spectrum levels in table 7.2 so that a feel for the degree of uncertainty in the results can be obtained.

Panel	OASPL (dB)	$\hat{G}_p(f_n)$ (Pa^2Hz^{-1})	Standard deviation
1	143.29	184.7	19.7
	149.97	1002.0	91.6
	154.75	3120.0	387.1
	159.28	8711.5	1120.1
	163.71	23692.0	1989.7
2	143.88	218.8	32.9
	149.91	737.8	169.4
	154.92	2138.9	431.3
	159.00	5493.0	1520.3
	163.09	13659.0	3089.5
3	143.51	234.2	44.4
	149.93	1080.7	212.9
	154.18	3093.9	681.5
	158.84	8264.9	1614.2
	162.82	20186.0	4615.2
4	143.20	203.7	35.4
	149.49	970.6	226.0
	154.69	3280.5	828.9
	159.49	10150.0	2157.0
	163.71	26325.0	6420.8

Table 7.2: OASPL and associated single-sided broadband pressure spectrum levels for the four panel tests in the PWT.

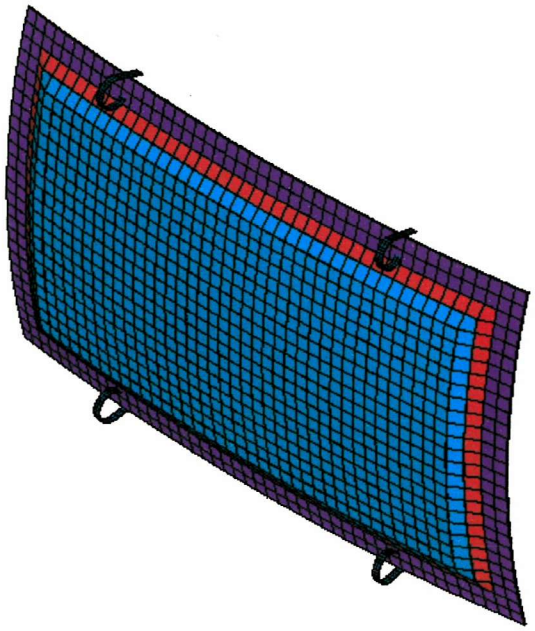

(a)

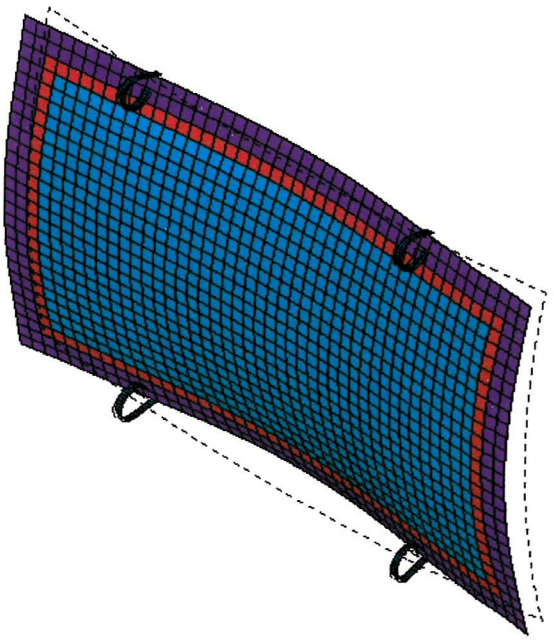

(b)

Figure 7.2: Panel 1 (a) FE model, and (b) calculated mode shape associated with the fundamental frequency of vibration excited by the PWT (calculated as 219.02 Hz, undeformed panel shown as dashed line).

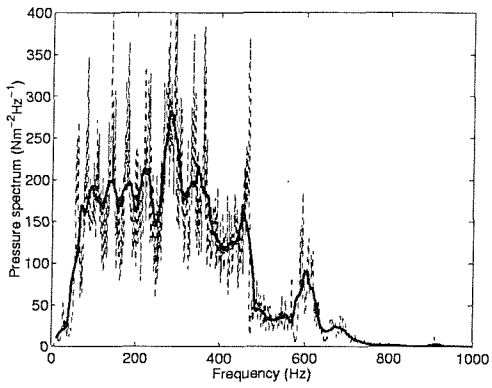

(a) 143.29 dB

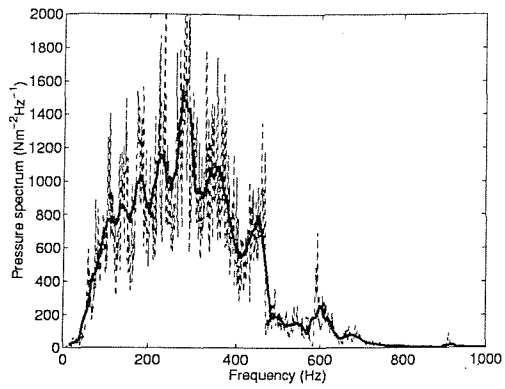

(b) 149.97 dB

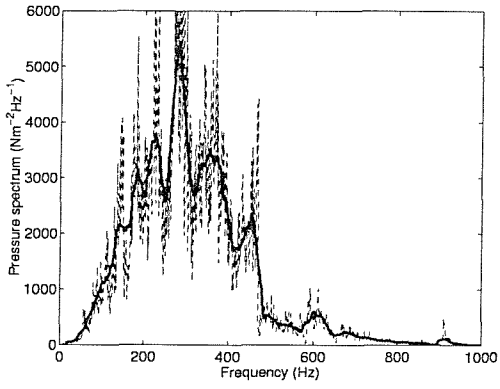

(c) 154.75 dB

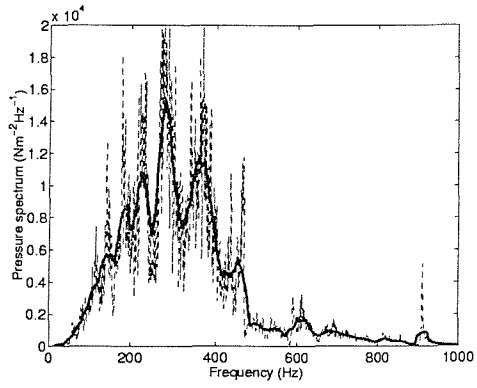

(d) 159.28 dB

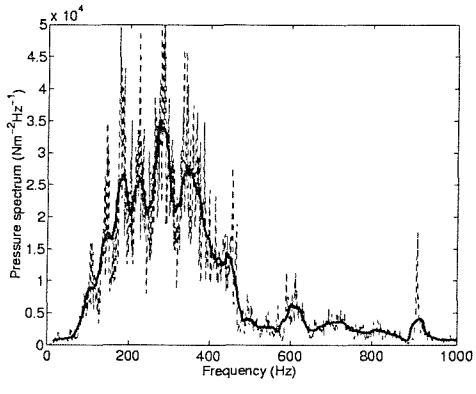

(e) 163.71 dB

Figure 7.3: Spectrum levels of acoustic pressure for panel 1 and for each OASPL. Original spectrum (- -), smoothed spectrum (thick line) with $n = 20$ (see equation 7.41).

The final value needed for the single-degree of freedom calculations is the modal damping for the fundamental mode excited by the PWT, which was obtained from the experimental measurements using the half-power point method as discussed in chapter 5. The damping values for each panel are given in table 5.9.

In order to compare the estimated results for RMS strain with the experimental results it was necessary to scale the latter since the single-degree-of-freedom calculations are based around the resonant response frequency of interest while the experimental measurements were an overall RMS over a 1000 Hz bandwidth. A graphical representation of the estimation method (equation 7.11) can be seen in figure 7.4 [72].

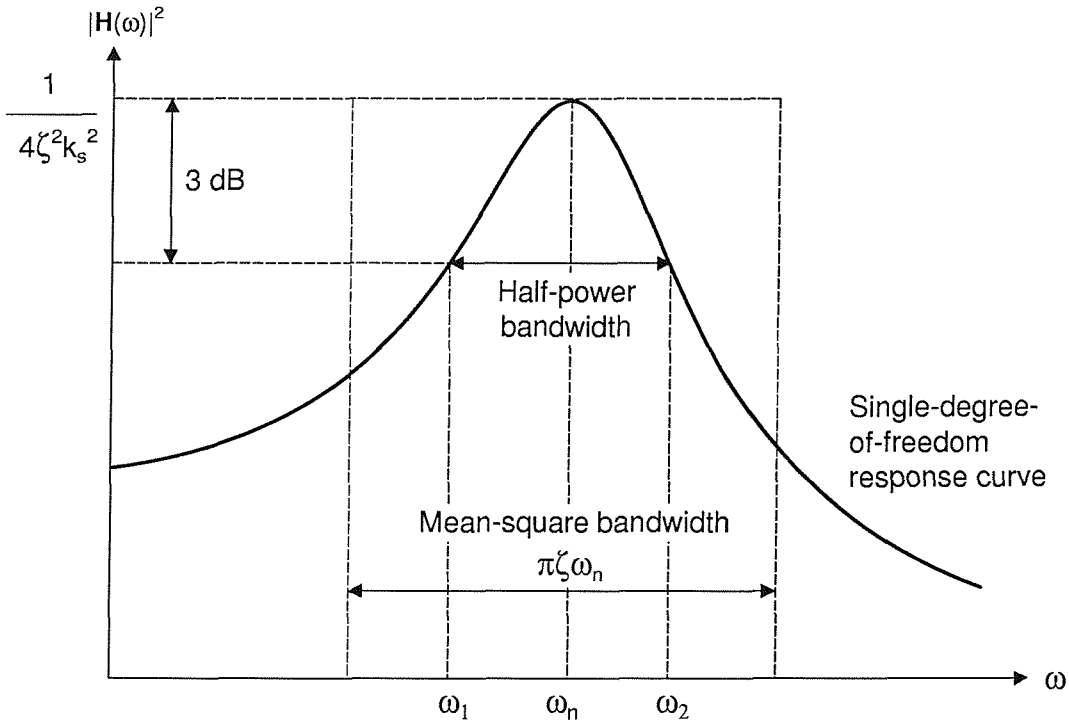

Figure 7.4: Estimation of the mean-square response of a single-degree-of-freedom system with broadband random excitation.

The frequency response curve for $|\mathbf{H}(\omega)|^2$ is shown in this figure. The approximate calculation of the response of the single-degree-of-freedom system to broadband random loading with a constant spectral density can be made by approximating the

area under the curve of $|\mathbf{H}(\omega)|^2$ with a rectangle of the same area [71, 72]. As can be seen, at resonance the peak value of $|\mathbf{H}(\omega)|^2$ is $1/c_v^2\omega_n^2 = 1/4\zeta_n^2 k_s^2$ and the bandwidth is approximated by $\pi\zeta_n\omega_n$ since the stiffness $k_s = \omega_n^2 m$ and the viscous damping $c_v = 2\zeta_n\omega_n m$. Hence the mean square response is simply the product of the input spectral density, the mean-square bandwidth and the peak of the frequency response function, $|\mathbf{H}(\omega)|^2$. It is therefore easy to see that, for the approximation method to be valid, the excitation bandwidth must be reasonably broadband and include ω_n, and the damping should be light with the natural frequencies of vibration well-spaced [72].

The mean square bandwidth of the approximation method is obviously much smaller than the response bandwidth of the experiments, therefore in order to scale the experimental results, the percentage contribution of the fundamental mode excited by the PWT to the overall response for each of the strain measurements was used as the scaling factor. This was obtained from the plots of the normalised integral across the strain power spectral density, examples of which can be found in chapter 5. The resulting narrow-band scaling factors for each of the strain gauges and for each panel are given in table 7.3.

For case 1, the integral of the mode shapes were found to be $7.82 \times 10^{-4} m^3$, $1.80 \times 10^{-3} m^3$, $4.00 \times 10^{-3} m^3$, and $1.10 \times 10^{-3} m^3$ for panels 1 to 4 respectively. Using equation 7.25 together with the calculated (FE) modal strains given in table 7.1 and the natural frequency of vibration, the narrow-band pressure spectrum levels given in table 7.2, and the previously measured damping value for the fundamental mode, the estimates for the strain response were calculated, and are presented in table 7.4. The results are significantly lower than the measured strains given in tables 5.4 to 5.7 as the standard deviation of strain, even after the latter have been scaled to account for the estimated response being centred around the fundamental mode. Now, the estimate of the response for case 3 (equation 7.39) is the general result, and it can be shown that this reduces to equation 7.25 when the appropriate assumption for the spatial distribution of the pressure loading, $\psi(\mathbf{x})$ is applied in the joint acceptance expression (equation 7.37). For case 1, the pressure loading has been assumed to be uniform over the panel area, as illustrated in figure 7.5. This pressure loading is analogous to the rigid body motion of the panel in the $z-$direction, and since the panels were located in the PWT aperture using circular steel springs, this mode would have been excited and was indeed recovered from the FE modal analysis. In addition, since the orthogonality principle of uncoupled modes was used in the FE modal analysis, i.e.,

$$\{\phi_j\}^T \mathbf{M} \{\phi_i\} = 0 \tag{7.42}$$

Panel	OASPL	*Narrow-band scaling factor*									
	(dB)	gi1	gi2	gi3	gi4	gi5	go1	go2	go3	go4	go5
1	143.29	0.88	0.88	0.84	0.85	0.80	0.93	0.77	0.75	0.87	0.88
	149.97	0.89	0.88	0.85	0.86	0.82	0.94	0.80	0.77	0.87	0.88
	154.75	0.90	0.90	0.87	0.87	0.84	0.94	0.83	0.80	0.90	0.90
	159.28	0.90	0.90	0.87	0.87	0.85	0.94	0.83	0.80	0.90	0.90
	163.71	0.93	0.92	0.90	0.91	0.89	0.96	0.87	0.85	0.93	0.93
2	143.88	0.86	0.91	0.91	0.90	0.85	0.91	0.91	0.89	0.94	0.93
	149.91	0.88	0.91	0.91	0.90	0.83	0.91	0.92	0.90	0.94	0.92
	154.92	0.83	0.87	0.87	0.86	0.79	0.88	0.89	0.87	0.92	0.88
	159.00	0.85	0.89	0.89	0.88	0.79	0.89	0.91	0.89	0.93	0.89
	163.09	0.88	0.91	0.91	0.89	0.82	0.90	0.93	0.91	0.94	0.91
3	143.51	0.80	0.82	0.81	0.25	0.27	0.82	0.79	0.80	0.33	0.43
	149.93	0.74	0.82	0.81	0.23	0.25	0.83	0.79	0.81	0.33	0.38
	154.18	0.76	0.85	0.84	0.26	0.28	0.86	0.83	0.84	0.38	0.41
	158.84	0.76	0.86	0.85	0.27	0.28	0.87	0.83	0.85	0.41	0.43
	162.82	0.78	0.88	0.88	0.33	0.32	0.89	0.86	0.88	0.48	0.49
4	143.20	0.77	0.69	0.72	0.61	0.78	0.72	0.54	0.55	0.09	0.24
	149.49	0.75	0.74	0.77	0.66	0.81	0.77	0.59	0.62	0.11	0.16
	154.69	0.77	0.79	0.81	0.70	0.85	0.81	0.64	0.66	0.14	0.18
	159.49	0.80	0.82	0.83	0.74	0.87	0.85	0.68	0.70	0.18	0.208
	163.71	0.82	0.84	0.84	0.76	0.89	0.87	0.70	0.72	0.19	0.23

Table 7.3: Narrow-band scaling factors applied to the experimental RMS strain measurements.

and,

$$\{\phi_j\}^T \mathbf{K} \{\phi_i\} = 0 \tag{7.43}$$

where $i \neq j$, the product of a uniform pressure loading (analogous to a lower rigid body displacement in z) and a higher mode shape of the panel would result in a small joint acceptance (see equation 7.37). This would explain the very low values of estimated strain using the assumption of uniform pressure loading. In addition, it is important to note that in practice, the pressure loading in the tunnel is in the form of travelling waves at grazing incidence to the structure, rather than a uniform pressure loading at normal incidence to the structure.

Panel	f_n (Hz)	ζ_n	$\int\{\phi_n\}_i dA$ (m^3)	$G_p(f)$ (Pa^2Hz^{-1})	*Estimated RMS Strain* ($\mu\epsilon$)									
					gi1	gi2	gi3	gi4	gi5	go1	go2	go3	go4	go5
1	219.02	0.0105	7.82e-4	184.90	0.096	0.169	0.178	0.067	0.064	0.219	0.130	0.134	0.224	0.216
				1002.0	0.225	0.394	0.414	0.155	0.149	0.511	0.304	0.313	0.524	0.504
				3120.0	0.397	0.695	0.731	0.274	0.263	0.902	0.537	0.553	0.924	0.890
				8711.0	0.663	1.161	1.222	0.458	0.440	1.507	0.897	0.923	1.544	1.487
				23692	1.093	1.914	2.015	0.755	0.726	2.486	1.479	1.523	2.546	2.453
2	164.30	0.0120	1.80e-3	200.00	0.403	0.405	0.418	0.406	0.396	0.588	0.324	0.325	0.506	0.491
				737.80	0.775	0.777	0.803	0.780	0.761	1.128	0.623	0.624	0.971	0.944
				2138.9	1.319	1.323	1.367	1.329	1.296	1.921	1.060	1.063	1.654	1.607
				5493.0	2.114	2.120	2.190	2.129	2.078	3.079	1.699	1.703	2.650	2.575
				13659	3.334	3.343	3.454	3.358	3.276	4.856	2.680	2.686	4.179	4.060
3	272.62	0.0125	4.00e-3	234.20	0.145	0.853	0.955	0.175	0.173	0.543	0.703	0.761	0.396	0.383
				1080.7	0.311	1.832	2.051	0.376	0.373	1.167	1.510	1.635	0.850	0.823
				3093.9	0.526	3.099	3.470	0.636	0.631	1.975	2.555	2.766	1.438	1.393
				8264.9	0.859	5.065	5.671	1.039	1.031	3.228	4.176	4.522	2.350	2.276
				20186	1.343	7.916	8.863	1.624	1.611	5.045	6.526	7.066	3.672	3.558
4	288.67	0.0102	1.10e-3	203.68	0.062	0.318	0.357	0.066	0.066	0.111	0.114	0.125	0.072	0.070
				970.62	0.134	0.694	0.779	0.145	0.145	0.241	0.250	0.273	0.158	0.153
				3280.5	0.247	1.275	1.432	0.266	0.266	0.443	0.459	0.503	0.290	0.282
				10150	0.435	2.243	2.519	0.468	0.469	0.780	0.808	0.884	0.510	0.496
				26325	0.700	3.613	4.058	0.753	0.755	1.256	1.301	1.424	0.821	0.799

Table 7.4: Estimated RMS strain for the ten strain gauges located on the four test panels. Single-degree-of-freedom approximation method (Case 1 - uniform pressure loading assumption).

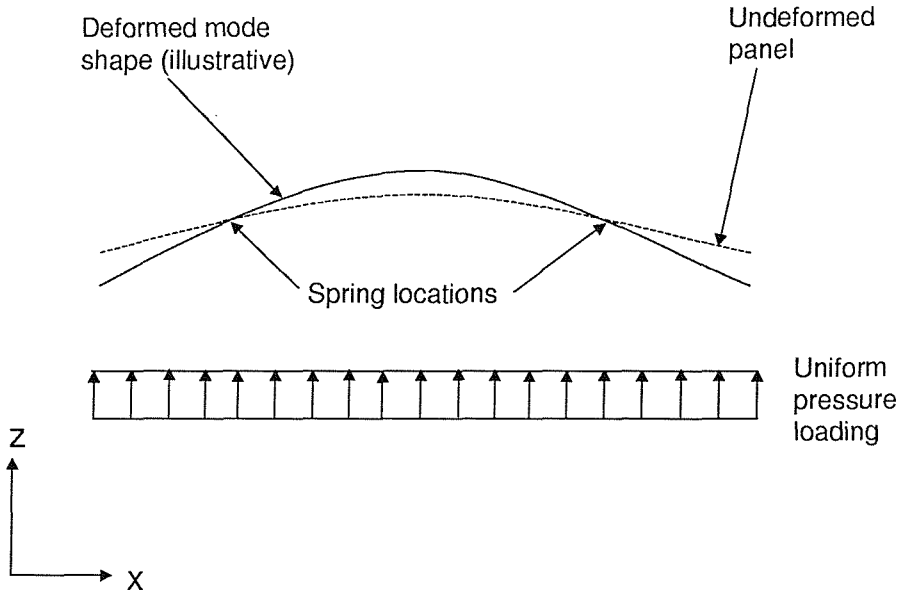

Figure 7.5: Illustration of the uniform pressure loading (case 1 assumption) and resulting fundamental mode of response of the doubly curved test panels located in the PWT.

The results for case 2, where the spatial distribution of the pressure loading was assumed to exactly match the response mode shape giving a joint acceptance of unity, are given in table 7.5. As can be seen, the assumption of a joint acceptance of unity results in an over-estimate of the response, as can be seen when one compares these results with the measured results given in tables 5.4 to 5.7. This is understandable since the assumption that the spatial distribution of the pressure load exactly matches the mode shape of the panel is unlikely in practice. This assumption was investigated further by Blevins [43], and will be covered in the next section. In any case, it can be seen that cases 1 and 2 provide the lower and upper bounds of the approximation, hence a more accurate estimation of the joint acceptance will be required in order the arrive at an improved estimate.

Panel	$G_p(f)$	*Estimated RMS Strain* ($\mu\epsilon$)									
	(Pa^2Hz^{-1})	gi1	gi2	gi3	gi4	gi5	go1	go2	go3	go4	go5
1	184.90	35.09	61.43	64.66	24.23	23.30	79.77	47.47	48.86	81.71	78.72
	1002.0	81.86	143.31	150.86	56.53	54.35	186.10	110.75	113.99	190.63	183.66
	3120.0	144.44	252.89	266.21	99.75	95.91	328.39	195.43	201.16	336.39	324.08
	8711.0	241.35	422.56	444.82	166.67	160.26	548.72	326.55	336.12	562.07	541.52
	23692	398.04	696.88	733.58	274.87	264.29	904.93	538.53	554.31	926.96	893.06
2	200.00	67.72	67.91	70.16	68.21	66.55	98.63	54.43	54.56	84.90	82.47
	737.80	130.06	130.44	134.76	131.00	127.82	189.44	104.54	104.79	163.06	158.41
	2138.9	221.45	222.09	229.45	223.05	217.63	322.55	178.00	178.41	277.64	269.71
	5493.0	354.89	355.91	367.71	357.45	348.77	516.90	285.26	285.92	444.92	432.23
	13659	559.62	561.23	579.84	563.67	549.97	815.10	449.82	450.86	701.60	681.58
3	234.20	10.93	64.41	72.12	13.21	13.10	41.05	53.10	57.50	29.88	28.95
	1080.7	23.47	138.36	154.92	28.38	28.15	88.18	114.06	123.51	64.19	62.18
	3093.9	39.71	234.11	262.12	48.03	47.63	149.21	192.99	208.98	108.60	105.21
	8264.9	64.91	382.63	428.41	78.50	77.85	243.87	315.43	341.56	177.51	171.96
	20186	101.44	597.98	669.53	122.67	121.66	381.12	492.96	533.80	277.41	268.74
4	203.68	16.92	87.29	98.04	18.20	18.23	30.35	31.43	34.41	19.84	19.29
	970.62	36.94	190.56	214.02	39.74	39.80	66.26	68.61	75.11	43.30	42.12
	3280.5	67.91	350.33	393.46	73.05	73.17	121.82	126.13	138.09	79.61	77.43
	10150	119.45	616.23	692.09	128.50	128.71	214.28	221.86	242.90	140.03	136.20
	26325	192.37	992.42	1114.6	206.95	207.29	345.10	357.30	391.18	225.52	219.35

Table 7.5: Estimated RMS strain for the ten strain gauges located on the four test panels. Single-degree-of-freedom approximation method (Case 2 - Unit joint acceptance assumption).

The joint acceptance was defined previously (see equation 7.37). In order to arrive at an improved prediction of the dynamic strain response, an estimate of the spatial distribution of the pressure and the mode shape of interest must be provided for each panel. Since the test panels were located in a PWT, the excitation can be considered to be travelling acoustic waves at grazing incidence, an assumption which was proved by means of spatial measurements taken in the test aperture, as presented at the beginning of chapter 5. Therefore, the spatial distribution of the pressure loading can be estimated using:-

$$\psi(x) = e^{-ik_a x} \tag{7.44}$$

where $k_a = 2\pi\omega_n/c$ is the acoustic wavenumber, ω_n is the natural frequency of vibration of the test panel, and c is the speed of sound which was found to be $342.8m/s$ from the spatial measurements presented in chapter 5. An estimate of the mode shape, $\phi_n(x, y)$, can be made by considering the measured and predicted mode shape for the fundamental mode excited by the PWT, as shown in figures 4.3, 4.5, 4.7, and 4.9 and figure 6.2 respectively. The excited mode (mode 2 for panels 1 to 3 and mode 3 for panel 4) is the first bending mode of vibration, which in the case of the panels being supported in the PWT with circular steel springs at four locations, has a half wavelength of approximately the distance between these springs along the long side. The shape can therefore be approximated as a cosine wave where:-

$$\phi_n(x, y) = cos(k_1 x)cos(k_2 y) \tag{7.45}$$

where the origin of x and y is in the centre of the panel, $k_1 = 2\pi/\lambda_x$ is the structural wavenumber, λ_x is the distance between the circular steel spring supports, and $k_2 = 0$ since there are no nodal lines along the short side and the panels are not supported along the edges.

Panel	$G_p(f)$	*Estimated RMS Strain* ($\mu\epsilon$)									
	(Pa^2Hz^{-1})	gi1	gi2	gi3	gi4	gi5	go1	go2	go3	go4	go5
1	184.90	5.56	9.74	10.25	3.84	3.69	12.64	7.52	7.74	12.95	12.48
	1002.0	12.97	22.71	23.91	8.96	8.61	29.50	17.55	18.07	30.22	29.11
	3120.0	22.89	40.08	42.19	15.81	15.20	52.05	30.98	31.88	53.32	51.37
	8711.0	38.25	66.98	70.50	26.42	25.40	86.97	51.76	53.27	89.09	85.83
	23692	63.09	110.46	116.27	43.57	41.89	143.43	85.36	87.86	146.92	141.55
2	200.00	8.71	8.73	9.02	8.77	8.56	12.68	6.99	7.02	10.92	10.61
	737.80	16.73	16.77	17.33	16.85	16.44	24.36	13.44	13.48	20.97	20.37
	2138.9	28.48	28.56	29.51	28.68	27.99	41.48	22.89	22.94	35.70	34.68
	5493.0	45.64	45.77	47.29	45.97	44.85	66.47	36.68	36.77	57.22	55.58
	13659	71.97	72.17	74.57	72.49	70.73	104.82	57.85	57.98	90.23	87.65
3	234.20	2.11	12.43	13.92	2.55	2.53	7.92	10.25	11.10	5.77	5.59
	1080.7	4.53	26.70	29.90	5.48	5.43	17.02	22.01	23.84	12.39	12.00
	3093.9	7.66	45.18	50.59	9.27	9.19	28.80	37.25	40.33	20.96	20.31
	8264.9	12.53	73.85	82.68	15.15	15.02	47.07	60.88	65.92	34.26	33.19
	20186	19.58	115.41	129.22	23.68	23.48	73.56	95.14	103.02	53.54	51.87
4	203.68	3.40	17.55	19.71	3.66	3.66	6.10	6.32	6.92	3.99	3.88
	970.62	7.42	38.30	43.02	7.99	8.00	13.32	13.79	15.10	8.70	8.47
	3280.5	13.65	70.42	79.09	14.68	14.71	24.49	25.35	27.76	16.00	15.56
	10150	24.01	123.86	139.11	25.83	25.87	43.07	44.59	48.82	28.15	27.38
	26325	38.67	199.48	224.03	41.60	41.66	69.36	71.82	78.63	45.33	44.09

Table 7.6: Estimated RMS strain for the ten strain gauges located on the four test panels. Single-degree-of-freedom approximation method (Case 3 - Estimated joint acceptance assumption).

The RMS strain results for case 3 are given in table 7.6. A comparison is made with the measured RMS strains, which have been scaled according to the percentage contribution of the fundamental mode response to the overall RMS measured strains, using the scale factors given in table 7.3. The comparison for each panel is shown in figure 7.6 and 7.7. The results show excellent agreement between measured and predicted values, with the majority of the results falling within a ±30% confidence band. This is a very favourable result when one considers that the current design guidelines are reported to give results within a factor of 2 compared with measured data [1].

Finally, the outer-to-inner RMS predicted strain ratios are given in table 7.7, for comparison with the measured ratios presented in chapter 5. The predicted ratios

Panel	Predicted (SDOF, Case 3)				
	go1/gi1	go2/gi2	go3/gi3	go4/gi4	go5/gi5
1	2.27	0.77	0.76	3.37	3.38
2	1.46	0.80	0.78	1.24	1.24
3	3.76	0.82	0.80	2.26	2.21
4	1.79	0.36	0.35	1.09	1.06
	Measured Mean (Standard Deviation shown in brackets)				
	go1/gi1	go2/gi2	go3/gi3	go4/gi4	go5/gi5
1	1.89 (0.083)	0.80 (0.013)	0.85 (0.011)	2.83 (0.262)	2.85 (0.133)
2	1.55 (0.105)	0.86 (0.011)	0.79 (0.016)	1.39 (0.015)	1.26 (0.039)
3	2.37 (0.380)	0.88 (0.017)	0.90 (0.009)	2.50 (0.110)	2.37 (0.080)
4	1.19 (0.133)	0.44 (0.027)	0.39 (0.016)	2.39 (0.094)	1.91 (0.172)

Table 7.7: Ratio of outer-to-inner RMS strain for the predicted results using the SDOF approximation method (case 3), and the measured mean ratios.

were found to remain constant with increasing OASPL. The ratios for gauges 2 and 3 compare very well with the average measured ratios for panels 1, 2, and 3, whereas for panel 4 the predicted ratio is slightly lower compared with the measured ratio. Gauges 4 and 5 show similar results except for panel 1 which shows a higher predicted ratio compared with the measured ratio.

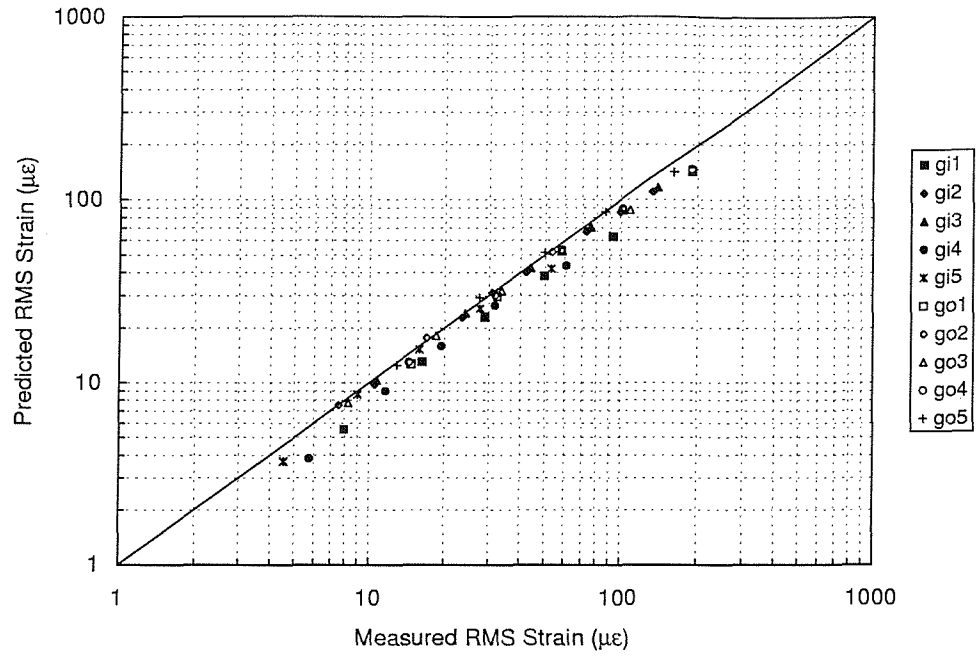

(a) Panel 1.

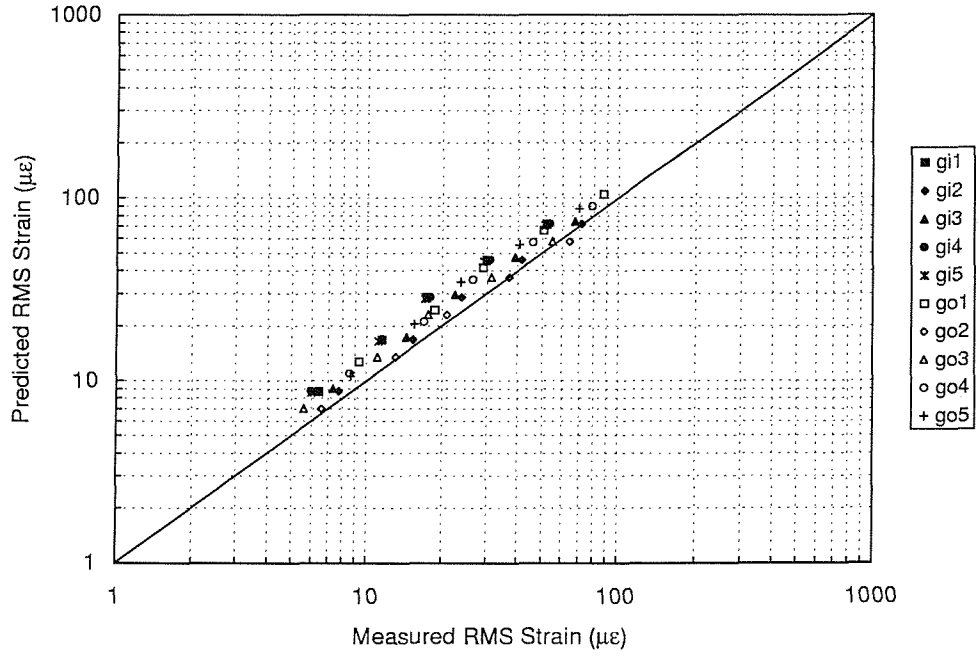

(b) Panel 2.

Figure 7.6: Comparison of measured and predicted (case 3) RMS strain for panels 1 and 2. Narrow-band response centred on the fundamental mode of vibration excited by the PWT.

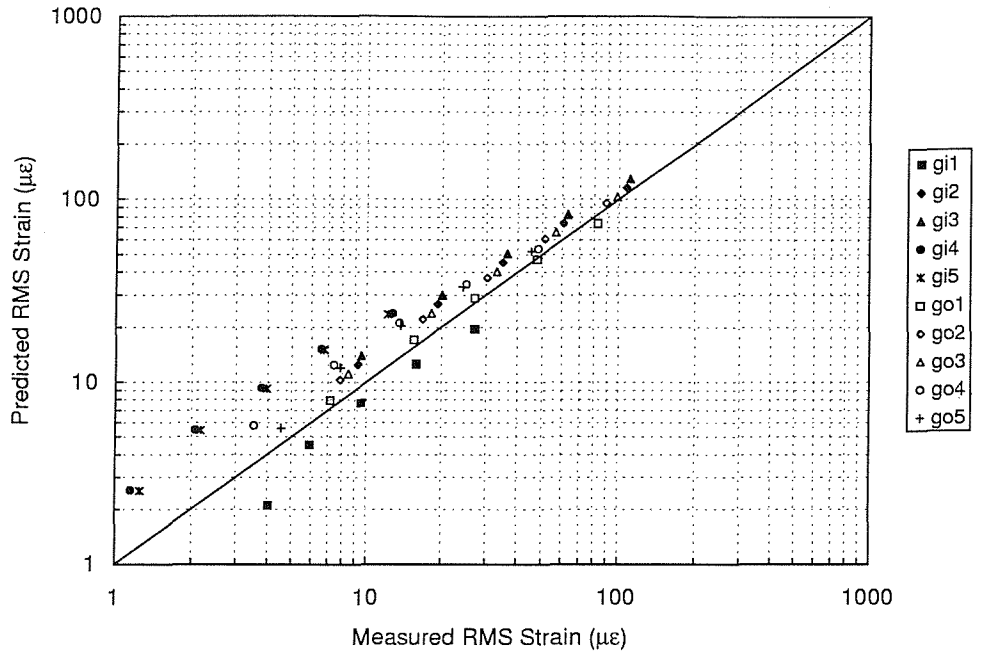

(a) Panel 3.

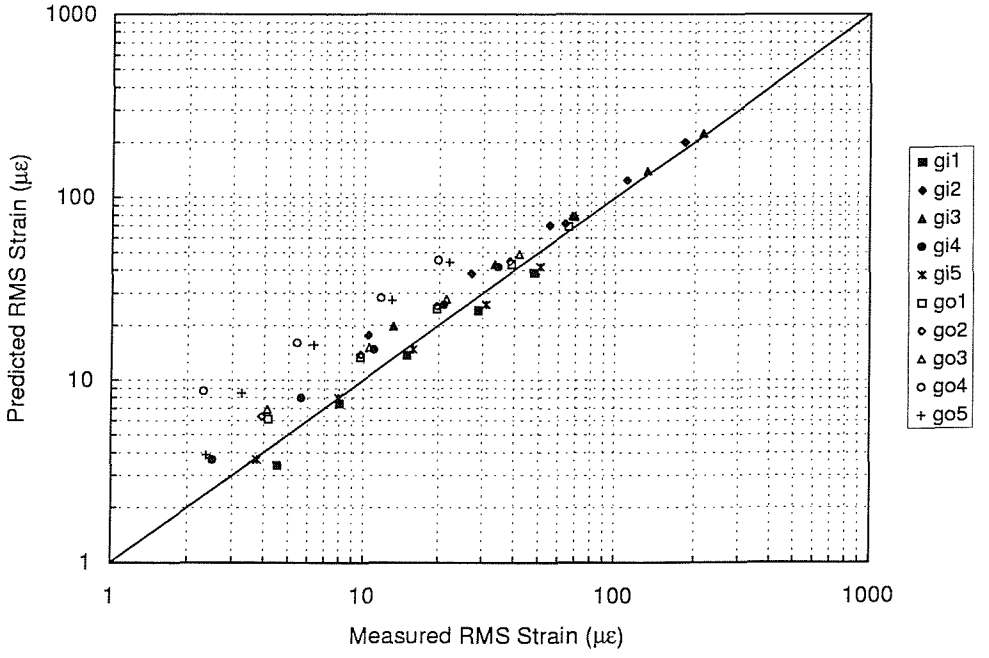

(b) Panel 4.

Figure 7.7: Comparison of measured and predicted (case 3) RMS strain for panels 3 and 4. Narrow-band response centred on the fundamental mode of vibration excited by the PWT.

7.3 Application of Blevins' Normal Mode Method

A modification of the classical Miles [25] equation has been proposed by Blevins [43]. In this study, the spatial characteristics of both the structural modes and the sound field were considered simultaneously and related in order to arrive at a method that extended the Miles approach to higher modes and complex shapes. In general, for a linear elastic plate or shell structure excited by an acoustic pressure over the entire surface, the response of each mode is given by [43]:-

$$(1/\omega_n^2)\ddot{w}(t) + (2\zeta_n/\omega_n)\dot{w}(t) + w(t) = J_n p(t) \tag{7.46}$$

where

$$J_n = \frac{\int \psi(\mathbf{x})\phi_n(\mathbf{x})d\mathbf{x}}{\omega_n^2 \int m\phi_n^2(\mathbf{x})d\mathbf{x}} \tag{7.47}$$

is the modal joint acceptance which is constant for each mode. The equations presented here have been written in notation consistent with that used throughout this chapter for reasons of clarity. As can be seen, the time and spatial dependence of the response have been separated, which allowed solutions to be generated independently and later assembled to give the complete solution [43]. The remainder of the study [43] concentrated on the approximation of the joint acceptance, J_n. Blevins noted that for aircraft applications where, generally, the acoustic pressure load has a very rich frequency content and complex distribution, the determination of J_n by means such as estimation from historical data, measurement from a number of microphones, or analytical prediction is by no means a simple task. This is particularly true for intake ducts where the acoustic pressure load consists of discrete tones superimposed on a broadband spectrum with a very complex spatial distribution along the duct. To this end, several approximations were suggested, such as $\phi_n(\mathbf{x}) = 1$, a constant over the surface which is basically the Miles approach. The approximation is most applicable when the acoustic half wavelength exceeds the lateral dimensions of the panel. However, the disadvantage of this approximation is that it is incapable of showing any excitation of antisymmetric modes, hence its restriction to the fundamental mode of fully clamped plates. Other suggestions included a $Sign(\phi_n(\mathbf{x}))$ function, sinusoidal functions, and finally the mass-weighted structural mode shape. The latter involves matching a point on the surface of the panel (generally the point of maximum displacement) to the applied sound pressure level, as opposed to using a unit pressure

over the entire surface. Substituting,

$$\psi(\mathbf{x}) = \omega_n^2 m \phi_n(\mathbf{x}) \tag{7.48}$$

the mass-weighted mode shape approximation, into equation 7.47 and integrating, produces a joint acceptance of $J_n = 1$. A crude estimation of the influence of the joint acceptance can be made by considering the acoustic wavelength in terms of the structural wavelength, i.e. if the acoustic half wavelength is greater than the structural half wavelength then the joint acceptance of unity is valid. When the acoustic half wavelength is very much greater than the structural half wavelength, the loading approaches the Miles assumption of uniform pressure over the surface of the panel, however, as the acoustic half wavelength becomes smaller than the structural half wavelength, the accuracy of the joint acceptance becomes more important to correctly estimate the response. Blevins' method should theoretically work best when the acoustic and structural half wavelengths match. A comparison of the acoustic and structural half wavelengths were obtained for the four experimental test panels by conducting a modal analysis using the FE models developed in the previous chapter with boundary conditions similar to that used the the PWT. A typical model, shown for panel 1, is shown in figure 7.2 with the corresponding fundamental mode shape excited by the PWT. As can be seen, the structural half wavelength is approximately equal to the length of the panel for the fundamental frequency of vibration excited by the PWT. A comparison is now made between the structural and acoustic half wavelengths, the latter calculated using the relationship $\lambda_a = c/(2f)$ where c is the speed of sound in air ($\approx 343m/s$) and f is the frequency of interest corresponding to the natural frequency of vibration of the structure. The results are presented for each of the four test panels in table 7.8.

Panel	Frequency (FE) (Hz)	$\lambda_s/2$ (m)	$\lambda_a/2$ (m)	λ_s/λ_a
1	219.02	0.912	0.78	1.17
2	164.30	0.912	1.04	0.87
3	272.62	0.912	0.63	1.45
4	288.67	0.912	0.59	1.54

Table 7.8: Comparison of structural and acoustic half wavelengths for the four test panels.

The results presented in table 7.8 indicate that the approximation method should work best for panel 1 and 2, although an accurate estimate of the joint acceptance will be more important for the former since the acoustic half wavelength is smaller than the structural half wavelength. The same is also true for panels 3 and 4, however the difference between the two wavelengths is greater which would suggest a less accurate estimate compared to the first two panels. It is important at this stage to point out that these assumptions are based on the plan dimensions of the panels, and no account has been made of the doubly curved geometry of the panels. This may have an affect on the calculation of the joint acceptance for panels of this geometry, and would make an interesting topic for further study.

7.3.1 Approximation procedure

For broadband random acoustic excitation, where the bandwidth of excitation is greater than the response bandwidth of the mode of interest, the estimate of the RMS strain using Blevins method is given by [43]:-

$$\epsilon_{n_{RMS}} = \left(\frac{\pi f_n G_p(f)}{4\zeta_n}\right)^{1/2} \frac{\bar{\epsilon}}{\tilde{P}_{ic}} \tag{7.49}$$

The pressure spectrum level, $G_p(f)$, and the natural frequencies of vibration, f_n, mode shapes, and modal strains, $\bar{\epsilon}$ were obtained as discussed in the previous section, and the characteristic pressure, $\tilde{P}_{ic}$, was calculated using the formula [43]:-

$$\tilde{P}_{ic} = m(2\pi f_n)^2 |\phi_n(\mathbf{x}_c)| \tag{7.50}$$

where m is the mass per unit area, f_n is the natural frequency of vibration in the mode of interest, and $\phi_n(\mathbf{x}_c)$ is the maximum modal displacement at a characteristic point on the panel. All of the inputs to equation 7.50 were obtained from the FE model by conducting a modal analysis.

7.3.2 Estimation of the RMS strain response using Blevins' method

All of the parameters needed to estimate the RMS strain response of the doubly curved panels to random acoustic excitation using Blevins' method [43] are presented in tables 7.2 and 7.9. The damping was obtained from the experimental results from the PWT tests, as presented in section 5.5.2, and the mass per unit area for each

panel was constant at $5.24kg/m^2$.

The predicted RMS strain values using Blevin's approximation procedure, for the ten strain gauge locations on the four test panels, are presented in table 7.10 and figures 7.8 and 7.9. The results over-predict the RMS strain that was measured, where the latter values have been scaled according to the percentage contribution of the fundamental mode response to the overall RMS response. As expected, panel 1 gave the best results, followed by panel 4, with panels 2 and 3 giving the worst results with an average error of one order of magnitude. In theory, the results for panel 2 should have been better, however the choice of the characteristic modal displacement is important when using this method and hence could explain the slight departure from the anticipated results. Finally, the results using Blevin's method compare well with those obtained using the case 2, SDOF method presented in the previous section, where a joint acceptance of unity has been used in both methods. The slight differences between these two methods can be attributed to the choice of the maximum modal displacement at a characteristic point on the panel, $\phi_n(\mathbf{x}_c)$, which may not match the applied acoustic pressure [43].

Panel	f_1 (Hz)	ζ_1	$\lvert\tilde{w}_1(x,y,z)\rvert$ (m)	$\tilde{P}_{ic}$ (Nm^{-2})	Modal Strain, $(\mu\epsilon)$								
					gi1	gi2	gi3	gi4	gi5	go1	go2	go3	go4	go5
1	219.02	0.0105	0.687	13.66e6	126.6e3	221.7e3	233.4e3	87.44e3	84.07e3	287.9e3	171.3e3	176.3e3	294.9e3	284.1e3
2	164.30	0.0120	0.653	7.850e6	162.9e3	163.3e3	168.7e3	164.0e3	160.0e3	237.2e3	130.9e3	131.2e3	204.2e3	198.3e3
3	272.62	0.0125	0.458	7.053e6	52.97e3	312.3e3	349.6e3	64.06e3	63.53e3	199.0e3	257.4e3	278.8e3	144.9e3	140.3e3
4	288.67	0.0102	0.653	11.26e6	86.6e3	446.7e3	501.7e3	93.1e3	93.3e3	155.3e3	160.8e3	176.1e3	101.5e3	98.7e3

Table 7.9: Parameters for the four doubly curved sandwich panels used in Blevin's method (modal strains, natural frequencies and maximum modal displacement obtained using FE model).

Panel	$G_p(f)$	Estimated RMS Strain ($\mu\epsilon$)									
	(Pa^2Hz^{-1})	gi1	gi2	gi3	gi4	gi5	go1	go2	go3	go4	go5
1	184.90	32.30	56.55	59.53	22.30	21.45	73.43	43.70	44.98	75.22	72.47
	1002.0	75.23	131.71	138.65	51.95	49.95	171.04	101.78	104.77	175.20	168.79
	3120.0	132.75	232.42	244.66	91.67	88.15	301.81	179.61	184.87	309.15	297.85
	8711.0	221.82	388.37	408.82	153.18	147.29	504.31	300.12	308.91	516.59	497.69
	23692	365.81	640.46	674.19	252.62	242.90	831.67	494.94	509.44	851.92	820.76
2	200.00	68.43	68.63	70.90	68.93	67.25	99.67	55.00	55.13	85.79	83.34
	737.80	125.66	126.02	130.20	126.57	123.49	183.03	101.01	101.24	157.54	153.05
	2138.9	213.96	214.57	221.68	215.50	210.27	311.63	171.98	172.38	268.24	260.58
	5493.0	342.87	343.86	355.26	345.35	336.96	499.41	275.60	276.24	429.86	417.60
	13659	540.68	542.23	560.21	544.59	531.36	787.51	434.60	435.60	677.85	658.51
3	234.20	15.04	88.68	99.29	18.19	18.04	56.52	73.11	79.16	41.14	39.86
	1080.7	32.32	190.50	213.30	39.08	38.76	121.42	157.04	170.06	88.38	85.62
	3093.9	54.68	322.33	360.90	66.12	65.58	205.44	265.72	287.73	149.53	144.86
	8264.9	89.37	526.82	589.86	108.08	107.19	335.77	434.30	470.28	244.40	236.76
	20186	139.67	823.33	921.84	168.90	167.51	524.75	678.73	734.96	381.95	370.02
4	203.68	16.36	84.38	94.76	17.60	17.62	29.34	30.38	33.26	19.17	18.65
	970.62	35.70	184.18	206.86	38.41	38.47	64.05	66.31	72.60	41.85	40.71
	3280.5	65.64	338.61	380.29	70.61	70.73	117.75	121.91	133.47	76.95	74.84
	10150	115.45	595.61	668.93	124.20	124.41	207.11	214.44	234.77	135.35	131.64
	26325	185.93	959.21	1077.29	200.02	200.35	333.55	345.34	378.09	217.97	212.01

Table 7.10: Estimated RMS strain for the ten strain gauges located on the four test panels. Blevin's approximation method.

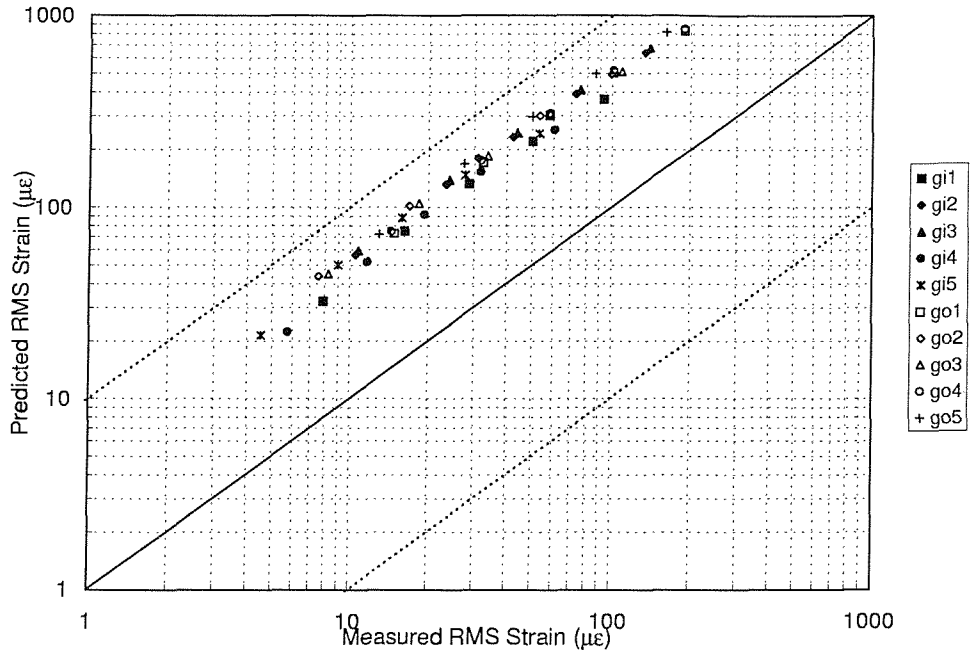

(a) Panel 1.

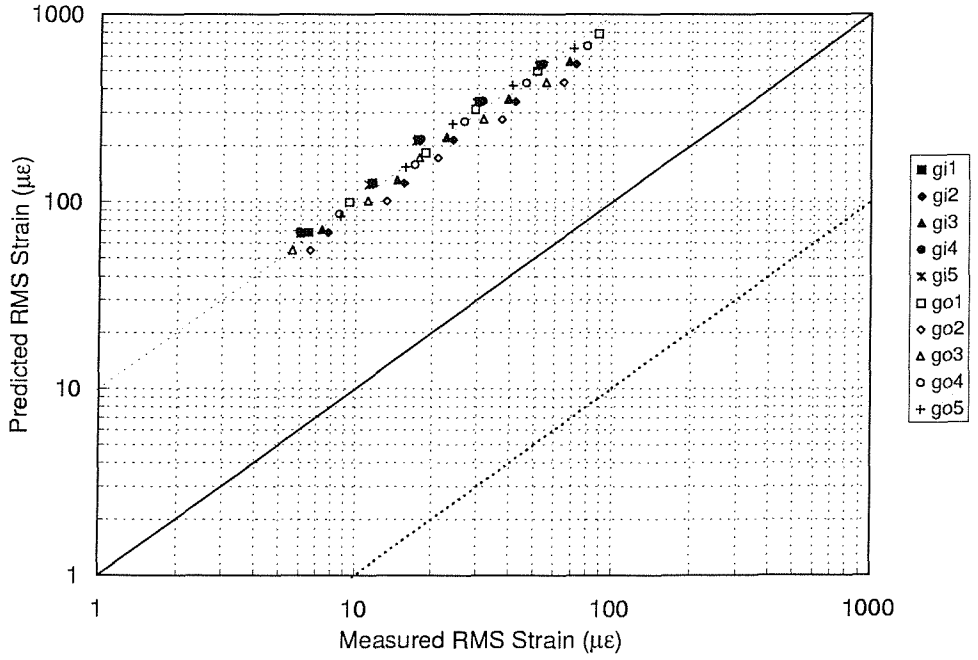

(b) Panel 2.

Figure 7.8: Comparison of measured and predicted RMS strain for panels 1 and 2 using Blevin's approximation method. Narrow-band response centred on the fundamental mode of vibration excited by the PWT.

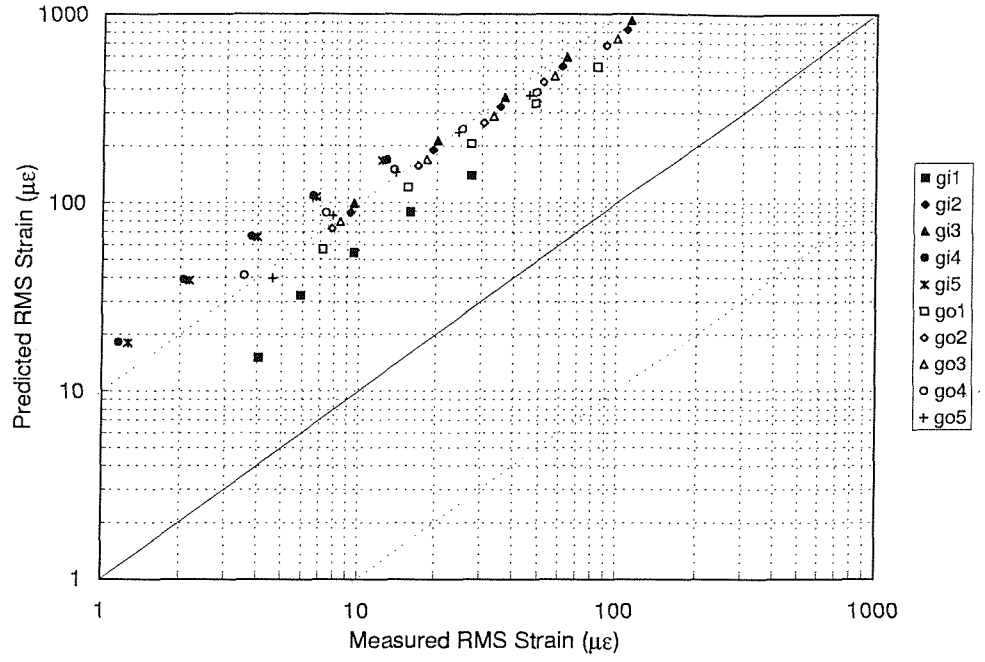

(a) Panel 3.

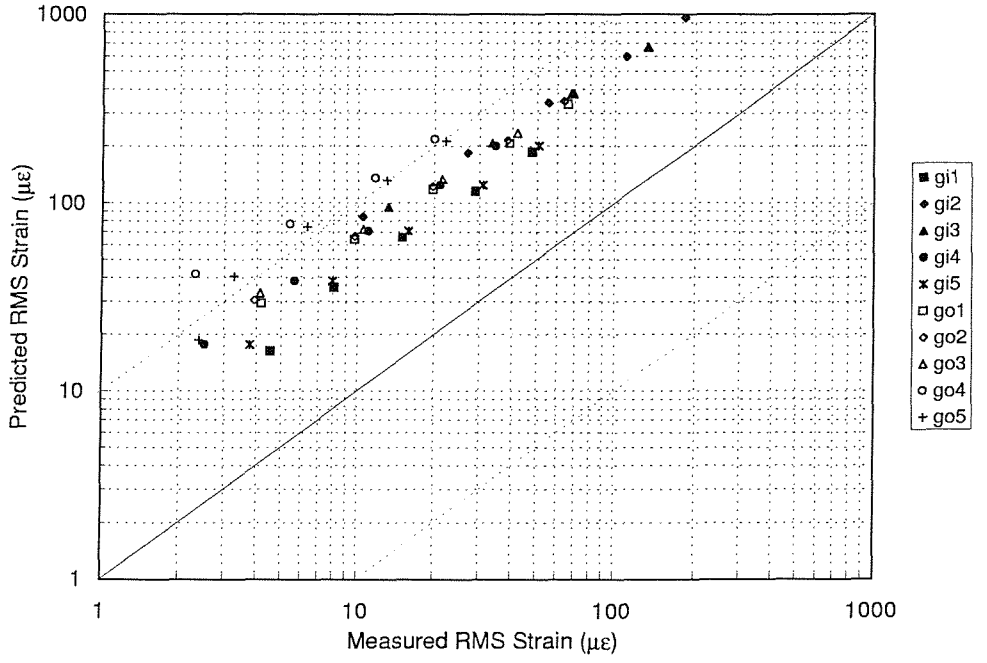

(b) Panel 4.

Figure 7.9: Comparison of measured and predicted RMS strain for panels 3 and 4 using Blevin's approximation method. Narrow-band response centred on the fundamental mode of vibration excited by the PWT.

7.4 Dynamic response prediction using the Finite Element Method

The ANSYS finite element models of the four test panels were used to predict the dynamic response to random acoustic excitation in the PWT. A full description of the FE models is presented in chapter 6, and the boundary conditions applied are discussed in chapter 5.

Two possible options exist for modelling the random acoustic pressure loading in the PWT. The first involves dividing the structure into zones of equal surface area, in which the pressure PSD is assumed to be spatially correlated over each zone. Ideally, each zone should be the size of each finite element in the model, but this would create a huge amount of data in this case since each model contains approximately 1200 elements. It would therefore be more convenient to define larger zones, say eight in total, over the entire surface of the panel. The loading can then be represented as a convecting noise field by means of the ANSYS propagating wave option (PSDWAV) in the spectrum analysis solution process. Here, the loading is assumed to propagate with a velocity which can be defined in any or all of the three cartesian coordinates, x, y, and z. Further investigation of this option revealed that the PSDWAV command could not be used with a specified pressure PSD loading. In any case, it was unclear whether the propagation was uni- or bi-directional in each coordinate axis.

The second option is to model a series of travelling waves over the whole surface of the panel within the frequency range of interest, and this was the option used to generate a solution for the acoustically excited doubly curved panels located in the PWT. The analysis was divided into 10 Hz frequency bands from 47 Hz to 545 Hz in which the acoustic wavenumber, k_a was held constant. A harmonic analysis was carried out in each frequency band with five sub-step calculations made, centred on the frequency step in the loop. Within each of these frequency bands, the loading was applied in lines which ran the length of the short side, and were spaced at intervals equal to the element edge length from one end of the panel to the other along the long side. Unit forces were applied at the corner nodes on these lines, and the real and imaginary parts of the load were defined according to the x_n-location of the nodal line, and the frequency step being analysed, which along with the convection velocity, $c = 342.8m/s$ (as previously calculated from experiments in chapter 5), defined the acoustic wavenumber, k_a, hence:-

$$\Re\{F_n\} = F_0 cos(k_a x_n) \tag{7.51}$$

and,

$$\Im\{F_n\} = F_0 sin(k_a x_n) \tag{7.52}$$

where $F_0 = 1N$, and $k_a = 2\pi f/c$. In this way, a travelling wave was simulated, as illustrated in figure 7.10. As can be seen, as one progresses along the panel (in the x-direction) each line of nodal harmonic forces has a phase which will lag behind the previous line of nodal forces according to the distance from the edge of the panel, i.e. at $x = 0$. Therefore, for each harmonic solution where the frequency is kept constant, a travelling wave is simulated by virtue of this phase difference between adjacent lines of nodal force. The concept is further illustrated in figure 7.12, where the FE model of panel 1 is shown with the real part of the nodal forces shown for the frequency band centred on, $f_c = 240$Hz. The real part of the nodal forces is shown (a) in-phase, (b) with a 20° phase lag, (c) with a 40° phase lag, and finally (c) with a 80° phase lag with respect to the initial phase angle. The solution process employed in ANSYS is illustrated in the flowchart in figure 7.11. As can be seen, a harmonic solution with five sub-steps is carried out in each frequency band during which the acoustic wavenumber was kept constant. Following this, the acoustic wavenumber is re-calculated according to the next centre frequency, and the load is re-applied and the harmonic solution obtained. The results are output in terms of the strain transfer function (in $\mu\epsilon/N$) versus the sub-step frequency values for each strain gauge location.

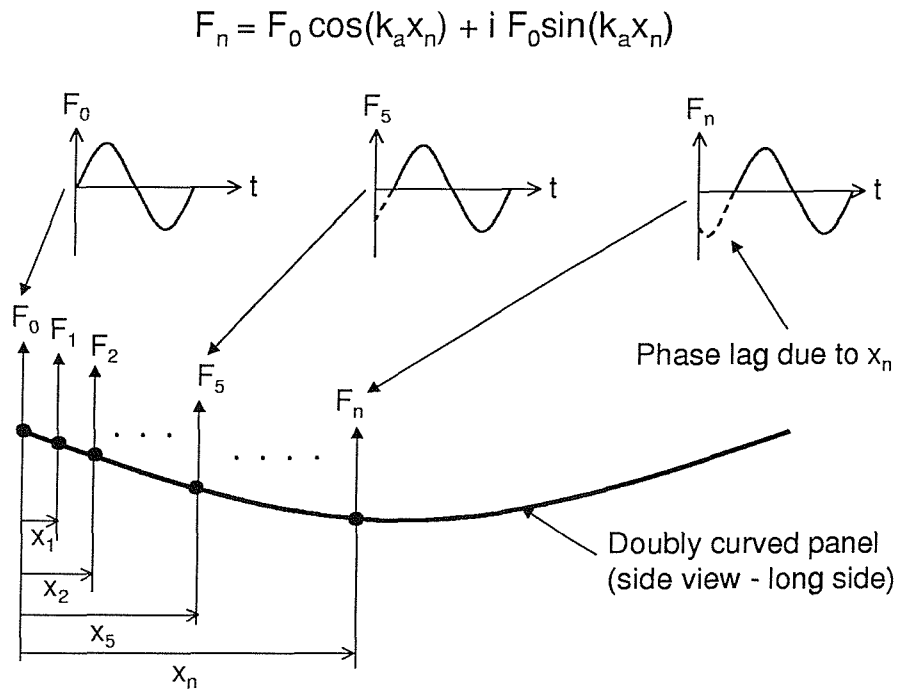

Figure 7.10: Illustration of the simulated travelling wave loading applied to the FE model. The phase of the individual line of nodal loads was calculated according to the nodal line location and acoustic wavenumber (defined by the centre frequency in the solution loop).

The strain PSD was obtained by first calculating the strain transfer function in terms of pressure, taking the absolute value and squaring, before finally multiplying by the measured pressure spectrum, $G_p(f)$ obtained from the experiments (see figure 7.3):-

$$G_\epsilon = \left| \frac{\mathbf{H}_\epsilon(f)}{(F_0 N/A)} \right|^2 . G_p(f) \tag{7.53}$$

where $\mathbf{H}_\epsilon(f)$ is the strain transfer function obtained from the FE model (in terms of force), N is the total number of nodes on which the unit force, F_0, was applied, and A is the panel surface area.

The results of the finite element analysis are shown in figures 7.13 to 7.28. Here, a comparison has been made between the predicted (FE) and measured strain power spectral density for the inner and outer centre gauges (gi3, gi4, go3, and go4) at the five overall sound pressure levels. For all four panels, the predicted response is almost entirely in the fundamental mode, with very little contribution evident from other modes. The measured response shows a contribution from the second, and in some cases, the third mode. This is particularly true for the outer x-wise centre gauge on each panel, and panels 3 and 4 shows a predominant response in a higher mode ($\approx$ 320 Hz for panel 3, and $\approx$ 500 Hz for panel 4) for this gauge. The FE predicted response compares very well with the measured response, and it appears that the FE method under-predicts in the majority of cases when one compares the maximum resonant responses. The RMS strain levels were calculated and compared with the measured RMS responses over the same frequency bandwidth (47 Hz to 550 Hz). The results for each of the four panels are shown in figures 7.29 and 7.30. As can be seen, the FE method resulted in a consistent under-predicted RMS strain response with the majority of the results falling within a 30% confidence limit. The best results were obtained for panels 1 and 2, which was also found to be the case for the SDOF analysis. For panel 4, the prediction for the outer centre gauges, go4 and go5, gave the worst results. From the plot of the strain PSD, it is clear that for gauge go4 this can be attributed to a higher mode predominating the response and therefore resulting in a higher RMS value compared to the FE prediction, where there was found to be little response from higher modes. In the FE analysis, the first four non-rigid body modes were included in the harmonic response, and damping values for each of these modes were included. It is therefore unclear why higher modes are not as apparent in the FE results compared with the measured response. However, the agreement between the experimental results and predicted response was very good for

the fundamental mode in all cases, and in some cases such as for gauge gi4 on panel 2 (figure 7.18), the agreement for the higher modes was reasonable. One possible explanation for the higher mode disagreement could be that in the PWT there was some asymmetric excitation across the width of the panel (i.e. from the top to the bottom of the aperture), which could have been enough to excite the higher modes which have nodal lines running along the length of the panel. Since the excitation in the travelling wave method adopted in the FE calculations was constant in phase across the width of the panel (y direction), any modes with nodal lines along the length of the panel would not have been excited. In any case, it is clear from the FE results that the travelling wave method works well for analysing the response of structures to random acoustic excitation.

There is certainly potential for using the travelling wave method in the FE analysis to study the response to various loading spectra, including spectra with discrete tones such as would be found in the duct of an engine intake. Once the harmonic analysis has been carried out and the transfer function obtained, it is a simple matter to find the response to different loading spectra. In addition, it would also be worthwhile investigating the effects of changing various panel design parameters and boundary conditions on the response to random acoustic excitation.

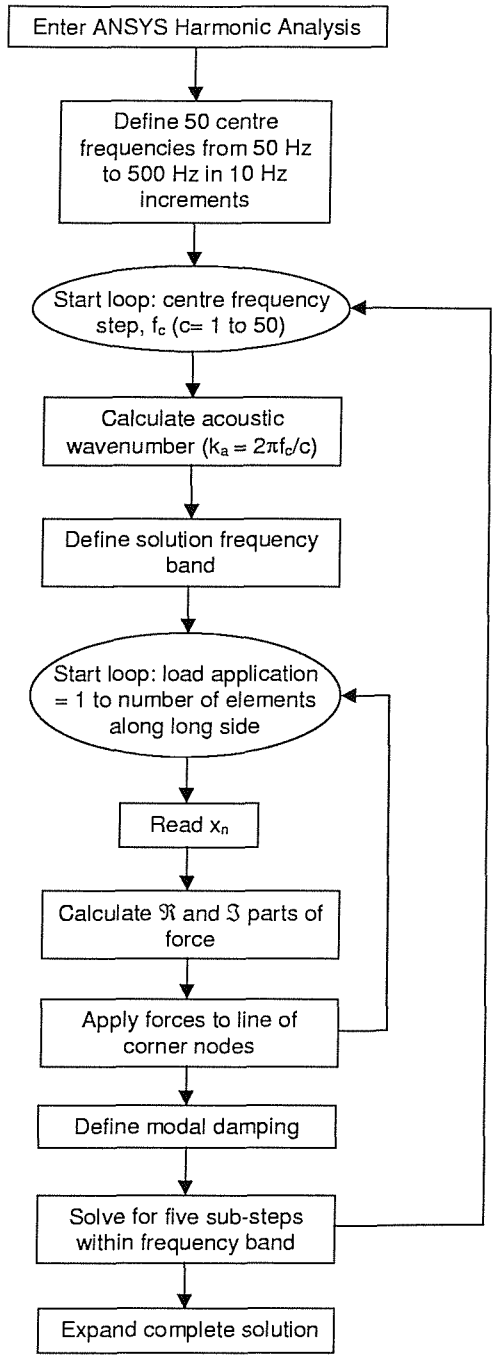

Figure 7.11: Flowchart illustrating the harmonic analysis solution process used in ANSYS to simulate travelling acoustic waves at frequencies from 47 Hz to 550 Hz).

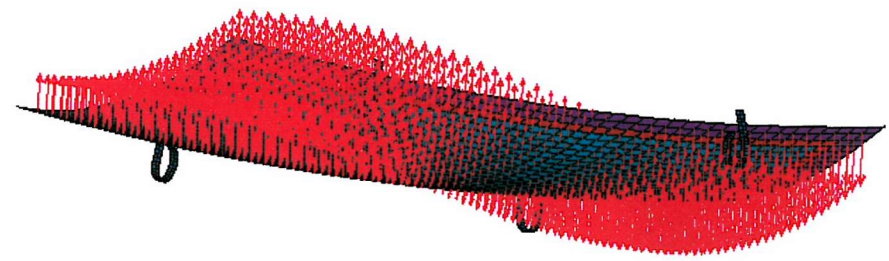

(a)

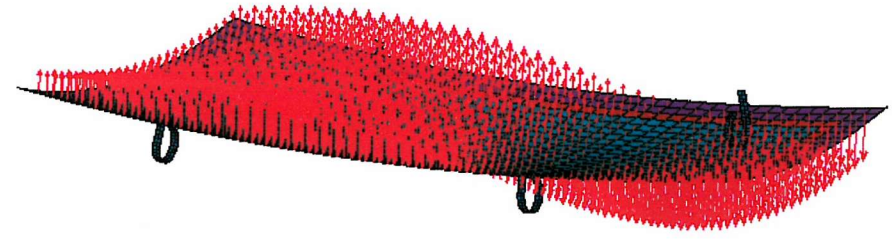

(b)

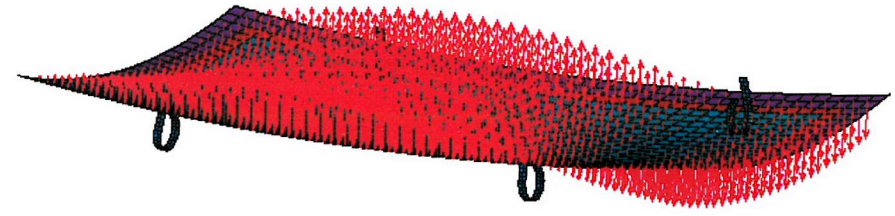

(c)

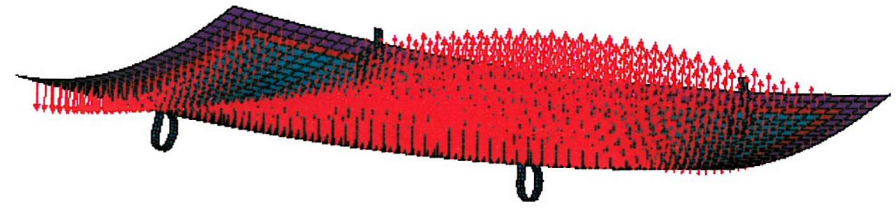

(d)

Figure 7.12: Finite Element Model of panel 1 with the real part of the nodal forces applied, (a) in-phase, (b) 20° phase lag, (c) 40° phase lag, and (c) 80° phase lag, with respect to the initial phase angle (centre frequency, $f_c = 240$ Hz).

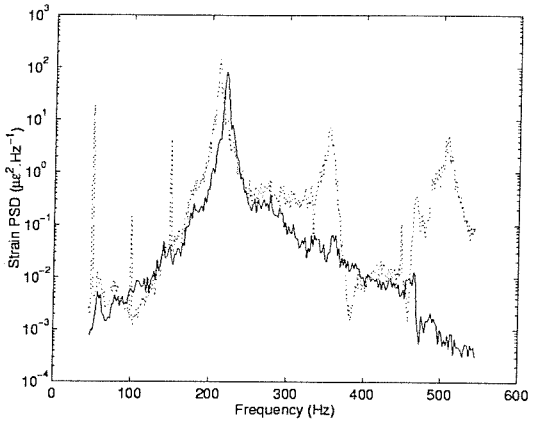

(a) 143.29 dB

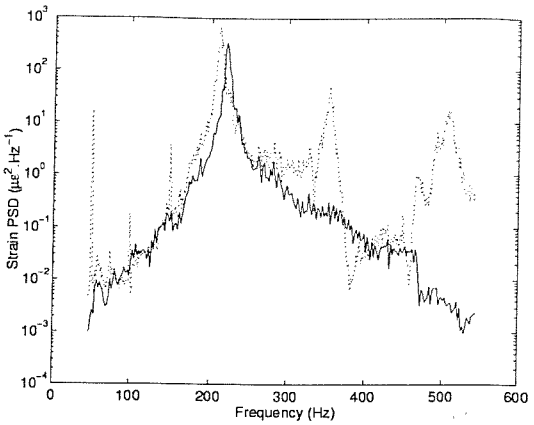

(b) 149.97 dB

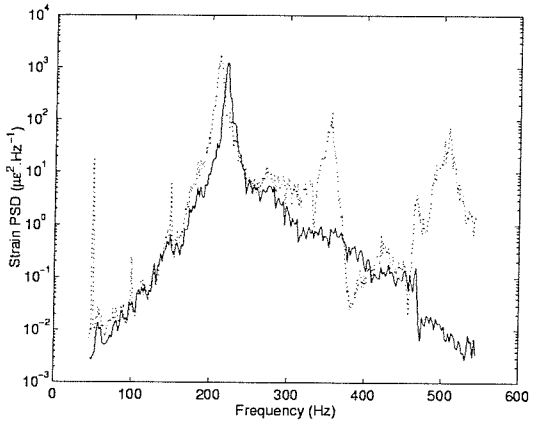

(c) 154.75 dB

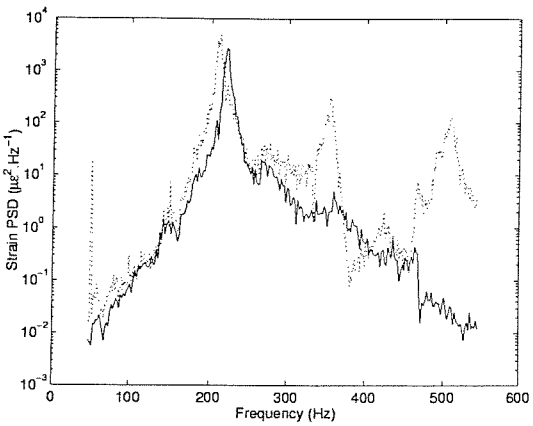

(d) 159.28 dB

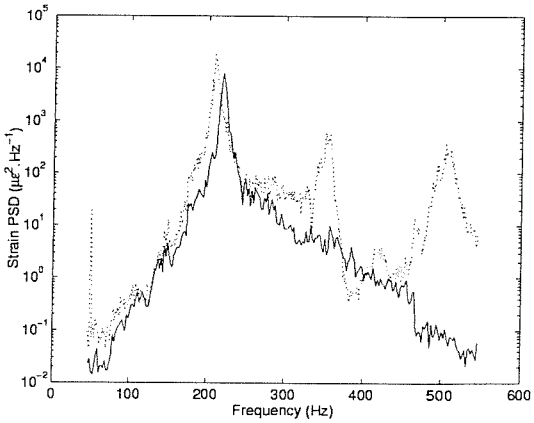

(e) 163.71 dB

Figure 7.13: Comparison of predicted FE (–) and measured (- -) strain PSD for inner centre gauge gi3 (y-wise), panel 1.

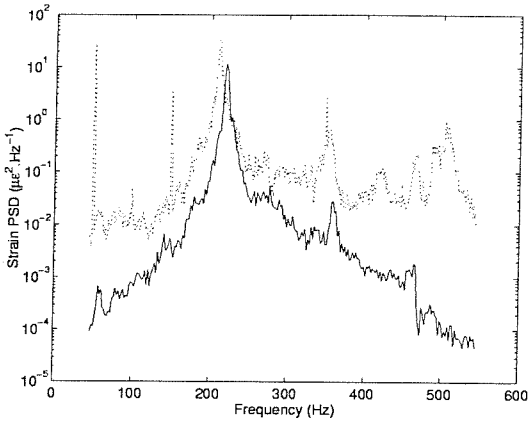

(a) 143.29 dB

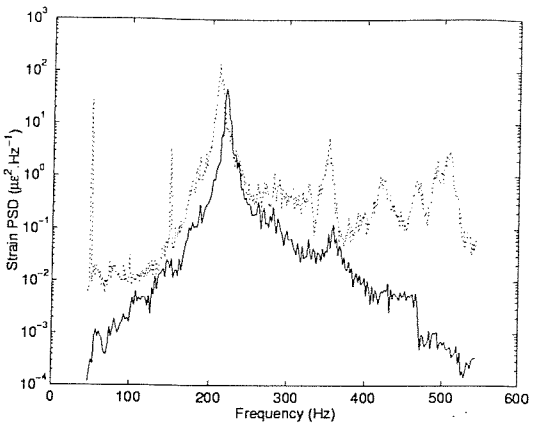

(b) 149.97 dB

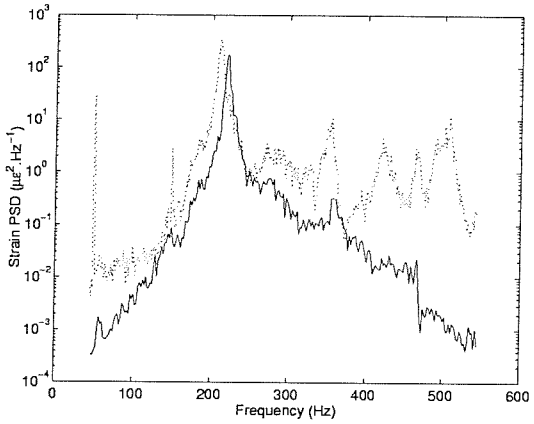

(c) 154.75 dB

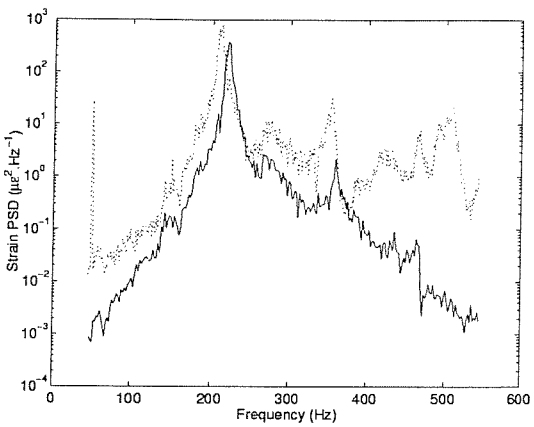

(d) 159.28 dB

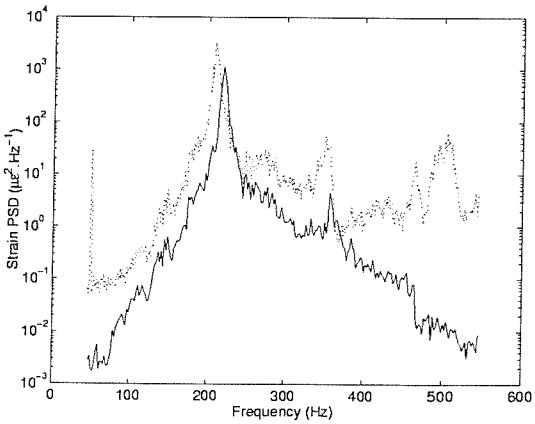

(e) 163.71 dB

Figure 7.14: Comparison of predicted FE (–) and measured (- -) strain PSD for inner centre gauge gi4 (x-wise), panel 1.

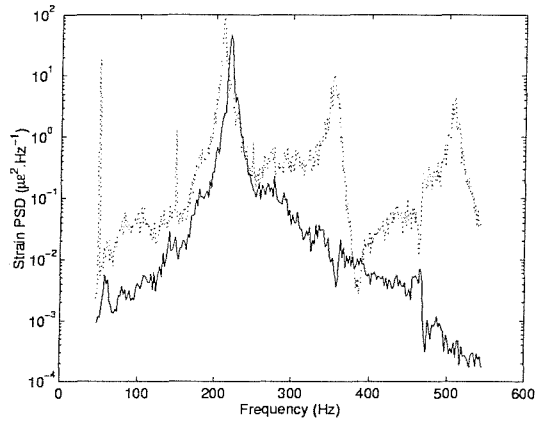

(a) 143.29 dB

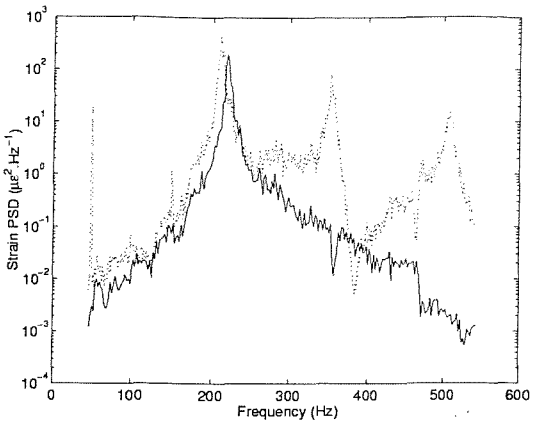

(b) 149.97 dB

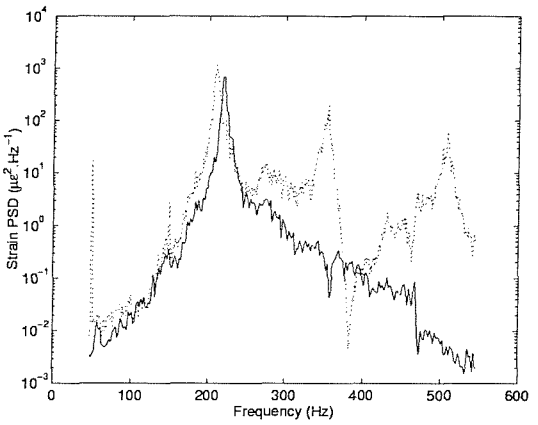

(c) 154.75 dB

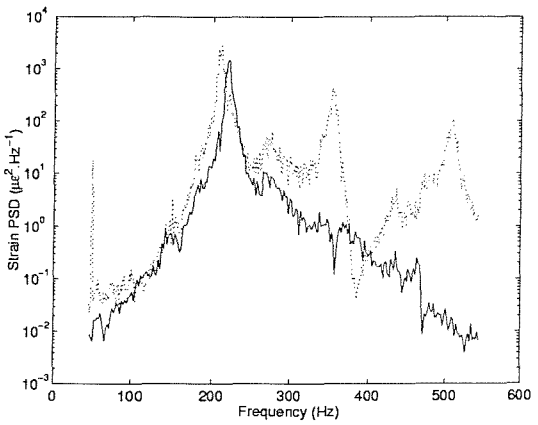

(d) 159.28 dB

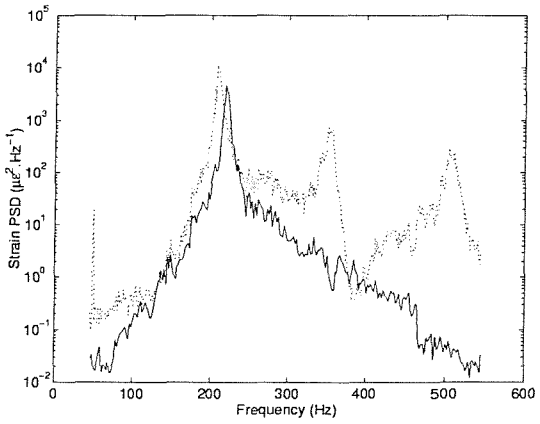

(e) 163.71 dB

Figure 7.15: Comparison of predicted FE (–) and measured (- -) strain PSD for outer centre gauge go3 (y-wise), panel 1.

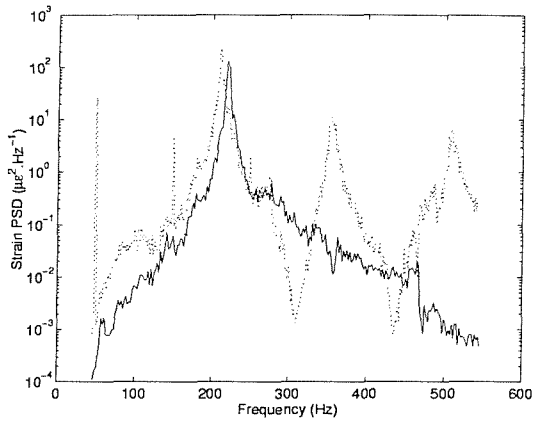

(a) 143.29 dB

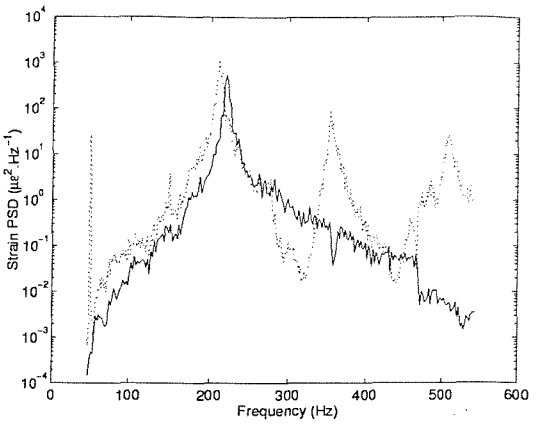

(b) 149.97 dB

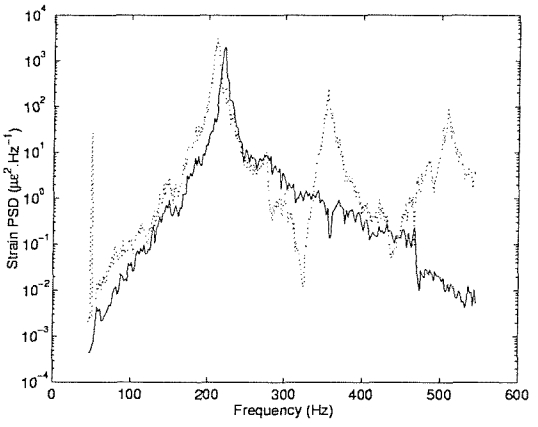

(c) 154.75 dB

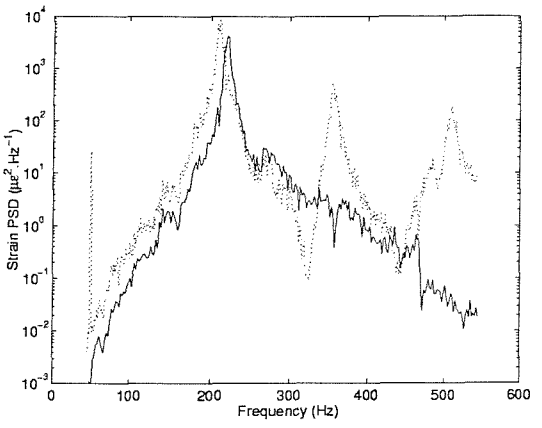

(d) 159.28 dB

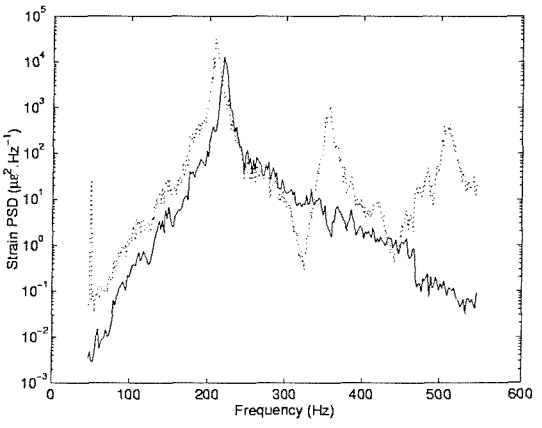

(e) 163.71 dB

Figure 7.16: Comparison of predicted FE (–) and measured (- -) strain PSD for outer centre gauge go4 (x-wise), panel 1.

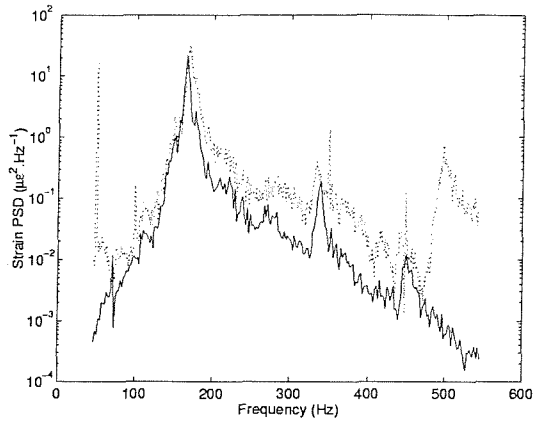

(a) 143.88 dB

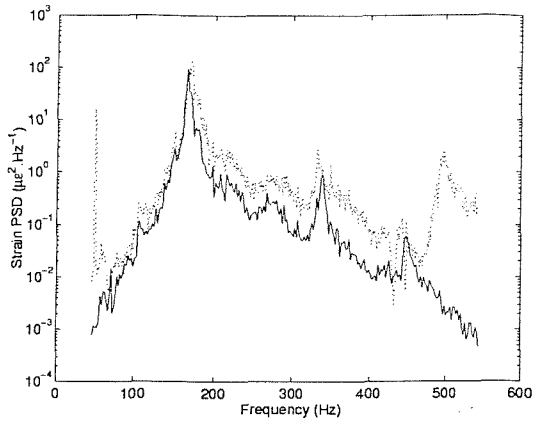

(b) 149.91 dB

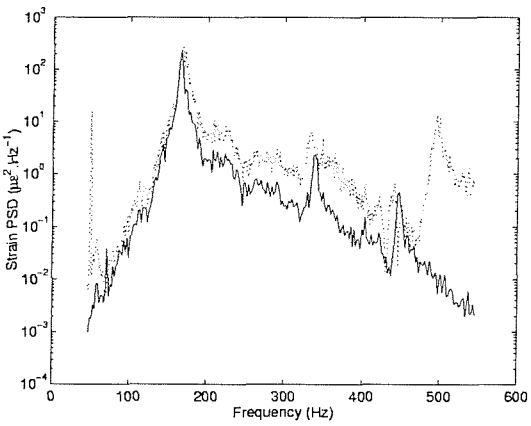

(c) 154.92 dB

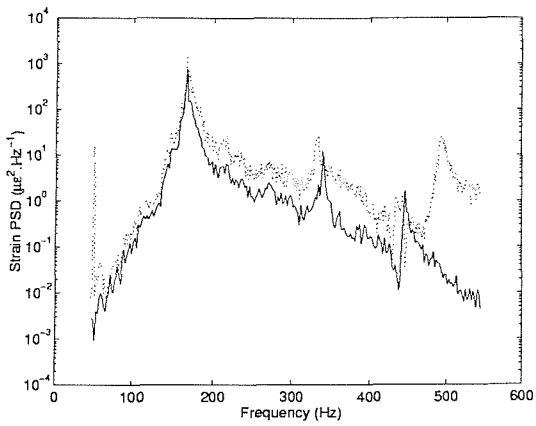

(d) 159.00 dB

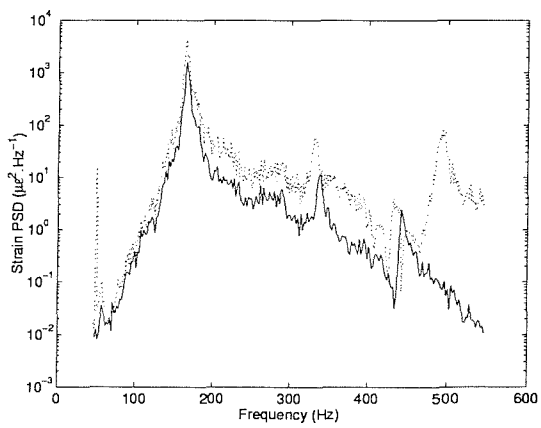

(e) 163.09 dB

Figure 7.17: Comparison of predicted FE (–) and measured (- -) strain PSD for inner centre gauge gi3 (y-wise), panel 2.

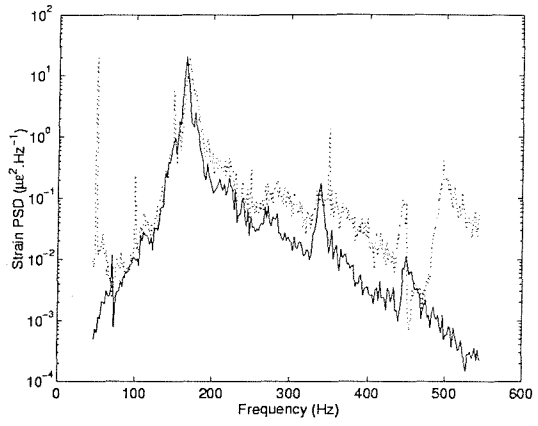

(a) 143.88 dB

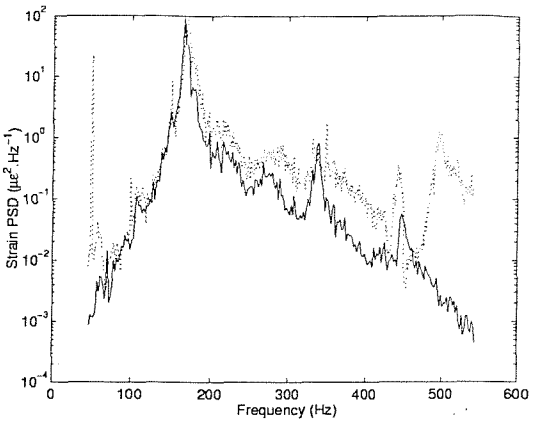

(b) 149.91 dB

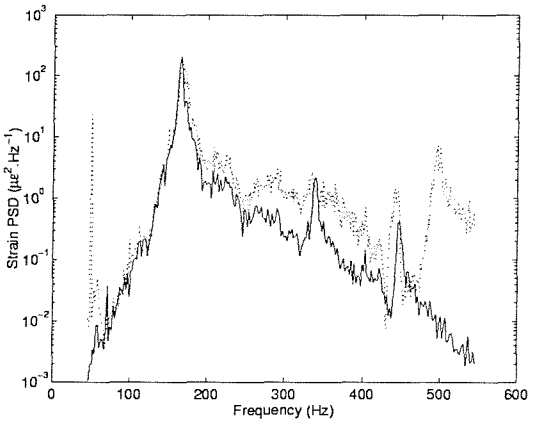

(c) 154.92 dB

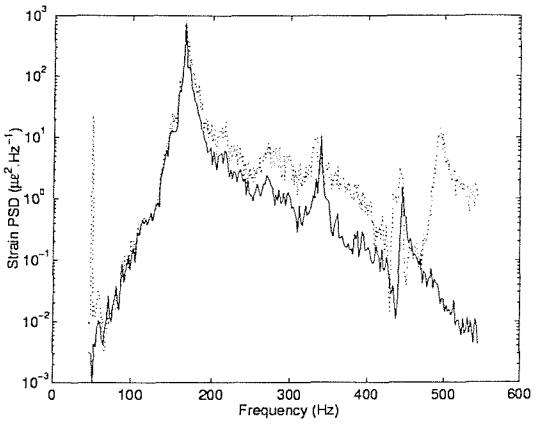

(d) 159.00 dB

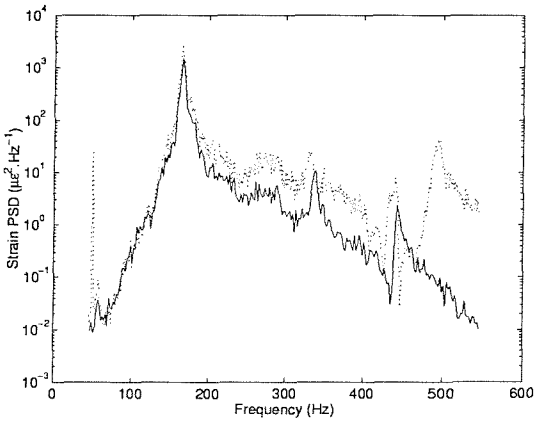

(e) 163.09 dB

Figure 7.18: Comparison of predicted FE (–) and measured (- -) strain PSD for inner centre gauge gi4 (x-wise), panel 2.

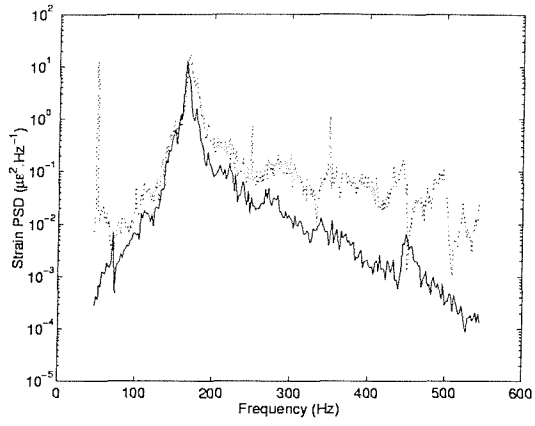

(a) 143.88 dB

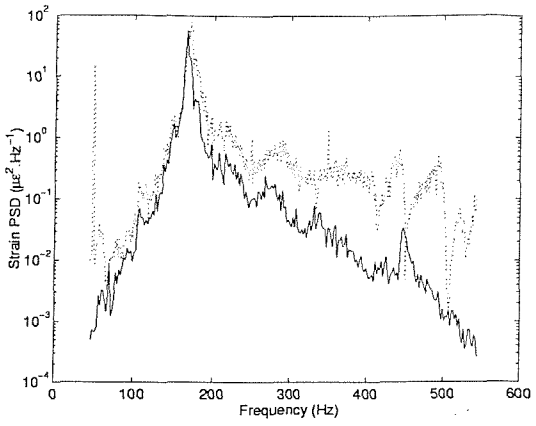

(b) 149.91 dB

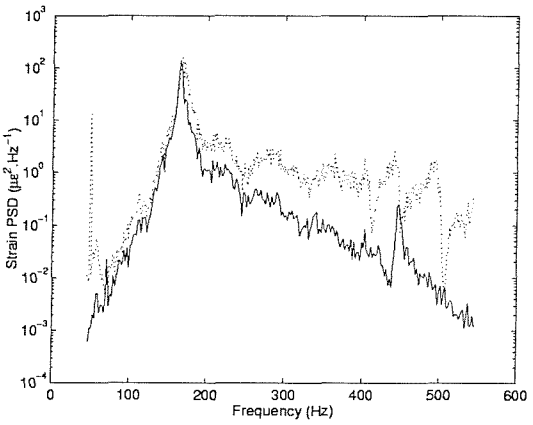

(c) 154.92 dB

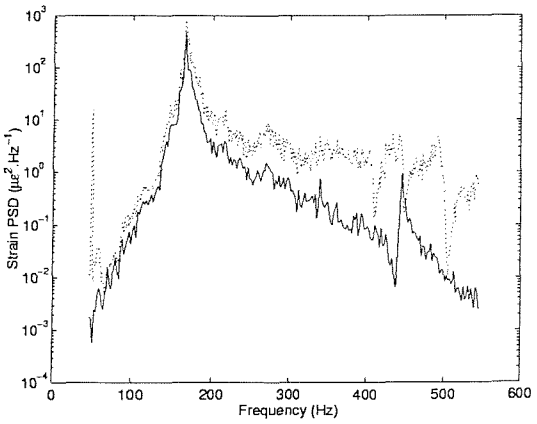

(d) 159.00 dB

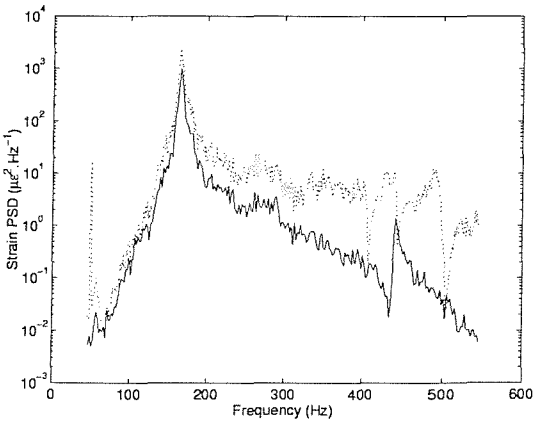

(e) 163.09 dB

Figure 7.19: Comparison of predicted FE (–) and measured (- -) strain PSD for outer centre gauge go3 (y-wise), panel 2.

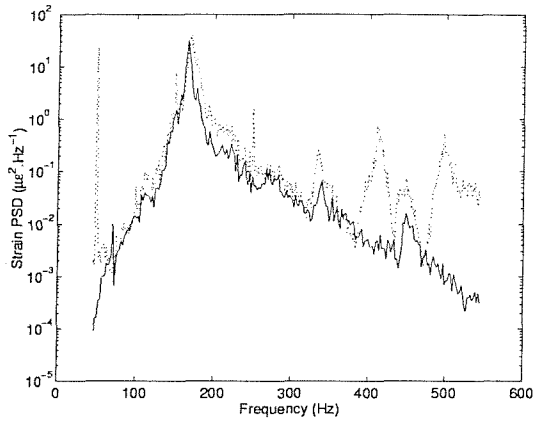

(a) 143.88 dB

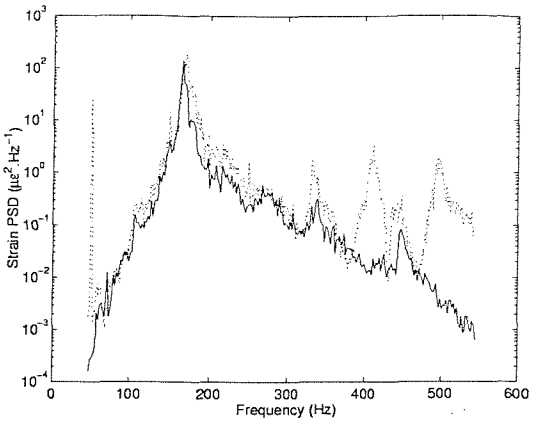

(b) 149.91 dB

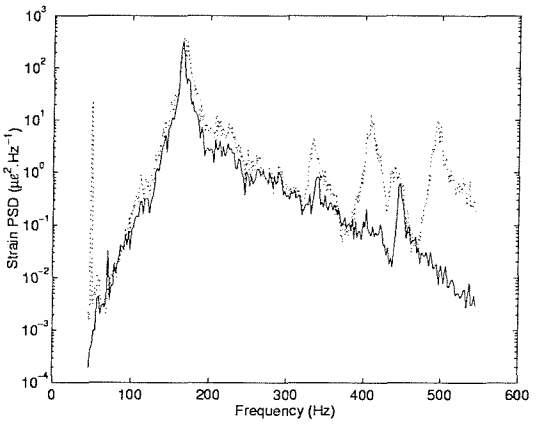

(c) 154.92 dB

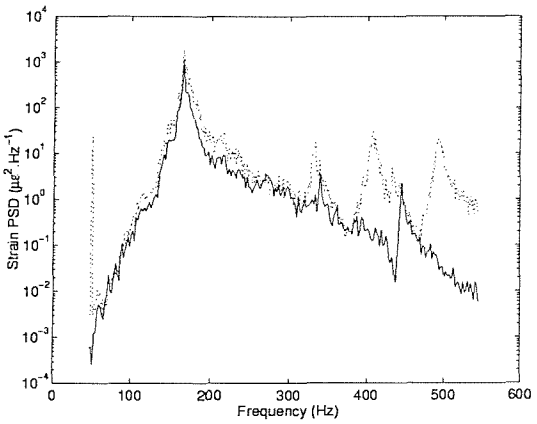

(d) 159.00 dB

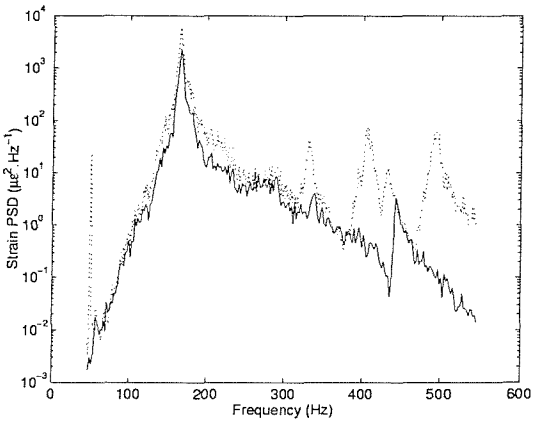

(e) 163.09 dB

Figure 7.20: Comparison of predicted FE (–) and measured (- -) strain PSD for outer centre gauge go4 (x-wise), panel 2.

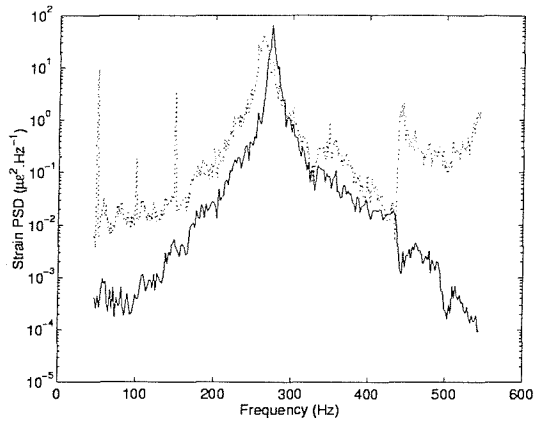

(a) 143.29 dB

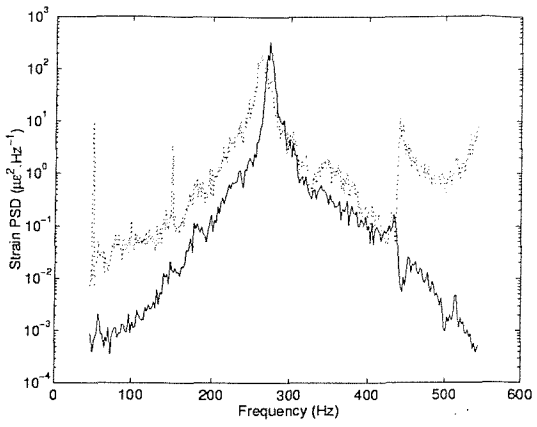

(b) 149.97 dB

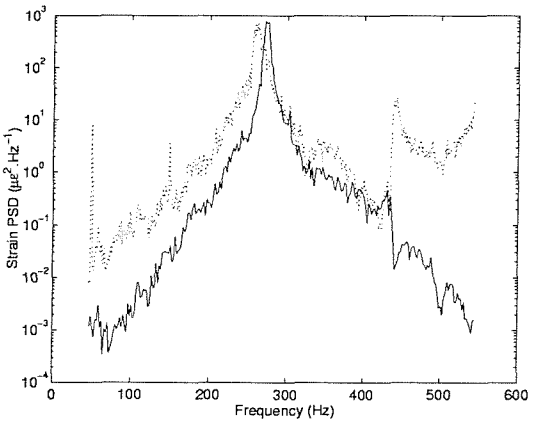

(c) 154.75 dB

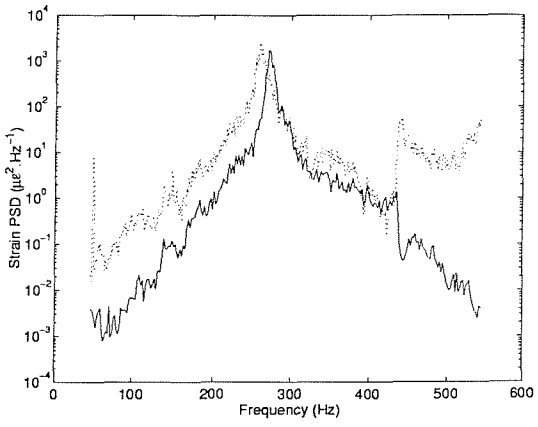

(d) 159.28 dB

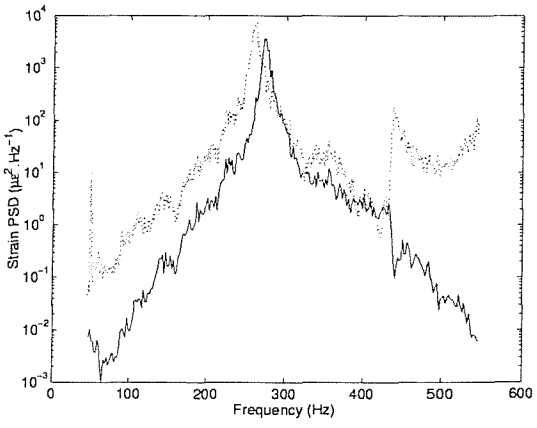

(e) 163.71 dB

Figure 7.21: Comparison of predicted FE (–) and measured (- -) strain PSD for inner centre gauge gi3 (y-wise), panel 3.

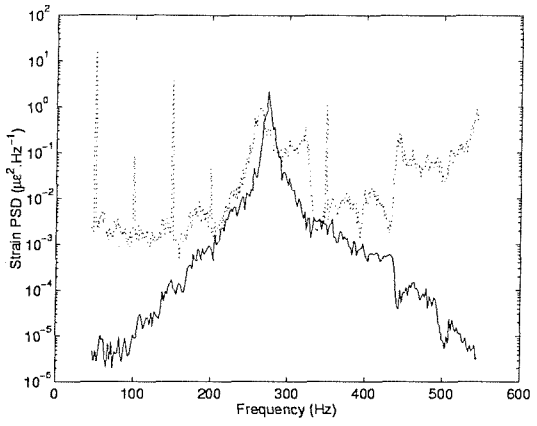

(a) 143.51 dB

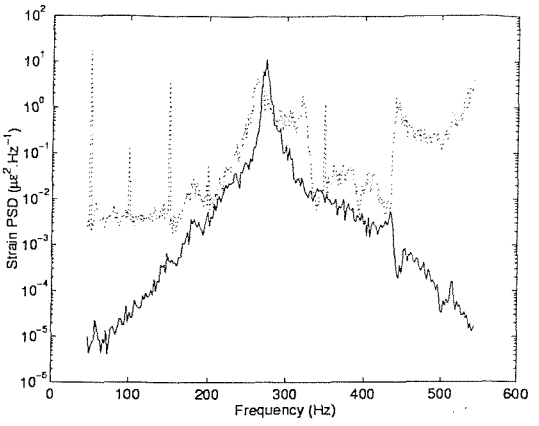

(b) 149.93 dB

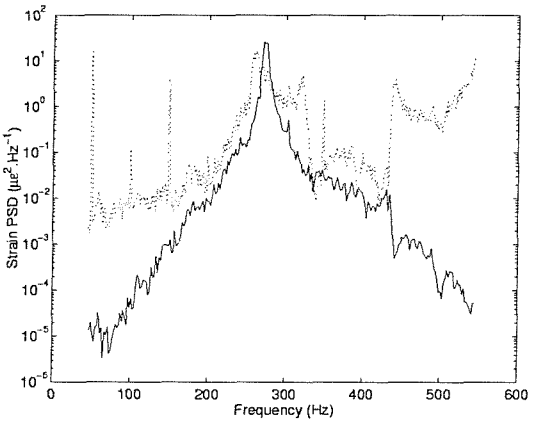

(c) 154.18 dB

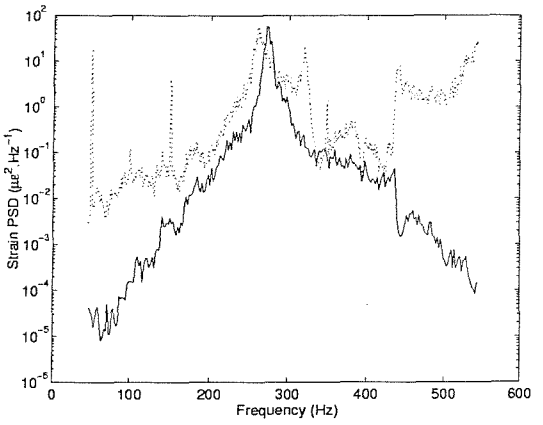

(d) 158.84 dB

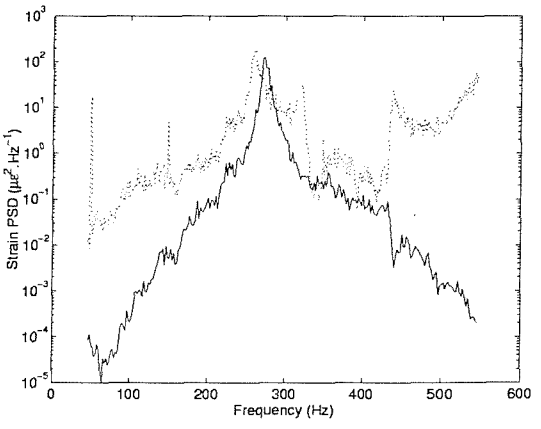

(e) 162.82 dB

Figure 7.22: Comparison of predicted FE (–) and measured (- -) strain PSD for inner centre gauge gi4 (x-wise), panel 3.

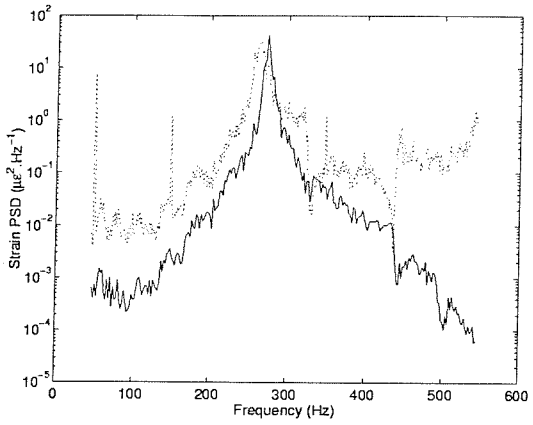

(a) 143.51 dB

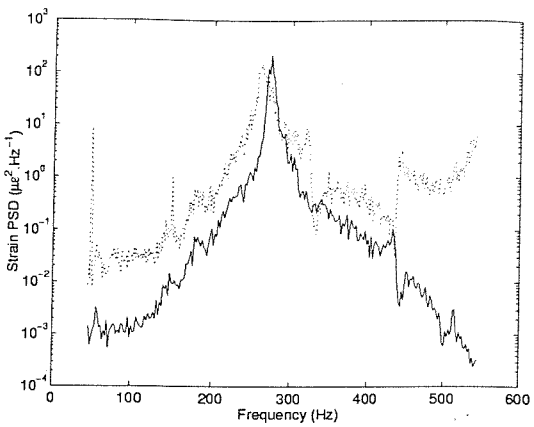

(b) 149.93 dB

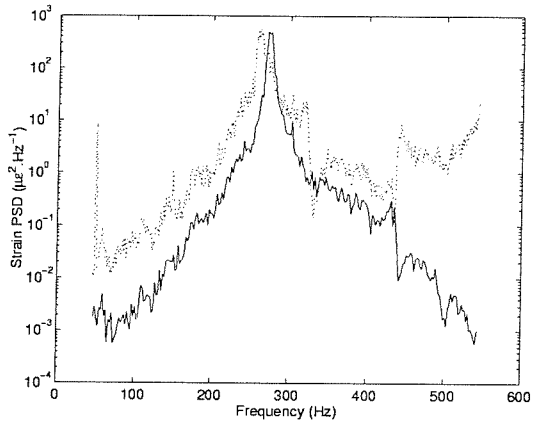

(c) 154.18 dB

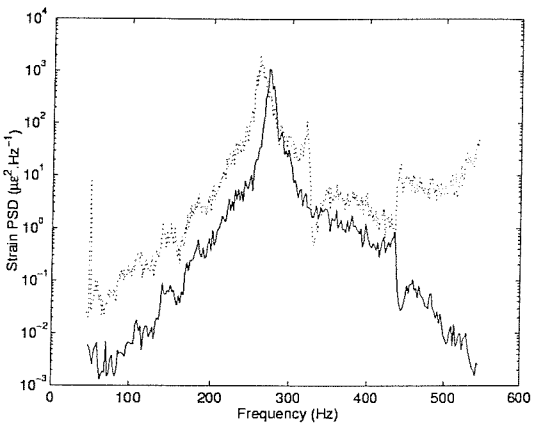

(d) 158.84 dB

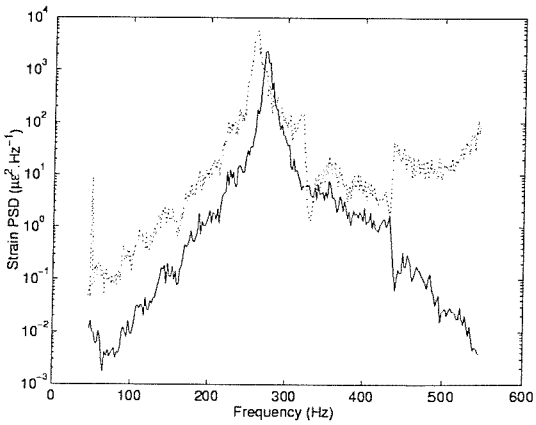

(e) 162.82 dB

Figure 7.23: Comparison of predicted FE (–) and measured (- -) strain PSD for outer centre gauge go3 (y-wise), panel 3.

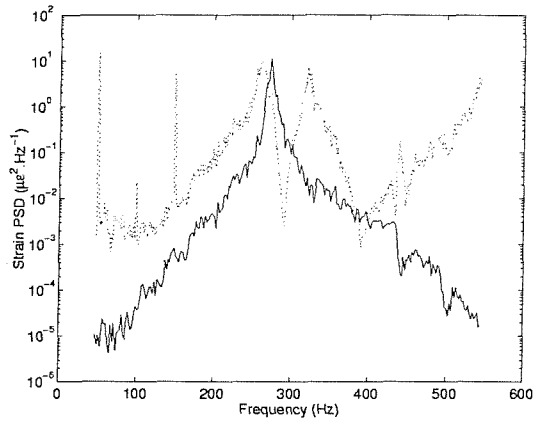

(a) 143.51 dB

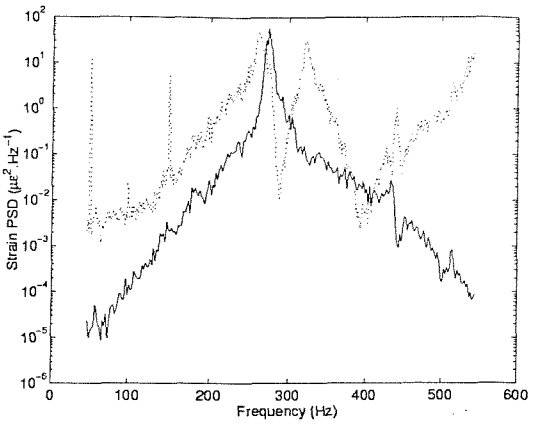

(b) 149.93 dB

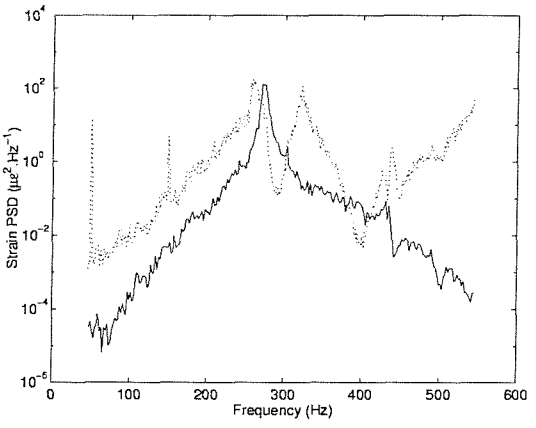

(c) 154.18 dB

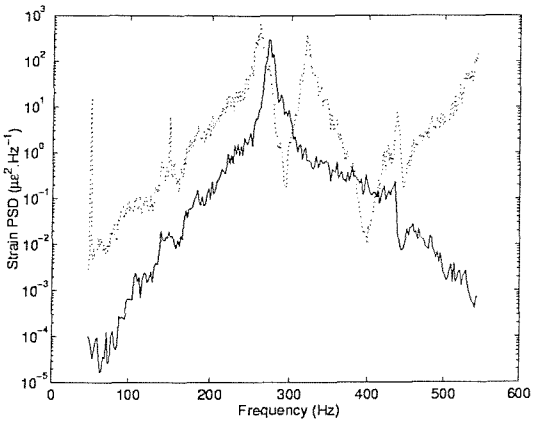

(d) 158.84 dB

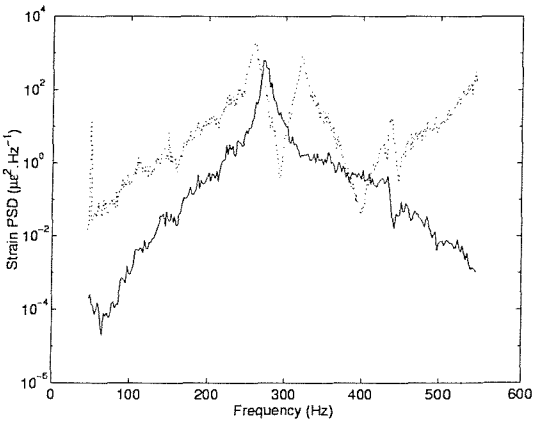

(e) 162.82 dB

Figure 7.24: Comparison of predicted FE (–) and measured (- -) strain PSD for outer centre gauge go4 (x-wise), panel 3.

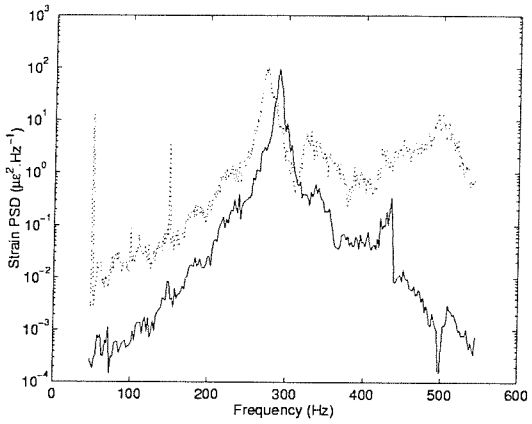

(a) 143.20 dB

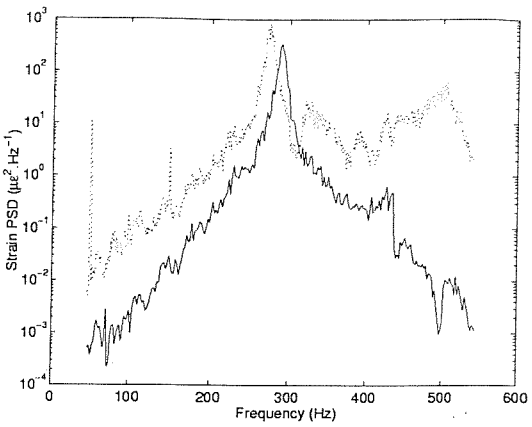

(b) 149.49 dB

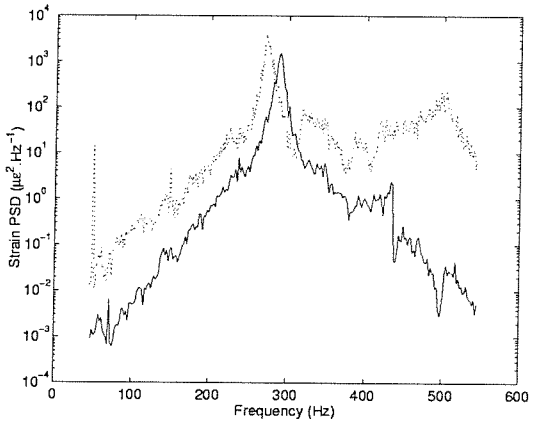

(c) 154.69 dB

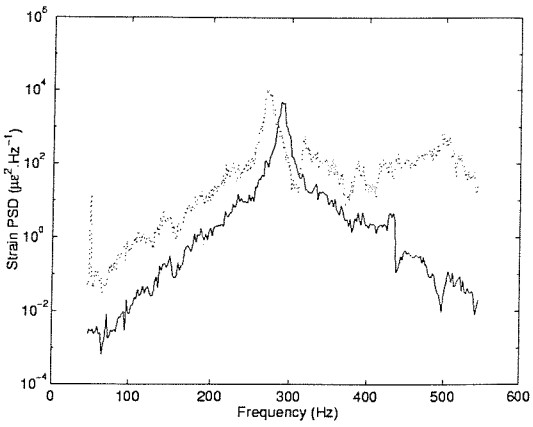

(d) 159.49 dB

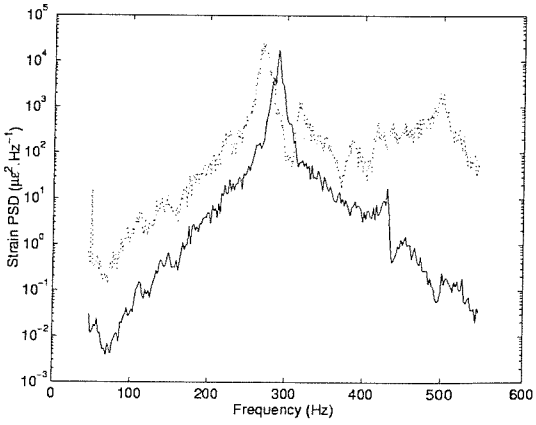

(e) 163.71 dB

Figure 7.25: Comparison of predicted FE (–) and measured (- -) strain PSD for inner centre gauge gi3 (y-wise), panel 4.

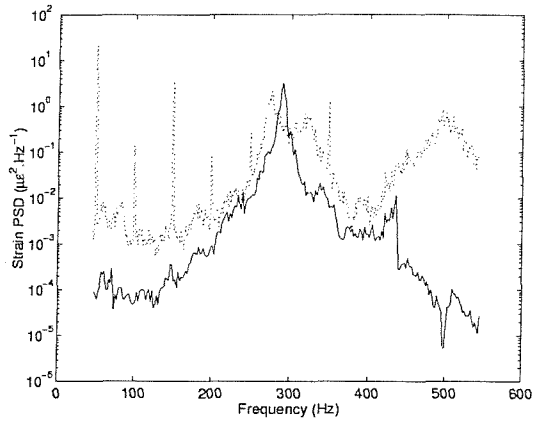

(a) 143.20 dB

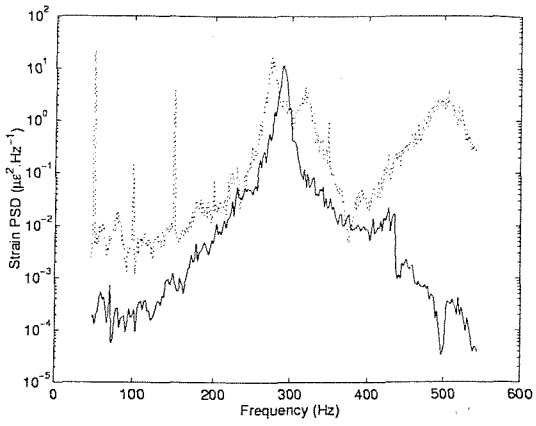

(b) 149.49 dB

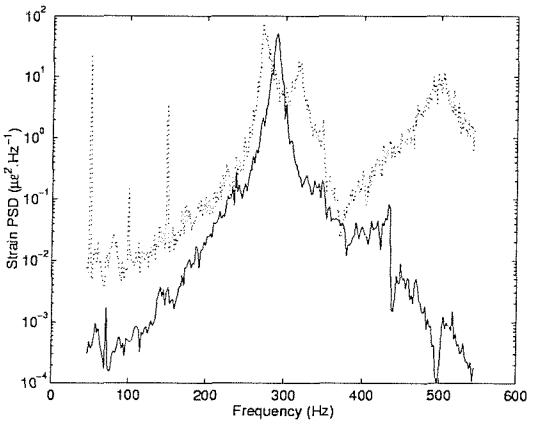

(c) 154.69 dB

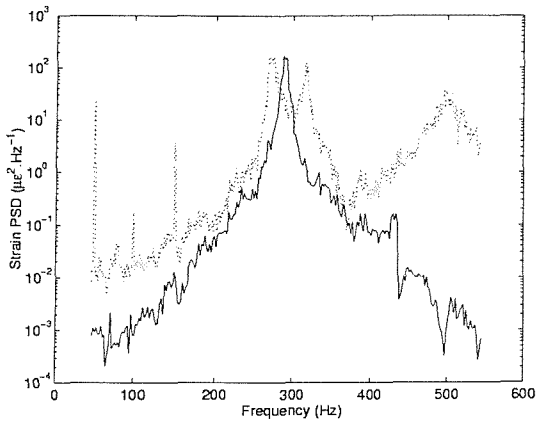

(d) 159.49 dB

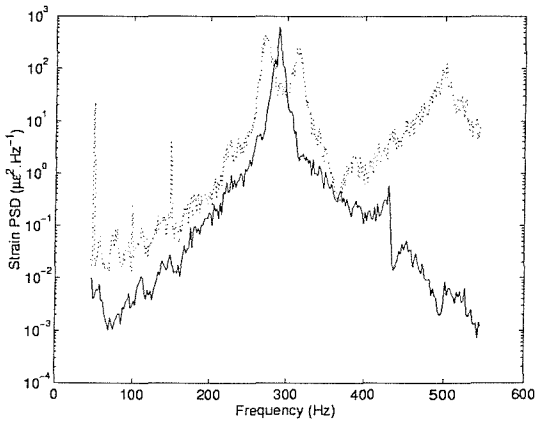

(e) 163.71 dB

Figure 7.26: Comparison of predicted FE (–) and measured (- -) strain PSD for inner centre gauge gi4 (x-wise), panel 4.

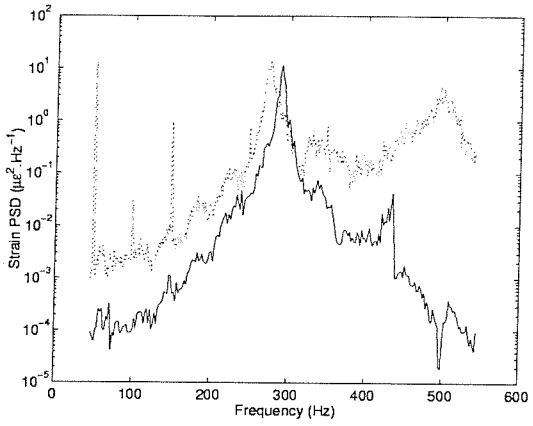

(a) 143.20 dB

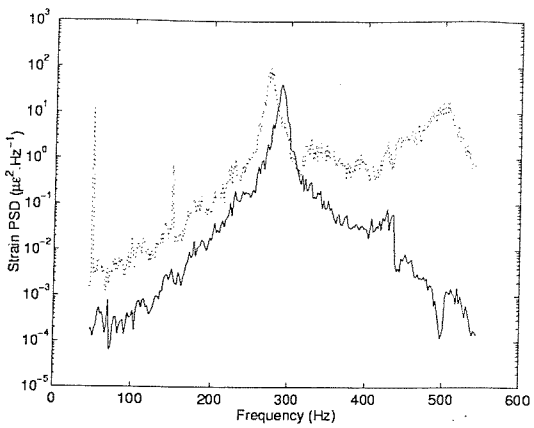

(b) 149.49 dB

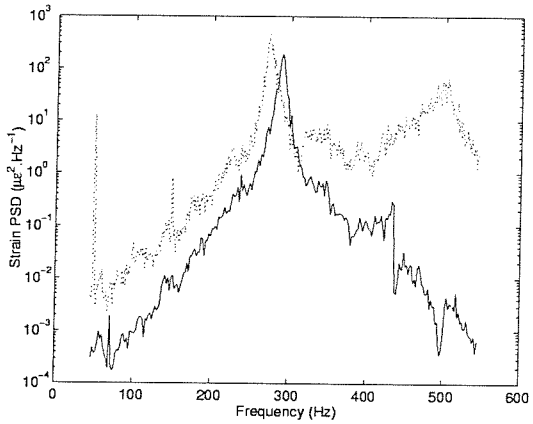

(c) 154.69 dB

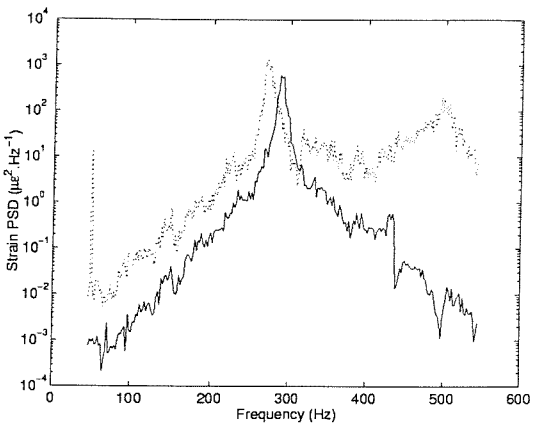

(d) 159.49 dB

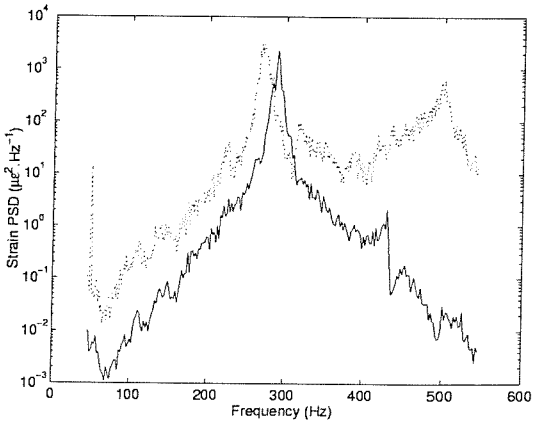

(e) 163.71 dB

Figure 7.27: Comparison of predicted FE (–) and measured (- -) strain PSD for outer centre gauge go3 (y-wise), panel 4.

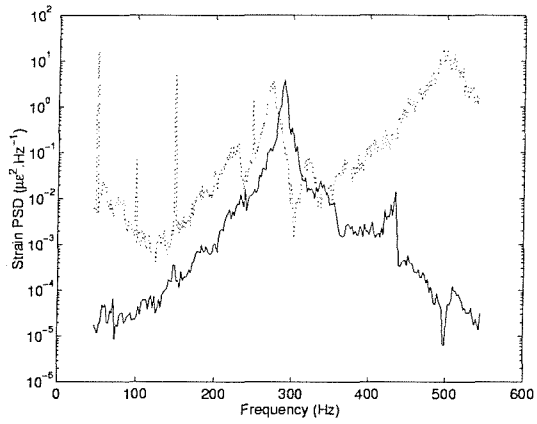

(a) 143.20 dB

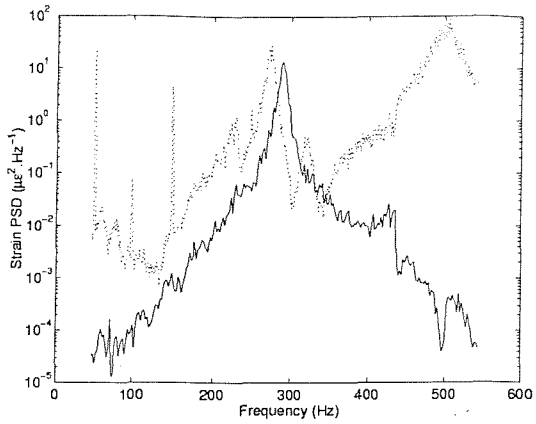

(b) 149.49 dB

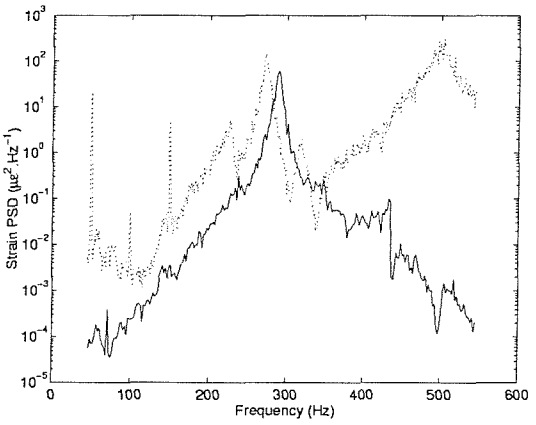

(c) 154.69 dB

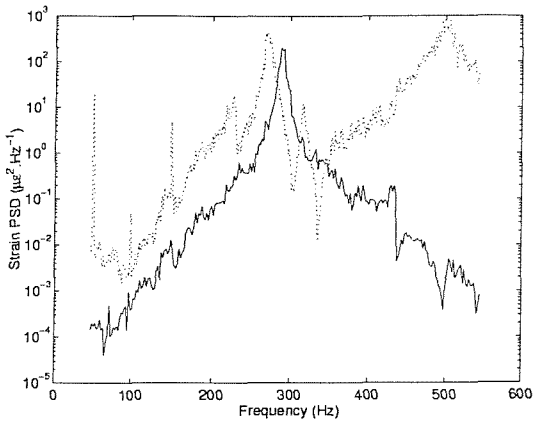

(d) 159.49 dB

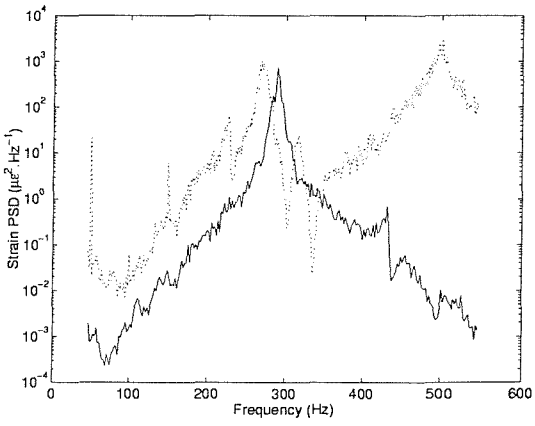

(e) 163.71 dB

Figure 7.28: Comparison of predicted FE (–) and measured (- -) strain PSD for outer centre gauge go4 (x-wise), panel 4.

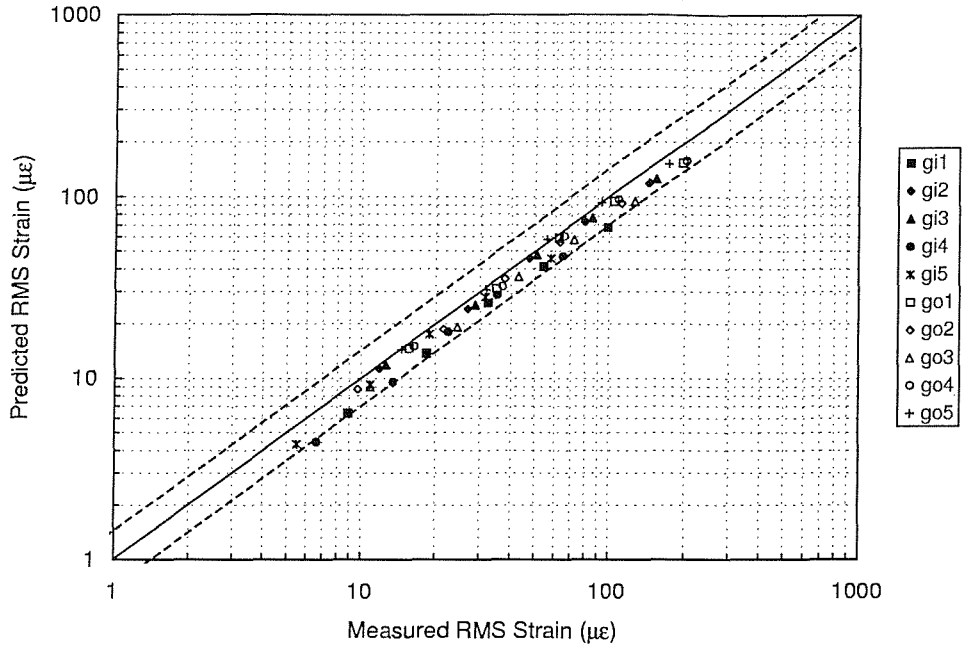

(a) Panel 1.

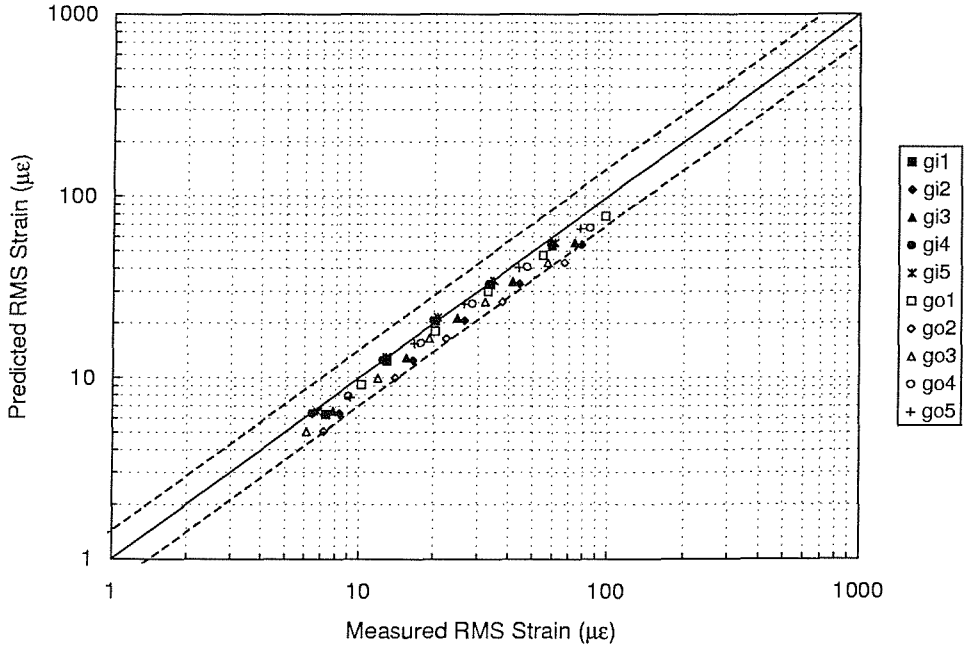

(b) Panel 2.

Figure 7.29: Comparison of measured and predicted RMS strain for panels 1 and 2 using the Finite Element Method. Overall RMS value calculated between 47 Hz and 550 Hz.

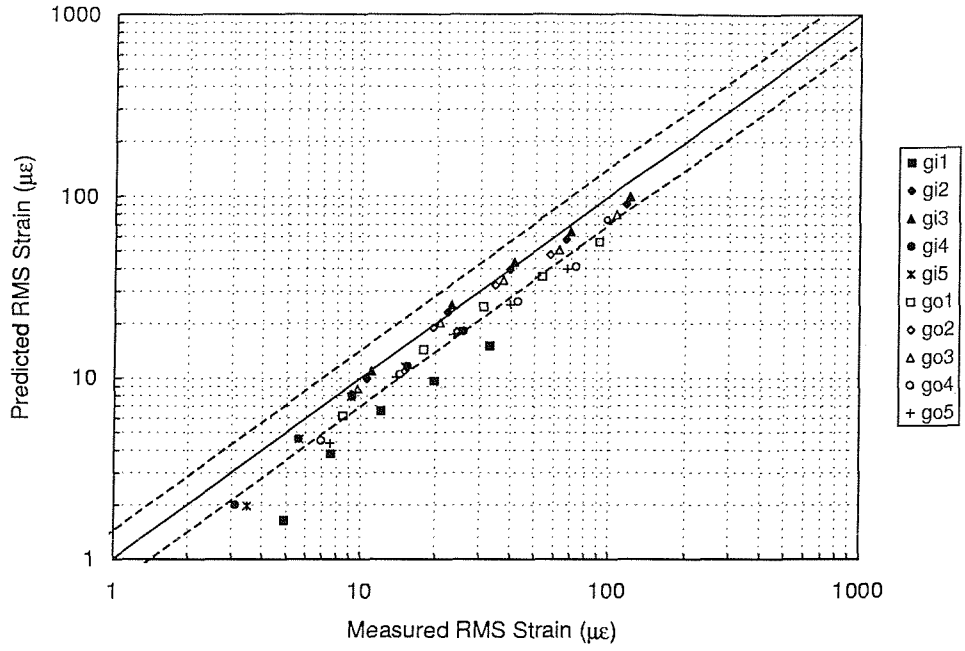

(a) Panel 3.

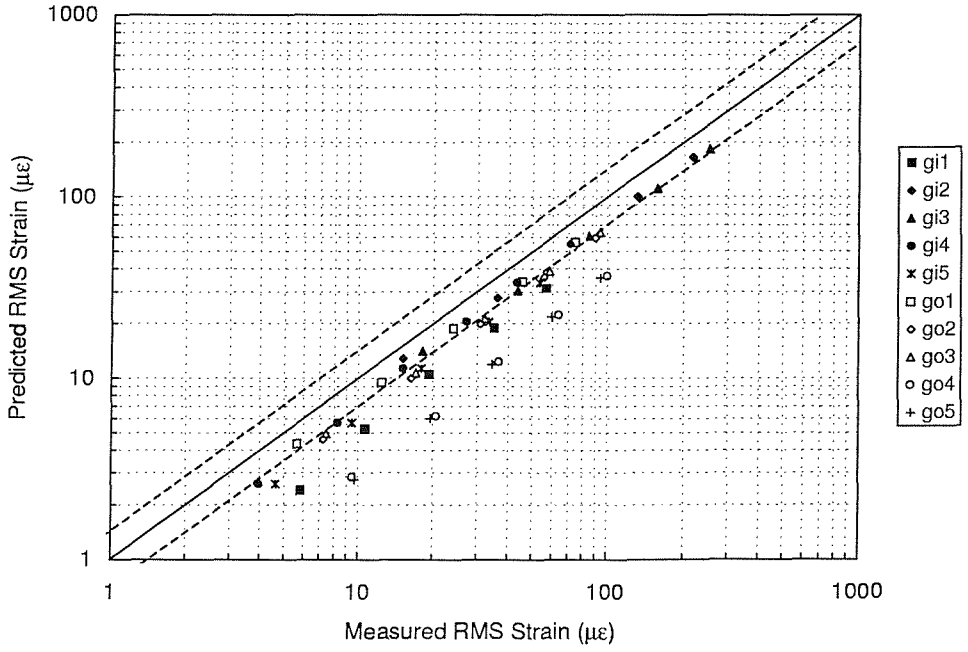

(b) Panel 4.

Figure 7.30: Comparison of measured and predicted RMS strain for panels 3 and 4 using the Finite Element Method. Overall RMS value calculated between 47 Hz and 550 Hz.

7.5 Comparison of predicted and estimated core shear strain

The RMS core shear strain in both the xz and yz planes was predicted using the SDOF method (case 3) and the FE model. In the latter case, both narrow-band (30 Hz centred on the fundamental response frequency) and broadband results were calculated and are presented in table 7.11, along with the SDOF (case 3) method results. The SDOF approximation and FEM (narrow-band) results compare very

Panel	OASPL (dB)	*SDOF Method (case 3)*		*FEM (Narrow-band)*		*FEM (Broad-band)*	
		γ_{xz} ($\mu\epsilon$)	γ_{yz} ($\mu\epsilon$)	γ_{xz} ($\mu\epsilon$)	γ_{yz} ($\mu\epsilon$)	γ_{xz} ($\mu\epsilon$)	γ_{yz} ($\mu\epsilon$)
1	143.29	2.86	30.07	2.98	33.67	8.97	34.92
	149.97	6.68	70.15	6.30	71.28	19.19	74.69
	154.75	11.79	123.79	12.04	136.14	35.57	141.47
	159.28	19.70	206.84	19.11	216.16	68.20	225.57
	163.71	32.48	341.11	31.21	352.93	101.96	368.58
2	143.88	2.05	11.94	1.70	11.46	7.95	12.56
	149.91	3.94	22.93	3.37	22.74	17.36	24.73
	154.92	6.70	39.03	5.55	37.51	29.11	40.86
	159.00	10.74	62.55	8.78	59.34	47.95	65.00
	163.09	16.94	98.64	14.62	98.79	67.12	106.95
3	143.51	2.28	54.26	1.85	49.66	2.98	51.50
	149.93	4.89	116.56	4.33	116.22	6.52	119.46
	154.18	8.28	197.21	7.47	200.75	10.42	205.36
	158.84	13.54	322.33	10.77	289.14	16.92	300.76
	162.82	21.16	503.74	16.76	450.02	26.18	468.72
4	143.20	0.69	54.10	0.58	45.75	0.62	48.33
	149.49	1.50	118.11	1.25	99.67	1.33	104.72
	154.69	2.77	217.13	2.52	200.21	2.65	209.01
	159.49	4.86	381.93	4.59	364.93	4.81	379.22
	163.71	7.83	615.08	7.56	602.01	7.92	624.7

Table 7.11: Predicted RMS core shear strain for locations mid-way between gauges 2 and 3 (y-wise), and mid-way between gauges 4 and 5 (x-wise), using the SDOF method (case 3) and the Finite Element Method (narrow-band and broad-band solution).

well for both γ_{xz} and γ_{yz} and for all four panels. In addition, it is apparent from the FEM broad-band results that the predominant response is in a higher mode than the fundamental for γ_{xz}, since these results are higher than the narrow-band predictions, particularly for the first three panels. This is confirmed when one plots the strain power spectral density for both γ_{xz} and γ_{yz} from the FE broad-band results, as shown in figure 7.31. Panels 1 and 2 in particular show a much higher response in the second mode excited by the PWT compared with the fundamental response.

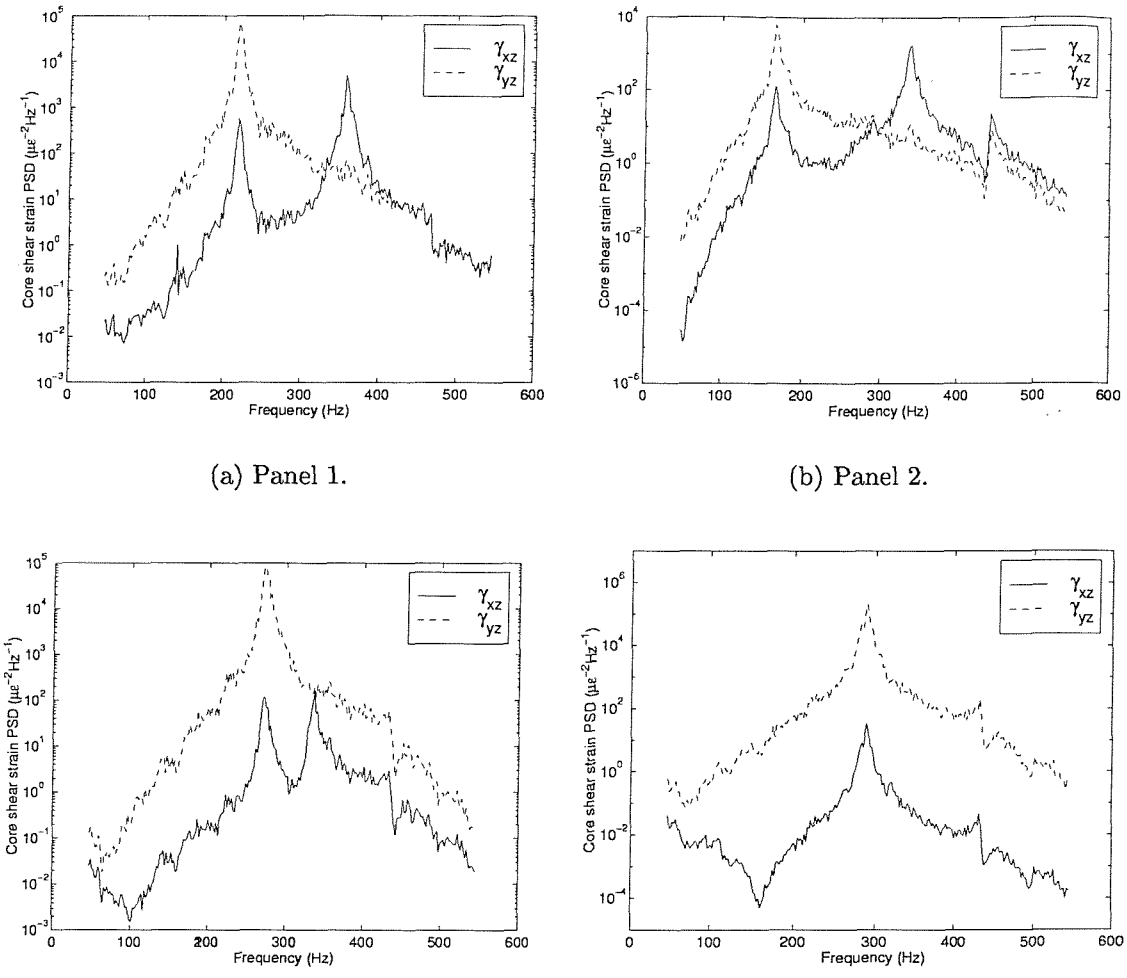

(a) Panel 1.

(b) Panel 2.

(c) Panel 3.

(d) Panel 4.

Figure 7.31: FE calculated core shear strain PSD (broad-band results).

Comparing the predicted core shear strain results with those estimated using the measurement technique developed in chapter 3, and applied in chapter 5 (table 5.10), it is clear that a problem exists with the estimation method when used for the doubly curved panels. There is no consistency in the difference between the predicted and estimated core shear strain which suggests that the method is extremely sensitive to the accuracy of the face plate strain values used to calculate the finite difference approximation. The FE calculated RMS face plate strain values agreed very well with those measured, and the method for calculating the semi-empirical constants was proved for flat panels at the end of chapter 3. Therefore, one possible explanation is in the method used to subtract the membrane strain from the measured direct strain,

details of which were given at the end of chapter 5. Since very small differences in strain are being calculated in equation 5.13, the method will clearly be very sensitive to the accuracy of the individual strain measurements, which could potentially result in very large errors in the estimated core shear strain. To verify this theory, a Monte-Carlo analysis was conducted using the FE model for panel 1. The calculated semi-empirical values given in table 5.10 were used in the estimate of core shear strain (these values were calculated using the FE model), and the calculated face plate strain values were varied randomly within a $\pm 10\%$ band using a random number generator in MATLAB that produces numbers chosen from a normal distribution with a mean of zero and a variance of one. Fifty estimations were made using the method and the results were compared with the actual FE calculated core shear strain. The results from the Monte-Carlo analysis are shown in figure 7.32, and as can be seen, errors within a $\pm 10\%$ band can result in very large errors in the estimated core shear strain. Positive errors in the outer face plate strains with negative errors in the inner face plate strains (and vice-versa) will obviously produce larger errors in the difference between these two values and hence lead to a large error in the final estimate. It is therefore apparent that the method, as it stands, is unsuitable for doubly curved panels due to the way the membrane strain is removed by taking differences between the inner and outer direct strain values. One possible solution is to use the known radius of curvature in the calculations to remove the membrane strain element since this will be a function of the reciprocal of the radius of curvature.

Further work needs to be carried out in order to improve the estimation method, which has been shown to work very well for beams and flat panels. Indeed, the method has great potential for use in coupon fatigue tests used to generate S/N curves for a particular structure. Details of this method of testing are given in the ESDU data series (Data Item 93027). In brief, beam coupons, which are representative of the parent structure, are excited with narrow-band random vibrations using a shaker. The strain, and hence the stress, is measured and monitored until the coupon fails giving the desired S/N curve. The core shear strain measurement technique, which has been validated for beams, could therefore be used to estimate the strain in the core of sandwich coupons, and hence generate S/N data for the core, which was not possible before due to the difficulties in measuring the strain in the core.

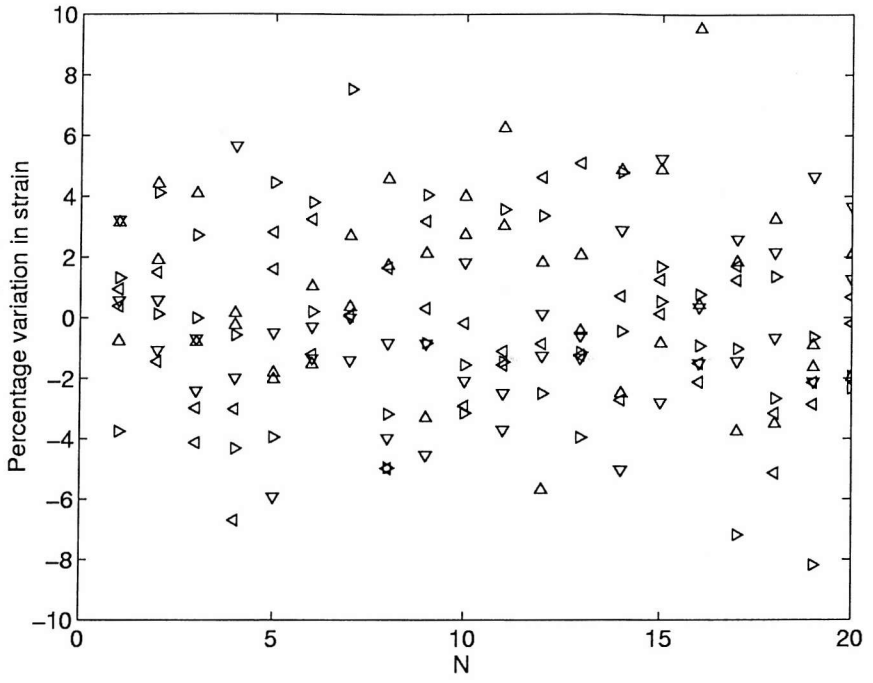

(a) Randomly generated variations in face plate strain.

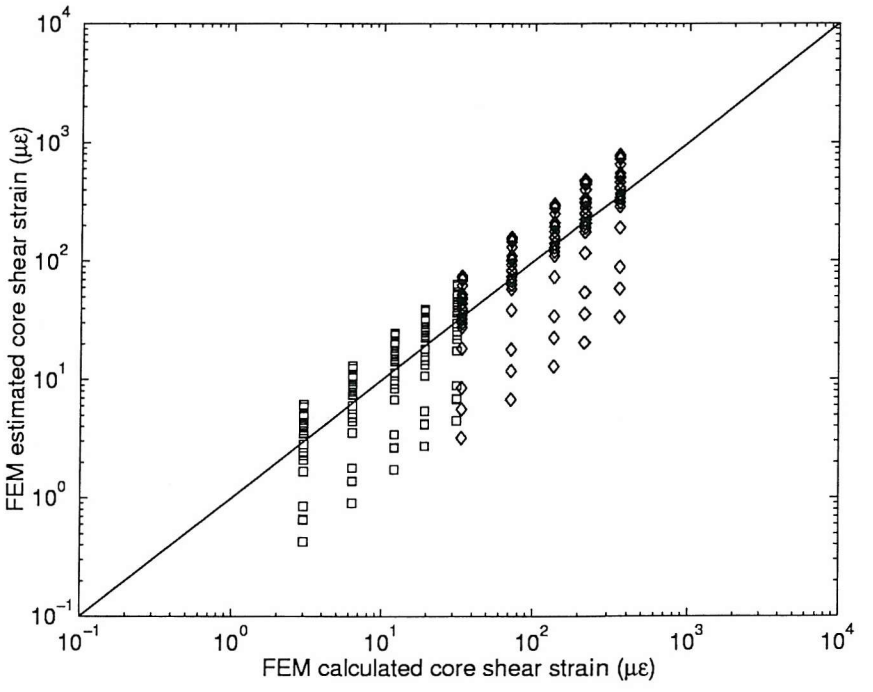

(b) Core shear strain estimates using the randomly varied strains.

Figure 7.32: Monte-Carlo analysis of the core shear strain measurement technique using the FE model for panel 1 (N=50 estimates).

7.6 Concluding summary

In this chapter, three methods used to predict the dynamic response of the doubly curved sandwich panels to random acoustic excitation have been presented. The first method, which combines the classical single-degree-of-freedom approach with the finite element method, was fully investigated. Three estimates of the spatial characteristics of the pressure loading were used and the results indicated that the Miles [25] approach of a uniform pressure loading resulted in a gross under-estimation, while the unit joint acceptance approach (i.e. where the spatial characteristics of the pressure loading exactly match the structural mode shape) resulted in an over-estimation. A more accurate estimate of the joint acceptance was formulated by considering the mode shape to be a product of cosine waves, and the spatial characteristics of the pressure loading to be a series of travelling waves (as proved by experiment in chapter 5). The resulting estimates compared very well with the measured RMS strain when the latter had been scaled according to the percentage contribution of the fundamental mode to the overall response.

Blevins' normal mode method was also used to predict the response [43]. This method is an extension of the Miles approach which can be used for higher modes and complex shapes. In this study, the mass-weighted mode shape approximation proposed by Blevins [43] was used, which was basically the same as the unit joint acceptance approximation. The results were very similar to those found using the SDOF method with unit joint acceptance (case 2), i.e. an over-estimation.

For the finite element analysis, the chamfered edge finite element models were used [85], and the spring supports used in the PWT were modelled as shown in chapter 5. In order to model the response to random acoustic excitation, the approach of finding the unit transfer function and multiplying by the pressure PSD was adopted. The unit transfer function was found by conducting a series of harmonic analyses with a simulated travelling wave load on the nodes of the panel. Solutions were found at each frequency where the spatial characteristics of the travelling wave were calculated and the unit force loads applied before each solution step. The results compared very well with the measured response in terms of both the PSD and RMS strain response, although for the former, the higher modes found during measurement were not as apparent from the FE calculations. This could be attributed to higher modes with nodal lines along the length of the panel being excited in the PWT, but not being recovered from the FE analysis due to the constant loading across the width (y direction) of the panel. In addition, the FE tended to under-predict the RMS response

whereas the SDOF approach generally over-predicted the response, particularly for panels 2, 3, and 4. It is clear from the work here that further work needs to be done for the prediction of the higher modes using this method.

Finally, both the SDOF method, and the travelling wave FE method were used to calculate the core shear strain. Comparisons were made with the estimates made in chapter 5, using the method developed in chapter 3, and the results indicated that the core shear strain estimation method could not successfully estimate the strain in the core compared with the calculated values. Further investigation revealed that there was no trend to the inconsistencies, which suggested that there was a sensitivity problem. The method used to extract the membrane strain from the direct strain measurements in the face plates relied on calculating the small difference between the strain in the inner and outer face plates, and from there calculating the rate of change between the two gauge locations. It was therefore possible that any errors introduced there could have a profound effect on the final result, and to confirm this a monte-carlo analysis was conducted using the FE model. The results indicated that a small error in the face plate strain values, within a $\pm 10\%$ band, could produce large errors, therefore it was suggested that an alternative solution should be sought for removing the membrane strain. In any case, the method has been proved for sandwich beams, and to this end has great potential for use in producing S/N data from sandwich coupon fatigue tests, which is something that has not previously been possible due to the difficulties in instrumenting the core.

Chapter 8

Conclusions

8.1 Background to current work

The main aims of the work were to investigate the dynamic response characteristics of doubly curved composite honeycomb sandwich structures which are subject to random acoustic excitation since this is an area that has not so far been addressed. The work was related to the problems experienced in industry with acoustic fatigue failures of aircraft engine intake barrel panels which have carbon fibre reinforced plastic faceplates and lightweight paper honeycomb cores.

The general problem has been addressed in chapter 1, together with a background of the main developments in acoustic fatigue research, in relation to both metallic and composite structures. The review has highlighted the lack of research into those structures having a doubly curved geometry which provided the impetus for the present work. In addition, a survey of the principal failure mechanisms of sandwich panels, particularly intake barrel panels, has been carried out.

In order to provide suitable structures for the experimental programme, a set of doubly curved composite honeycomb sandwich panels were designed and manufactured at the University of Southampton, as detailed in chapter 2. Four panels were manufactured, three symmetric sandwich panels with different radii of curvature representative of small medium and large nacelle structures, and an asymmetric sandwich panel which has an identical curvature to one of the symmetric panels. The work presented in this chapter proved to be very challenging since it is the first time that this type of structure had been manufactured within the Faculty. The quality of the test structures was high, which was confirmed by Aerostructures (Hamble Group) Ltd. using their A-Scan machine.

8.2 A new measurement technique for the estimation of core shear strain

The literature survey highlighted the need for further investigations into the strains experienced by the core since the majority of the failures were attributed to core cracking. This prompted the development of a new, and novel measurement technique for estimating the core shear strain from face plate direct strain measurements, which was presented in chapter 3. This technique has been fully validated using both static and dynamic experiments, and theoretical models using the finite element method, all of which proved the validity of the technique. The technique has great potential for use in the aircraft industry, and one possible use is in the generation of S/N data from coupon fatigue tests. The ESDU acoustic fatigue design guide series presents a generally accepted method for estimating the fatigue life of structures subject to random acoustic excitation, as reviewed in chapter 1. The method involves determining the areas of stress concentration on the acoustically loaded structure, and then designing coupons that represent the parent structure in the region of the stress concentrations. These coupons are then randomly vibrated within a frequency band that encompasses the predominant response frequency, and strains are measured from which S/N data can be derived. The fatigue life of the core has not previously been considered when generating fatigue life data of sandwich configurations, and this is where this technique would be extremely useful.

The technique was extended to panel type structures using a semi-empirical method, which was validated using FE model of a flat sandwich plate. In order to apply the method to doubly curved sandwich panels, a technique was developed to remove the membrane strain element from the direct strain measurements using gauges located on both the inner and outer face plates. Estimates of the core shear strain were then made from the measurements of face plate strain obtained from the PWT tests in chapter 5, and comparisons with the predicted values using the SDOF and FE methods developed in chapter 7 revealed that the estimates of core shear strain were very different from the predicted values. A sensitivity analysis was conducted which revealed that the method for removing the membrane strain was producing large errors in the final result due to the extreme sensitivity of this method to any small differences in the face plate measurements. It is evident from this that further work needs to be carried out to develop the measurement technique fully for panel type structures which have curvature.

8.3 Experimental studies of the dynamic response of doubly curved sandwich panels

The resonance frequencies of vibration of some of the lower modes of the experimental test panels have been obtained under free boundary conditions as detailed in chapter 4, with the intention of providing a comparative set of results to be used in the development of the finite element model which was presented in chapter 6. The experimental results indicated that the panels had very light damping and well spaced lower resonance frequencies which enabled good estimates of the deflection shapes to be obtained without the need for curve fitting.

The panels have also been tested in the ISVR Progressive Wave Tube facility. Support in the test aperture was provided using four circular steel springs which enabled higher panel centre strains to be obtained, and prevented any difficulties when using the FE method to model the boundary conditions in the PWT. Although not representative of in service boundary conditions, the support method was considered the best compromise between obtaining reasonable strain levels, providing easy to model boundary conditions, and in addition it enabled a direct comparison of the modal damping values measured in chapter 4 with those measured in the PWT. As expected, the modal damping measurements in the PWT were higher, probably due to acoustic impedence effects in the test section. Initial experiments in the PWT established the existence of travelling acoustic waves, a fact which was later utilised in the prediction of the dynamic response. Following this, the panels were tested at various overall sound pressure levels from 142 dB to 164 dB (re 2×10^{-5} Pa) over a frequency range from 60 Hz to 600 Hz. The response was found to be predominantly in the fundamental bending mode of vibration, which accounted for around 80% of the overall response, except for the inner and outer centre x-wise gauges of panels 3 and 4 were it accounted for around 20-40%. The response was also found to be linear over all measured OASPL's from a consideration of the strain statistics where a Gaussian response was noted with skewness values close to zero and kurtosis values close to three. This result was surprising when one considers that the spatial measurements in the test section indicated a non-Gaussian response, particularly at low sound pressure levels. However, the differences in the way the test section was closed for the spatial measurements compared with the way the panels were secured in the test section could account for this to some degree. The ratios of outer-to-inner RMS face plate strain were reported to be in the region of 2.5 to 3 for panel 1, which is consistent with reported values of around 2.5 for flat rectangular sandwich panels [49, 15]. The

degree of double curvature, and the symmetry of the sandwich lay-up, both had a profound effect on these ratios. The estimates of core shear strain were found to be inconsistent with the predicted values from the theoretical analyses of chapter 7. This has highlighted the need for further work on the measurement technique for panel structures with a curved geometry.

8.4 Response prediction of acoustically excited, doubly curved sandwich panels

The development of the finite element model has been presented in chapter 6. The results from the model were in excellent agreement with the experimental results for the resonance frequencies of vibration and deflection shapes. This model was altered to include greater detail of the bevelled edge region, and the results were again in very good agreement. The model was then used to investigate the effect of various design parameters on the free vibration response of doubly curved sandwich panels. These included the effect of changing radii of curvature, orthotropy of the core, and face plate ply orientation on the first few natural frequencies of vibration. During the parameter studies, the curve veering phenomenon was observed. However, it was unclear whether veering was a result of the approximation method used or was actually occurring in the physical system. A summary of the major sensitivities was made, which revealed that panels that have geometries similar to that of small engine intake barrel panels are more sensitive to changes in the radii of double curvature than larger engine intake barrel panels. In addition, changes in the orthotropy of the core were found to have a lesser effect on the natural frequencies of vibration, particularly for high shear stiffness cores. Finally, increasing double curvature was found to increase the sensitivity to changing ply orientation in terms of the natural frequencies of vibration compared with panels with a low amount of curvature.

The finite element models were later used in chapter 7 to predict the dynamic strain response of the doubly curved panels to random acoustic excitation in the PWT. Three methods were adopted, all of which relied on modal results from the FE models. The single-degree-of-freedom approximation method was fully investigated, and it was found that the commonly adopted Miles approach of using the approximation of uniform pressure loading resulted in grossly-underestimated strains for the doubly curved panels. This was due to the method of attaching the panels in the aperture using circular steel springs, which allowed rigid body displacement of the panels and

hence resulted in a joint acceptance which approached zero. The unit joint acceptance approach, which was also adopted in the Blevins normal mode method resulted in an over-estimation. A more accurate estimate of the joint acceptance was therefore derived by considering the spatial characteristics of the pressure loading to be a series of travelling waves, which was proved to be the case in practice in chapter 5, and the structural mode shape was estimated to be a product of cosine waves. Excellent agreement was obtained between the new predictions and measured RMS strains, with the latter being scaled according to the percentage contribution of the fundamental mode to the overall response. With this method, which is a hybrid technique utilising the FE method for modal data, and the single-degree-of-freedom method for the response to random acoustic excitation, it is possible to obtain very reliable estimates providing the spatial characteristics of the pressure loading and the structural mode shape can be estimated.

Finally, the finite element model was used exclusively to estimate the response due to random acoustic loading. A similar approach to applying the load was adopted here in that a series of travelling acoustic waves, with unit force amplitude, were applied to the nodes of the model. Using the harmonic analysis procedure in ANSYS, the problem was solved for frequencies between 47 Hz and 550 Hz using a looping structure. The resulting strain transfer function was then converted into pressure units, squared, and multiplied by the measured pressure spectrum data obtained from the PWT experiments. The results for both the strain PSD, and the overall RMS strain agreed extremely well with the measured values. The FE predicted response was found to be predominately in the fundamental mode, more so than in the experiments, and the reason for this was unclear. In conclusion, the technique has great potential for use in a parameter investigation, since to study the effects of various loading spectra is a simple matter of multiplying the FE solution by the new spectra, without the need to re-run the FE model.

8.5 General conclusions

In the present work, complementary experimental and theoretical studies have been presented for doubly curved sandwich panels subject to random acoustic excitation. The results indicated that this type of structure can be tested and analysed by existing techniques and, in the expected acoustic regime, linear behavior was observed which clearly demonstrated that linear modelling was sufficient to analyse the response of the structures. However, in more severe environments such as higher sound pressure

levels and temperatures, linear modelling may not be valid.

The Finite Element method was found to give excellent results when used to predict the natural frequencies of vibration, and a series of parameter studies revealed the veering phenomenon, which has been encountered by others in similar studies on flat and singly curved panels. In addition to the natural frequencies of vibration, the predicted response mode shapes agreed very well with the measured deflection shapes at resonance.

Several methods were employed to predict the strain response of the structures to random acoustic excitation in the form of travelling waves at grazing incidence. The nature of the pressure field was estimated by means of the joint acceptance in the single degree-of-freedom method, and a novel travelling wave approach was used in the finite element analysis. Both methods gave excellent results compared to the measured strain response from tests carried out in a PWT facility. The work carried out here has clearly demonstrated that if the nature of the pressure field is known, both analytical and Finite Element methods could be used to predict the surface strains to a reasonable degree of accuracy.

Finally, a new method has been developed for the estimation of the core shear strain using surface face plate strain measurements. The method worked very well for beam structures, and therefore could be used for the prediction of fatigue life if a similar technique were applied to test coupons.

8.6 Recommendations for further work

The work carried out here has resulted in several possible topics for future investigation, which are listed below:

- **Further work on the core shear strain measurement technique.**

  The new technique developed in chapter 3 has great potential for use in the estimation of shear strain in the core of both sandwich beams and panels. For the former type of structure, the technique has been fully validated and will be particularly beneficial in the estimation of S/N data from coupon fatigue tests, which has previously not been possible due to the difficulties in instrumenting the cells of the core. For sandwich panels, there is a need for further work to validate the technique for panels with a curved geometry. A new method of removing the membrane strain from such panels should be sought, possibly using the radius of curvature in the equations to account for the membrane strain. In

addition, a method of separating out the bending and shear deflections in the measurements would be particularly beneficial since it would help to validate the technique for a variety of panel configurations, such as those were the shear deflection can no longer be considered negligable.

- **Testing of the doubly curved panels with a fabricated test fixture.**

  The main aims of the work were to investigate the response of doubly curved sandwich panels to random acoustic excitation both experimentally and theoretically. The latter dictated the method of fixing the panels in the test aperture, however, further tests carried out using either an fabricated aluminium alloy or composite test fixture similar to that found in service would be beneficial. This is particularly true for investigating the panel edge strains in the analysis since the geometry in the bevelled edge region is quite complicated and the results for this region need to be validated against experimental measurement. The only problem with carrying out these tests is that the strains developed will probably be very low, therefore testing at higher sound pressure levels in the region of 170-175 dB (which is now being experienced in service, particularly for the new generation of military aircraft) would be recommended.

- **Testing of intake barrel panels with perforated facing skins.**

  During the literature survey in chapter 1, the problem of in-service core cracking was highlighted. The panels that experienced these failures were intake barrel panels, which have a perforated liner or facing skin which, along with the honeycomb core, provides noise attenuation in the intake duct since the cells act like an array of Helmholtz resonators. A possible reason for the failures could be varying cell geometry leading to an inbalance in the resonant frequency of neighbouring cells, therefore leading to cell wall vibrations and hence fatigue failures. This is a topic worthy of further investigation, and tests could be carried out with a section of structure which is instrumented in such a way to provide information on the dynamic response of individual cell walls. A complementary finite element investigation could also be carried out.

- **Parameter studies of the response of doubly curved sandwich panels to various loading spectra.**

  One of the main advantages of the finite element travelling wave analysis is that the response of the panels to various loading spectra can be studied without the need to re-run the finite element model. It is therefore recommended that a parameter study be carried out by considering different in-service loading spectra, such as a typical engine fan spectrum which will contain the blade passing frequency tone and associated harmonics superimposed on a broadband frequency spectrum. In this way, the related effects of resonant and forced response could be studied.

- **Prediction of the spatial characteristics of random pressure fields using Computational Fluid Dynamics.**

  There is a need to know, and be able to predict, the spatial characteristics of random pressure fields on all regions of aircraft structures and from a variety of sources such as engine fans, jet efflux, and turbulent boundary layers. This could be done using techniques such as Computational Fluid Dynamics, or more specifically Computational Aero-Acoustics. If used in conjunction with the Finite Element Method, this would provide the designer with a very powerful response prediction tool.

References

[1] Clarkson, B.L. Review of sonic fatigue technology. Technical Report CP-4587, NASA, April 1994.

[2] Green, P.D. Current and future problems in structural acoustic fatigue. In *AGARD SYMPOSIUM, 'Impact of Acoustic Loads on Aircraft Structures'*, pages 1.1–1.5, Lillehammer, Norway, 1994.

[3] Richards, E.J. and Mead, D.J. (editors). *Noise and Acoustic Fatigue in Aeronautics.* John Wiley and Sons Ltd., 1968.

[4] White, R.G. Developments in the acoustic fatigue design process for composite aircraft structures. *Composite Structures*, 16:171–192, 1990.

[5] Hess, R.W. and Herr, R.W. and Mayes, W.H. A study of the acoustic fatigue characteristics of some flat and curved aluminium panels exposed to random and dicrete noise. Technical Report TN D1, NASA, 1959.

[6] Clarkson, B.L. and Ford, R.D. The response of a typical aircraft structure to jet noise. *Journal of the Royal Aeronautical Society*, 66:31–40, 1962.

[7] Clarkson, B.L. The design of structures to resist jet noise fatigue. *Journal of the Royal Aeronautical Society*, 66:603–616, 1962.

[8] Clarkson, B.L. Stresses in skin panels subjected to random acoustic loading. *The Aeronautical Journal of the Royal Aeronautical Society*, 72:1000–1010, 1968.

[9] Jacobs, L.D. and Lagerquist, D.R. Finite element analysis of complete panel response to random loads. Technical Report TR-68-44, AFFDL, 1968.

[10] Arcas, N.R. Prediction of stress and fatigue life of acoustically excited aircraft structure. *Shock and Vibration Bulletin*, 39(2), 1969.

[11] Thompson, A.G.R. and Lambert, R.F. The estimation of rms stresses in stiffened skin panels subjected to random acoustic loading. Technical Report Section 5: AGARD-AG-162, Advisory Group for Aerospace Research and Development, North Atlantic Treaty Organization, November 1972.

[12] Nacelles Systems Division booklet. Nacelles Systems Capabilities. Short Brothers plc. P.O. Box 241, Airport Road, Belfast, BT3 9DZ, Northern Ireland.

[13] Ballentine, J.R. et.al. Refinement of sonic fatigue structural design criteria. Technical Report TR 67-156, AFFDL, January 1968.

[14] Jacobson, M.J. Acoustic fatigue design information for fiber reinforced structures. Technical Report TR 68-107, AFFDL, October 1968.

[15] Soovere, J. *Dynamic response of acoustically excited stiffened composite honeycomb panels.* Ph.D. Thesis, University of Southampton, 1984.

[16] Holehouse, I. Sonic fatigue of aircraft structures due to jet engine fan noise. *Journal of Sound and Vibration*, 17(3):287–298, 1971.

[17] Hess, R.W. and Lassiter, L.W. and Hubbard, H.H. A study of the response of panels to random acoustic excitation. Technical Report RM L55E13C, NACA, 1955.

[18] Hess, R.W. and Lassiter, L.W. and Hubbard, H.H. An experimental study of the response of simple panels to intense acoustic loading. *Journal of Aeronautical Sciences*, 24(1):19–24, 1957.

[19] Hess, R.W. and Lassiter, L.W. Calculated and measured stresses in simple panels subject to intense random acoustic loading. Technical Report TN-1367, NACA, 1958.

[20] Wagner, J.G. Caravelle acoustic fatigue. In *ICAF/AGARD Symposium on Aircraft Fatigue*, Paris, May 1961.

[21] Clarkson, B.L. and Ford, R.D. Further analysis of the random vibration of the caravelle test section. Technical Report AASU 175, University of Southampton, June 1961.

[22] Clarkson, B.L. and Ford, R.D. Experimental study of the random vibrations of an aircraft structure excited by jet noise. Technical Report AASU 128, University of Southampton, June 1961.

[23] Clarkson, B.L. and Ford, R.D. Random excitation of a tailplane section by jet noise. Technical Report AASU 171, University of Southampton, March 1961.

[24] McGowan, P.R. Structural design for acoustic fatigue. Technical Report TDR-63-820, ASD, October 1963.

[25] Miles, J.W. On structural fatigue under random loading. *Journal of the Aeronautical Sciences*, 21:753–762, 1954.

[26] Miner, M.A. Cumulative damage in fatigue. *Journal of Applied Mechanics*, 12(3):159–164, 1945.

[27] Powell, A. On the fatigue failure of structures due to vibrations excited by random pressure fields. *The Journal of the Acoustical Society of America*, 30(12):1130–1135, 1958.

[28] Bozich, D.J. Spatial correlation in acoustic-structural coupling. *Journal of the Acoustical Society of America*, 36(1):52–58, 1964.

[29] Barnoski, R.L. and Maurer, J.R. Distributed system response characteristics in random pressure fields. Technical Report CR-1660, NASA, 1970.

[30] Bayerdorfer, G. Acoustic fatigue tests for the production of design charts. In *Proceedings of a Conference on Current Developments in Sonic Fatigue*, University of Southampton, 1970.

[31] Rudder, F.F. and Plumblee, H.E. Sonic fatigue design for military aircraft. Technical Report AFFDL-TR-74-112, Acoustics and Vibration Associates, Atlanta, GA, USA, February 1975.

[32] Lindberg, G.M. Accurate finite element modelling of flat and curved stiffened panels. In *AGARD CONFERENCE PROCEEDINGS No. 113 on 'Symposium on Acoustic Fatigue'* [89].

[33] Olson, M.D. and Lindberg, G.M. Jet noise excitation of an integrally stiffened panel. *Journal of Aircraft*, 8:847–855, 1971.

[34] Jacobs, L.D. and Lagerquist, D.R. A finite element analysis of a simple panel response to turbulent boundary layers. Technical Report TR-67-81, AFFDL, 1967.

[35] Soovere, J. Correlation of sonic fatigue failures in large fan engine ducts with simplified theory. In *AGARD CONFERENCE PROCEEDINGS No. 113 on 'Symposium on Acoustic Fatigue'* [89], pages 11.1–11.13.

[36] Hawkings, D. Multiple pure tone generation by transonic compressors. *Journal of Sound and Vibration*, 17(2):241–250, 1971.

[37] Sofrin, T. and Pickett, G. Multiple pure tone noise generated by fans at supersonic tip speeds. Technical Report SP-304 Part II, NASA, 1970.

[38] White, R.G. A comparison of some statistical properties of the responses of aluminium alloy and cfrp plates to acoustic excitation. *Composites*, 9:251–258, 1978.

[39] Wolfe, N.D. and Jacobson, M.J. Design and sonic fatigue characteristics of composite material components. In *AGARD CONFERENCE PROCEEDINGS No. 113 on 'Symposium on Acoustic Fatigue'* [89].

[40] White, R.G. and Mousley, R.F. Dynamic response of cfrp plates under the action of random acoustic loading. In *Proceedings of the Fourth International Conference on Composite Structures* [90], pages 1519–1535.

[41] ESDU International plc., 27 Corsham Street, LONDON, N1 6UA. *Engineering Sciences Data Unit Design Guide Series: Vibration and Acoustic Fatigue.*

[42] Drew, R.C. and White, R.G. An experimental investigation into damage propagation and its effects upon dynamic properties in cfrp composite material. In *Proceedings of the Fourth International Conference on Composite Structures* [90], pages 245–256.

[43] Blevins, R.D. An approximate method for sonic fatigue analysis of plates and shells. *Journal of Sound and Vibration*, 129(1):51–71, 1989.

[44] Galea, S.C. and White, R.G. Effect of temperature on acoustically induced stresses in cfrp plates. In *Proceedings of the Third International Conference on Recent Advances in Structural Dynamics*, pages 629–640, ISVR, University of Southampton, July 1988.

[45] Holehouse, I. Sonic fatigue characeristics of high temperature materials and structures for hypersonic vehicle applications. In *Structural Dynamics. Recent*

Advances. Proceedings of the 6th International Conference. Volume 2 [88], pages 935–949.

[46] Udrescu, R. Nonlinear vibrations of thermally buckled panels. In *Structural Dynamics. Recent Advances. Proceedings of the 7th International Conference. Volume 2* [91], pages 757–768.

[47] Dhainaut, J.M., Duan, B., Mei, C., Spottswood, S.M. and Wolfe, H.F. Non-linear response of composite panels to random excitations at elevated temperatures. In *Structural Dynamics. Recent Advances. Proceedings of the 7th International Conference. Volume 2* [91], pages 769–784.

[48] Rizzi, S.A. and Muravyov, A.A. Comparison of nonlinear random response using equivalent linearization and numerical simulation. In *Structural Dynamics. Recent Advances. Proceedings of the 7th International Conference. Volume 2* [91], pages 833–846.

[49] Sweers, J.E. Prediction of response and fatigue life of honeycomb sandwich panels subjected to acoustic excitation. In Trapp, W.J. and Forney, D.M. [51], pages 389–402.

[50] Wallace, C.E. Stress response and fatigue life of acoustically excited sandwich panels. In Trapp, W.J. and Forney, D.M. [51], pages 225–244.

[51] Trapp, W.J. and Forney, D.M., editor. *Acoustical Fatigue in Aerospace Structures*, Dayton, Ohio, April 29 - May 1 1964.

[52] Jacobson, M.J. and van der Heyde, R.C.W. Acoustic fatigue design information for honeycomb panels with fiber-reinforced facings. *Journal of Aircraft*, 9(1):31–42, 1972.

[53] Soovere, J. Random vibration analysis of stiffened honeycomb panels with bevelled edges. *AIAA Journal of Aircraft*, 23(6):537–544, 1986.

[54] Discussions with technical personnel at Short Brothers plc, January–May 1997.

[55] Millar, D.M.A. *Analysis of a honeycomb sandwich panel failure.* MSc. Thesis, University of Sheffield, 1995.

[56] Millar, D.M.A. The behaviour of light weight honeycomb sandwich panels under acoustic loading. In *Structural Dynamics. Recent Advances. Proceedings of the 6th International Conference. Volume 2* [88].

[57] Hexcel Composites, Duxford, Cambridge CB2 4QD, UK. *Aeroweb Honeycomb Selector Guide.*

[58] Cawley, P. and Adams, R.D. The non-destructive testing of honeycomb structures by the coin-tap technique. In *Sixth International Conference on Composite Materials and Second European Conference on Composite Materials*, pages 1.415–1.423, London, July 1987.

[59] Allen, H.G. *Analysis and design of structural sandwich panels.* Pergamon Press, London, 1969.

[60] Filon, L.N.G. On antiplane stress in an elastic solid. *Proceedings of the Royal Society (A)*, 160:137–154, 1937.

[61] Plantema, F.J. *Airplane, Missile and Spacecraft Structures, edited by Nicholas J. Hoff, Volume 3. Sandwich Construction.* John Wiley and Sons, Inc., 1966.

[62] Measurements Group Inc., P.O. Box 27777, Raleigh, North Carolina 27611, USA. *Strain Gage Rosettes - Selection, Application and Data Reduction*, tech. note tn-515 edition.

[63] ASTM Standard C 273 - 61. *Standard method of shear test in flatwise plane of flat sandwich constructions or sandwich cores*, 1970.

[64] Randall, R.B. *Frequency analysis.* Bruel & Kjaer, 3rd edition, 1987.

[65] ANSYS Inc., 201 Johnson Road, Houston, PA 15342-1300, USA. *ANSYS Users Manual Version 5.4.*

[66] Ewins, D.J. *Modal testing: theory and practice.* Research Studies Press, Hertfordshire, 1984.

[67] J.N. Little and L. Shure. *Signal Processing Toolbox. For use with MATLAB.* The MATH WORKS Inc.

[68] Cooper, J.E. and Wright, J.R. To fit or to tune? - that is the question. In *IMAC XV, Proceedings of the 15th International Modal Analysis Conference*, pages 1353–1359, Kissimmee, FL, U.S.A, 1997.

[69] Wright, J.R., Cooper, J.E. and Desforges, M.J. Normal-mode force appropriation - theory and application. *Mechanical Systems and Signal Processing*, 13(2):217–240, 1999.

[70] Xiao, Y. and White, R.G. Development of design techniques for the avoidance of acoustic fatigue of box-type aircraft structures - final report, part 5: Sound pressure field measurement at the test section of the progressive wave tube (pwt) facility. Technical report, Department of Aeronautics and Astronautics, University of Southampton, January 1999.

[71] Newland, D.E. *An introduction to random vibrations, spectral and wavelet analysis.* Longman Scientific & Technical, 1993.

[72] Norton, M.P. *Fundamentals of noise and vibration for engineers.* Cambridge University Press, 1996.

[73] Fahy, F.J. and Walker, J. (editors). *Fundamnetals of noise and vibration.* E & F.N. Spon, London, 1998.

[74] Bruel & Kjaer, DK-2850, Naerum, Denmark. *B&K pistonphone type 4220 instruction manual*, September 1973.

[75] Bruel & Kjaer, DK-2850, Naerum, Denmark. *B&K measuring amplifier type 2609 instruction manual*, March 1985.

[76] Bruel & Kjaer, DK-2850, Naerum, Denmark. *B&K measuring amplifier type 2608 instructions and applications*, September 1971.

[77] Bruel & Kjaer, DK-2850, Naerum, Denmark. *B&K spectrum shaper type 5612 instruction manual*, 1977.

[78] Cunningham, P.R. and White, R.G. Free vibration of doubly curved composite honeycomb rectangular sandwich panels. In *IMAC XVII, Proceedings of the 17th International Modal Analysis Conference*, pages 65–71, Kissimmee, FL, U.S.A, 1999.

[79] Leissa, A.W. On a curve veering abberation. *Journal of Applied Mathematics and Physics ZAMP*, 25:99–111, 1974.

[80] Perkins, N.C. and Mote,JR, C.D. Comments on curve veering in eigenvalue problems. *Journal of Sound and Vibration*, 106(3):451–463, 1986.

[81] Kuttler, J.R. and Sigillito, V.G. On curve veering. *Journal of Sound and Vibration*, 75:585–588, 1981.

[82] Chen, P.T. and Ginsberg, J.H. Modal properties and eigenvalue veering phenomena in the axisymmetric vibration of spheroidal shells. *Journal of the Acoustical Society of America*, 92(3):1499–1508, 1992.

[83] Petyt, M. Vibration of curved plates. *Journal of Sound and Vibration*, 15(3):381–395, 1971.

[84] Jacobson, M.J. Effects of orthotropic cores on the free vibration of sandwich plates. *The Shock and Vibration Bulletin*, 35(3):9–14, 1966.

[85] Cunningham, P.R., White, R.G. and Aglietti, G.S. The effects of various design parameters on the free vibration of doubly curved composite sandwich panels. *Journal of Sound and Vibration*, 230(3):617–648, 2000.

[86] ASTM Standard D 3039 - 76. *Standard test method for tensile properties of fibre-resin composites*, 1989.

[87] ASTM Standard D 3518 - 76. *Standard practice for inplane shear stress-strain response of unidirectional reinforced plastics*, 1982.

[88] ISVR. *Structural Dynamics. Recent Advances. Proceedings of the 6th International Conference. Volume 2*, Southampton, July 1997.

[89] *AGARD CONFERENCE PROCEEDINGS No. 113 on 'Symposium on Acoustic Fatigue'*, Toulouse, France, 1972.

[90] *Proceedings of the Fourth International Conference on Composite Structures*, Paisley College of Technology, 1987.

[91] ISVR. *Structural Dynamics. Recent Advances. Proceedings of the 7th International Conference. Volume 2*, Southampton, July 2000.

Appendix A

Experimental measurement of the CFRP material properties

The methods used to determine the tensile and in-plane shear properties of the carbon fibre-reinforced plastic material used in the manufacture of the sandwich panel face plates are presented in this appendix. The ASTM test standard D 3039-76 [86] was used as a guide when carrying out the tensile tests, and the method for determining the in-plane shear material property tests followed the recommendations made in the ASTM standard D 3518-76 [87].

A.1 Tensile test method

The test specimens used to determine the tensile properties of the CFRP material were manufactured from 9 layers of SE84/RC200P pre-impregnated plain weave carbon fabric. A plate of dimensions $300mm \times 300mm$ was consolidated under vacuum pressure and cured for four hours at 100° C, following an identical manufacturing procedure as that used for the face plates. Ten test specimens, examples of which are shown in figure A.1, were then cut from this plate using a water-jet cutter to the dimensions shown in figure A.3. The width at the wasted region, and the thickness of each of the tensile test specimens is shown in table A.1. All of the specimens were instrumented with tee-rosette strain gauges (TML FRA-3-23), with a gauge factor of 2.11 and a gauge resistance of 120Ω, in order to measure the strains along the load axis and perpendicular to the axis, which enabled Poission's ratio to be determined. A Zwick 1474 tensile test specimen was used to load the specimens, and an extensiometer was fitted to each specimen during the test to provide the necessary stress-strain data in order to calculate the Young's modulus, as shown in figure A.2. The load was

steadily increased until the specimen failed, and a typical stress-strain curve for one of the specimens is shown in figure A.4.

Specimen No.	Breadth, b (mm)	Thickness, t (mm)
1	13.04	2.15
2	12.98	2.13
3	13.10	2.15
4	12.96	2.25
5	12.98	2.27
6	12.97	2.28
7	12.97	2.26
8	12.95	2.29
9	12.93	2.28
10	12.97	2.29

Table A.1: Tensile test specimen dimensions.

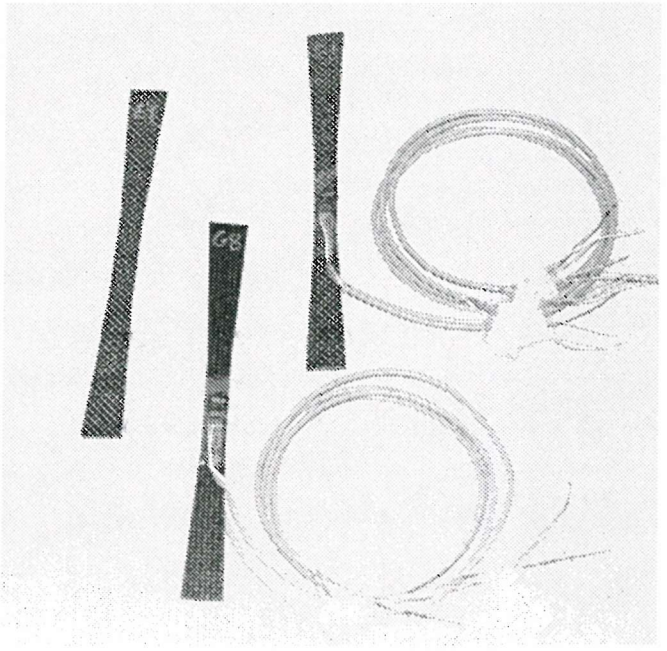

Figure A.1: Tensile and in-plane shear test specimens.

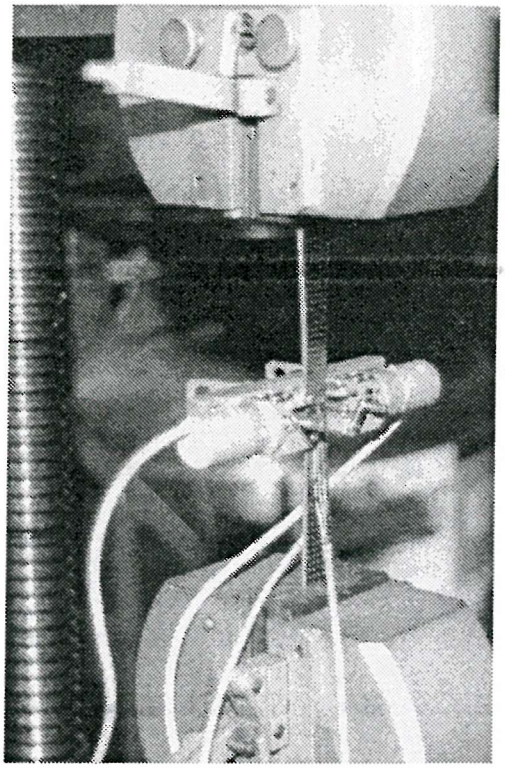

Figure A.2: Test set-up in the Zwick 1474 tensile test machine.

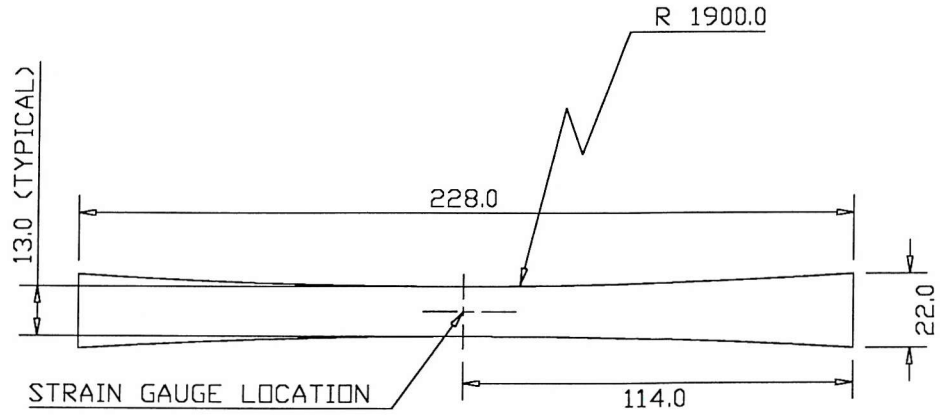

Figure A.3: Test specimen dimensions.

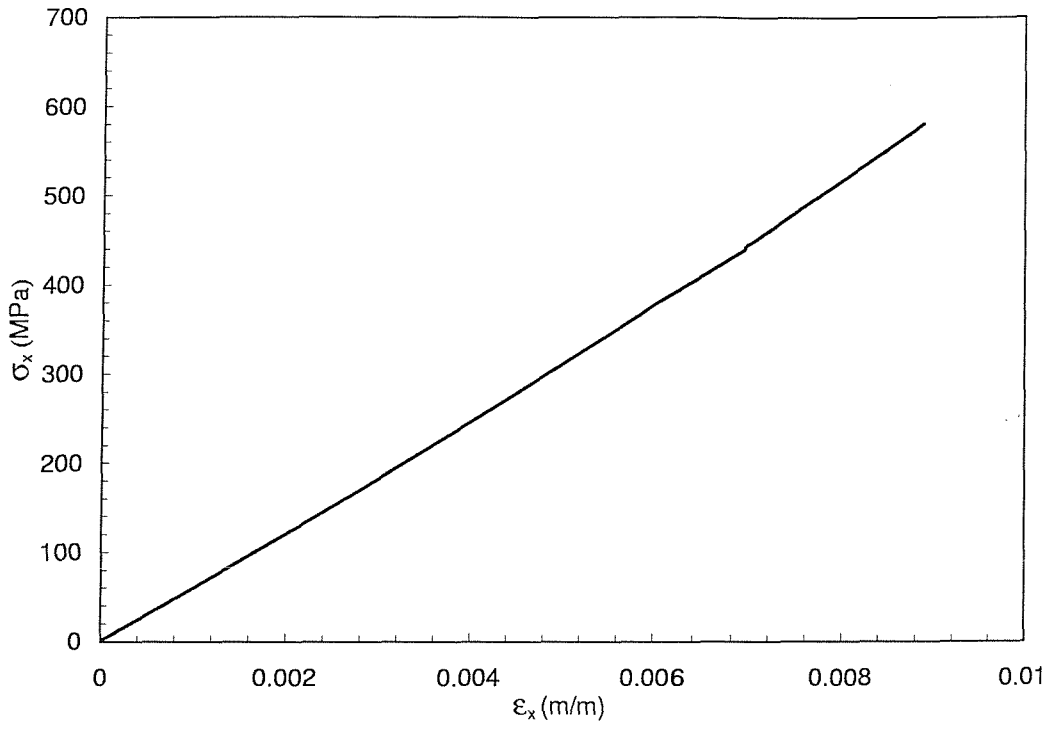

Figure A.4: Typical tensile test results for one of the CFRP test specimens.

The Young's modulus was calculated from the slope of the stress strain curve in figure A.4, and Poisson's ratio was calculated from the ratio of longitudinal and transverse strain:-

$$\nu = \frac{-\Delta\epsilon_x}{\Delta\epsilon_y} \tag{A.1}$$

The tensile test results were averaged to give the final measure of the Young's modulus and Poisson's ratio for the material, which were found to be 57.93GPa and 0.04 respectively.

A.2 In-plane shear test method

The method used to determine the in-plane shear properties is based on the uni-axial tensile stress-strain response of a $\pm 45°$ laminate which is symmetrically laminated about the mid plane [87]. The test specimens were manufactured in the same way and cut to the same dimensions as the tensile test specimens, the only difference being the $\pm 45°$ lay-up. The test specimens were again instrumented with tee-rosette

strain gauges, and testing was carried out in the same Zwick machine to failure, and the load, deflection, and bi-axial strain were again recorded. Both longitudinal and shear stress-strain curves were produced, examples of which can be seen in figure A.5 and A.6. The latter was calculated from the measured longitudinal stress and strain using the relationships:-

$$\tau_{12} = \frac{P_x}{2bd} \tag{A.2}$$

$$\gamma_{12} = \epsilon_x - \epsilon_y \tag{A.3}$$

where τ_{12} is the shear stress in MPa, P_x is the load in N, b is the breadth of the specimen at the wasted region, d is the thickness of the specimen, γ_{12} is the shear strain, ϵ_x is the measured longitudinal strain, and ϵ_y is the measured transverse strain. The shear modulus was calculated from the first linear portion of the shear stress strain curve shown in figure A.6.

$$G_{12} = \frac{\Delta\tau_{12}}{\Delta\gamma_{12}} \tag{A.4}$$

The ten measured shear modulii were again averaged to give the final result of 3.7GPa.

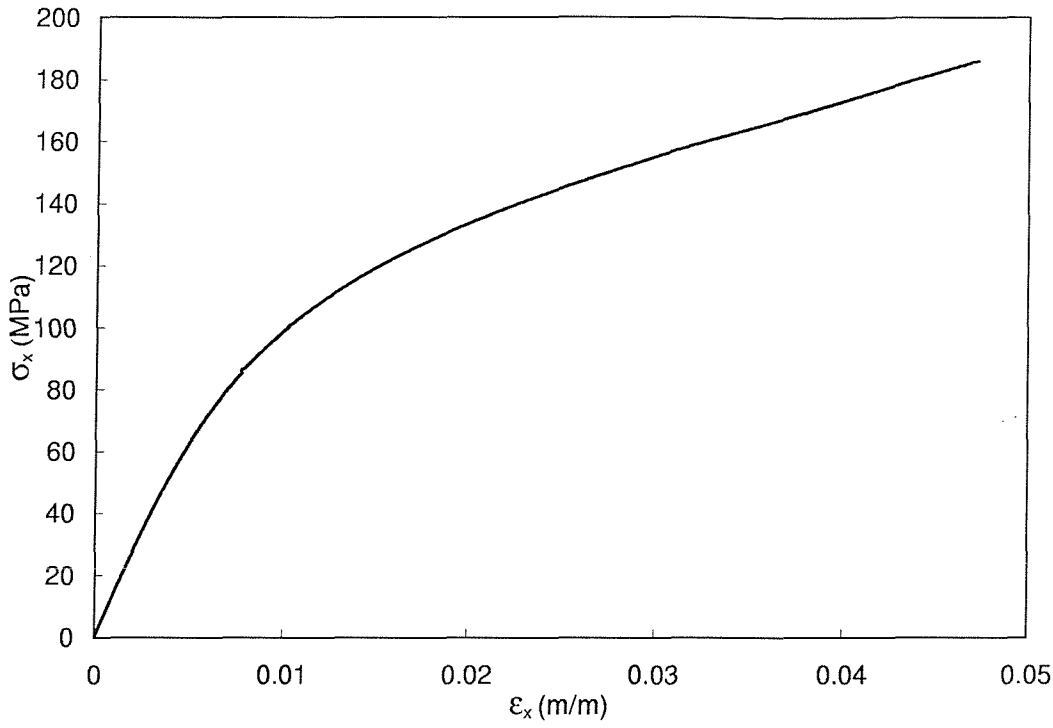

Figure A.5: Typical longitudinal stress-strain curve for one of the CFRP in-plane shear test specimens.

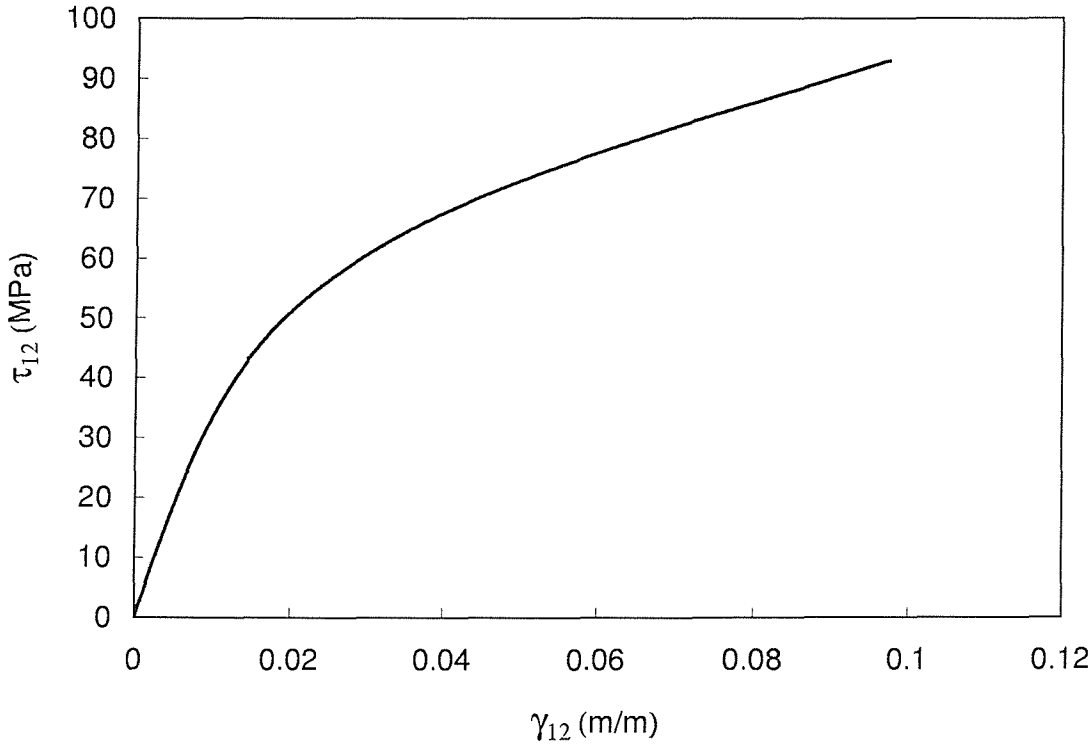

Figure A.6: Typical shear stress-strain curve for one of the CFRP in-plane shear test specimens.